Multi-scale analysis of current-driven spin dynamics in magnetic tunnel junctions

by

Mario Galante

A thesis submitted in partial fulfillment for the

degree of Doctor of Philosophy in the

School of Physics, Trinity College Dublin

Febraury 2020

Declaration of Authorship

I declare that this thesis has not been submitted as an exercise for a degree at this or any other university and it is entirely my own work. I was involved in a number of collaborations, and where it is appropriate my collaborators are acknowledged for their contributions.

I agree to deposit this thesis in the University's open access institutional repository or allow the library to do so on my behalf, subject to Irish Copyright Legislation and Trinity College Library conditions of use and acknowledgement.

Date: _____ Signature: _____

Abstract

Magnetic materials are of fundamental importance for the next generation of sensing and storage applications. The operating principle of such devices is based upon manipulating the orientation of the atomic magnetic moments. The dynamics of the latter can be efficiently driven through the injection of spin-polarised currents that generate effective torques, by spin conservation. These are commonly known as spin torques. State-of-the-art devices employ two ferromagnets sandwiching an insulating spacer, i.e. a magnetic tunnel junction, where information is stored in the mutual orientation of the two magnetisations. These structures are engineered so that the magnetisation vector of one magnetic layer is kept fixed along a given direction, while the magnetisation of the other ferromagnet, also known as free layer, can be reversed with an electric current. The elevated sensitivity of the magnetisation switching to factors such as the properties of the ferromagnet, the quality of the interfaces and temperature fluctuations makes the search of novel materials for these applications a troublesome task. Here we present a multi-scale study of the magnetisation switching in Fe/MgO-based magnetic tunnel junctions for different compositions of the free magnetic layer. We begin by investigating the atom-dependence of the spin torques with the objective of determining the factors that define their materials dependence. This is done by the means of quantum transport calculations performed with a combination of non-equilibrium Green's functions and density functional theory. The calculated spin torques are then used as input for spin dynamics simulations at the atomistic scale, in order to compare the current-driven magnetisation switching in the different systems at different temperatures. We find that the general spatial profile of

the spin torques for a given free layer can be predicted from the band structure of the ferromagnet. However, in many cases the presence of additional interfaces or non-uniform magnetic textures drastically modifies the predicted profile. Nevertheless, the details of the decay of the spin torques do not imply significant modifications of the switching properties. In fact, we find that the critical voltage required to obtain magnetisation reversal is essentially dictated by the total torque acting on the free layer. We continue with a study of antiferromagnetism in the Mn_3Ga and Fe_2MnGa Heusler compounds, in which magnetic properties are dominated by the moments at the Mn sites. Antiferromagnetic materials are of great interest for spintronic applications, since they may push the spin dynamics in the THz range, as opposed to the GHz range of the one in ferromagnets. Our results show that the spin model for Mn_3Ga displays an extremely high-frequency oscillation mode, which is found to be characteristic of this system. In contrast, we find that the induced moments at the Fe sites in Fe_2MnGa are extremely sensitive to the presence of interfaces and to the alignment of the neighbouring Mn atoms. This is observed through both spin dynamics simulations and first principles quantum transport calculations. Finally, we derive a novel parameter-free method for the estimation of the Gilbert damping from first principles simulations.

Acknowledgements

None of this work would have been possible without the support of many people. First and foremost, I would like to express my deepest gratitude to my supervisor, Prof. Stefano Sanvito, for his guidance, teachings and patience. His great curiosity and passion for science have been an inspiration and it has been a privilege to work under his supervision. Secondly, I am grateful to all my colleagues, past and present, in the Computational Spintronics Group for their support. Special thanks are due to Dr. Matthew Ellis, who generously shared his computer code and experience on atomistic spin dynamics and without whom large part of this thesis would not have been possible. He has been been incredibly patient and helpful for the entire four years, and he has always been there to lend his advice, both at a professional and a personal level, despite his numerous other commitments. A second round of special thanks goes to Emanuele Bosoni, Dr. Alessandro Lunghi and James Nelson (collectively known as the B. F.) for their friendship. Emanuele was a great companion since my very first week in Dublin and a wonderful friend along the way, while I will always be indebted to Alessandro for generously sharing his pearls of wisdom and tips on both private and professional life. I am also very grateful to Dr. Mario Žic, Dr. Subhayan Roychouduri, Dr. Rajarshi Tiwari, Dr. Aswhinee Kumar, Anais Colibaba, Urvesh Patil and Dr. Stella Skiadopoulou for their companionship. Finally, I would like to thank Stefania Negro for her generous support in many administrative and financial matters.

I would like to thank the Science Foundation of Ireland (Grants No. 14/IA/2624 and 16/US-C2C/3287) for paying my fees and maintenance and for providing me

support for attending conferences. I also acknowledge TCHPC (Research IT, Trinity College Dublin) and the Irish Center for High-End Computing (ICHEC) for the provision of computational facilities and assistance.

I also would like to thank all the other friends that I made in Dublin, who made my stay here most enjoyable. Janne Shoening, for her company around the many trips around Ireland. Èlia Cantoni i Gòmez, for being an excellent jogging partner and an irreplaceable friend. Dr. Silvia Fogli, for her support in the last few months and for sharing her father's boar meat. Finally, I am greatful to my flatmates, Maria Pilar Guerola Fuentes, Christina Clarke and Rachel Cregan for their support, with a special mention to Maria for her great friendship during these years.

Last but not least, I would like to thank all my family who always supported me during my studies. Special mention goes to my parents and to my uncles Marco and Stefano, who are always there for me no matter what.

Contents

List of Figures

Chapter 1

Magnetic random access memories

"The story so far: in the beginning the Universe was created.
This has made many people very angry and has been widely
regarded as a bad move."

- Douglas Adams

The continuous miniaturisation and performance enhancement of electronic components have been essential to improve the quality of our everyday life. The advent of portable electronic devices led to a growing inclusion of technology in daily tasks and consequently to an increasing demand of efficient tools for data processing and storage. Modern computers largely rely on dynamic random-access memory (DRAM) technologies for computing power. These devices store data in the charge state of a capacitor made of two metallic plates separated by a dielectric (mostly Si). Although information can be efficiently written by simply modifying the amount of charge accumulated in the capacitor, the reading procedure is more energetically expensive, since it requires deleting and rewriting the charge state. In addition, charge leakage implies the need of a frequent charge refresh to prevent the loss of information, and such effect grows as the capacitor size is reduced. The destructive read protocol, the issue of charge refresh and the need of a constant power supply to maintain the stored data imply elevated power consumption and poor scalability. Therefore, these drawbacks are likely to eventually make DRAMs unable to offer the performances that

will be required for future technological developments. Improvements of DRAMs are still considered to be possible thanks to the introduction of three-dimensional structures and materials with high relative dielectric constant [1], but their intrinsic limitations encourage the search of alternative technologies.

The idea of replacing DRAMs with memories that do not require constant power to retain data, i.e. that are *non-volatile*, is particularly attractive due to the low energy operational costs. Among the memories currently available to the public, flash memory is the only one which is non-volatile and at the same time has adequate read/write speed to replace DRAMs. Flash memories store information in the charge state of a transistor that is electrically isolated to preserve the non-volatility. Nevertheless, the device integrity deteriorates after a relatively low number of program-erase cycles. Together with their high fabrication costs, the reduced durability of flash memories makes them unsuitable to be used as main processing units. In order to bypass the low endurance of flash memories and the scalability and volatility issues of DRAMs, various memory prototypes that do not use charge states to store information were proposed. Ferroelectric memories (FeRAMs) [2] have a structure, which is similar to DRAMs, but they replace the dielectric layer with a ferroelectric slab, i.e. made of a material with a spontaneous electric polarization. The charged/discharged capacitor configurations that embody the "0" and "1" states in DRAMs are here represented by the two opposite orientations of the electric polarisation in the active layer, which can be controlled by external electric fields. As an alternative, an analogous role can be played by the different phases of a material, provided that the phase transformation can be efficiently and accurately performed. State-of-the-art phase changing memories (PCMs) [3] adopt a slab of GeSbTe as active layer. In fact, it is possible to liquefy GeSbTe through heating to then obtain either an amorphous or crystalline phase by controlling the rapidity of its cooling. Both the latter two prototypes are considered to be promising candidates for future non-volatile memories. On the one hand, FeMRAMs have exceptional write speed, high endurance and ultra-low power consumption. However, similarly to DRAMs, they suffer from low integration density. On the other hand,

PCMs offer good scalability and at the same time fast data access and write/erase speeds, but their operational temperature range is rather limited. Neither of these devices is thus suitable for applications such as automotive vehicles that require energy efficient, high density and durable memories, that must also be able to maintain satisfactory performances at high temperatures.

Magnetic random-access memories (MRAMs) are currently believed to be the technology that is more likely to be able to satisfy such requirements. Such devices store data in the direction of the magnetisation vector of a magnetic layer: if the "0" state is represented by a specific orientation of such vector, the opposite direction will represent the "1" state. Their working principle is routed in the use of spin polarised electric currents to perform both the reading and the writing procedures. This allows for extremely low energy consumption, high durability and fast operation. Furthermore, the appropriate choice of the magnetic material yields natural non-volatility, high scalability and elevated resistance to radiation and high temperatures. These reasons make MRAMs also potential candidates for a "universal memory", i.e. capable of replacing the functions currently covered by the simultaneous employment of DRAMs, flash and static RAMs (SRAMs).

This chapter begins with a review of the main discoveries that made the realisation of magnetic memories possible, together with the physical phenomena that underpin their operating principles. An analysis of the possible material choices for efficient MRAMs follows, including a description of the relative issues and challenges. In conclusion, an overview of the contents of the rest of this thesis will be presented.

1.1 The development of STT-MRAMs

1.1.1 Giant magnetoresistance and the advent of spintronics

The working principles of electronic devices rely on the manipulation of electrons through their intrinsic charge. It is then only natural to wonder whether it is possible to exploit at the same time the electron intrinsic spin angular momentum. In

the field of spin electronics, or *spintronics*, magnetic materials are embedded into electronic components to generate spin polarised electrical currents and increase the capability and the functionality of electronic devices. The idea that the spin state of electrons influences their mobility can be traced back to Mott's early work on the spin dependence of the conduction properties of ferromagnets [4]. The general spin state of an electron is defined as a 3-component vector with modulus $\hbar/2$, hence can be represented as the linear combination of two fundamental states. It is customary to identify these two states with the directions parallel and anti-parallel to the spin quantisation axis, thus call them as the spin-$\uparrow$ and spin-$\downarrow$ state. Since ferromagnets are characterised by an asymmetry in the population of the two spin states, the latter are also known as majority- and minority-spin states. In particular, Mott proposed that electrons in spin-$\uparrow$ and spin-$\downarrow$ states constitute two independent conducting channels. Since the electrical resistivity depends on the density of states at the Fermi level, the spin asymmetry in the electronic population of ferromagnets generates a difference in the resistivity of the two spin channels. Such prediction was later observed experimentally through conduction measurements in doped Ni [5]. These findings already suggest that the magnetic state of a material plays a role in its electrical resistance, although such effect is not pronounced for the scale and systems considered in Refs. [4, 5].

The advent of deposition techniques, such as molecular beam epitaxy (MBE), in the 1980s made it possible the fabrication of thin films down to the nm scale. This proved to be vital for the discovery of new magnetoresistance phenomena that appear where the layer thicknesses are comparable to the mean free path of electrons. In the early years of research on magnetic thin films, multilayers composed of alternating Fe and Cr layers emerged as the ideal system where the relative orientation of magnetisations of adjacent layers could be controlled. Although the presence of antiferromagnetic layer-exchange couplings favours the anti-parallel alignment of the magnetisations [6], the parallel alignment can be realised by applying external magnetic fields. The electrical resistance offered by the system when adjacent magnetisations are parallel was found significantly lower than that of the anti-parallel

alignment. The difference in the two resistances is essentially due to the change in available states throughout the stack for each spin channel, as represented in Fig. 1.1. If the magnetisations are all parallel, the majority spin state will have the same direction, say ↑, for all magnetic layers. As a consequence, the constantly higher number of states close to the Fermi energy available by spin-↑ electrons implies that the resistivity for the spin-↑ channel will be significantly lower than the one for the spin-↓ channel. On the contrary, in the anti-parallel configuration the majority spin state alternates direction between adjacent magnetic layers, and so does the number of available states for each spin channel. The conductivity of spin-↑ and spin-↓ electrons is thus equally suppressed in the antiparallel state. This effect is commonly known as giant magnetoresistance (GMR) and was simultaneously discovered by Albert Fert and Peter Grünberg [7, 8], reason for which they were jointly awarded the Nobel price for physics in 2007. Early studies on GMR were

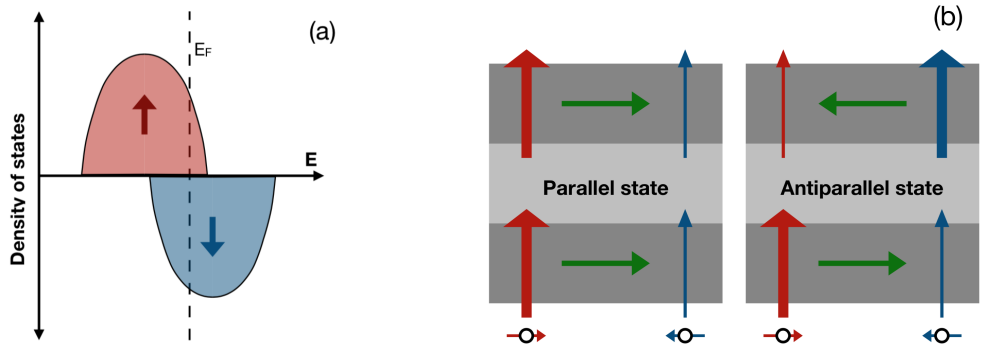

Figure 1.1: (a) Graphic representation of the density of states of a ferromagnet around the Fermi energy. (b) Schematic illustration of the GMR effect. The green arrows represent the orientation of the magnetisation vectors, while red (blue) arrows represent the intensity of the transmission for the majority (minority) spin channel. For parallel magnetisations (left) the conductivity is enhanced for one spin channel and suppressed for the other, so that the short-circuit through the former channel implies a reduced resistance. On the contrary, in the anti-parallel state (right) the two spin channels have the same conductivity, hence the resistance is higher compared to the parallel magnetisation state.

all performed with current flowing along the layers direction, i.e. with the geometry that is nowadays known as "current in plane" (CIP). However, geometries where the current is driven parallel to the stacking direction, i.e. in the "current perpendicular to plane" (CPP) geometry, were found more convenient for applications [9, 10]. First of all, the difference between the resistances in the parallel (P), R_P, and antiparallel (AP) configurations, usually quantified through the *GMR ratio*,

$$GMR = \frac{R_{\mathrm{AP}} - R_{\mathrm{P}}}{R_{\mathrm{P}}}, \tag{1.1}$$

is more pronounced in the CPP geometry with respect to the CIP one [9]. According to theoretical investigations [11], this is due to the reduced spin-asymmetry of interfacial scattering in the CIP geometry.

GMR devices represent one of the first prototypes of magnetic memories. However, magnetisation switching in metallic spin valves is not efficient enough to offer a competitive alternative. Nevertheless, the GMR effect is widely used to this day to construct efficient magnetic field sensors.

1.1.2 Magnetic tunnelling junctions

The separation of two magnetic layers with an insulating barrier, i. e. employing a *magnetic tunnelling junction (MTJ)*, offers an alternative to metallic junctions since the spacer strongly suppresses interlayer couplings. MTJs were found to have magnetoresistive properties as early as 1975 by Julliére [12]. In fact, thin enough insulating barriers allow the flow of electric currents between the two ferromagnetic electrodes thanks to the establishment of a tunnelling regime. These experiments proved that magnetic tunnelling junctions exhibit an effect similar to the giant magnetoresistance, nowadays known as *tunnelling magnetoresistance (TMR)*. The TMR effect was explained by Julliére neglecting spin-flip phenomena and using a two current model analogous to the one adopted above for explaining the GMR [Fig. 1.1 (b)]. The argument is based on estimating the conductance in terms of the transmission amplitudes for each spin channel. If t_1 and t_2 are the tunnelling probabilities for electrons in the majority spin state in ferromagnet 1 and 2, respectively, minority

spin electrons will have tunnelling probabilities $1-t_1$ and $1-t_2$, respectively. Hence, the total conductance, $G_{\mathrm{P}}, G_{\mathrm{AP}}$, in the two possible magnetic configuration are given by

$$G_{\mathrm{P}} = t_1 t_2 + (1-t_1)(1-t_2) = \frac{1+\mathcal{P}_1\mathcal{P}_2}{2}, \tag{1.2}$$

$$G_{\mathrm{AP}} = t_1(1-t_2) + (1-t_1)t_2 = \frac{1-\mathcal{P}_1\mathcal{P}_2}{2}, \tag{1.3}$$

where $\mathcal{P}_i = 2t_i - 1$ denotes the spin polarisation of the i-th ferromagnet, with $i = 1, 2$. Since by definition $0 \leq \mathcal{P}_i \leq 1$, we find that the conductance is higher in the P configuration than in the AP one, as in the case of GMR. Moreover, Eqs. (1.2) and (1.3) can be easily combined to yield an expression for the tunnelling magnetoresistance ratio in terms of the spin polarisations, i.e.

$$TMR \equiv \frac{G_{\mathrm{P}} - G_{\mathrm{AP}}}{G_{\mathrm{AP}}} = \frac{2\mathcal{P}_1\mathcal{P}_2}{1-\mathcal{P}_1\mathcal{P}_2}. \tag{1.4}$$

This equation is known as the Julliére formula for the TMR ratio and its validity is limited to cases, where spin-flip processes are negligible. Since spin excitations imply a breakdown of the independence of the two spin channels, conditions that favour their presence (high voltages, elevated temperatures or concentration of defects) will unavoidably cause a deterioration of the TMR. Nevertheless, Eq. (1.4) shows that the TMR is maximised for $\mathcal{P}_1 = \mathcal{P}_2 = 1$, thus implying that a high degree of spin polarisation of the current is essential to obtain high TMRs.

In his experiments Julliére employed Fe/GeO/Co junctions with barrier thicknesses ranging between 10 and 15 nm, measuring TMR ratios of about 14% at low temperatures. The modest magnitude of such effect was due to the relatively low spin polarisation of the magnetic electrodes, the large spacer thickness and the amorphous barrier. Hence, the discovery of the TMR effect did not attract much attention at the time. The interest in MTJs was renewed with the development of GMR, and in the mid 1990s room temperature (RT) TMRs of 11.8% and 18% were observed in FeCo/Al_2O_3/Co and Fe/Al_2O_3/Fe MTJs by Moodera [14] and Miyazaki [15], respectively. The tunnelling barriers in these cases had thicknesses below 5 nm and were amorphous. However, later studies showed that a crystalline insulating spacer can

strongly enhance the TMR ratio, if it is well matched with the electronic structure of the ferromagnets. In fact, tunnelling properties across crystalline insulators were shown to be remarkably influenced by the spatial symmetry of the Bloch states, meaning that the barrier favours the tunnelling of electrons in states with certain symmetries (Fig. 1.2). As a consequence, if the occupation of the electronic states which tunnelling is more favourable is higher for one spin state than for the other, the transmission probabilities for the two spin channels will be remarkably different. In other terms, the insulator can effectively select electrons depending on their spin state, i.e. acting as a spin filter.

The first prediction of the so-called *spin filtering* effect is due to Butler *et al.* [17] and Mathlon *et al.* [18] who calculated the electronic, magnetic and transport properties of Fe(100)/MgO(100)/Fe(100) tunnelling junctions. The authors show that in such structures the conductance is dominated by electrons with wave-vectors orthogonal to the current direction, and that Bloch states with a particular symmetry have particularly low decay rate across MgO. The latter feature can be evinced

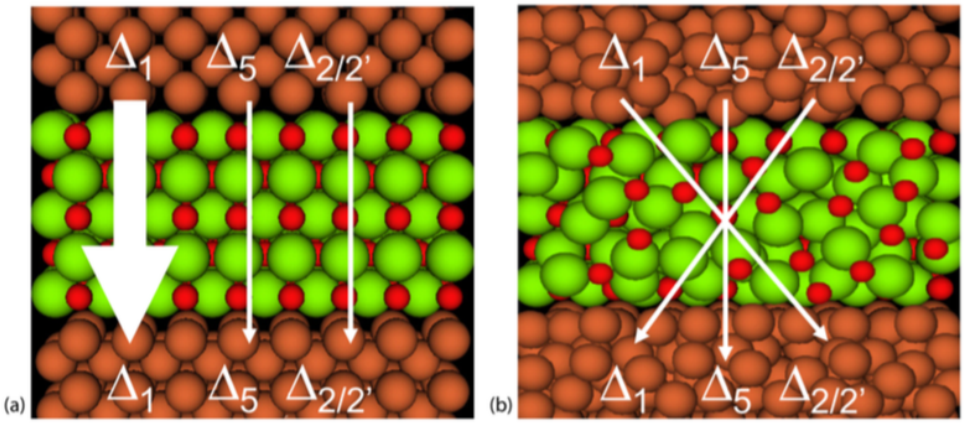

Figure 1.2: Schematic of the difference tunnelling properties in crystalline MgO and amorphous Al_2O_3 barriers. In Fe/MgO/Fe tunnelling is enhanced for electrons of a Δ_1 symmetry state, while Bloch state symmetries do not play a role in the determination of tunnelling probabilities across amorphous barriers. Image credit: [13] .

by comparing the (real) band structure of Fe with the complex band structure of MgO [panels (a) to (d) of Fig. 1.3]. Although in infinite solid state systems the Schrödinger equation admits solutions only for real momentum vectors, $\boldsymbol{k}$, solutions corresponding to purely imaginary vectors, $\boldsymbol{\kappa}$, appear in the presence of interfaces. Their physical meaning relates to vanishing states propagating from the interface within the material. In particular, states with elevated imaginary wavenumber, identified with $\kappa^2 = |\boldsymbol{\kappa}|^2$, will have a lower probability of tunnelling across the barrier, hence κ^2 quantifies the decay factor in the insulator. Panel (a) of Fig. 1.3 highlights the difference in symmetry states of different segments of the first Brillouin Zone in the calculated real band structure of MgO, while panel (b) displays the associated complex bands. For simplicity, we assume here that the transport direction is aligned with the z axis. Given that electrons propagating orthogonally to the stacking direction constitute most of the current, only the corresponding direction in k-space is displayed. By convention, Δ_1 states transform like linear combinations of functions with 1, z and $2z^2 - x^2 - y^2$ symmetry; Δ_5 denotes symmetry properties of linear combinations of functions with zx and zy symmetry, $\Delta_{2'}$ of functions with

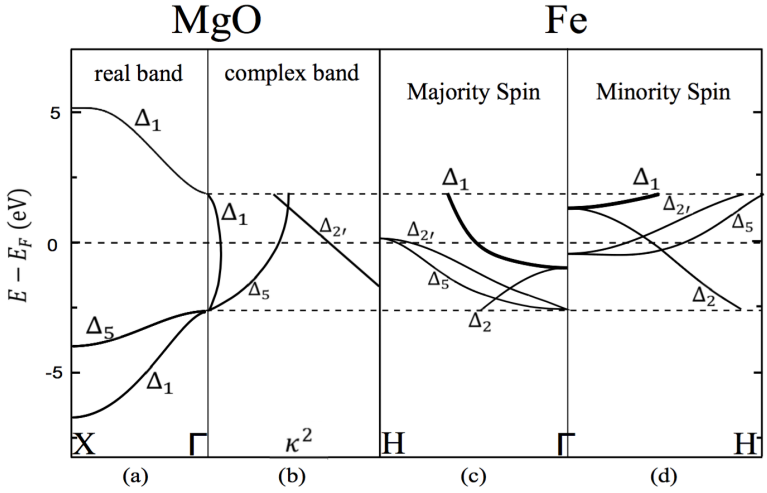

Figure 1.3: Comparison between the real (a) and complex (b) band structure of MgO and the majority (c) and minority (d) spin real band structure of bcc Fe. Image credit: [16].

$y^2 - z^2$ symmetry. From [Fig. 1.3 (b)] it is then evident that the decay rate at the Fermi level of Δ_1 states is significantly smaller than that of states with Δ_5 or $\Delta_{2'}$ symmetries. Importantly, the majority spin band structure of Fe [Fig. 1.3 (c)] has a Δ_1 band crossing the Fermi level, while the same does not hold for the minority spin bands [Fig. 1.3 (d)]. In conclusion, the symmetry match between the complex bands in MgO and the real bands in Fe allows for a strongly spin polarised current across the barrier, hence a large TMR ratio, in Fe/MgO/Fe junctions.

The findings presented by Butler *et al.* were later confirmed with the observation of room temperatures TMRs as large as 180% for single-crystal Fe/MgO/Fe [19] and 220% for polycrystalline MTJs [20]. It must be noted, however, that all measured TMRs in Fe/MgO/Fe MTJs at both low and high temperature are systematically lower than the theoretical estimations of several 1000%. The cause of this disagreement is related to the presence of a wide range of deviations from epitaxy at the Fe/MgO interfaces [21, 22]. For example, the formation of an interfacial FeO layer was shown to strongly deteriorate the spin filtering properties [23]. In conclusion, the optimisation the TMR of Fe/MgO/Fe MTJs ultimately translates into an engineering of Fe/MgO interfaces.

The realisation of high TMRs at room temperatures made it possible to use MTJs to store information, since the TMR can be exploited to efficiently read the magnetic state (P or AP). Nevertheless, writing procedures relying on the application of magnetic fields imply a high power consumption because of the large fields required to switch the magnetisations between the two states. Furthermore, the difficulties in realising strictly localised magnetic fields considerably reduce the affordable integration density. Hence, an alternative writing protocol is needed for efficient memories.

1.1.3 Spin transfer torque random access memories

The possibility of inducing magnetisation dynamics through the use of spin polarised currents was first theorised by Slonczewski [24] and Berger [25] independently. The two authors proposed the idea that a spin polarised current injected in a magnetic film can induce spin excitations, and hence spin dynamics, by transferring angular

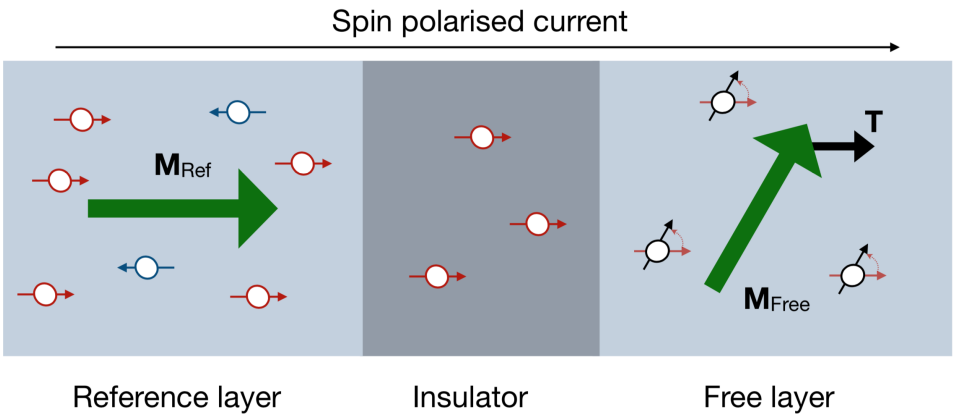

Figure 1.4: Schematic representation of the mechanism that gives rise to a spin-transfer torque in an MTJ. If an electric current is flowing from left to right, it enters the free (right hand side) layer with the spin polarisation of the reference (left hand side) magnetic layer. The exchange interaction causes electrons emerging from the barrier to adapt their spins to the static local magnetisation, $\boldsymbol{M}_{Free}$, thus transferring angular momentum to the free layer. As a result of spin conservation, the local magnetisation vector is driven to align with the spin polarisation of the current, i.e. it experiences an effective spin torque.

momentum to the local magnetisation. In particular, the effect is such that the static magnetisation vector is driven towards the alignment with the spin polarisation of the current. In other terms, a spin polarised current effectively exerts a *spin transfer torque (STT)* on the static magnetisation vector and can be exploited to control its orientation.

In order to elucidate this mechanism we consider a magnetic tunnelling junction where the magnetisations of the two magnetic layers are misaligned, as shown in Fig. 1.4. In these conditions a current flowing from the left-hand side to the right-hand side enters the barrier with a spin polarisation, which is aligned with the magnetisation of the former. For the moment, the spacer is assumed to yield a perfectly spin-polarised current. However, a similar argument holds for cases such as metallic spacers where the polarisation of the injected current is not 100%. The current entering the right (or free) layer is then entirely populated by electrons with

spins aligned with the magnetisation of the left layer, $\boldsymbol{M}_{\mathrm{Ref}}$. Given the magnetisation misalignment, the spin quantisation axis of the transport electrons is not the same of the one of the free layer. As a consequence, the exchange interaction between the spins of the transport electrons and the static magnetisation, $\boldsymbol{M}_{\mathrm{Free}}$, causes the former to align with the latter. In turn, the magnetisation vector of the free layer is driven to align with the direction of the current, i. e. $\boldsymbol{M}_{\mathrm{Ref}}$, by spin conservation, and such effect corresponds to the spin transfer torque. Since the angular momentum carried by the current is provided by the left-hand side layer, $\boldsymbol{M}_{\mathrm{Ref}}$ also feels a torque because of an analogous mechanism, and by spin conservation it has the same intensity but opposite sign than the torque acting $\boldsymbol{M}_{\mathrm{Free}}$. Nevertheless, the multilayered structure can be engineered so that reference layer can act as reservoir for angular momentum. Hence, its magnetisation vector can be kept constant and exploited as reference, while the free layer can be driven to align or antialign with the former by applying the current in a verse or the other.

The exploitation of the TMR and STT effects thus allow to effectively read and write the magnetic state of an MTJ by the means of an electric current, and embodies the operational principle of *spin-transfer torques random-access memories (STT-MRAMs)*. Such prototypes represent a significant improvement with respect to field-switched MRAMs for their potentially lower energy consumption and enhanced scalability, since STT-MRAM cells can reach sub-20 nm size compared to the $60\,\mathrm{nm}\times150\,\mathrm{nm}$ limit for field-switched MRAMs. The realisation of high performance memories depends, however, on a thorough engineering of the stack containing the magnetic tunnelling junction. The goal of the structure design is to obtain devices with high TMR at room temperature, where magnetisation reversal can be realised with the lowest current intensity possible and remains stable to thermal fluctuations. The accomplishment of such objective requires, however, an understanding of which properties influence the magnetisation switching.

The dynamics of the global magnetisation vector, $\boldsymbol{M}$, in the presence of spin torques is commonly described by the Landau-Lifshitz-Gilbert-Slonczewski equation

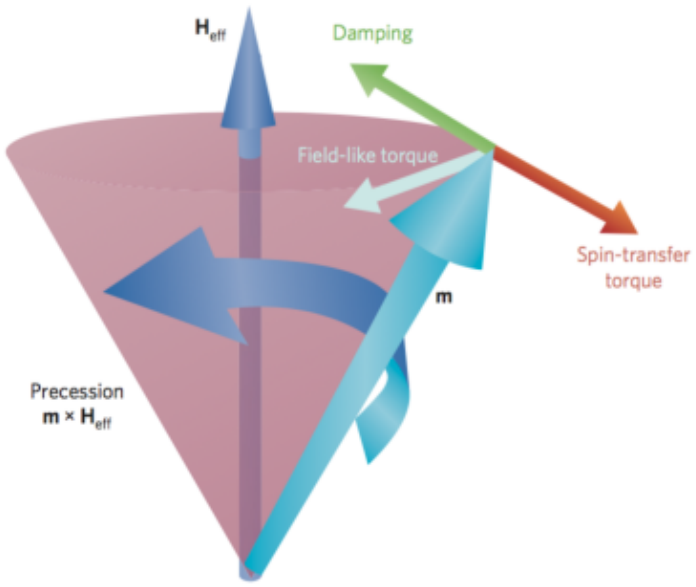

Figure 1.5: Schematic representation of current-driven magnetisation dynamics. The field-like torque and the interaction with the effective field, $\boldsymbol{H}_{\text{eff}}$, induce a precession around $\boldsymbol{H}_{\text{eff}}$, while the spin-transfer torque and damping effects control the alignment between the magnetisation vector, $\boldsymbol{m}$, and $\boldsymbol{H}_{\text{eff}}$. Image credit: [26].

(LLGS),

$$\frac{\partial \boldsymbol{M}}{\partial t} = -\gamma \boldsymbol{M} \times \boldsymbol{H}_{\text{eff}} - \alpha \boldsymbol{M} \times \frac{\partial \boldsymbol{M}}{\partial t} + \boldsymbol{T}. \tag{1.5}$$

Here we will limit the discussion of this equation to a qualitative description of the defining features of spin dynamics in STT-MRAMs, while a more detailed analysis will be presented in § 4. The first term of Eq. (1.5) describes the precession motion of the magnetisation, $\boldsymbol{M}$, around the effective field acting on $\boldsymbol{M}$,

$$\boldsymbol{H}_{\text{eff}} = -\frac{1}{|\boldsymbol{M}|}\frac{\partial E}{\partial \boldsymbol{M}} = -\frac{1}{|\boldsymbol{M}|}\frac{\partial}{\partial \boldsymbol{M}}\left[E_{\text{exch}} + E_{\text{app}} + E_{\text{ani}}\right] \tag{1.6}$$

with γ denoting the gyromagnetic ratio for the electron. The last term of Eq. (1.6) describes the contributions of the total magnetic energy that are relevant for the dynamics here considered. The exchange energy, E_{exch}, arises from the local spin-spin quantum-mechanical exchange interactions; E_{app} quantifies the interaction with an external magnetic field, and the anisotropy energy, E_{ani}, favours the alignment of the magnetisation along a certain direction. The latter is normally represented by

the so-called *easy axis* and is determined by various factors, ranging from the geometrical shape of single crystal magnets to the presence of interfaces and spin-orbit mediated interactions between atomic spins and the crystal structure (magnetocrystalline anisotropy). The second term in Eq. (1.5) is a "friction" term that drives the tendency of the magnetisation to align along its equilibrium orientation, i. e. the easy axis. The strength of this torque is quantified by the phenomenological damping parameter, α, known as Gilbert damping. Such quantity is fundamental to determine the magnetisation switching times since it embodies the friction-like effect to be overcome by the spin torque in order to achieve the magnetisation reversal. Let us note that the current-induced torques are introduced as a vectorial quantity, $\boldsymbol{T}$, which is traditionally divided into two components, one contributing to the reversal motion, one to the precession [Fig. 1.5]. The former corresponds to the spin-transfer torque described above, and is also known as *in-plane* torque since it does not drive the magnetisation vector out of the plane defined by the magnetisations of the two magnetic layers. In contrast, the *out-of-plane* or *field-like* torque is parallel to the precession term of Eq. (1.5) and it is normally attributed to phenomena such as the precession of electronic spins or the presence of transport electrons with minority spin state. Although the field-like torque does not influence directly the magnetisation reversal, it was argued that its interplay with the in-plane component plays a role in the stability of the switching process [27, 26]. Nevertheless, the out-of-plane component can be exploited to force the magnetisation into a constant precession with frequencies in the microwave range, hence to realise spin torque nano-oscillators (STNOs) [28].

1.2 Designing magnetic tunnel junctions for high-performance memories

In the last section we showed that the use of MTJs in memory applications offers natural non-volatility and potentially high integration density. Moreover, spin-

transfer torque writing can potentially allow for extremely low energy consumption and switching times of the order of the ns. The realisation of such potential into efficient STT-MRAMs requires, however, the minimisation of bit sizes and of the current intensities, while maintaining high performances at elevated temperatures. This translates in the search for multilayered structures with reduced cross sections, with high TMRs at room temperature ($> 150\%$) for efficient reading and that can be written with low current intensity. The exceptional spin filtering performed by MgO barriers matched with *bcc* Fe layers has made Fe/MgO/Fe the most chosen starting material composition for the fabrication of high TMR MTJs. Nevertheless, the high Gilbert damping of Fe makes junctions with perpendicular geometry and efficient switching troublesome to realise. In addition, the spin polarisation induced by a pure Fe layer suffers of the presence of parasitic tunnelling of Δ_2 and Δ_5 symmetry electrons, pushing the search for material alternatives. Contrarily to Fe, in *bcc* Co only Δ_1 states populate the majority band at the Fermi level hence the higher spin polarisation grants Co/MgO/Co junctions a higher predicted TMR than Fe-based MTJs [29]. Furthermore, the higher magnetic anisotropy of Co implies enhanced stability of the magnetic properties to thermal fluctuations. Nevertheless, when Co is deposited on MgO it nucleates in a non uniform island-like pattern rather than growing in a regular *bcc* lattice. Such deviation from an ideal crystalline structure strongly reduces the achievable spin polarisation, since it favours the formation of interfacial resonant states that in turn enhance the tunnelling of spin-down electrons. The use of Co_xFe_{1-x} alloys offers improved spin polarisation and crystalline order compared to elemental crystals. Although the optimal Co concentration is debated, rich Co compositions are normally preferred for higher stability to temperature fluctuations. The resulting TMR then depends on the amount of defects and disorder at the magnet/insulator interfaces, since any additional source of scattering alters the predicted electronic states and hence yields deviations from ideal spin filtering. The key objective to be achieved in order to realise high TMR MTJs is thus to engineer multilayered structures that can be grown while keeping the ferromagnet/insulator interfaces as clean as possible. State-of-the-art Fe/MgO based-MTJs are deposited

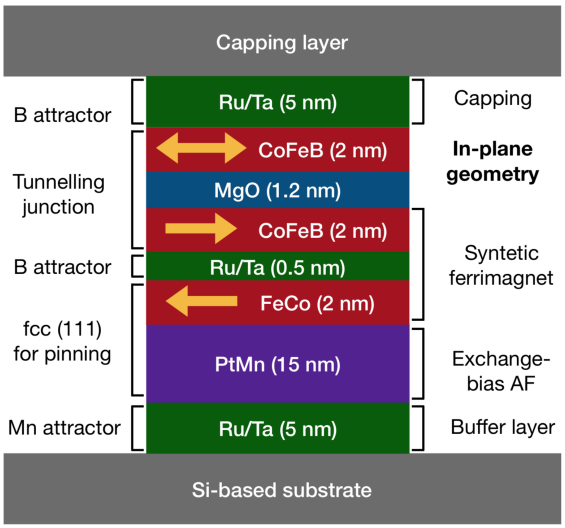

Figure 1.6: Typical multilayered stack including a magnetic tunnel junction with an in-plane magnetisation geometry for STT-MRAM applications.

in an amorphous phase, and crystallisation and epitaxy are then obtained through annealing. This is possible thanks to the high stability of the MgO rock salt-like structure, which dictates the crystal phase of the stack during the high temperature annealing [30]. Moreover, the addition of B to Co_xFe_{1-x} was found to help the crystallisation of the electrodes on MgO and TMRs beyond 200% at room temperature were observed in $(CoFe)_{80}B_{20}/MgO/(CoFe)_{80}B_{20}$ MTJs [31].

Nevertheless, the capability of fabricating high TMR junctions alone is not sufficient to realise efficient STT-MRAMs. The key challenge is in fact to achieve low write currents and good data retention at the same time, meaning that the free layer magnetisation is required to be stable to thermal noise but reversible with low current intensities. Moreover, the reliability of the reading and writing procedures heavily depends on how effectively the magnetisation of the reference layer can be constrained. In early prototypes of STT-MRAMs magnetisation pinning was realised exploiting the exchange bias coupling exhorted by an antiferromagnetic layer to form a synthetic ferrimagnet (SyF). Fig. 1.6 shows the typical multilayered structure adopted with such a purpose. Starting from the bottom of the stack, a thick ($\sim$ 15 nm) layer of an antiferromagnetic (AF) material, such as PtMn or IrMn, is grown

in a fcc structure oriented along the (111) on top of a seed layer usually made of Ru or Ta. The 3-fold in-plane symmetry of fcc (111) lattices is commonly adopted because of its consolidated reliability for pinning structures and growth techniques for Si-based substrates. A relatively thin layer of the *fcc* CoFe is deposited on the AF, so that the interlayer exchange coupling strongly bounds the magnetisation of the former in a given direction. In particular, the whole structure aims to force the magnetisations to lie in the plane defined by the films, i.e. adopting an *in-plane* geometry for the magnetisations. In fact, the thickness of the ferromagnetic layers is kept to a minimum and the pillar is edged in an elliptical pattern so that shape contributions to the magnetic anisotropy aid the pinning of the magnetisations within the plane along a single axis. As explained above, MgO offers efficient spin filtering to currents where majority-spin electrons have the Δ_1 state symmetry. The use of a ferromagnet in a crystal phase with symmetry properties analogous to MgO, i. e. with a 4-fold in-plane symmetry, is thus essential to achieve high spin polarisations. A metallic layer of Ru or Ta is normally interposed between the fcc FeCo layer and the FeCoB/MgO/FeCoB junction. In this way the post-annealing crystalline structure of the MTJ is dictated by the MgO rather than by the substrate. Furthermore, the thickness of the metallic layer is usually kept below 1 nm so that the inter-layer exchange between the fcc FeCo and the bcc FeCoB layers yields an antiferromagnetic coupling. The choice of Ru or Ta for the metallic layers is also made because they attract B and Mn atoms during annealing [30]. This helps to prevent such atoms to diffuse towards the interfaces with the ferromagnets and hence deteriorate the device performances.

Although the in-plane magnetisation geometry offers a good thermal stability for reading, it is not advantageous for energy efficient switching. In fact, the intrinsic anisotropy field induced by the shape of the free layer adds to the anisotropy contributions external to such layer, hence enhancing the energy barrier to be overcome to achieve magnetisation reversal. This can be seen by examining an approximated

formula for the critical current intensity,

$$I_c^{\parallel} = \frac{2\alpha e M_S V}{\hbar \mathcal{P}} \mu_0 \left(H_{\text{ani}}^{\parallel} + \frac{M_S}{2} \right), \tag{1.7}$$

which can be evinced from the LLGS equation (see Ref. [32] for more details). Here e indicates the electronic charge, while μ_0 is the vacuum permeability. This expression clearly shows that the critical current depends linearly on the Gilbert damping, α, on the saturation magnetisation of the free layer, M_S, and on its volume, V, while it is inversely proportional to the spin polarisation of the current, $\mathcal{P}$. The terms in brackets embody the effective magnetic field, where $H_{\text{ani}}^{\parallel}$ is the anisotropy contribution, while the second represents the demagnetising field. Importantly, the two contributions have the same sign, meaning that the out-of-plane precession that the magnetisation undergoes to while switching is obstructed by the magnetising field, hence yielding a penalty to I_c. This, however, does not occur when the easy axis of the free layer is aligned along the stacking direction, namely it is in a *perpendicular-to-plane* geometry. In this condition the critical current becomes

$$I_c^{\perp} = \frac{2\alpha e M_S V}{\hbar \mathcal{P}} \mu_0 \left(H_{\text{ani}}^{\perp} - M_S \right), \tag{1.8}$$

where the anisotropy field is here denoted as $H_{\text{ani}}^{\perp}$ to highlight its different intensity as compared to the one characteristic of in-plane geometries, $H_{\text{ani}}^{\parallel}$. Importantly, the demagnetising field contribution has opposite sign with respect to Eq. (1.7), meaning that the demagnetising field in this case favours the out-of-plane precession and hence lowers the critical current.

These considerations brought to the realisation of MRAMs based on junctions with a perpendicular-to-plane magnetisation geometry (pMTJs) [33]. In contrast to in-plane geometry devices, pinning is not obtained through inter-layer exchange bias but the perpendicular magnetic anisotropy (PMA) arising at the CoFeB/MgO interfaces is exploited instead. It was in fact shown that the overlap between O-p_z and hybridised transition metal d_{z^2} orbitals at the magnetic metal/oxide interfaces enhances the spin-orbit coupling induced splitting around the Fermi energy, thus producing a strong perpendicular anisotropy [34]. In these conditions a strong in-plane

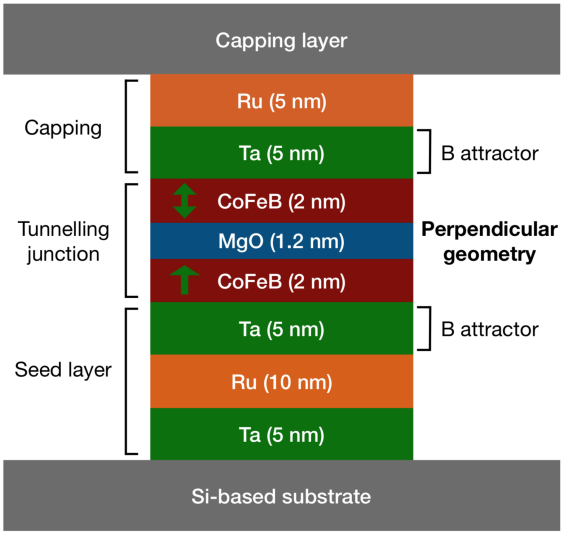

Figure 1.7: Typical multilayered stack including a magnetic tunnel junction with a perpendicular-to-plane magnetisation geometry for STT-MRAM applications.

anisotropy is no longer needed, hence a circular shape of the nano-pillar containing the junction becomes more convenient than the elliptical one adopted for the in-plane geometry. Moreover, the pinning layers can be eliminated from the multilayered structure that is thus significantly simplified [Fig. 1.7]. The magnetic tunnel junction is here deposited directly to a Ta/Ru/Ta buffer layer that promotes the transition to the *bcc* structure of CoFeB and attracts B during annealing. The thicknesses of the magnetic layers are then further reduced to enhance the out-of-plane anisotropy. This also diminishes the critical switching current given its linear dependence with the volume of the free layer, as shown in Eq. (1.8). Such equation also demonstrate that a low Gilbert damping parameter helps efficient switching. The latter is known to grow larger with the intensity of the spin-orbit interaction, which increases with the atomic number. Hence relatively heavy atoms such as Pt or Pd are normally avoided in the stack.

1.2.1 Current challenges and perspectives

Perpendicular STT-MRAMs based on CoFeB/MgO MTJs constitute the current state-of-the-art of magnetic memories. Their diameter can be shrank down to below 20 nm and they can be switched with currents with densities as low as 19 $MAcm^{-1}$ [35]. Smaller cross sections are possible but become of troublesome realisation because of the edge damage caused by etching. Nevertheless, these prototypes do not offer the level of reliability and thermal scalability required by automotive-vehicle or internet of things applications. The main remaining challenges are to reduce the temperature dependence of the magnetic anisotropy and to lower the critical currents to improve the device endurance. Perpendicular anisotropy can be enhanced by adopting materials with high magnetocrystalline anisotropy. However, the latter increases with the strength of the spin-orbit coupling and hence it implies an increase of the Gilbert damping. Further improvements can be made by adopting double barrier MTJs, which allows for enhanced thermal stability. However, the pillars are more difficult to etch and the reduced epitaxy deteriorates the TMR [36].

The only alternative to a further optimisation of the current multi-layered structure is to look for a different magnet/insulator combination with improved capabilities with respect to the established CoFeB/MgO. This translates into the search for a tunnelling barrier where the symmetries of the electronic states are similar to MgO and for a magnetic material with compatible crystal structure and state symmetries dominating the majority spin state around the Fermi level. However, the chemical and structural simplicity of magnesium oxide makes its replacement troublesome. Most of the alternatives proposed in literature are based on modifications of MgO (e. g. see Ref. [37]), but for the moment none of such candidates comes close to the efficiency of the original barrier. The simplest option is then to search for a different ferromagnet with improved spin polarisation. Half-metallic compounds, namely ferromagnets that are conducting in one spin channel and insulating in the other, constitute a particularly attractive alternative because of their intrinsically perfect spin polarisation. Nevertheless, a suitable replacement of FeCoB is yet to be found.

In recent years, many efforts have been focused on exploring a different mechanism to induce magnetisation reversal by driving an electric current along the plane of ferromagnet/non-magnet (NM) bilayers. Spin-orbit effects at the FM/NM interface generate transverse spin currents, which allow one to manipulate the magnetisation of a FM layer by the means of *spin-orbit torques* (SOTs). This effect was shown to be capable of efficiently controlling a number of magnetic ordering, including domain walls and skyrmions. Devices operated by driving the current in-plane, rather than out-of-plane, are particularly attractive since they offer decoupled read/write paths. Large currents flowing across an MTJ can in fact lead to the breakdown of the insulating barrier. This problematic is not relevant in SOT-based memories since a minimal current intensity is required for reading, hence they allow for better thermal stability than that of STT-MRAMs.

A second research topic with great promises for spintronics applications is the one of antiferromagnetic materials. The anti-alignment of atomic spins, as opposed to the alignment in ferromagnets, yield a locally magnetic environment but with a total zero magnetisation. This implies, on one hand, the absence of stray fields that can interact with neighbouring layers and make the use of ferromagnetic material more troublesome. On the other hand, the typical time scales of spin dynamics in antiferromagnets of the order of 1 fs, that is three orders of magnitude faster than the one in ferromagnets. Although electrical switching in such materials was experimentally demonstrated [38], their practical use still require a number of technological advancements [39].

1.3 Summary and thesis overview

Devices based on magnetic materials are promising candidates for the next generation of random access memories. Among their most relevant features, their writing procedure based on current-driven spin torques allows for improved switching times and energy-efficiency. Advancement with respect to existing prototypes requires the further optimisation of the growth techniques for CoFeB/MgO junctions or the use

of novel material combinations. Nevertheless, the high number of factors to be considered to assess the performances of a given structure makes the individuation of material candidates rather complicated.

The main goal of this thesis is to develop and use a computational scheme to probe the features of current-driven magnetisation switching in a range of magnetic materials, in order to understand its material dependence and aid the material optimisation of magnetic memories. Spin dynamics is considered at the atomistic scale as the numerical solution of the atomic LLG equation within a classical spin Hamiltonian [40]. The spin model is tailored to a given system by specifying a number of parameters of quantum mechanical nature, including atomic magnetic moments, inter-atomic exchange constants, magnetic anisotropy, Gilbert damping and spin transfer torques. Ideally, each of the latter is to be assessed within the same level of approximation for each system, since a consistent parameterisation favours the comparison of different systems. First principles approaches based on density functional theory allow to calculate ground state and transport properties of a structure given only the atomic positions and relative species. The main concepts and methods for electronic structure calculations will be presented in Chapter 2, together with the implementation techniques that will be adopted throughout the rest of the thesis.

Chapter 3 contains results for spin-dependent quantum transport calculations in Fe/MgO based MTJs, where different material compositions for the free layer are considered. Particular attention is dedicated to the estimation of spin transfer torques in such structures, in the attempt of determining the factors that define the material dependence of the STT. We begin by considering free layers composed by Fe, Co and Ni, and we discuss the link between the spatial profile of the spin torques with the band structure of each material. We then move to study the influence of partially oxidised interfaces, of magnetic layers contacted with non-magnetic electrodes and of the induced moments in $L1_0$ FePt layers. The obtained data is then employed in Chapter 4, where the results of current-driven spin dynamics calculations are presented. The Chapter begins with a description of the simulation method for atomistic spin modelling, along with a discussion on the spin Hamiltonian to model

the magnetic properties of *bcc* Fe. We then detail an approach to extend the spin dynamics to the case of time-dependent spin lengths, which is then adopted to analyse the properties of $L1_0$ FePt. The spin models for Fe and FePt are then combined with the spin torques calculated from first principles to study the magnetisation switching for different free layers at finite temperatures and for a range of applied voltages.

We continue in Chapter 5 with an analysis of the magnetic properties of the antiferromagnetically ordered Mn_3Ga and Fe_2MnGa Heusler alloys. The formulation of a spin Hamiltonian to reproduce the thermodynamical magnetic properties of the former is presented and employed to study of spin excitations in such material. The peculiarity of Fe_2MnGa lies on the fact that magnetic properties are determined by the moments at Mn sites, while spins at Fe sites behave as induced moments with length strongly dependent to the orientation of Mn moments. We formulate a spin model to describe the magnetic ground-state configuration, that corresponds to antiferromagnetically coupled Mn atoms and non-magnetic Fe atoms. We then present results of spin transport calculations on a $Fe/MgO/Fe_2MnGa$ junction, and discuss the differences between the case of aligned and anti-aligned moments at Mn sites.

We conclude in Chapter 6 by discussing the derivation of a novel approach to estimate the Gilbert damping parameter within first principle simulations that does not require the input of external parameters.

Chapter 2

Ground-state and transport properties of magnetic materials

"*The best way is to use the abstract field idea. That it is abstract is unfortunate, but necessary.* "

- Richard P. Feynman

An accurate estimation of the electronic structure of a material is of key importance for the prediction of its magnetic properties. In fact, magnetism is caused by the asymmetry between the energies of spin-↑ and spin-↓ states that essentially originates from the Pauli exclusion principle. In the simple case of a two electron system this can be shown by imposing the anti-symmetry of the total wavefunction, $\Psi(1,2)$, under the exchange of the two electrons, $1 \leftrightarrow 2$. Assuming that a single-particle wavefunction, ψ, can be factorised as the product between a spatial component, φ, and a spin component, χ, i.e. neglecting relativistic corrections, the possible resulting total wavefunctions are

$$\Psi_S(1,2) = \frac{1}{2}[\varphi_a(1)\varphi_b(2) + \varphi_a(2)\varphi_b(1)][\chi_\uparrow(1)\chi_\downarrow(2) - \chi_\uparrow(1)\chi_\downarrow(2)], \tag{2.1}$$

$$\Psi_T(1,2) = \frac{1}{2}[\varphi_a(1)\varphi_b(2) - \varphi_a(2)\varphi_b(1)] \begin{cases} \chi_\uparrow(1)\chi_\uparrow(2) \\ \chi_\uparrow(1)\chi_\downarrow(2) + \chi_\uparrow(2)\chi_\downarrow(1) \\ \chi_\downarrow(1)\chi_\downarrow(2) \end{cases} . \tag{2.2}$$

Importantly, the spatial component of the "singlet", Ψ_S, and of the "triplet", Ψ_T, states are respectively symmetric and anti-symmetric under coordinates swap, while the opposite holds for the spin states so that the anti-symmetry of the total function is obtained. It is then straightforward to evaluate the expectation value of the Hamiltonian of the system, $\hat{H}$, and find that the energies of the two eigenstates are

$$E_S = C + J \qquad \text{and} \qquad E_T = C - J \ , \tag{2.3}$$

where the level separation is given by the *exchange integral*,

$$J = \int d1d2 \ \varphi_a^*(1)\varphi_b^*(2)\hat{H}\varphi_a(2)\varphi_b(1) \ . \tag{2.4}$$

High exchange energies, however, are not sufficient to grant magnetic properties in extended systems, since a major role is played by the number of electronic states at the Fermi energy, $N(E_F)$. In fact, ferromagnetism arises in solids only when the exchange energy is stronger than the kinetic energy at the Fermi level, hence favouring the splitting of the energy levels of different spin states. This condition is typically expressed by the means of the phenomenological *Stoner criterion*, that predicts the emergence of ferromagnetic properties upon the satisfaction of the condition $N(E_F)J > 1$. In this context J is known as the Stoner exchange parameter and has a definition, which is analogous to that of Eq. (2.4), chosen to embody a uniform energy splitting between spin-↑ and spin-↓ energies in an extended system [41].

A uniform exchange however provides only a qualitative description of ferromagnetism, hence quantitative studies require a material-specific analysis of the electronic structure. An exact estimation of the latter corresponds to the exact solution of the full interacting many-body problem, which is not practically possible in any case of interest. A popular alternative to overcome this limitation is to use model Hamiltonians, i.e. Hamiltonians formulated to reproduce the electronic structure of the material of interest and defined by several system-dependent parameters. The need of an external parameterisation thus makes these approaches more suitable to perform qualitative analyses rather than systematic studies of large sets of materials.

On the contrary, first principles methods based on density functional theory (DFT) provide a stand-alone theoretical framework capable of providing material-specific properties given as sole input the atomic species in a system and their coordinates. The remainder of this chapter begins with a general description of the electronic structure methods that are most relevant to this dissertation, starting with spin-dependent model Hamiltonians for the study of $3d$ transition metals to move on to the basics and implementation techniques used in density functional theory. The next section is then focused on the explanation of the non-equilibrium Green's functions (NEGF) approach to calculate electronic structure properties under steady state currents. Particular attention will be dedicated to detailing the SIESTA [42] and SMEAGOL [43, 44] packages, since these were the main tools used to produce the results presented here.

2.1 Electronic structure theory

The knowledge of the electronic structure of a material enables access to a number of its properties, not only of mechanical but also of thermodynamical or optical nature. However, to gain such information from a theoretical point of view one has to solve the many-body problem for N electrons interacting with one another and with the atomic nuclei. Throughout this thesis we will assume that the nuclear and electronic motions can be treated separately, i.e. we will work within the Born-Oppenheimer approximation. Moreover, since we will be interested into equilibrium electronic properties, the atomic dynamics will be completely neglected. Under these conditions the complete many-electron problem can be written in terms of the Schrödinger Hamiltonian

$$H = \sum_i \left[-\frac{\hbar^2}{2m_e}\nabla_i^2 + V_{\text{ion}}(\mathbf{r}_i) \right] + \frac{e^2}{2}\sum_{i,j}\frac{1}{|\mathbf{r}_i - \mathbf{r}_j|}. \tag{2.5}$$

Here $\mathbf{r}_i$ for $i, j = 1, \ldots, N$ labels the electronic coordinates, e and m_e are the electronic charge and mass, respectively. The first term represents the kinetic energy, T, the second the interaction potential of the i-th electron with the ions and the last

addend is the electron-electron Coulomb interaction, V_{el}. A complete solution of such problem corresponds to the determination of all the possible states, ψ_n^σ, with their respective energies, ε_n^σ. Here we explicitly denote separately the spatial quantum numbers with the single symbol, n, and the spin state, $\sigma = \uparrow, \downarrow$, to mark its relevance for the present dissertation. Magnetic systems are characterised by the presence of an asymmetry in the occupation of electronic states with different spin orientation. This is attributed to the presence of strong interactions between electrons occupying the highest energy levels, i.e. at the Fermi energy. Note, however, that all interactions considered in Eq. (2.5) are not spin-dependent. This holds only if one neglects relativistic corrections, a fact that is acceptable in a large number of cases. If this is not possible, one needs to replace the Schrödinger Hamiltonian Eq. (2.5) with a Dirac-like one. In practice, in most cases one can treat the relativistic corrections within perturbation theory and include them in Eq. (2.5) by adding additional terms expressing the interaction between the electronic orbital and spin angular momenta. The latter is commonly known as *spin-orbit coupling* and it is of fundamental importance to capture phenomena such as the magnetic crystalline anisotropy or the Gilbert damping.

2.1.1 Model Hamiltonians

The many-body problem is of formidable difficulty and it is not exactly solvable unless one considers an extremely reduced number of electrons. A number of methods have been formulated to calculate approximate solutions, especially for cases where electron-electron correlations are not particularly strong. An extensive introduction and overview of the latter can be found in Ref. [45]. The vast majority of the results that will be presented in this work are obtained with approaches based on the Kohn-Sham (KS) formulation of density functional theory (DFT). DFT provides a direct solution of the many-body problem by treating it as a non-interacting-particle problem where electron-electron interactions are embodied by an effective single-particle potential. DFT then allows to perform quantitative predictions of material-specific properties, where the only input is the crystal structure of the system. The

cost of such universality consists in a relatively elevated complexity of the numerical implementation and computational costs. Moreover, obtaining accurate and reliable results can be practically troublesome, given that a number of simulation parameters depending on both the system and the properties of interest are to be specified and monitored. Thus, in cases where one is after qualitative rather than quantitative information the use of simplified models defined by a minimal number of variables can be more convenient. Most of such models are based on the *tight binding* (TB) approximation, namely on the assumption that each eigenstate, $\psi_n(\boldsymbol{r})$, of an electron in a periodic system an be written as a linear combination of atomic orbitals (LCAO), $\varphi_\mu(\boldsymbol{r})$,

$$\psi_n(\boldsymbol{r}) \equiv \frac{1}{\sqrt{N_k}} \sum_{\boldsymbol{k}} \psi_n^{\boldsymbol{k}}(\boldsymbol{r}) = \frac{1}{\sqrt{N_k}} \sum_{\mu\boldsymbol{k}} \mathrm{e}^{i\boldsymbol{k}\cdot\boldsymbol{r}} c_{n\mu}^{\boldsymbol{k}} \varphi_\mu(\boldsymbol{r}). \tag{2.6}$$

Here the sum on the N_k wavevectors, $\boldsymbol{k}$, sampling the Brillouin zone represents a Bloch state expansion, μ labels the different atomic orbitals and $c_{n\mu}^{\boldsymbol{k}}$ are the expansion coefficients for the state n on the basis $\{\varphi_\mu\}$. One can then express the electronic structure of the system by considering an Hamiltonian such as

$$\hat{H}_{\mathrm{TB}} = \sum_{\mu} \varepsilon_\mu \hat{a}_\mu^\dagger \hat{a}_\mu + \sum_{\mu\nu} t_{\mu\nu} \hat{a}_\mu^\dagger \hat{a}_\nu, \tag{2.7}$$

where $\hat{a}_\mu^\dagger$ and $\hat{a}_\mu$ are the creation and destruction operators for the atomic state μ that satisfy the fermionic anti-commutation rules,

$$\left\{\hat{a}_\mu, \hat{a}_\nu^\dagger\right\} = \delta_{\mu,\nu}, \qquad \text{and} \qquad \left\{\hat{a}_\mu^\dagger, \hat{a}_\nu^\dagger\right\} = 0 = \left\{\hat{a}_\mu, \hat{a}_\nu\right\}, \tag{2.8}$$

for $\{\hat{A}, \hat{B}\} = \hat{A}\hat{B} + \hat{B}\hat{A}$. The on-site energies, ε_μ, and the hopping parameters, $t_{\mu\nu}$, are respectively defined as

$$\varepsilon_\mu = \int d^3r \varphi_\mu^*(\boldsymbol{r}) H \varphi_\mu(\boldsymbol{r}), \tag{2.9}$$

$$t_{\mu\nu} = \int d^3r \varphi_\mu^*(\boldsymbol{r} - \boldsymbol{R}_\mu) H \varphi_\nu(\boldsymbol{r} - \boldsymbol{R}_\nu), \tag{2.10}$$

where $\boldsymbol{R}_\mu$ denotes the position of the site at which the atomic orbital φ_μ is centered. These parameters are then to be specified in order to reproduce the electronic properties of the system of interest. For example, they can be obtained by fitting the

band structure of the chosen material taken either from experiment or from a density functional theory calculation. Note that parameters obtained by fitting implicitly include many-body features at the mean-field level.

The above described Hamiltonian can then be used as a starting point to investigate more complex material properties. For example, the $s-d$ or *Kondo* model for ferromagnetism [46] introduces an inter-orbital exchange interaction and can be used to explain the arising of localised magnetic moments in alloys based on $3d$ transition metals and rare-earth ions. In fact, magnetism in such materials is known to be caused by the exchange coupling between itinerant conduction electrons and localised electrons, originating respectively from $4s$ and $3d$ orbitals in $3d$ metals and by $5s$, $4d$ and $4f$ orbitals in rare-earth compounds. Such mechanism can be reproduced by an Hamiltonian of the form

$$\hat{H}_{sd} = \sum_{ij\sigma} t_{ij}\hat{a}^{\dagger}_{i\sigma}\hat{a}_{j\sigma} - J\sum_{i}\hat{\boldsymbol{S}}_i \cdot \hat{\boldsymbol{s}}_i. \tag{2.11}$$

where i, j label the atomic sites and $\sigma = \uparrow, \downarrow$ denotes the electronic spin state. The first term embodies the kinetic energy, where the operators $\hat{a}_{i\sigma}$, $\hat{a}^{\dagger}_{i\sigma}$ destroy and create electrons in s orbitals located at the i-th site and the hopping parameters t_{ij} are assumed to be orbital independent. Since d electrons are strongly localised at the atomic sites, their contribution to the kinetic energy is negligible when compared to the one of itinerant s electrons, therefore it can be omitted. The second term accounts for the on-site sd-exchange interaction between s electrons with spin operators

$$\hat{\boldsymbol{s}}_i = \left(\frac{\hat{a}^{\dagger}_{i\uparrow}\hat{a}_{i\downarrow}+\hat{a}^{\dagger}_{i\downarrow}\hat{a}_{i\uparrow}}{2}, \quad \frac{\hat{a}^{\dagger}_{i\uparrow}\hat{a}_{i\downarrow}-\hat{a}^{\dagger}_{i\downarrow}\hat{a}_{i\uparrow}}{2i}, \quad \frac{\hat{a}^{\dagger}_{i\uparrow}\hat{a}_{i\uparrow}-\hat{a}^{\dagger}_{i\downarrow}\hat{a}_{i\downarrow}}{2i}\right)^{T} \tag{2.12}$$

and d electrons with spins, $\hat{s}_i$. The strength of this latter coupling is controlled by the exchange parameter, J, that is defined in an analogous way to Eq. (2.4). The Hamiltonian in Eq. (2.11) can then be used as starting point for investigation of various spin-dependent properties in such systems, see for example Ref. [47].

The two Hamiltonians (2.7) and (2.11) represent two simple examples to show how model Hamiltonians can be tailored to target a specific physical property in a simplified framework. The applicability range of such models covers a variety of

physical phenomena (see e. g. Refs. [48, 49]), although a growing complexity generally implies the need to specify additional parameters. The latter can be normally determined by fitting data obtained from either experiments or first principles simulations. Such procedure becomes the more complicated the more quantities are needed to define the model Hamiltonian. Hence it is not convenient for complex chemical and/or crystalline structures. Moreover, the requirement of a parameterisation from an external source makes model Hamiltonians not suitable to analyse a large number of systems or to explore novel materials.

2.1.2 Density functional theory and the Kohn-Sham problem

The main goal of first principles, or *ab-initio*, methods in electronic structure theory is to recover the properties of a certain system of electrons and atomic nuclei given solely the knowledge of the coordinates and the species of each atom, together with the values of the fundamental physical constants. This translates in the need of solving the eigenproblem associated to the many-body Hamiltonian in Eq. (2.5) for a ionic potential, $V_{\text{ion}}(\boldsymbol{r})$, that is uniquely determined by the atomic positions and species. Most properties of each system are then encoded in its ground-state (GS) electronic configuration that is defined by the $3N$ × 2-dimensional eigenfunctions $\psi_n(x, y, z)$ corresponding to the lowest eigenvalues, with N being the total number of electrons. Modern first principles approaches are formulated in the framework of density functional theory (DFT) which is based on the Hohemberg-Kohn (HK) theorems [50]. The latter do not provide a practical recipe for the solution of the many-body problem, but prove that it can be reformulated in terms of the total electron density, $\rho(\boldsymbol{r}) \equiv \rho(x, y, z)$, thus drastically reducing its dimensionality from $3N \times 2$ to 3. The theorems apply to any system of interacting particles in an external potential, $V_{\text{ext}}(\mathbf{r})$, which in Eq. (2.5) is played by the ionic potential.

Hohember-Kohn theorem I. *For any system of interacting particles in an external potential, $V_{ext}(\boldsymbol{r})$, the potential $V_{ext}(\boldsymbol{r})$ is determined uniquely, except for a*

constant, by the ground state particle density, $\rho_0(\boldsymbol{r})$.

Hohember-Kohn theorem II. *A universal energy functional* $E[\rho]$ *the electron density,* $\rho(\boldsymbol{r})$*, can be defined, valid for any external potential,* $V_{ext}(\boldsymbol{r})$*. For any particular* $V_{ext}(\boldsymbol{r})$*, the exact ground-state energy of the system is the global minimum of this functional, and the density* $\rho(\boldsymbol{r})$ *that minimises the functional is the exact ground-state density,* $\rho_0(\boldsymbol{r})$.

The content of the first theorem is not of any particular practical use, and it implies that any property depending on ground- or excited states can be determined given the knowledge of the sole ground-state density, $\rho_0(\mathbf{r})$. However, according to the second HK theorem, the knowledge alone of the functional of the density, $E[\rho]$, is sufficient to determine the *exact* ground-state energy and density. Moreover, the latter can also be viewed as a variational principle for the ground-state in terms of the electron density. In summary, the Hohenberg-Kohn theorems state that for any choice of a potential $V_{\text{ext}}(\mathbf{r})$ the ground-state of a system can be found by minimising a unique functional of the electron density, obtaining an exact result if the adopted functional is exact. This implies that the electronic system for any configuration of the ions is completely determined given the knowledge of the universal functional, $E[\rho]$. This is a rather powerful statement. However, the complexity of the problem was simply moved to the determination of the functional that should account for the full electron-electron correlations to be exact. A form for such functional is unknown, hence the introduction of approximations is still required to make this formulation practically tractable. Nevertheless, the variational principle can be exploited to recover the ground-state electron density, hence the total energy and the remaining ground-state properties of the system. As a matter of fact, the variational principle holds not only for functional dependencies expressed in terms of the electron density, but also for generalised densities [51].

By far the most widely used method that translates density functional theory into an operative and computationally viable approach is based on the *Kohn-Sham ansatz*, which is founded on two main assumptions:

Kohn-Sham ansatz I (Non-interacting-V-representability)**.** *The exact ground-state density can be represented as the ground-state density of an auxiliary system of non-interacting particles.*

Kohn-Sham ansatz II (Exchange-correlation (XC) potential)**.** *In the Hamiltonian of the auxiliary system electron-electron interaction can be described by an effective local potential, $V_{XC}(\boldsymbol{r})$, known the* exchange-correlation potential*.*

The original interacting many-body problem is then reduced to an independent particle problem, uniquely determined by the *Kohn-Sham energy functional*

$$E_{\mathrm{KS}}[\rho(\mathbf{r})] = T[\rho(\mathbf{r})] + \int d^3r\ V_{\mathrm{ext}}(\mathbf{r})\rho(\mathbf{r}) + \int d^3r\ d^3r'\ \frac{\rho(\mathbf{r})\rho(\mathbf{r}')}{|\mathbf{r}-\mathbf{r}'|} + E_{\mathrm{XC}}[\rho(\mathbf{r})]. \quad (2.13)$$

The function ρ now is the electron density of the auxiliary non-interacting system. The first term contains the kinetic energy of the non-interacting system, the two middle terms embody the electrostatic energy (the latter is also known as the *Hartree energy*), while the last term is the exchange-correlation (XC) energy. It is evident that the second and third terms are immediately known for a given choice of electron density. This might not seem immediate for the kinetic energy, but it becomes so if one expresses the electron density in terms of the electron eigenfunctions, $\psi_n(\mathbf{r})$, namely

$$\rho(\mathbf{r}) = \sum_{n=1}^{N} |\psi_n(\mathbf{r})|^2, \quad (2.14)$$

since

$$T[\rho(\mathbf{r})] = -\frac{\hbar^2}{2m}\sum_{n=1}^{N}\langle\psi_n|\nabla^2|\psi_n\rangle = -\frac{\hbar^2}{2m}\sum_{i=1}^{N}\int d^3r|\nabla\psi_i(\mathbf{r})|^2. \quad (2.15)$$

The remaining term is the XC energy, E_{XC}, which contains electron-electron interaction and for which an explicit exact form cannot be found. Note that this term does not contain the difference between the kinetic energy of the interacting and non-interacting systems. An approximated form of the latter is then used to make the Kohn-Sham (KS) problem solvable. Before detailing the most common approximations, we reformulate the KS problem expressed as the energy functional in Eq. (2.13) as a Schrödinger-like eigenproblem in terms of the eigenvectors, $\psi_n(\mathbf{r})$, known as the

KS wavefunctions. This is achievable by performing a functional differentiation with respect to $\psi_n^*(\mathbf{r})$ of the Kohn-Sham energy, namely

$$\frac{\delta E_{\mathrm{KS}}}{\delta \psi_n^*(\mathbf{r})} = \frac{\delta T}{\delta \psi_n^*(\mathbf{r})} + \left[\frac{\delta E_{\mathrm{ext}}}{\delta \rho(\mathbf{r})} + \frac{\delta E_{\mathrm{Hartree}}}{\delta \rho(\mathbf{r})} + \frac{\delta E_{\mathrm{xc}}}{\delta \rho(\mathbf{r})}\right] \frac{\delta \rho(\mathbf{r})}{\delta \psi_n^*(\mathbf{r})} = 0, \tag{2.16}$$

where the last member of the latter equation descends directly from the second HK theorem. We note that such expression corresponds to the stationary point of the functional. Each of the functional derivatives in the square brackets corresponds to the definition of a potential acting on an electron at the position $\mathbf{r}$, i.e. $V(\mathbf{r}) = \delta E/\delta\rho(\mathbf{r})$. In other terms, in Eq. (2.16) the variational principle was exploited to define an effective single-particle potential acting on a non-interacting (KS) wavefunction. As a result, the Kohn-Sham problem can be formulated in terms of the Kohn-Sham equations ($n = 1, \ldots, N$)

$$H_{\mathrm{KS}}(\mathbf{r})\psi_n(\mathbf{r}) = \left[-\frac{\hbar^2}{2m}\nabla^2 + V_{\mathrm{ext}}(\mathbf{r}) + V_{\mathrm{Hartree}}(\mathbf{r}) + V_{\mathrm{xc}}(\mathbf{r})\right]\psi_n(\mathbf{r}) = \varepsilon_n\psi_n(\mathbf{r}), \tag{2.17}$$

which constitute a Schrödinger-like problem for N non-interacting particles described by the so-called Kohn-Sham Hamiltonian, H_{KS}. The HK theorems along with the KS ansatz then imply that given the exact form of $V_{\mathrm{xc}}(\mathbf{r})$, the respective eigenfunctions, $\psi_n(\mathbf{r})$, can be used to construct the ground-state density matrix of the original many-body Hamiltonian. However, there is no indication that each single KS eigenstate corresponds to an eigenstate of the original problem, namely to a physically-interpretable state. In other words, the individual KS states do not have a straightforward physical meaning. Nevertheless, since the HK theorems guarantee that the correct electron density is produced, the KS eigenstates must be usable to construct physically meaningful quantities. Let us remark however that Eq. (2.17) was obtained by using a variational principle based on the wavefunctions that contribute to the electron density, i. e. corresponding to occupied electronic states, while there was no specific mention of eigenfunctions of unoccupied (or virtual) states. Therefore, we conclude that the solution of the KS equations do not yield physically sound information on excited states. Moreover, the only quantity that can be defined with the KS eigenvalues and that is well-defined by itself is the lowest occupied molecular orbital (HOMO).

The key feature of the Kohn-Sham formulation is the use of the exchange-correlation potential, V_{XC}, to include electron-electron interactions. An exact determination of V_{XC} equals to an exact solution of the original, full-interacting many-body problem and it is not practically solvable as it is. As a consequence, approximated forms of the XC energy are to be adopted in order to completely determine the KS equations and their solution. The simplest approximation is based on the observation that in most solids the electrons can be considered as close to the limit of the homogeneous electron gas. We can then approximate the exchange-correlation energy density of a generic system at each point, $\epsilon_{\mathrm{XC}}(\boldsymbol{r})$, as the one of the homogeneous electron gas, $\epsilon_{\mathrm{xc}}^{\mathrm{hom}}$, with the same electron density. In other terms,

$$E_{\mathrm{XC}}^{\mathrm{LDA}}[\rho(\boldsymbol{r})] = \int d^3r \ \rho(\mathbf{r})\epsilon_{\mathrm{xc}}^{\mathrm{hom}}(\rho(\mathbf{r})). \tag{2.18}$$

This form of the XC energy is known as *local density approximation* (LDA). The most straightforward improvement of the LDA functional introduces in the XC energy density a dependence on the gradient of the electron density,

$$E_{\mathrm{XC}}^{\mathrm{GGA}}[\rho(\boldsymbol{r})] = \int d^3r \ \rho(\mathbf{r})\epsilon_{\mathrm{xc}}^{\mathrm{hom}}(\rho(\mathbf{r}), |\nabla\rho(\mathbf{r})|), \tag{2.19}$$

and is known as *generalised gradient approximation* (GGA). The LDA and GGA functionals can be considered to be local functionals, since they explicitly depend on a single position vector, $\boldsymbol{r}$. As a consequence, they both fail in situations where relatively strong electron-electron correlation introduces non-locality, where fully non-local potentials should be used [52]. In some situations it is possible to introduce corrections to improve the estimation of specific physical properties, such as the Hubbard U [53] and the self-interaction [45] corrections in the case of band gaps of insulators. Nevertheless, the latter techniques introduce additional computational costs, therefore they are generally employed only when both LDA and GGA provide a strikingly wrong estimation of the property of interest. Although in many cases the GGA exchange-correlation potential yields improved accuracy with respect to LDA [54], in others the choice of the latter remains preferable.

2.1.2.1 Spin density functional theory

The description of DFT provided so far is valid in cases where the spin degrees of freedom do not play a relevant role for the system of interest, since the dependence of the electronic structure on the electronic spin is completely neglected. In practice, the inclusion of spin degrees of freedom implies the explicit functional dependence of the energy upon the densities of spin-↑ and spin-↓ electrons, namely

$$E \equiv E[\rho^{\uparrow}(\boldsymbol{r}), \rho^{\downarrow}(\boldsymbol{r})], \quad \text{where} \quad \rho^{\sigma}(\boldsymbol{r}) = \sum_{i=1}^{N} |\psi_{i\sigma}|^2. \tag{2.20}$$

Hereon $\psi_{i\sigma}(\boldsymbol{r})$ will denote the spin-σ $=\uparrow,\downarrow$ component of the i-th electronic eigenfunction. In analogy to the spin-independent case, the Kohn-Sham equations for spin-density functional theory (SDFT) can be obtained through functional derivatives with respect to $\psi^*_{i\sigma}(\boldsymbol{r})$. We note here that the form of the functional dependence chosen in Eq. (2.20) neglects the possibility of mixing between the two spin channels. In fact, if the spin degrees of freedom are represented by 2×2 complex matrices expanded in the basis $\{|\uparrow\rangle, |\downarrow\rangle\}$, in this formulation the electron density is a diagonal matrix in spin space, namely $\rho^{\sigma\sigma'} \equiv \delta^{\sigma\sigma'}\rho^{\sigma}$. As a consequence, the KS Hamiltonian will have an analogous spin dependence and each spin state will admit an equation analogous to Eq. (2.17). Although the generalisation of the external and Hartree potentials to a spin-dependent system is trivial, the treatment of the exchange-correlation term requires some precautions. Within the "collinear-spin" approximation represented by Eq. (2.20), the spin-independent definitions of the LDA and GGA exchange-correlation energies can be easily extended by introducing the appropriate spin-density functional dependencies,

$$E_{\mathrm{XC}}^{\mathrm{LSDA}}[\rho^{\uparrow}(\boldsymbol{r}), \rho^{\downarrow}(\boldsymbol{r})] = \int d^3\ \rho(\mathbf{r})\epsilon_{\mathrm{xc}}^{\mathrm{hom}}(\rho^{\uparrow}(\mathbf{r}), \rho^{\downarrow}(\boldsymbol{r})), \tag{2.21}$$

$$E_{\mathrm{XC}}^{\mathrm{GGA}}[\rho^{\uparrow}(\boldsymbol{r}), \rho^{\downarrow}(\boldsymbol{r})] = \int d^3r\ \rho(\mathbf{r})\epsilon_{\mathrm{xc}}^{\mathrm{hom}}(\rho^{\uparrow}(\boldsymbol{r}), \rho^{\downarrow}(\mathbf{r}), |\nabla\rho^{\downarrow}(\mathbf{r})|, |\nabla\rho^{\downarrow}(\mathbf{r})|). \tag{2.22}$$

Difficulties, however, arise if the spin quantisation axis is allowed to vary, i. e. in the "non-collinear spin" case. In these conditions the electron density has non-zero off-diagonal spin components, and its spin dependence is often expressed in the basis

for 2×2 complex matrices defined by the Pauli matrices, $\boldsymbol{\sigma} = (\sigma_x\ \sigma_y\ \sigma_z)^T$, namely

$$\rho = \begin{pmatrix} \rho^{\uparrow\uparrow} & \rho^{\uparrow\downarrow} \\ \rho^{\downarrow\uparrow} & \rho^{\downarrow\downarrow} \end{pmatrix} = \begin{pmatrix} n + \mu_z & \mu_x - i\mu_y \\ \mu_x + i\mu_y & n - \mu_z \end{pmatrix} \equiv n\mathbb{1}_2 + \boldsymbol{\mu} \cdot \boldsymbol{\sigma}, \tag{2.23}$$

where $\mathbb{1}_2$ is the 2x2 identity matrix and

$$n = \frac{\rho^{\uparrow\uparrow} + \rho^{\downarrow\downarrow}}{2}, \qquad \mu_x = \frac{\rho^{\uparrow\downarrow} + \rho^{\downarrow\uparrow}}{2}, \qquad \mu_y = i\frac{\rho^{\uparrow\downarrow} - \rho^{\downarrow\uparrow}}{2}, \qquad \mu_z = \frac{\rho^{\uparrow\uparrow} - \rho^{\downarrow\downarrow}}{2}. \tag{2.24}$$

In this notation the spin-independent part of the electron density, n, is isolated from the spin-dependent one, $\boldsymbol{\mu}$, and the direction of the local quantisation axis coincides with the local direction of $\boldsymbol{\mu} \equiv \boldsymbol{\mu}(\boldsymbol{r})$. Note that spin collinearity is recovered by setting $\mu_x = \mu_y = 0$, since the spin quantisation axis is normally assumed to be aligned along z by convention. The challenge of including a spatially varying spin quantisation axis in the KS Hamiltonian comes down to finding a form of the XC potential suitable to consider non-collinear electronic spins. By construction, the LSDA energy of Eq. (2.21) is invariant for rotations of the quantisation axis, meaning that it is functionally dependent solely on $n(\boldsymbol{r})$ and $|\boldsymbol{\mu}(\boldsymbol{r})|$, as in the spin collinear case. This implies that the same functional can be employed for both collinear and non-collinear spin calculations. On the contrary, the functional dependence on the gradients of the spin densities makes GGA potentials not easily adaptable to include non-collinearity. In some SDFT implementations this limitation is neglected and the GGA energy is assumed to be functionally dependent on $n(\boldsymbol{r})$, $|\boldsymbol{\mu}(\boldsymbol{r})|$ and their derivatives, although this is not the most general and rotationally invariant functional (e.g. see Ref. [55]). The inconsistency of GGA potentials with spin non-collinearity then makes the choice of such formulations for the XC energy not appropriate for the description of several complex magnetic systems. It must be noted that although LDA is fully consistent with spin-collinearity, the resulting magnetisation vector is everywhere parallel to the exchange-correlation field. This is problematic, for example, to correctly describe the time evolution of the magnetisation dynamics from a quantum mechanical point of view [56], and in such conditions non-local exchange-correlation potentials are required [57, 58].

Although spin non-collinearity allows for a spatially varying spin quantisation axis, in the current level of approximation its direction remains entirely independent from the crystal structure. In fact, the KS Hamiltonian considered so far is purely non-relativistic, hence does not include any spin-orbit (SO) coupling ($[\hat{\boldsymbol{L}}, \hat{\boldsymbol{S}}] = 0$). A full relativistic treatment of the KS problem would require to replace Schrödinger's equation with the Dirac equation. In practice, it is possible to describe the motion of an electron in an external electric field, $\boldsymbol{\mathcal{E}}(\boldsymbol{r})$, by using a two-component Dirac equation within perturbation theory with respect to the electron velocity [59]. The electric field generated by the atomic nucleus in its proximity can be assumed to be generated by a spherical potential of the form $V(r) = -Ze/r$, Z being the atomic number. This implies that the leading-order term that couples the spin angular momentum with the electron velocity can be written as

$$\frac{\mu_B}{m_e c}\boldsymbol{S} \cdot (\boldsymbol{\mathcal{E}}(\boldsymbol{r}) \times \boldsymbol{p}) = \frac{\mu_B}{m_e c}\frac{1}{r}\frac{dV(r)}{dr}\boldsymbol{S} \cdot (\boldsymbol{r} \times \boldsymbol{p}) = \xi \boldsymbol{S} \cdot \boldsymbol{L}. \tag{2.25}$$

The strength of the SO interaction is here controlled by the parameter, ξ, which is directly proportional to the atomic number, Z. As a consequence, we can conclude that spin-orbit coupling becomes more relevant for heavy atoms. This workaround, hence, allows one to introduce SO interaction in the Schrödinger-like KS equation of Eq. (2.17) by simply adding a factor of the form $\xi \boldsymbol{L} \cdot \boldsymbol{S}$.

2.1.2.2 Constrained density functional theory

The inclusion of spin-orbit coupling is fundamental to study properties such as the magneto-crystalline anisotropy. In a simple way, this can be estimated by comparing the total energy associated to different directions of the magnetisation with respect to the lattice vectors. In practice this is not always possible with a standard (relativistic) DFT calculation. In fact, despite the atomic spin can be initialised in arbitrary directions, it is likely that at convergence the orientation will differ from the initial one. This is especially true when the chosen spin initialisation is strongly energetically disfavored. To overcome this issue, it is possible to perform a constrained density functional theory (CDFT) simulation, thus limiting the explorable

phase space to the electron densities that satisfy the desired condition [60, 61, 62, 63]. This is normally realised by adding a Lagrange multiplier that introduces a penalty to the total energy if a certain condition is not met. For example, the total energy of a system with total magnetisation constrained to form an angle, ϑ, with the z axis can be defined as

$$E(\vartheta) = \max_{\lambda} \min_{\rho} \left\{ E[\rho(\boldsymbol{r})] + \lambda \left(\cos^{-1} \left(\frac{M_x}{M_z} \right) - \vartheta \right) \right\}, \tag{2.26}$$

where the total magnetisation vector, $\boldsymbol{M} = (M_x, M_y, M_z)$, is to be calculated for each given electron density. From Eq. (2.26) is clear that a CDFT calculation requires two self-consistent cycles, one to minimise the energy with respect to the electron density and one to maximise it with respect to the multiplier λ. In practice, configurations corresponding to local minima can be often probed without the use of CDFT, although this is possible only because the whole phase space is not being thoroughly explored during the energy minimisation.

Spin non-collinearity and relativistic effects combined with CDFT schemes allow one to sample a large number for magnetic configurations of a given system, but do not cover all possible states. This limitation is due to the assumption that the electronic ground-state can be expressed by a single Slater determinant formed by the N single-particle KS eigenstates that minimise the total energy. Such states are by construction eigenstates of $\{\hat{\boldsymbol{S}}^2, \hat{S}_z, \hat{\boldsymbol{L}}^2, \hat{L}_z\}$. However, there are systems which ground-state is not an eigenstate of either of the latter operators, hence they cannot be correctly estimated within SDFT and bases including multiple Slater determinants must be adopted [64].

2.1.3 The SIESTA code

A number of different numerical implementations of DFT are currently available [65, 66, 55, 67, 68, 69]. The defining features of each code normally lies on the basis set which expands the wavefunctions and a number of other approximations that aim at a good compromise between efficiency and numerical accuracy. The SIESTA code adopts a basis set composed of non-orthogonal atomic orbitals and

allows one to tackle systems of sizes up to few thousands atoms [42]. The local character of the basis functions makes it particularly suitable to study atom-resolved material properties, in opposition to basis functions such as plane waves which require additional post processing to recover local information.

2.1.3.1 Pseudopotentials and relativistic corrections

The generation of the atomic orbitals basis plays a central rôle in a SIESTA calculation. On the one hand, strictly localised orbitals, i. e. vanishing beyond a certain radius, allow one to obtain good scaling with respect to system size. On the other hand, the use of a basis set, which is not optimised for the system of interest, may lead to non-physical results. In principle, one should include a basis element for each atomic state of the electronic configuration of every atom in the system. This implies a considerable size of the basis set, which in turn greatly increases the computational costs especially in presence of heavy elements. However, in many cases electrons occupying inner electronic states do not actively participate to the chemical bond, hence the corresponding atomic orbitals are not significantly modified by the presence of neighbouring atoms. Their contribution to the properties of the system then consists only on the generation of an electrostatic potential that can be considered to be independent on the environment. Hence, it is possible to reduce the computational costs of the calculation by considering explicitly only outer shells, i. e. valence, electrons and by representing the presence of inner shells, i. e. core, electrons with an effective electrostatic potential known as *pseudopotential*. Pseudopotentials can be fitted from experiments or constructed in order to reproduce the results of a calculation for the isolated atom considering core and valence electrons alike, i. e. an *all-electron* calculation. This second method is normally preferable since it allows for more accurate and transferable pseudopotentials, meaning that can yield the correct electronic structure in a variety of chemical environments. Nevertheless, pseudopotentials generally imply a reduced accuracy with respect to all-electron simulations regardless of how they are generated, hence their use become disadvantageous in studies where elevated numerical precision is essential.

In SIESTA pseudopotentials are employed in order to tackle systems of significant sizes that are not computationally affordable otherwise. The pseudopotential to be used for a given atomic orbital basis set consists in a set of effective atomic potentials, $V_{\mathrm{PS},l}$, for each valence electron type. All pseudopotentials used in this work are based on the Troullier-Martins scheme [70] and are composed by wavefunctions that maintain the reciprocal orthogonality. The latter feature is known as *norm-conservation*, and is sometimes sacrificed in favour of a potential of increased smoothness, or *softness*, to reduce computational costs. The pseudopotential component for an atomic (valence) orbital with orbital quantum number, l, corresponds to the sum of the potential generated by the nucleus and the core electrons, $V_{\mathrm{eff,c}}$, and the one produced by the the rest of the valence electrons, V_{v}. Assuming that the total potential is spherical, $V_{\mathrm{PS},l}$ is calculated by self-consistently solving the Kohn-Sham equation for the radial part of the atomic wavefunction, $R_{nl}(r)$,

$$\left[-\frac{1}{2}\frac{d^2}{dr^2}+\frac{l(l+1)}{2r^2}+V_{\mathrm{eff,c}}(r)+V_{\mathrm{v}}(r)\right]rR_{nl}(r)=\varepsilon R_{nl}(r), \tag{2.27}$$

to then construct the corresponding pseudo-wavefunction, $R_{\mathrm{PS},l}(r)$, so that it satisfies

$$\left[-\frac{1}{2}\frac{d^2}{dr^2}+\frac{l(l+1)}{2r^2}+V_{\mathrm{PS},l}(r)+V_{\mathrm{v}}(r)\right]rR_{\mathrm{PS},l}(r)=\varepsilon R_{\mathrm{PS},l}(r). \tag{2.28}$$

The mapping between the atomic and the pseudo-wavefunctions is uniquely determined by a set of constrains. First of all, the two must correspond to the same eigenvalue and must be identical beyond a user defined cutoff radius, r_c, as shown in Fig. 2.1. The only constrain imposed to $R_{\mathrm{PS},l}(r)$ in the region within r_c is that it must represent the same total charge as its atomic counterpart. Finally, the pseudo-wavefunction is generated with no nodes for simplicity, in contrast with the $n-1$ nodes of the atomic function with principal quantum number, n.

The procedure described above is correct in the absence of relativistic corrections. Nevertheless, the latter can be easily included by considering the Dirac equation and extract the pseudopotential from its self-consistent solution as done in the non-relativistic case [72]. The result is a pseudopotential including relativistic corrections up to the second order in the fine structure constant. It is then possible to

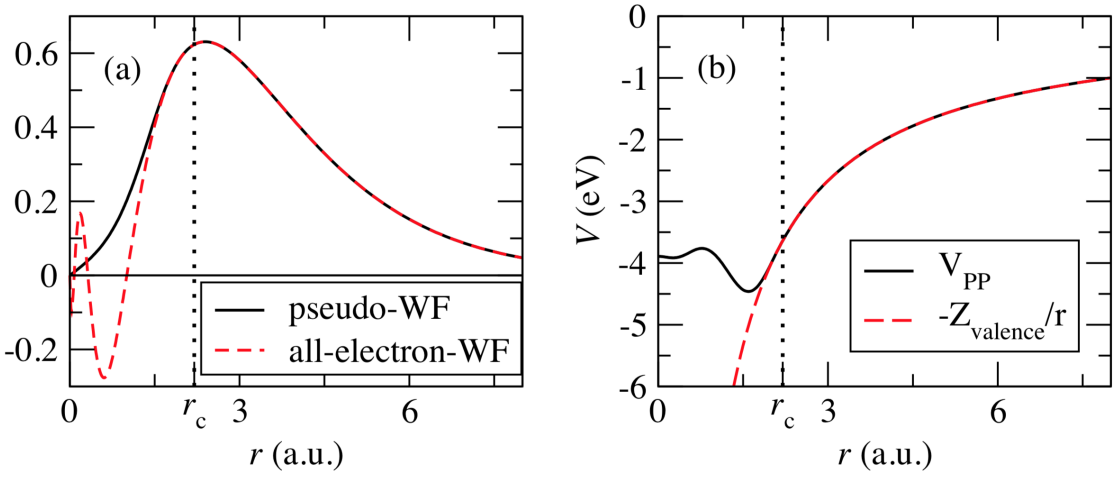

Figure 2.1: (a) Pseudo-wavefunction and all-electron wavefunction for the Fe-4*s* shell and (b) corresponding pseudopotential. Image credit: [71]

express the spin-orbit coupling operator directly on the basis formed by the pseudo-wavefunctions,

$$\hat{V}^{\mathrm{SO}} = \sum_{jm_j} \bar{V}_j |j, m_j\rangle\langle j, m_j| = \sum_{jM} \left[V_l^{\mathrm{sc}} \mathbb{1}_2 + V_l^{\mathrm{SO}} \hat{\boldsymbol{L}} \cdot \hat{\boldsymbol{S}} \right] |l, M\rangle\langle l, M|, \tag{2.29}$$

where the total angular momentum states, $|j, m_j\rangle$, are rewritten in the third member in terms of the real spherical harmonics states, $|l, M\rangle$, with

$$V_l^{\mathrm{s\,c}} = \frac{1}{2l+1} \left[(l+1)\bar{V}_{l+\frac{1}{2}} + l\bar{V}_{l-\frac{1}{2}} \right], \tag{2.30}$$

$$V_l^{\mathrm{SO}} = \frac{2}{2l+1} \left[\bar{V}_{l+\frac{1}{2}} - \bar{V}_{l-\frac{1}{2}} \right]. \tag{2.31}$$

This operation allows one to write the relativistic pseudopotential in a form that is consistent with the non-relativistic PS (here contained in V_l^{sc}) and with the real matrix representation of the Hamiltonian. The expression in Eq. (2.29) can then be used to calculate the spin-orbit matrix elements on the atomic orbital basis set, $\{|\varphi_i\rangle\}_i \equiv \{|R_{n_i,l_i}\rangle \otimes |l_i, M_i\rangle\}_i$, as

$$V_{ij}^{\mathrm{SO}} = \sum_{a,l_a,M_a} \langle\varphi_i|V_{l_a}^{\mathrm{SO}} \hat{\boldsymbol{L}} \cdot \hat{\boldsymbol{S}}|l_a, M_a\rangle\langle l_a, M_a|\varphi_j\rangle. \tag{2.32}$$

Here the sum expresses the complete relations of the real spherical harmonics centered at the a-th site, $|l_a, M_a\rangle$. Since the evaluation of all of such matrix elements

would significantly increase the computational costs and since $V_{l_a}^{\mathrm{SO}}$ is rather short-ranged, only the matrix elements involving orbitals centered on the same site are usually taken into account. In other terms, the spin-orbit coupling can approximated as an on-site operator

$$V_{ij}^{\mathrm{SO}} \approx \langle R_{n_i,l_i}|V_{l_i}^{\mathrm{SO}}|R_{n_i,l_i}\rangle\langle l_i, M_i|\hat{\boldsymbol{L}}\cdot\hat{\boldsymbol{S}}|l_j, M_j\rangle\delta_{l_i,l_j}. \tag{2.33}$$

The angular matrix elements can be evaluated analytically and can be found in Ref. [73] together with extensive details on the implementation. In contrast, the radial matrix elements depend on the specific choice of the radial part of the basis functions, $R_{n_i,l_i} \equiv \varphi_l(r)$.

2.1.3.2 Basis set

The atomic orbital basis set constitutes one of the defining features of SIESTA. While the angular component of each basis atomic orbital is determined by the respective orbital quantum number, the radial function, $\varphi_l(r)$, must be determined numerically. In SIESTA, the radial component is chosen as the numerical eigenfunction of the pseudopotential $V_l(r)$ with eigenvalue $\varepsilon_l + \delta\varepsilon_l$, i. e. it satisfies the equation

$$\left[\frac{-1}{2r}\frac{d^2}{dr^2} + \frac{l(l+1)}{2r^2} + V_l(r)\right]\varphi_l(r) = (\varepsilon_l + \delta\varepsilon_l)\varphi_l(r). \tag{2.34}$$

The energy shift, $\delta\varepsilon_l$, is set in order to control the cutoff radius, r_l^c, at which $\varphi_l(r)$ has its first node. Usually, one chooses an energy shift which is uniform for all orbitals to obtain a well balanced basis. An alternative approach could be to define a common cutoff radius instead. However, this would imply a different level of approximation for each atomic orbital, since r_l^c depends on the angular momentum and on the species of the atom the orbital is centered at. On the contrary, a common energy shift yields a similar confinement for all orbitals and automatically determines the corresponding cutoff radius for each basis function.

A basis set made of one basis element for each atomic orbital, however, proves to often be not sufficient to guarantee accurate results. In fact, such minimal basis set is often a too coarse approximation of a complete basis, hence the energy minimisation

becomes troublesome and the obtained result lacks accuracy. The solution to such problem is to adopt a number of copies of the same atomic orbitals with slightly different radial components, an approach usually known as a *multiple-ζ* scheme. The recipe employed in SIESTA is described in Ref. [74] and is based on the "split-valence" method that is widely used in quantum chemistry [75]. The starting point of the latter is the orbital generated from Eq. (2.34), usually called first-ζ orbital and denoted as $\varphi_l^{1\zeta}(r)$. An additional basis element with the same angular dependence of $\varphi_l^{1\zeta}(r)$ is then called a second-ζ orbital and its radial component is defined as

$$\varphi_l^{2\zeta}(r) = \begin{cases} r^l(a_l - b_l r^2) & \text{if } r < r_l^s \\ \varphi_l^{1\zeta}(r) & \text{if } r \geq r_l^s \end{cases}. \tag{2.35}$$

In other terms, the tail of the orbital beyond a "split radius", r_l^s, is kept the same as the one of the first-ζ orbital, while a polynomial radial dependence is assumed for the second-ζ for $r < r_l^s$. The parameters a_l and b_l are determined by imposing the continuity of $\varphi_l^{2\zeta}(r)$ and its first derivative, while r_l^s is chosen by setting the norm of $\varphi_l^{1\zeta}(r)$ outside the split radius. The same procedure can be employed to generate an arbitrary number of ζ orbitals, however this is often not sufficient to yield converged results and orbitals with higher angular momentum must be included. Nevertheless, it is not always possible to calculate the pseudopotential for such additional orbitals. Hence, it is customary to consider the *polarisation* orbital that is obtained as the solutions of the Schrödinger equation in presence of a small fictitious electric field,

$$\left[-\frac{1}{2r}\frac{d^2}{dr^2}r + \frac{(l+1)(l+2)}{2r^2} + V_l(r) - E_l\right]\varphi_{l+1}(r) = -r\varphi_l(r). \tag{2.36}$$

It must be noted that the total energy is not single-parameter variational with respect to the basis set, meaning that a basis set with more elements than another is not guaranteed to obtained more accurate results. Nevertheless, it was found that in most cases the use of two ζ-orbitals with a polarisation (DZP) for a given atomic orbital is normally satisfactory.

2.1.3.3 Kohn-Sham Hamiltonian

Once the atomic orbitals are defined the KS Hamiltonian can be directly written in terms of such basis, that will be denoted as $\{|\varphi_\mu\rangle\}$. Each spin component, $\hat{H}^{\sigma\sigma'}(\boldsymbol{r})$ with $\sigma, \sigma' = \uparrow, \downarrow$, is represented as a $N_\mathrm{o} \times N_\mathrm{o}$ matrix where N_o is the total number of atomic orbitals in the basis. Hence, the total spin-dependent Hamiltonian is a $2N_\mathrm{o} \times 2N_\mathrm{o}$ matrix with elements

$$H_{\mu\nu}^{\sigma\sigma'} = \int d^3r \varphi_\mu^*(\boldsymbol{r}) \left[\delta^{\sigma,\sigma'} \left(-\frac{\hbar^2}{2m}\nabla + V_\mathrm{PP}(\boldsymbol{r}) + V_\mathrm{Hartree}(\boldsymbol{r}) \right) + V_\mathrm{SO}^{\sigma\sigma'} + V_\mathrm{xc}^{\sigma\sigma'}(\boldsymbol{r}) \right] \varphi_\nu(\boldsymbol{r}). \tag{2.37}$$

In analogy, each electronic eigenstate is written as,

$$\psi_n(\boldsymbol{r}) = \sum_{\mu\sigma} c_{n\mu}^\sigma \varphi_\mu(\boldsymbol{r}) \tag{2.38}$$

and satisfies the generalised eigenvalue equation,

$$\sum_{\nu\sigma'} (H_{\mu\nu}^{\sigma\sigma'} - \delta^{\sigma\sigma'}\varepsilon_n S_{\mu\nu})\psi_n^{\sigma'} = 0. \tag{2.39}$$

The overlap matrix, $S_{\mu\nu}$, is defined as,

$$S_{\mu\nu} = \int d^3r \varphi_\mu(\boldsymbol{r})\varphi_\nu(\boldsymbol{r}), \tag{2.40}$$

and accounts for the non-orthogonality of the atomic orbitals centered on different atoms. Since such two-center integrals depends solely on the atomic orbitals, they can be calculated only once, before to the energy minimisation. In case of a periodic system, one needs to consider not only integrals between orbitals in the unit cell, but also all non-vanishing overlaps between each atomic orbitals in the unit cell, φ_μ, and all the other atomic orbitals, $\varphi_{\nu'}$, in an auxiliary supercell. The latter is constructed large enough to contain all atoms whose basis orbitals have non-zero overlap with the basis orbitals of the atoms in the unit cell. The sum of such contributions can be expressed as a discrete Fourier transform,

$$\varphi_\mu(\boldsymbol{r}, \boldsymbol{k}) = \sum_{\mu' \equiv \mu} \varphi_{\mu'}(\boldsymbol{r}) = \sum_{\mu' \equiv \mu} \mathrm{e}^{i\boldsymbol{k}\cdot\boldsymbol{R}_{\mu'}} \varphi_\mu(\boldsymbol{r} - \boldsymbol{R}_{\mu'}), \tag{2.41}$$

where the sum is restricted to the orbitals in the supercell, μ', that are equivalent to the orbital, μ, in the unit cell. Here $\boldsymbol{r}$ is contained in the unit cell, $\boldsymbol{R}_{\mu'}$ is the center of the orbital μ' and the Bloch theorem is used in the last equality. In this way the overlap matrix can be written as

$$S^{\boldsymbol{k}}_{\mu\nu} = \sum_{\mu'\equiv\mu}\sum_{\nu'\equiv\nu} \mathrm{e}^{i\boldsymbol{k}\cdot(\boldsymbol{R}_{\nu'}-\boldsymbol{R}_{\mu'})} S_{\mu'\nu'}. \tag{2.42}$$

Here μ' (ν') denotes any basis orbital in the supercell that is equivalent to the basis orbital μ (ν) in the unit cell. The Fourier transforms of the wavefunction and the Hamiltonian will then have expressions analogous to those in Eqs. (2.41) and (2.42), respectively. This allows one to define an eigenvalue equation as the one in Eq. (2.39) for each vector in the Brillouin zone, $\boldsymbol{k}$.

The information obtained by solving such eigenproblems can then be used to construct the density matrix of the system. In general, the density matrix operator is defined as

$$\hat{\rho}^{\sigma\sigma'} = \sum_{i=1}^{N} \eta_n |\psi_n^{\sigma}\rangle\langle\psi_n^{\sigma'}|, \tag{2.43}$$

where η_n is the occupation of the n-th eigenstate, and its matrix elements in terms of the SIESTA basis are

$$\rho^{\sigma\sigma'}_{\mu\nu} = \frac{1}{N_k}\sum_{\boldsymbol{k}} \eta^{\boldsymbol{k}}_n c^{\sigma\boldsymbol{k}}_{n\mu} c^{\sigma'\boldsymbol{k}}_{n\nu} \mathrm{e}^{i\boldsymbol{k}\cdot(\boldsymbol{R}_{\nu'}-\boldsymbol{R}_{\mu'})} \tag{2.44}$$

It is straightforward to show that the trace over spin and spatial degrees of freedom of the operator product $\hat{\rho}\hat{O}$ yields the "expectation value", $\langle\hat{O}\rangle$ of any single-particle operator, $\hat{O}$. As a consequence, it is easy to demonstrate that, for example,

$$N_{\mathrm{el}} = \sum_{\mu\sigma} \rho^{\sigma\sigma}_{\mu\mu}, \qquad \boldsymbol{M} = \sum_{\substack{\mu \\ \sigma\sigma'}} \rho^{\sigma\sigma'}_{\mu\mu} \boldsymbol{\sigma}^{\sigma'\sigma}, \qquad E_{\mathrm{tot}} = \sum_{\substack{\mu\nu \\ \sigma\sigma'}} \rho^{\sigma\sigma'}_{\mu\nu} H^{\sigma'\sigma}_{\nu\mu}. \tag{2.45}$$

Moreover, the localisation of the basis set allows one to easily retrieve atom-resolved information by restricting the trace to orbitals that are centered on the same atom, a. In fact, the atomic magnetic moments can be calculated as

$$\boldsymbol{m}_a = \sum_{\substack{\mu\in a \\ \sigma\sigma'}} \rho^{\sigma\sigma'}_{\mu\mu} \boldsymbol{\sigma}^{\sigma'\sigma}. \tag{2.46}$$

Finally, the total KS energy can be estimated as

$$E = \sum_{\substack{\mu\nu \\ \sigma\sigma'}} \rho_{\mu\nu}^{\sigma\sigma'} H_{\nu\mu}^{\sigma'\sigma} - \frac{1}{2}\int d^3 r V_H(\boldsymbol{r})\rho(\boldsymbol{r}) + E_{\mathrm{xc}}[\rho] - \int d^3 V_{\mathrm{XC}}(\boldsymbol{r}) + E_{\mathrm{nuclei}}. \quad (2.47)$$

2.1.4 Summary

Density functional theory allows one to calculate the electronic structure of a material starting from the atomic species and positions. It relies on the assumption that the electronic system can be mapped onto a non-interacting system and that the XC potential correctly accounts for electron-electron correlation. The functional dependence of the total energy with respect to the density allows to find the ground-state density as the one that minimises the total energy. The use of the LDA or the GGA approximations for the XC potential successfully reproduce the electronic properties in many systems, although it fails in cases where electrons are delocalised or in presence of spin degenerate states [76]. Nevertheless, the generality of DFT makes it the ideal tool to consider a large number of materials within the same framework and compare their properties. Moreover, it can be used as starting point to explore phenomena beyond the ground-state properties, as explained in the next section.

2.2 Green's function method for electronic transport

This section is dedicated to the derivation of the mathematical formalism at the foundation of the adopted approach to evaluate transport properties of nanoscale systems. The entire theory we are about to present has its foundations in the concept of Green's function (GF). Originally conceived as a mathematical tool to solve non-homogeneous linear differential equations, the term is nowadays commonly used to refer to different types of correlation functions. It is ubiquitous in many fields of physics, ranging from quantum field theory to aerodynamics. Extensive descriptions

of the application of Green's functions in condensed matter physics are available in a number of textbooks [77, 78, 79, 80, 81]. Here we will limit to an overview of the features of the GFs that are essential in order to capture the physical meaning of the approximations assumed in the transport approach.

In the specific case of the time-dependent (homogeneous) Schrödinger equation for a system described by the Hamiltonian $H(\mathbf{x}, t)$,

$$\left[i\hbar\frac{\partial}{\partial t} - H(\mathbf{x}, t)\right]\psi(\mathbf{x}, t) = 0, \tag{2.48}$$

the Green's function can be defined as

$$\left[i\hbar\frac{\partial}{\partial t} - H(\mathbf{x}, t)\right]G(\mathbf{x}, \mathbf{x}'; t, t') = \delta(\mathbf{x} - \mathbf{x}')\delta(t - t'). \tag{2.49}$$

In presence of a perturbation, $H_1(\mathbf{x}, t)$, Eq. (2.48) must be modified by inserting the term $H_1(\mathbf{x}, t)\psi(\mathbf{x}, t)$ at the right-hand side. The solution of the resulting inhomogeneous differential equation can be elegantly written as

$$\psi(\mathbf{x}, t) = \int d\mathbf{x}'dt'G(\mathbf{x}, \mathbf{x}'; t, t')H_1(\mathbf{x}', t')\psi(\mathbf{x}', t'). \tag{2.50}$$

The above defined GF thus represents a two points correlation function that embodies the linear response of the system at $(\mathbf{x}, t)$ to the generic perturbation H_1 at $(\mathbf{x}', t')$. Moreover, Eq. (2.50) also states that $\psi(\mathbf{x}, t)$ is the result of the temporal and spatial evolution of the function $\psi(\mathbf{x}', t')$, for any $(\mathbf{x}', t')$, under the effects of the perturbation. The Green's function, $G(\mathbf{x}, \mathbf{x}'; t, t')$, thus describes the propagation of a solution ψ between the position-time pairs $(\mathbf{x}, t)$ and $(\mathbf{x}', t')$. Such point of view is often adopted within quantum field theories, in which GFs are also called *propagators*. Eqs. (2.48) and (2.49) are nothing but two different formulations of the same problem in the case of a closed system. However, the inclusion of semi-infinite reservoirs or thermal baths yields to an infinite-dimensional Schrödinger equation, which cannot be easily cast into a practically solvable form. On the contrary, the Green's function problem for an open system can be expressed as a finite-dimensional equation by introducing the self-energy functions to account for the coupling of the system with the environment.

The following treatment deals with electronic transport across a two-terminal device, although it can be generalised to a generic number of contacts. The system of interest will then be divided into three parts: two semi-infinite regions that will act as electron reservoirs, hence called leads, and a central region. By construction, the leads are to be free from any scattering phenomenon. In order to ensure such condition, the central region, that will be referred to as scattering region (SR) or extended molecule (EM), must include the system of interest as long as part of the leads, as depicted in Fig. 2.2. This allows one to include all the modifications in the electronic structure caused by the presence of interfaces in the scattering region, and consider the leads made of pure bulk material in thermodynamic equilibrium. Furthermore, the contacts can be thought to be semi-infinite chains of blocks, or principal layers (PLs), each coupled exclusively with its nearest neighbours. If each principal layer can be successfully described by a basis of M atomic orbitals, it can be represented as a $M \times M$ Hamiltonian matrix, H_0. Inter-block interactions also can be expressed by a $M \times M$ matrix, H_1 ($H_{-1} = H_1^\dagger$). In a similar manner, we can assume that the scattering region is defined by N atomic orbitals through a $N \times N$ matrix, H_M. The interaction between the extended molecule and the first principal

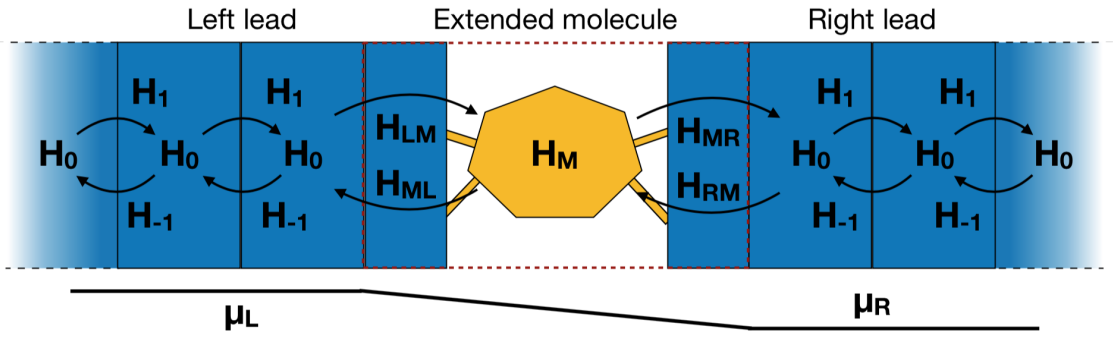

Figure 2.2: Schematics of a two-terminal device. A lead can be represented by a semi-infinite series of blocks described by Hamiltonians, H_0, each interacting only with adjacent blocks via the coupling matrix, H_1 ($H_{-1} = H_1^\dagger$). The extended molecule is described by the Hamiltonian, H_M, and with the first block of the left- (right-) hand side lead through, H_{ML} (H_{MR}), with $H_{LM} = H_{ML}^\dagger$ ($H_{RM} = H_{MR}^\dagger$).

layer of the left- (right-) hand side lead will then be contained in the $N \times M$ matrix, H_{ML} (H_{MR}), with $H_{LM} = H_{ML}^{\dagger}$ ($H_{RM} = H_{MR}^{\dagger}$). The Hamiltonian of the entire system, comprising of leads and scattering region, can thus be written in the block matrix form

$$\mathcal{H} = \begin{pmatrix} \ddots & \ddots & \ddots & \vdots & & & \\ \ddots & H_0 & H_1 & 0 & \cdots & & \\ \ddots & H_{-1} & H_0 & H_{LM} & 0 & \cdots & \\ \dots & 0 & H_{ML} & H_M & H_{MR} & 0 & \cdots \\ & \vdots & 0 & H_{RM} & H_0 & H_1 & \ddots \\ & & \vdots & 0 & H_{-1} & H_0 & \ddots \\ & & & \vdots & \ddots & \ddots & \ddots \end{pmatrix} = \begin{pmatrix} \mathcal{H}_L & \mathcal{H}_{LM} & 0 \\ \mathcal{H}_{ML} & H_M & \mathcal{H}_{MR} \\ 0 & \mathcal{H}_{RM} & \mathcal{H}_R \end{pmatrix}. \quad (2.51)$$

Italic characters will hereon denote infinite-dimensional objects. In particular, $\mathcal{H}_{L,R}$ refer to the Hamiltonians of the entire semi-infinite isolated leads, while $\mathcal{H}_{ML} = (\cdots \quad 0 \quad H_{ML})$ and $\mathcal{H}_{MR} = (H_{MR} \quad 0 \quad \cdots)$ are the infinite-dimensional row vectors of $N \times M$ matrices that contain the coupling between the extended molecule and the leads. Since H_M and H_0 describe systems at equilibrium, they are hermitian. The same does not hold, however, for the coupling matrices, namely $H_1 \neq H_1^{\dagger} = H_{-1}$ and $H_{M\alpha} \neq H_{M\alpha}^{\dagger} = H_{\alpha M}$, $\alpha = L, R$. The Green's function defined by such Hamiltonian will have the same dimensionality, i.e. will be infinite-dimensional, and is given by

$$[(E + i\delta)\mathcal{S} - \mathcal{H}]\,\mathcal{G}(E) = -\mathcal{K}(E)\mathcal{G}(E) = \mathcal{I}. \quad (2.52)$$

Here $\mathcal{S}$ accounts for the non-orthogonality of the basis set the wave-function of the complete system is expanded on. In analogy to Eq. (2.51), $\mathcal{S}$ can be written as a block diagonal matrix with elements the overlap matrices $\mathcal{S}_L$, S_M and $\mathcal{S}_R$ associated with the left-hand side lead, the scattering region and right-hand side lead, respectively. By its definition, $\mathcal{K}$ has the same block matrix structure of $\mathcal{H}$, while $\mathcal{I}$ is the infinite-dimensional identity matrix. The small imaginary part, δ, added to the energy, E, is assumed to be positive and it is introduced in order to ensure the convergence of the time/energy Fourier transform. More insights on its role and physical meaning will be provided in the following subsection. Let us note that this equation can be

obtained from Eq. (2.49) performing a time-Fourier transform and integrating over the spatial degrees of freedom, which are now contained in the localisation of the atomic orbital basis elements.

In order to make Eq. (2.52) practically solvable it is necessary to reformulate it in order to eliminate the dependence from the leads degrees of freedom. In other words, the presence of each lead must be included through a quantity, $\Sigma_{L,R}$, called *surface self-energy*, that is to be defined completely in terms of the atomic basis of the extended molecule. In such way one can obtain a defining equation of the scattering region Green's function, G_M, of the form,

$$[-K_M(E) - \Sigma_L(E) - \Sigma_R(E)]\, G_M(E) = I_M, \tag{2.53}$$

where all terms are $N \times N$ matrices and the surface self-energy for lead $\alpha = L, R$ is defined as

$$\Sigma_\alpha = K_{M\alpha} G_\alpha K_{\alpha M}. \tag{2.54}$$

The rest of this section will discuss how it is possible to use the Keldysh Green's functions formalism to calculate the Green's functions for the leads G_L, G_R and for the extended molecule G_M, and how to combine them to yield the transport properties of the system. Firstly, the fundamental notions on how the concept of Green's function can be applied in non-equilibrium conditions will be outlined. Next, the main quantities and relations that form the essence of the NEGF approach will be presented. In conclusion, the practical implementation techniques adopted in the SMEAGOL code will be presented, along with some considerations on the limits of validity of the present method.

2.2.1 Non-equilibrium Green's functions theory

Here we outline here the fundamental conceptual steps necessary to define the quantities involved in the NEGF method for transport. We start our dissertation by discussing the evaluation of the quantum average of a time-dependent operator, $\hat{O}(t)$. If the dynamics of a system can be described by the Schrödinger equation

and the state at a time, t_0, is $|\Psi(t_0)\rangle$, the time-dependent expectation value of the observable, $O(t)$, is given by

$$O(t) = \frac{\langle\Psi(t)|\hat{O}(t)|\Psi(t)\rangle}{\langle\Psi(t)|\Psi(t)\rangle} = \frac{\langle\Psi(t_0)|\hat{U}(t_0,t)\hat{O}(t)\hat{U}(t,t_0)|\Psi(t_0)\rangle}{\langle\Psi(t_0)|\hat{U}(t_0,t)\hat{U}(t,t_0)|\Psi(t_0)\rangle}. \tag{2.55}$$

Here $\hat{U}(t,t')$ dictates the time evolution of the system from time t to time t'. In the last term the state at a general time, t, is rewritten in terms of the initial state. Hence, one can estimate the quantum average at the time, t, given the knowledge of the time evolution operator, $\hat{U}(t,t_0)$, and the state, $|\Psi(t_0)\rangle$.

In ground-state quantum field theory, it is customary to consider inter-particle interactions, $\hat{H}_1(t)$, as a time-dependent perturbation that vanishes for long times and to introduce the full many body correlations at $t = 0$. This is a formal procedure known as *adiabatic switching on*, and it allows one to recover ground-state properties of a full-interacting system once the ground-state of its respective non-interacting system, $|\Phi\rangle$, is known,

$$O(t) = \frac{\langle\Phi|\hat{U}(+\infty,t)\hat{O}(t)\hat{U}(t,-\infty)|\Phi\rangle}{\langle\Phi|\hat{U}(+\infty,-\infty)|\Phi\rangle}. \tag{2.56}$$

This result can be derived within the interaction picture, i. e. by assuming the evolution expressed by $\hat{U}$ is only dictated by the perturbation Hamiltonian, $\hat{H}_1$ [82]. The time evolution operator is commonly written in the form

$$\begin{aligned}\hat{U}(t,t') &= \sum_{n=0}^{\infty}\left(\frac{-i}{\hbar}\right)^n \frac{1}{n!}\int_{t'}^{t} dt_1 \ldots \int_{t'}^{t} dt_n \mathcal{T}\left[\hat{H}_1(t_1),\ldots,\hat{H}_1(t_n)\right] \\ &= \mathcal{T}\left\{\exp\left[\frac{-i}{\hbar}\int_{t'}^{t} d\bar{t}\hat{H}_1(\bar{t})\right]\right\},\end{aligned} \tag{2.57}$$

assuming $t > t'$. The symbol $\mathcal{T}$ here stands for the *time-ordering operator*, which by definition arranges a sequence of operators according to the time at which they are calculated, positioning the operators with later times at the left-hand side. It is in fact essential that such ordering stands for all operators in the matrix element, since it allows for the application of Wick's theorem and the achievement of an operationally useful result. In the case of Eq. (2.56) the operators are already in the correct order. The same does not hold for Eq. (2.55), as the two evolution operators

propagate from t to t_0 and vice versa, therefore the correct time-ordering is verified only if $t = t_0$. However, if $|\Psi(-\infty)\rangle = |\Psi(+\infty)\rangle$ then the group properties of $\hat{U}$ imply that

$$\hat{U}(-\infty, +\infty) = \hat{\mathbb{1}} \qquad \text{and} \qquad \hat{U}(t, t_0) = \hat{U}(t, +\infty)\hat{U}(+\infty, -\infty)\hat{U}(-\infty, t_0). \quad (2.58)$$

Hence, assuming $t_0 < t$, the time ordering is recovered. Nevertheless, this procedure can be applied in equilibrium conditions only because one can safely assume that the evolution does not depend on the specific way it is performed, namely on the evolution path. In other terms, the history of the system does not influence its state as far as it remains in equilibrium at all times. However, this assumption does not hold when factors, such as interaction with an external reservoir, bring the system out of equilibrium. In such cases the problem can be overcome by considering a closed ordered contour going forward in time from t_0 to $+\infty$ to then proceed from $+\infty$ backwards in time up to t_0, as depicted in Fig. 2.3. By definition, an operator calculated at a time $t = t^+$ belonging to the forward segment, (γ_+), will have the same value as one calculated at the equivalent time $t = t^-$ in the backwards segment (γ_-). In this way the same evolution path is followed twice but going in different directions in time, so that the effects of the evolution are naturally cancelled out. Using this contour Eq. (2.55) can be rewritten as

$$O(t) = \frac{\langle \Psi(t_0)|\hat{U}(t_0^+, +\infty)\hat{U}(+\infty, t^-)\hat{O}(t^-)\hat{U}(t^-, t_0^-)|\Psi(t_0)\rangle}{\langle \Psi(t_0)|\hat{U}(t_0^+, +\infty)\hat{U}(+\infty, t^-)\hat{U}(t^-, t_0^-)|\Psi(t_0)\rangle}. \quad (2.59)$$

The closed path $\gamma = \gamma_+ \cup \gamma_-$ was named Keldysh contour in honor of Leonid Keldysh, who first adapted the notion of closed contour in the context of non-equilibrium Green's functions [83].

Let us now imagine the time variable, t, to be the real part of a complex quantity, say z. Then the segment γ_+ can be thought as lying on the positive complex semiplane, in other words as the path $(t, i\delta) \to (+\infty, i\delta)$, with δ being a positive infinitesimal number. Likewise, γ_- can be written as a path on the negative complex semiplane, namely $(+\infty, -i\delta) \to (t, -i\delta)$. As a matter of fact, the notion of Keldysh contour can be further generalised to comprise segments parallel to the imaginary

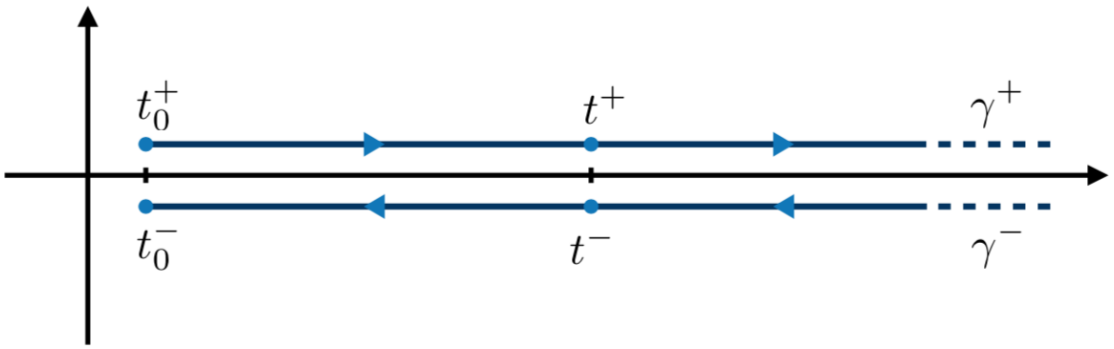

Figure 2.3: Graphical representation of the Keldysh path as divided into two segments, $\gamma_\pm$, with its orientation is given by the light blue arrows. The contour starts at time t_0 in the upper complex semiplane, it continues to $+\infty$ to then return to t_0 from the lower complex semiplane. The position of a generic time $t \geq t_0$ on the contour is also depicted. Quantities evaluated at equivalent times that belong to different segments assume by definition the same value, hence the contour is a closed line.

axis. As segments on the real axis represent time averages (Re $z = t$), segments on the imaginary axis can represent ensemble averages (Im $z = (k_B T)^{-1}$). One can then define the Green's functions and other operators as dependent on such complex times and design an entire theory that in principle can yield information on the evolution of a fully out of equilibrium quantum system. A complete treatment of such theory can be found in Ref. [81] and it goes far beyond our scope. In the following we will focus only on quantities that are defined on the real time axis and that enter directly in the algorithm for quantum transport calculations.

2.2.1.1 Green's functions and self-energies on the Keldysh contour

The definition of Green's functions and related quantities in the context of the Keldysh formalism is analogous to the one adopted in the ground state framework,

e. g. the one-particle correlator reads

$$G(1;2) = -i\frac{\mathrm{Tr}\left\{\mathcal{T}\left[\mathrm{e}^{-i\int_\gamma \hat{H}(z)dz}\hat{\psi}(1)\hat{\psi}^\dagger(2)\right]\right\}}{\mathrm{Tr}\left\{\mathcal{T}\left[\mathrm{e}^{-i\int_\gamma \hat{H}(z)dz}\right]\right\}}. \tag{2.60}$$

Here the numerical arguments stand for a pair of space-time variables, e.g. $1 = (\mathbf{x}_1, z_1)$, "Tr" represents the trace over all possible many-body states and $\hat{\psi}$ ($\hat{\psi}^\dagger$) is the destruction (creation) one-body field operator. We assume that the Hamiltonian has the form

$$\hat{H} = \int d^3x\; d^3x'\; \hat{\psi}^\dagger(\mathbf{x})\langle\mathbf{x}|\hat{h}|\mathbf{x}'\rangle\hat{\psi}(\mathbf{x}') + \frac{1}{2}\int d^3x\; d^3x'\; v(\mathbf{x},\mathbf{x}')\hat{\psi}^\dagger(\mathbf{x})\psi^\dagger(\mathbf{x}')\hat{\psi}(\mathbf{x}')\hat{\psi}(\mathbf{x}), \tag{2.61}$$

where the time dependencies are omitted for simplicity, $\hat{h}$ is the one-particle operator and v is the electron-electron interaction. The equations of motion for G can be obtained simply by deriving with respect to each of the time variables and by exploiting the equation of motion for the field operators. As an example, differentiation with respect to z_1 yields to

$$\left[i\frac{d}{dz_1} - h(1)\right]G(1;1') = \delta(1,1') + \int d2\; v(1;2)G_2(1,2;1',2^+). \tag{2.62}$$

The variable 2^+ corresponds to the pair $(\mathbf{x}_2, z_2 + i\delta)$, with δ being positive and infinitesimal. The definition of the two-particle Green's function, G_2, is similar to that given in Eq. (2.60), only containing four field operators instead of two. In principle, the equations of motion for the latter needs to be calculated to fully determine the dynamics for $G(1;1')$. However, that involves the three-particle Green's function and an entire hierarchy of equations can be constructed. In order to solve the equation the hierarchy must be truncated. If one neglects the possibility of formation of two-particle bound states, G_2 can be written in terms of the single-particle GF:

$$\begin{aligned} G_2(1,2;1',2^+) &= G(1;1')G(2;2^+) - G(1;2^+)G(2;1') \\ &= \left[\delta(1;2)V_H(1) + iv(1;2)G(1;2^+)\right]G(2;1') \\ &\equiv \Sigma(1;2)G(2;1'). \end{aligned} \tag{2.63}$$

The latter formula constitutes the Hartree-Fock approximation for the two-particle Green's function, as the Hartree and exchange interactions are recovered. In the

last equality we implicitly define the function, Σ, that describes all the interactions between an electron and the rest of the system. Such quantity is commonly called *self-energy*, which constitutes a ubiquitous concept in quantum field theory. It can represent a general space-time dependent correction to the electronic energies induced by the presence of an interaction. Let us note that the surface self-energies mentioned in Eq. (2.53) belong to the just described category. Furthermore, Eq. (2.63) indicates that the self-energies are defined as combinations of single-particle Green's functions and time-independent operators. Therefore, any consideration on the properties of G on the Keldysh contour will be naturally extendable to the respective self-energies.

2.2.1.2 Lesser, greater, retarded and advanced Green's functions

The structure of the time dependence of the one-particle Green's function, $G(t,t')$, can be analysed by separating it into different components depending on the mutual relation between t and t'. A first distinction is the one between the *lesser* and *greater* components, denoted with $G^<$ and $G^>$, respectively,

$$G(t,t') \equiv \vartheta(t-t')G^>(t,t') + \vartheta(t'-t)G^<(t,t'), \tag{2.64}$$

where $\vartheta(t,t')$ is the generalisation of Heaviside's theta function defined over the Keldysh contour. The latter components contain information on how the system was initially prepared and how it evolves in time. A better intuition of their physical meaning can be obtained by expressing the one-body $G^<$ in terms of the creation and destruction operators, $\hat{d}^\dagger$ and $\hat{d}$,

$$\begin{aligned} G^<(t,t') &= i\sum_{ij}\langle\Psi_{N,0}|\hat{U}(t_0,t')\hat{d}_i^\dagger\hat{U}(t',t)\hat{d}_j\hat{U}(t,t_0)|\Psi_{N,0}\rangle \\ &= \sum_{ij} G_{ij}^<(t,t'), \end{aligned} \tag{2.65}$$

i,j labelling single particle states. We will limit our discussion to systems that are initially prepared in a pure state with N particles, $|\Psi_{N,0}\rangle$, that can be either the ground state or an excited one. Each matrix element embodies the probability amplitudes that the removal of a particle with the state i at t' yields the same

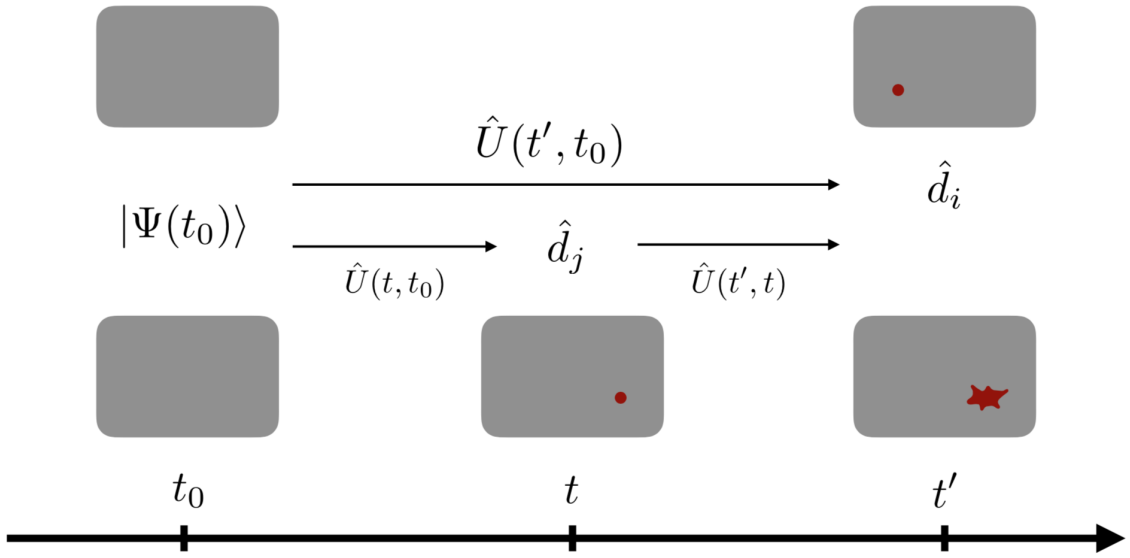

Figure 2.4: Graphic representation of the two states obtained through the different evolution patterns considered in Eq. (2.65). In the evolution path considered in the top of the figure the final state is obtained through the destruction of a particle in the state i at a time, t', represented by the red circle. On the contrary, the evolution pattern shown at the bottom is obtained by destroying a particle in the state j at an intermediate time, $t_0 < t < t'$. The resulting state is then evolved until the final time, t', and the "spreading" of the absence of the particle state with quantum number j is represented with the irregular red shape in the bottom right figure.

evolution obtained by removing a particle in the j-th state at t to then evolve until time t'. Fig. 2.4 is a graphic representation of what is described above. A non-zero contribution is then obtained when j is no longer a good quantum number at time t', hence it "spreads" with time. Furthermore, the lesser Green's function can be used to calculate the time-dependent average of any one-body operator, $\hat{O} = \sum_{ij} \hat{c}_i^\dagger O_{ij} \hat{c}_j$, by setting $t = t'$,

$$O(t) = -i \sum_{ij} O_{ij} G^<_{ji}(t, t). \tag{2.66}$$

Let us also note that, if $\hat{O}$ is the identity operator, we will recover the time-dependent average of the density operator, and therefore $O(t)$ becomes the time-dependent

quantum average of the density matrix.

The above discussion holds for a general time-dependent Hamiltonian. In most cases of interest, however, the system can be considered to be in a steady- state regime, and hence it can be described by a time-independent Hamiltonian. This assumption simplifies the form of the evolution operator and allows us to rewrite Eq. (2.65) as

$$G^{<}_{ji}(t,t') = i\sum_{m}\langle\Psi_{N,0}|\hat{d}_i^{\dagger}|\Psi_{N-1,m}\rangle\langle\Psi_{N-1,m}|\hat{d}_j|\Psi_{N,0}\rangle \mathrm{e}^{-i(E_{N,0}-E_{N-1,m})(t'-t)}, \tag{2.67}$$

where $\{|\Psi_{N\pm1,m}\rangle\}_m$ hereon denotes a complete set of eigenstates of $\hat{H}$ with $N\pm1$ particles. The formulation of the Green's function in terms of eigenstate energies is usually known as the *Lehmann representation*. Since the time-dependence is fully contained in the exponential, the Fourier transform of $G^{<}$ can be simply performed by replacing the latter with a Dirac delta, namely

$$G^{<}_{ji}(\omega) = 2\pi i\sum_{m}\langle\Psi_{N,0}|\hat{d}_i^{\dagger}|\Psi_{N-1,m}\rangle\langle\Psi_{N-1,m}|\hat{d}_j|\Psi_{N,0}\rangle\delta(\omega - E_{N,0} + E_{N-1,m}). \tag{2.68}$$

Let us note however that if the Fourier transform is performed on the entire Green's function [Eq. (2.64)] instead, particular attention must be dedicated to the treatment of the time integrals due to the presence of the Heaviside functions, $\vartheta(\pm t \mp t')$. In order to ensure the convergence of the latter is indeed essential to add a small imaginary energy, $\pm i\eta$, in the exponent, where η is a positive infinitesimal and the sign depends on the ordering of the time arguments. In particular, a positive imaginary energy is to be summed for $t > t'$, a negative one for $t < t'$. One can then define the *retarded* and *advanced* Green's functions, G^R and G^A, respectively as

$$\hat{G}^R(t,t') = \vartheta(t-t')\left[\hat{G}^{>}(t,t') - \hat{G}^{<}(t,t')\right], \tag{2.69}$$

$$\hat{G}^A(t,t') = -\vartheta(t'-t)\left[\hat{G}^{>}(t,t') - \hat{G}^{<}(t,t')\right] \equiv \left[\hat{G}^R(t',t)\right]^{\dagger}. \tag{2.70}$$

The Lehmann representation of the Fourier transform of such components can then be calculated to be

$$G^{R,A}_{ji}(\omega) = \sum_{m}\frac{\langle\Psi_{N,0}|\hat{d}_j|\Psi_{N+1,m}\rangle\langle\Psi_{N+1,m}|\hat{d}_i^{\dagger}|\Psi_{N,0}\rangle}{\omega - E_{N,0} + E_{N+1,m} \pm i\eta}. \tag{2.71}$$

It is important to notice that both functions have poles at frequencies corresponding to single particle excitations. However, all the poles of the retarded Green's function lie in the lower half of the complex frequency plane, while all the poles of G^A belong to the upper half. This suggests that the retarded and advanced functions yield information on two separate kinds of propagation. The Heaviside function in Eq. (2.69) implies that G^R contains the response to a perturbation at time t that is delayed by $t - t'$, in agreement with the *causality* principle. However, the same does not hold for the advanced component, which describes effects that seem to violate temporal causality. It is thus customary to interpret the retarded component as the propagator for occupied states (electrons), while the advanced component is associated to the propagation of unoccupied electronic states, also referred to as *holes*. The latter is an example of a *quasi-particle*, i. e. an emergent phenomenon that occurs in the context of a many-particle system. Such concept is often adopted in solid state physics since it allows to describe complex excitations of the interacting many-body system as objects that behave more similarly to non-interacting particles. In the case of stationary conditions one normally expresses all quantities in terms of the retarded GF, since the advanced component can be simply written as $G^A = [G^R]^\dagger$. Therefore, hereon we will work only with the retarded component, i. e. assuming for simplicity the notation $G \equiv G^R$ unless stated otherwise.

As the retarded and advanced components can be expressed one in terms of the other, the lesser Green's function can be written in terms of the greater and vice versa. In order to recover such relation one needs, however, to take into consideration an ensemble average on top of a quantum average. The latter allows us to introduce information on the occupation of the electronic states at a given energy, ω, and can be introduced considering Keldysh path segments parallel to the imaginary axis as mentioned in Section 2.2.1. All results on the Green's function as defined on the Keldysh contour still hold as presented for pure initial states, and for fermions one finds [see Section 6.3.1 of Ref. [81] for more details]

$$\hat{G}^{>}(\omega) = -e^{\beta(\omega-\mu)}\hat{G}^{<}. \tag{2.72}$$

Here we defined $\beta = (k_B T)^{-1}$ for a system at temperature, T, and with chemical potential, μ (k_B is the Boltzmann constant). Moreover, from the definitions of Eqs. (2.69), (2.70) it is straightforward to obtain the relation

$$\hat{G}^{>}(\omega) - \hat{G}^{<}(\omega) = \hat{G}(\omega) - \hat{G}^{\dagger}(\omega), \tag{2.73}$$

where G denotes the retarded Green's function so that $G^{\dagger}$ is the advanced one. The combination of the latter with Eq. (2.72) yields the important result

$$\hat{G}^{<}(\omega) = -f(\omega - \mu)\left[\hat{G}(\omega) - \hat{G}^{\dagger}(\omega)\right], \tag{2.74}$$

where $f(\omega) = [1 + \exp(\beta\omega)]^{-1}$ is the Fermi-Dirac distribution. The above attained equation embodies the so called *fluctuation-dissipation theorem* and provides an expression for the lesser Green's function given a chemical potential, μ, and the retarded Green's function of the system, G. Let us now recall that $G^{<}$ is strictly related to the density matrix [see Eq. (2.66)]. As a matter of fact, for a steady-state situation one can easily prove that

$$\rho = \frac{i}{2\pi}\int d\omega\; G^{<}(\omega). \tag{2.75}$$

Thus, the fluctuation-dissipation theorem allows us to calculate the density matrix of a system at steady-state given its retarded Green's function. This is probably the most important result of this subsection, since allows us to cast the solution of the transport problem analogous to the one found for the ground state case. In the next subsection we will show how the latter results can be adapted in the specific case of a two terminal device as defined at the beginning of the current section [see Fig. 2.2].

2.2.2 The SMEAGOL code

We will now focus our attention on describing the fundamental implementation scheme contained in the SMEAGOL code, mostly contained in Refs. [44, 16]. Once again, we do not aim to provide a rigorous derivation of all quantities, but rather to go through the relevant logical and procedural steps that are essential to detail the computational procedure. We begin by analysing the computational scheme adopted to calculate the surface self-energies, to then derive the operative formulas that yield

the population of the electronic states and the intensity of the electric current in the system in presence of a constant voltage.

2.2.2.1 Leads self-energies

The fundamental procedure that allows the practical solution of the transport problem consists in the calculation of the surface self-energies, $\Sigma_{L,R}$, introduced in Eq. (2.53). The first step of the algorithm is the solution of the Schrödinger equation for an infinite lead thought as a quasi-1D chain of principal layers, as introduced in Fig. 2.2. The eigenstates then yield the Green's function for the infinite system, from which the surface Green's function can be extracted by considering a truncation of the chain. Once the GF is known, the estimation of the surface self-energy as expressed in Eq. (2.54) is straightforward. In this context the surface self-energy contains information on how the semi-infinite chain couples to any material inserted at the truncation site. In principle, it must be evaluated individually for each scattering region. However, if one embeds a unit block of the leads at each side of the extended molecule, the calculation of the self-energies for some specific leads can be performed independently of the choice of scatterer. This procedure thus allows one to express the transport problem in terms of a finite number of degrees of freedom by performing a single preliminary calculation for a fixed lead.

We start by considering an infinite chain of principal layers, each described by an Hamiltonian, H_0. Each principal layer interacts only with its nearest neighbour principal layers, and such coupling is quantified by the matrices, H_1 and H_{-1}. Moreover, we assume these three Hamiltonians to be $N \times N$ matrices defined on a non-orthogonal basis with overlap matrix S, although the following results hold regardless of the shape of S. The total Hamiltonian of the system will have a traditional expression of the form,

$$H_{z,z'} = H_0\delta_{z,z'} + H_1\delta_{z,z'-1} + H_{-1}\delta_{z,z'+1}, \tag{2.76}$$

with z, z' labeling blocks along the transport direction, z. The overlap matrix consequently takes a form analogous to the latter. The eigenproblem of such Hamiltonian

has $2N$ solutions in the form of Bloch functions, $\psi_z = e^{ikz}\phi$. Each of these, denoted with ϕ_n, is associated to a complex wave vector, k_n, and satisfies the eigenvalue equation

$$(K_0 + K_1 e^{ik_n z} + K_{-1} e^{ik_n z})\phi_n = 0 \tag{2.77}$$

where $K_\alpha = H_\alpha - ES_\alpha$ ($\alpha = 0, \pm 1$). Note that for real energies $K_\alpha^\dagger = K_\alpha$. The functions ϕ_n are by definition the right eigenvectors of such equation, although similar results can be obtained for the left eigenvectors. One can then prove [84] that the Green's function of the infinite chain can be cast in the form

$$g_{z,z'} = \begin{cases} T_{z-z'}\mathcal{V}^{-1} & z \geq z' \\ \bar{T}_{z'-z}\mathcal{V}^{-1} & z \leq z' \end{cases} \qquad \text{with} \quad \mathcal{V} = K_{-1}(T^{-1} - \bar{T}), \tag{2.78}$$

where the transfer matrices T, $\bar{T}$ are defined in terms of right-going (Re $k_n > 0$) solutions, ϕ_n, and of the left-going (Re $\bar{k}_n < 0$) solutions, $\bar{\phi}_n$:

$$T_z = \sum_{n=1}^{N} \phi_n e^{ik_n z}(\phi_n^\dagger)^{-1} \quad \text{and} \quad \bar{T}_z = \sum_{n=1}^{N} \bar{\phi}_n e^{i\bar{k}_n z}(\bar{\phi}_n^\dagger)^{-1}. \tag{2.79}$$

Note that although the transfer matrices are always well defined, the same does not hold for their inverse matrices in cases where $K_{\pm 1}$ are singular. This problem can be overcome by making use of both left and right eigenvectors to define the Green's function. This workaround is simply a mathematical reformulation and does not add any further physical approximation. Here is therefore omitted and any interested reader can find further details in Refs. [16, 85].

The surface Green's function, $G_L^{z,z'}$, of a semi-infinite lead terminating at $z = z_0 - 1$ from negative z can then be determined from $g_{z,z'}$ imposing the condition $g_{z_0,z_0} = 0$, which yields [84]

$$G_L^{z,z'} = g_{z,z'} - g_{z,z_0}\mathcal{V}g_{z_0,z'}. \tag{2.80}$$

In analogy, the consideration of a semi-infinite chain truncated at $z = z_0$ that extends for $z > z_0$ will yield the Green's function of a right-hand side lead, G_R. The surface self-energies are then given by Eq. (2.54). Note that the most computationally expensive part of the above described procedure is the determination of the $2N$

eigenvectors, ϕ_n and $\bar{\phi}_n$, through the solution of an equation equivalent to Eq. (2.77). In this way one can examine the effects of the coupling between the extended molecule and two reservoirs, each at thermodynamic equilibrium. A current will flow across the system when the chemical potentials of the two leads, $\mu_{R,L}$, differ. If these are constant in time, the system will reach a stationary state and charge will redistribute within the scattering region. The purpose of the next subsections is to derive a computational scheme to self-consistently calculate the out-of-equilibrium occupation of electronic levels and an expression for the intensity of the electric current flowing across the EM.

2.2.2.2 Out-of-equilibrium density matrix

The construction of the density matrix for a system in equilibrium is rather straightforward. If the eigenstates of the Hamiltonian are known, the electronic states can be populated according to the Fermi-Dirac distribution and the density matrix is given by the definition provided in Eq. (2.43). However, the presence of a coupling between the system and a set of reservoirs introduces modifications in the occupations of the electronic states that are not easily quantifiable. Eq. (2.75) provides an alternative formula to evaluate ρ, although it requires the knowledge of a form for the lesser Green's function of the scattering region, $G_M^<$. To recover the latter, we partition the wavefunction of the entire system, ψ, as a vector with three components, ψ_L, ψ_M and ψ_R, which represent the part of ψ extending over the left-hand side lead, the extended molecule and the right-hand side lead, respectively. At this point we assume that the total density matrix of the scattering region, and consequently $G_M^<$, can be calculated as the sum of contributions resulting from the components $\psi_{L,R}$, namely

$$\rho_M = \rho_{ML} + \rho_{MR} = \frac{1}{2\pi i}\int d\omega\ G_M^<(\omega) = \frac{1}{2\pi i}\int d\omega\ [G_{ML}^<(\omega) + G_{MR}^<(\omega)]. \quad (2.81)$$

This assumption descends from the fact that the leads can be considered to have a density of states, which is continuous in energy given their infinite size. As a consequence, the scattering region will also have a continuum spectrum, if there are

no states localised in the extended molecule, i. e. in the absence of *bound states*. If the latter hypothesis is verified G_M will have no poles, hence the limit $\delta \to 0$ can be safely taken. However, bounds states are known to arise at interfaces in situations, where the leads have no open channels at a given energy or for specific k-points in the 2D Brillouin zone perpendicular to the transport direction. In these cases the limit for vanishing δ cannot be taken and an additional correction is to be included in order to take account for bound states. The procedure required to introduce the latter is extensively described in Ref. [16] and its description is here omitted, since it is not relevant for the scope of this thesis.

Therefore, we start from Eq. (2.81) and assume $\delta = 0$, so that for the lesser GF generated by states coming from the lead $\alpha = L, R$ we obtain

$$\begin{aligned} G^{<}_{M\alpha}(\omega) &= -f(\omega - \mu_\alpha)\left[G_{M\alpha} - G^{\dagger}_{M\alpha}\right] \\ &= -f(\omega - \mu_\alpha) G_{M\alpha}\left[(G^{\dagger}_{M\alpha})^{-1} - (G_{M\alpha})^{-1}\right] G^{\dagger}_{M\alpha}. \end{aligned} \tag{2.82}$$

Here, we have used the fluctuation-dissipation theorem of Eq. (2.74) for $G_{M\alpha}$ and reformulated it with the help of the identities $(G^{\dagger}_{M\alpha})^{-1}\, G^{\dagger}_{M\alpha} = 1 = (G_{M\alpha})^{-1}\, G_{M\alpha}$. We consider now the GF as written in Eq. (2.53). If we only consider contributions to the Green's functions originating from the lead α, in the limit $\delta \to 0^+$ we have

$$\begin{aligned} (G_{M\alpha})^{-1} &= (E + i\delta) S_M - H_M - \Sigma_R - \Sigma_L \\ &= E S_M - H_M - \Sigma_\alpha. \end{aligned} \tag{2.83}$$

The latter relation holds if the ψ_α component is not influenced by the self-energy Σ_β with $\beta \neq \alpha$, i. e. if ψ_L and ψ_R are not coupled to the right-hand side and left-hand side lead respectively. Note that both S_M and H_M are hermitian matrices, while Σ_α is not. Therefore we find

$$\begin{aligned} G^{<}_{M\alpha} &= -f(\omega - \mu_\alpha) G_{M\alpha}\left[(E S_M - H_M - \Sigma^{\dagger}_\alpha) - (E S_M - H_M - \Sigma_\alpha)\right] G^{\dagger}_{M\alpha} \\ &= -f(\omega - \mu_\alpha) G_{M\alpha}\left[\Sigma_\alpha - \Sigma^{\dagger}_\alpha\right] G^{\dagger}_{M\alpha} \\ &\equiv i f(\omega - \mu_\alpha) G_{M\alpha} \Gamma_\alpha G^{\dagger}_{M\alpha}. \end{aligned} \tag{2.84}$$

In the last step we have defined the rate function for each lead, $\Gamma_{L,R}$, which quantifies the rate of electrons flowing from each lead. If again the component of ψ on one lead is not influenced by the coupling with the other lead, products of the type $G_{M\alpha}\Gamma_\beta G^\dagger_{M\alpha}$ vanish for $\alpha \neq \beta$. As a consequence, we can sum the contributions to the Green's function from each lead to finally obtain

$$\rho_M = \frac{1}{2\pi}\int d\omega\; G^<_M(\omega) = \frac{1}{2\pi}\int d\omega\; G_M\left[f(\omega-\mu_R)\Gamma_R + f(\omega-\mu_L)\Gamma_L\right] G^\dagger_M. \quad (2.85)$$

The latter equation can be easily generalised to an arbitrary number of leads, and it is the final result that yields the electronic structure of the system in presence of coupling with external reservoirs.

2.2.2.3 Electric current and transmission

The last key quantities to be introduced to complete the overview of the SMEAGOL method for quantum transport are the transmission coefficients and the current intensity. When the difference between the chemical potentials of the two leads is constant in time, $\mu_L - \mu_R = eV$, a steady state current flows across the system. This implies that the total charge is constant in time within the scattering region. Moreover, since the leads are by construction in thermodynamical equilibrium, charge conservation for a wavefunction $\psi = (\psi_L, \psi_M, \psi_R)^T$ can be written in the form of a continuity equation, i. e.

$$\frac{dq_M}{dt} = \frac{\partial}{\partial t}\left[\psi^\dagger_M S_M \psi_M\right] = 0, \quad (2.86)$$

where we have omitted the contributions of $\psi_{L,R}$ to the charge of the EM. We now recall that the Schrödinger equation for the block Hamiltonian of the form (2.51) can be written as $K\psi = 0$, where $K = H - ES$. Thus, for the ψ_M component one finds

$$K_{LM}\psi_L + H_M\psi_M + K_{RM}\psi_R = ES_M\psi_M, \quad (2.87)$$

which allows us to cast the time derivative of ψ_M into the form

$$\mathrm{e}^{\frac{i}{\hbar}t} S_M \frac{\partial \psi_M}{\partial t} = -\frac{i}{\hbar} E S_M \psi_M = -\frac{i}{\hbar}(K_{ML}\psi_L + H_M\psi_M + K_{MR}\psi_R). \quad (2.88)$$

Eq. (2.86) together with the latter and its adjoint allows one to achieve the result

$$\begin{aligned}\frac{dq_M}{dt} &= \frac{i}{\hbar}(\psi_L^\dagger K_{LM}\psi_M - \psi_M^\dagger K_{ML}\psi_L) + \frac{i}{\hbar}(\psi_R^\dagger K_{RM}\psi_M - \psi_M^\dagger K_{MR}\psi_R) \\ &= I_L + I_R = 0. \end{aligned} \tag{2.89}$$

Here the two terms $H_M\psi_M$ cancel and the remaining ones have been rearranged to yield the contributions to the current coming from the left-hand side and the right-hand side lead, $I_{L,R}$. We remark that here the subscript L indicates quantities that contribute to the current flow from the left-hand side to the right-hand side, while R denotes quantities flowing in the opposite direction. As expected from the steady state conditions, the net probability current across the system is zero, i.e. the current coming from the left lead, I_L, has equal intensity but opposite sign to the one coming from the right lead, I_R. Now, the current from the left lead to the EM, I_L, is result of the propagation of wave functions originating in the left-hand side lead, ψ_L^L, that are connected to left-going wave functions in the right one, ψ_L^R. Here the superscripts, L, R, denote which lead the wave function, $\psi^{L,R}$, is electronic eigenstate for. These eigenfunctions can be written in terms of each of the states in the unperturbed leads, denoted as $\varphi^{L,n}$ and $\varphi^{R,n}$, using an expression for the retarded GF of the entire system discussed in Ref. [16], i.e.

$$\psi_L^{L,n} = \begin{pmatrix} \mathbb{1}_L + G_L K_{LM} G_M K_{ML} \\ G_M K_{ML} \\ G_R K_{RM} G_M K_{ML} \end{pmatrix} \varphi^{L,n}, \quad \psi_L^{R,n} = \begin{pmatrix} G_L K_{LM} G_M K_{MR} \\ G_M K_{MR} \\ \mathbb{1}_R + G_R K_{RM} G_M K_{MR} \end{pmatrix} \varphi^{R,n}. \tag{2.90}$$

These wavefunctions clearly extend over the entire system and each contain the coupling with each lead. These expressions can also be used to quantify the contribution to the current flowing from the left-hand side lead into the system for each state originating from the left- or right-hand side lead as

$$\begin{aligned} I_L^{L,n} &= \frac{i}{\hbar}(\psi_L^{L,n\dagger} K_{LM}\psi_M^{L,n} - \psi_M^{L,n\dagger} K_{ML}\psi_L^{L,n}) \\ &= \frac{1}{\hbar}\varphi^{L,n\dagger} K_{LM} G_M^\dagger \Gamma_R G_M K_{ML}\varphi^{L,n} \end{aligned} \tag{2.91}$$

and

$$\begin{aligned} I_L^{R,n} &= \frac{i}{\hbar}(\psi_L^{R,n\dagger} K_{LM} \psi_M^{R,n} - \psi_M^{R,n\dagger} K_{ML} \psi_L^{R,n}) \\ &= -\frac{1}{\hbar} \varphi^{R,n\dagger} K_{RM} G_M^\dagger \Gamma_L G_M K_{MR} \varphi^{R,n}. \end{aligned} \tag{2.92}$$

These are the probability currents flowing from the left-hand side lead to the scattering region due to the state n originating in the left and right lead respectively, at a given energy E. In order to obtain the total current intensity $I \equiv I_L = -I_R$ one needs to sum over all $N_{L,R}(E)$ unperturbed states of the leads and integrate over all possible energies. Note that Eqs. (2.91), (2.92) are already cast in a row vector - matrix - column vector product, which is equivalent to a trace hereby denoted as Tr . Eq. (2.91) can thus be employed to write

$$\sum_{n=1}^{N_L(E)} \eta_{n,L}(E) I_L^{L,n} = \mathrm{Tr}\left\{ K_{ML} \left[\sum_{n=1}^{N_L(E)} \eta_{n,L}(E) \varphi^{L,n} \varphi^{L,n\dagger} \right] K_{LM} G_M^\dagger \Gamma_R G_M \right\}, \tag{2.93}$$

where $\eta_{n,L}(E)$ is the occupation of the n-th unperturbed state of the left lead at energy E. As a matter of fact, the sum in the square bracket is easily identifiable with the equilibrium definition of the density matrix for the left lead for a given energy, $\rho_L(E)$. Therefore, it can be replaced with its non-equilibrium counterpart, $-2\pi i\ G_L^<$ [Eq. (2.66)]. We can then use the fluctuation-dissipation theorem given in Eq. (2.74) and the definition of surface self-energy provided in Eq. (2.54) to find

$$\begin{aligned} K_{ML}\rho_L K_{LM} &= -2\pi i\ K_{ML} G_L^< K_{LM} = 2\pi i\ f_L K_{ML} \left[G_L - G_L^\dagger \right] K_{LM} \\ &= 2\pi i \left[\Sigma_L - \Sigma_L^\dagger \right] = 2\pi \Gamma_L. \end{aligned} \tag{2.94}$$

In order to simplify the notation we have omitted all the energy dependence and adopted the notation $f_L = f(E - \mu_L)$. The argument of the trace in Eq. (2.93) can consequently be cast in the compact form $\Gamma_L G_M^\dagger \Gamma_R G_M$. A completely analogous procedure can be performed for states originating from the right lead. These results

can be used to finally write

$$\begin{aligned} I &= \int dE \left[\sum_{n=1}^{N_L(E)} \eta_{n,L}(E) I_L^{L,n} + \sum_{n=1}^{N_R(E)} \eta_{n,R}(E) I_L^{R,n} \right] \\ &= \frac{1}{h} \int dE \ \mathrm{Tr} \left\{ \Gamma_L G_M^\dagger \Gamma_R G_M \right\} [f_L - f_R] \\ &= \sum_{\sigma=\uparrow,\downarrow} \frac{1}{h} \int dE \ T^\sigma(E) [f_L - f_R] \equiv I^\uparrow + I^\downarrow. \end{aligned} \tag{2.95}$$

In the last line we have defined the transmission coefficient for the spin channel $\sigma = \uparrow, \downarrow$, $T^\sigma(E)$, by considering a partial trace over the spin degrees of freedom. This allows us then to separately analyse the current deriving from electrons with different spin states. Note that Eq. (2.95) gives us the probability current, I, while the electric current is found by multiplying by the electric charge, i.e. $I_e = eI$. Moreover, in the case of a constant transmission, $T^\sigma = T$, the electric current becomes $I_e = G_c T V$, where $G_c = e^2/h$ is known as the quantum conductance and V is the applied bias.

2.2.2.4 Self-consistency and influence of the bias voltage

The SMEAGOL code is an implementation of the results presented in this section and is based upon the framework of the SIESTA code. In other words, the transport properties are evaluated by generalising the SIESTA density matrix to include the modifications of the electronic structure introduced by an applied bias voltage, V. The essential steps of the self-consistent cycle are summarised in Algorithm 1. The surface self-energies that couple the scattering region to the contacts are calculated with preliminary, independent simulations. Given an input density matrix, often taken as the DFT (equilibrium) density matrix of the EM, the effective Hamiltonian of the open system is constructed and the bias is applied through an asymmetric shift, $\pm eV$, of the chemical potentials in the contacts. The retarded and lesser components of the Green's function are then constructed, and the non-equilibrium density matrix for each step is obtained by performing the energy integration of the Green's function. The latter must be performed both along the imaginary and real energy axes. The former integration evaluates the poles of the equilibrium

Algorithm 1 Self-consistent transport calculation for an applied voltage V

Require: surface self-energies of the leads, $\Sigma_{L,R}$ ▷ From leads calculation

ρ_{in} = DFT ground state of the EM

repeat ▷ SCF cycle begins

  for all $\mathbf{k}$, E **do** ▷ Points on BZ and energy sampling grids

    $\rho(\mathbf{k}) = \rho_{\text{in}}(\mathbf{k})$

    $H_{\text{eff}}(\mathbf{k}, E) = [H_M[\rho_{\text{in}}] + H(V) + \Sigma_L + \Sigma_R](\mathbf{k}, E)$ ▷ leads coupling and bias

    $G_M(\mathbf{k}, E) = [(E - i\delta)S - H_{\text{eff}}]^{-1}(\mathbf{k}, E)$ ▷ Retarded GF (Eq. 2.54)

    $G_M^<(\mathbf{k}, E) = [G_M(f_L\Gamma_L - f_R\Gamma_R)G_M^\dagger](\mathbf{k}, E)$ ▷ Lesser GF (Eq. 2.85)

  end for

  $\rho_{\text{out}} = (2\pi)^{-1} \sum_{\mathbf{k},\mathbf{E}} G_M^<(\mathbf{k}, E)$ ▷ Non-equilibrium density matrix

until $||\rho_{\text{out}} - \rho_{\text{in}}|| < tolerance$ ▷ Convergence condition

$T^\sigma(E) = \sum_{\mathbf{k}} \text{Tr}\{\Gamma_L G_M \Gamma_R G_M^\dagger\}(\mathbf{k}, E)$ ▷ k-points sum for transmission coefficients

$I^\sigma = \sum_E T^\sigma(E)[f_L - f_R]$ ▷ Energy integration in bias window for current

contribution to the density matrix, while the latter samples energy points within the bias window, $[E_F - eV, E_F + eV]$ [86]. Importantly, the Green's function is the smoother the further away from the real axis is calculated, hence a rather fine mesh is normally required for the real energy integration. Therefore, transport calculations performed in the limit of vanishing bias voltage, $V \to 0$, hereon called simply *zero-bias calculations*, are strikingly more computationally cheap than their finite bias counterpart. In fact, since the bias window is infinitesimal, the expensive real energy integration can be neglected within the zero-bias limit. Moreover, in many conditions finite bias calculations need additional care because they require the introduction of the so-called bound states corrections. The latter account for localised states in the EM for which there are no open channels in the leads with the same energy. These are not correctly estimated by the non-equilibrium Green's function within the assumptions here adopted, hence the NEGF must be reformulated accordingly.

The details of such modifications are not relevant for this thesis and will not be discussed, but can be found in Refs. [16, 71].

The additional complications and costs of finite bias calculations makes the use of the zero-bias limit preferable when the explicit bias dependence of the transport is not of interest. When the intensity of the voltage becomes relevant, it is often convenient to avoid full self-consistent finite bias calculations. Instead, it is possible to perform a self-consistent zero-bias calculation and introduce the bias dependence by a single self-consistent cycle step. The main difference between the two approaches consists in the determination of the electrostatic potential, V_H, across the scattering region. In a SCF calculation, V_H is given by how charge distributes in response to the bias and is updated together with the electron density. In contrast in a non-self consistent (NSCF) calculation the electrostatic potential is assumed to drop linearly across the scattering region, hence the profile of the electron density along the transport direction follows. This assumption is particularly justified in the case of magnetic tunnel junctions, where a finite bias (smaller than the band gap) is likely to cause little no redistribution of electrons within the insulator.

2.2.3 Summary

We have presented an introduction to the Keldysh formalism of Green's function, that allows one to study an electronic system under non-equilibrium conditions. Such formalism was then used to describe an implementation that yields the quantum-mechanical transport properties of nano-scale systems for a finite applied bias potential. We note that, by construction, our approach has the same applicability range of density functional theory. Hence, correct predictions of transport properties are only possible where the KS Hamiltonian and the chosen form of the XC potential correctly describe the ground-state electronic structure. Moreover, the transport formalism described above completely neglects inelastic scattering that may be caused by electron-phonon or electron-photon scattering. Nevertheless, the advantage of SMEAGOL with respect to other implementation is the possibility of calculations within the non-collinear spin approximation. This is of essential importance for the

estimation of the spin torques, as explained in the next Chapter.

Chapter 3

Spin torques in Fe/MgO-based magnetic tunnel junctions

"I think I can safely say that nobody understands quantum mechanics."

- Richard P. Feynman

The understanding of the material dependence of electronic and spin transport phenomena in multilayered systems is fundamental to the development of efficient spintronic applications. The performance of devices based on magnetic tunnel junctions heavily relies on efficient magnetisation switching, which is characterised by low switching times and critical currents. The key factor that controls the details of the current-driven magnetisation dynamics in a given free magnetic layer is the response of the static magnetic moments to the spin current, normally quantified by the notion of spin transfer torque (STT) introduced in §1.1.3 . The aim of this chapter is to investigate the alterations of the spatial profile of the spin torques in a magnetic layer introduced by structural disorder and variations of its chemical composition. The implications on the dynamics that different spatial torque profiles have on the resulting spin dynamics will then be analysed in the next Chapter by the means of atomistic simulations.

The simplest way to define the spin torques in a material is in terms of points of discontinuity in the spin current. This Chapter begins by adopting this point

of view to discuss some general properties of the STT and to predict the spatial trend from the band structure of the magnetic layer. This perspective, however, is only applicable in the case of uniform magnetic moments and in the absence of spin-orbit interactions. We continue by presenting the approach developed by Nuñez and MacDonald [87] that estimates the STT as the result of the interaction between the static magnetisation and the spin of the transport electrons. The rest of the Chapter contains results for the spin torques calculations in different MTJs performed with an implementation of such method within the SMEAGOL code. All the junctions considered here are based on the well-known Fe/MgO/Fe structure. This represents a simplified version of the prototypical CoFeB/MgO/CoFeB multilayers, where the complications introduced by the strong site-disorder in the CoFeB alloy is overcome by replacing it with the well-known bcc Fe structure. The similarities between the electronic structure of Fe and Co around the Fermi energy and the low concentration of B atoms at the interfaces with MgO imply a strong similarity between the features of spin transport in the two junctions. Nevertheless, disorder at the Fe/MgO interfaces is known to strongly affect the spin filtering effect, hence it is likely to play a role in the resulting magnetisation dynamics. We begin by considering a perfectly ordered Fe/MgO/Fe junction in order to set a point of reference and discuss the details of the approach and the simulation parameters. Next, a multi-scale approach to assess the influence of the deviations from structural epitaxy in the magnetisation switching is presented, together with the results of spin torques calculations in junctions with different barrier thicknesses and partially oxidised interfaces. In the last section the material composition of the free layer is altered in order to study the material dependence of the spin torques. The STT acting on a Fe free layer is then compared to that of Co and Ni, and the differences between the spatial profiles will be explained through the analysis of the state-symmetry resolved band structures of each material (calculated by Emanuele Bosoni). We note that in practice infinite magnetic layers cannot be realised, therefore we continue by considering the truncation of the magnetic free layer with a non-metallic (Cu) electrode. The atomic structure is here kept uniform across all the systems to allow for a better comparison

between the different cases. We conclude with an analysis of the transport properties and the spin torques acting on FePt, FePt/Fe and Fe/FePt/Fe free layers. The key difference between the different systems is the presence of the induced magnetic moment on Pt. This will allow us to study the spin torques in non-uniform magnetic structures.

3.1 Spin transfer torques: a theoretical overview

Spin transfer torques arise when the flow of a spin current is modified by the presence of magnetic textures where the atomic spins are misaligned with respect to the spin polarisation of the current. This happens in the case of currents flowing perpendicular to magnetic tunnel junctions with non-collinear magnetic layers, as well as when spin-polarised electrons pass through a non-uniform magnetic distribution. According to this definition the spin torque, $\boldsymbol{T}$, acting on a magnetic layer at a given position corresponds to the transverse component of the absorbed spin current, namely

$$\boldsymbol{T} = \boldsymbol{J}_s - \big(\boldsymbol{J}_s \cdot \boldsymbol{M}\big)\boldsymbol{M}. \tag{3.1}$$

Here the vectors $\boldsymbol{M}$ and $\boldsymbol{J}_s$ indicate the local direction and intensity of the static magnetisation and of the spin-polarisation of the current, respectively. This torque vector is the result of two contributions that can be defined in terms of the direction, $\boldsymbol{J}_0$, of the spin polarisation of the current when it enters the magnetic layer,

$$\boldsymbol{T} = T_{\parallel}\boldsymbol{M} \times (\boldsymbol{J}_0 \times \boldsymbol{M}) + T_{\perp}\boldsymbol{M} \times \boldsymbol{J}_0. \tag{3.2}$$

We remark that in the case of a magnetic tunnel junction $\boldsymbol{J}_0$ coincides with the direction of the magnetisation of the reference layer. The first term corresponds to the spin-transfer torque predicted by Slonczewski [24], also known as the in-plane torque since it induces the magnetisation vector to move within the plane defined by $\boldsymbol{M}$ and $\boldsymbol{J}_0$. This is the component that competes against the Gilbert damping term and it is responsible for the magnetisation switching. In contrast, the out-of-plane component, $T_{\perp}$, is often called field-like torque since it drives the magnetisation vec-

tor into a precession around $\boldsymbol{J}_s$, in analogy to the effects of an applied magnetic field. The out-of-plane torque can be related to the precession of the spins of the transport electrons caused by the exchange field generated by the static magnetisation. In particular, $T_\perp$ is caused by itinerant spins that either briefly precess at the non-magnet/ferromagnet interface while being reflected or that undergo a rotation while propagating in the ferromagnet [88, 89]. Such process clearly depends on interfacial scattering, in particular on the phase of the reflection coefficient. These quantities are particularly sensitive to the details of the electronic structure and their estimation within a ballistic transport approach may be far from their real value. This is because of the presence of inelastic scattering, temperature fluctuations and deviations from ideal interfaces. In some conditions the out-of-plane torque is of fundamental interest for device modelling. In fact, it is employed to manipulate the precession frequency in spin-torque oscillations (STOs) applications and can induce back-hopping in MTJs with an in-plane easy magnetisation axis [90, 91]. Nevertheless, it plays a minor role in the switching dynamics of perpendicular magnetic tunnelling junctions, that are the system at the centre of this thesis. For such reasons our analysis will focus on the material dependence of the in-plane torques, often neglecting the consequences of the out-of-plane component.

A qualitative insight into the microscopical phenomenon that gives rise to the spin torque can be obtained by considering an electron travelling in a non-magnetic material along the z axis and that is transmitted into a magnetic layer. Following Ref. [89] we assume that the spin quantisation axis is parallel to the static magnetisation, $\boldsymbol{M}$, which is along the z axis. Denoting with ϑ and φ the angles in the $x-z$ and $y-z$ planes, respectively, that the electronic spin forms with $\boldsymbol{M}$ while passing through the normal layer, the incident electron wave-function is simply

$$\psi_{\text{in}} = \begin{pmatrix} \cos\frac{\vartheta}{2}\exp\left\{-i\frac{\varphi}{2}+i\boldsymbol{k}\cdot\boldsymbol{r}\right\} \\ \sin\frac{\vartheta}{2}\exp\left\{+i\frac{\varphi}{2}+i\boldsymbol{k}\cdot\boldsymbol{r}\right\} \end{pmatrix}. \tag{3.3}$$

We note that in the normal layer the two spin channels propagate with the same wave-vector, $\boldsymbol{k}$. Since the transport properties are dominated by states at the Fermi energy, the modulus of such vector corresponds to the Fermi wave-vector $k_F = \sqrt{2m_e E_F/\hbar}$,

where E_F is the Fermi energy of the non-magnet. According to Eq. (3.1), spin torques arise in presence of a local discontinuity of the spin current. We focus here on the component of the spin current associated with electrons flowing along z and with spin aligned along the x direction (orthogonal to $\boldsymbol{M}$). The latter is defined as

$$J_{\mathrm{s}}^{x} = \frac{\hbar}{2}\sum_{\sigma\sigma'}\mathrm{Re}\left[\psi_{\sigma}^{*}\sigma_{x}^{\sigma\sigma'}\left(-\frac{i\hbar}{2m_e}\right)\frac{d}{dz}\psi_{\sigma'}\right]. \tag{3.4}$$

It is then straightforward to calculate the incident spin current,

$$J_{\mathrm{s,in}}^{x} = \frac{\hbar}{2}v_z\sin\vartheta\cos\varphi, \tag{3.5}$$

where $v_z = \hbar k_z/m_e$ is the electron velocity in the normal layer. Importantly, electrons transmitted to the ferromagnet will propagate differently depending on their spin orientation. We will denote with $\boldsymbol{k}^{\sigma}$ the wave-vector associated with the spin state $\sigma =\uparrow,\downarrow$ within the ferromagnet. Since majority- and minority-spin bands in the ferromagnet have different Fermi energies, E_F^{σ}, the modulus of these two wave-vector will also differ, $k^{\sigma} = \sqrt{2m_e E_F^{\sigma}/\hbar}$. Therefore, the transmitted wave-function is

$$\psi_{\mathrm{tr}} = \begin{pmatrix} t_{\uparrow}\cos\left(\frac{\vartheta}{2}\right)\exp\left\{-i\frac{\varphi}{2}+i\boldsymbol{k}^{\uparrow}\cdot\boldsymbol{r}\right\} \\ t_{\downarrow}\sin\left(\frac{\vartheta}{2}\right)\exp\left\{+i\frac{\varphi}{2}+i\boldsymbol{k}^{\downarrow}\cdot\boldsymbol{r}\right\}\end{pmatrix}, \tag{3.6}$$

where the spin-dependent transmission coefficients, $t_{\uparrow}$, $t_{\downarrow}$, will generally depend on the specific state of the electron before entering the ferromagnet and on the available states in the latter. Similarly to the incident spin current, the correspondent transmitted component can be found to be

$$J_{\mathrm{s,tr}}^{x} = \frac{\hbar}{4}(v_z^{\uparrow}+v_z^{\downarrow})\sin(\vartheta)\mathrm{Re}\left[t_{\uparrow}^{*}t_{\downarrow}\exp\{i\varphi+i(k_z^{\downarrow}-k_z^{\uparrow})z\}\right], \tag{3.7}$$

where $v_z^{\sigma} = \hbar k_z^{\sigma}/m_e$ is the electron velocity for spin-σ in the ferromagnet. We note that the wave-vector difference can be written in terms of the z components only as scattering from a flat interface conserves the components orthogonal to the transport direction. Similarly, the corresponding reflected component of the spin current can be estimated to be

$$J_{\mathrm{s,r}}^{x} = -\frac{\hbar}{4}|v_z|\sin\vartheta\mathrm{Re}\left[r_{\uparrow}^{*}r_{\downarrow}\exp\left[i\varphi\right]\right], \tag{3.8}$$

where r_σ is the reflection coefficient for the spin-σ state. A comparison between Eqs. (3.5), (3.7) and (3.8) shows that in this simple model the spin current develops a discontinuity that corresponds to the presence of a spin torque. The expressions derived here, despite their simplicity, allow us to infer which quantities are responsible for the spatial trend of the spin torques in the magnetic layer. These are encoded in the spatial dependence of the transmitted current in Eq. (3.7). First of all, $J_{\mathrm{s,tr}}$ is proportional to the sine of the angle between the spin of the incident electron and the static magnetisation, as the in-plane component included in Eq. (3.2). It is then clear that the transmitted spin current, hence the spin torque, is sensitive to phase factors introduced by scattering from an interface, here included in the transmission coefficients. Moreover, it can be evinced that the STT has spatial oscillations with a frequency controlled by the difference between the z components of the wave-vectors of the two spin states, Δk_z. The extension of this single-electron model to a distribution of electrons also indicates that the same quantity dictates the spatial decay of the spin torques within the ferromagnet. In such conditions the total spin current is given by an integral over all the possible parallel wave-vectors, $\boldsymbol{k}_\parallel^\sigma$. Ref. [89] then shows that a wide range of vectors $\boldsymbol{k}_\parallel^\sigma$ promotes the self-cancellations of the integrals defining the transverse spin components, namely $J^x_{\mathrm{s,tr}}$ and $J^y_{\mathrm{s,tr}}$. This induces the transmitted spin currents to asymptotically decay with a rate controlled by Δk_z calculated at the Fermi energy, namely

$$\lim_{z\to\infty} J^z_{s,tr}(z) \propto \frac{\sin\left[\left(k_z^\downarrow - k_z^\uparrow\right) z\right]}{\left(k_z^\downarrow - k_z^\uparrow\right) z}. \tag{3.9}$$

We note that this mechanism is possible only when both majority- and minority-spin channels are present at the Fermi energy in the magnetic layer. Namely, if transport electrons can propagate along the majority-spin channel only their spin will quickly align with the local quantisation axis. As a consequence, the misalignment of the spin current with the static magnetisation, i.e. the spin torque, vanishes within a few layers from the interface.

3.1.1 Going from the continuum scale to *ab-initio* modelling

All the considerations made above indicate that the material dependence of the spin-transfer torque is encoded in the details of the interfacial scattering and in the band structure of the ferromagnet around the Fermi energy. So far, the magnetic moment distribution was assumed to be uniform and the details of the atomic structure of the magnetic material were completely ignored. First principle methods offer a framework in which quantitative information on the material properties can be calculated down to the atomic scale. The combination of DFT and NEGF provides the capability of assessing the response of a material to the flow of a steady state current, as shown in the previous Chapter. We present here a method described in Refs. [87, 92] for a non-orthogonal basis set that is suitable for the SMEAGOL code. We also present here an adaptation of the approach described in Refs. [87, 92] that is suitable to be implemented in the SMEAGOL code. Such method evaluates the spin torques by quantifying the interaction between the local static magnetisation and the non-equilibrium spin accumulation, rather than following the flow and conservation of the spin-angular momentum through the system, as discussed before. Thus, *ab-initio* theory enables the study of spin torques acting on generally complex magnetic structures, such as antiferromagnetic metals, and current-induced torques beyond spin-transfer [93].

The final objective of the approach is to express the interaction between the local magnetic moments and the spin current in terms of the electronic degrees of freedom. The motion of an electronic system can be analysed by the means of the quantum Liouville equation,

$$i\hbar\frac{\partial\hat{\rho}^{\sigma\sigma'}}{\partial t} = \left[\hat{H},\hat{\rho}\right]^{\sigma\sigma'}, \tag{3.10}$$

where $\hat{\rho}$ is the density matrix operator defined in Eq. (2.43) and $\hat{H} = \hat{H}[\hat{\rho}]$ is here assumed to be the Kohn-Sham Hamiltonian, although the approach is valid for a general Hamiltonian that is variationally dependent on the electron density. The first step consists in isolating the contributions to the system dynamics that cause a change in the orientation of the direction of the electronic spins, i.e. that can be

interpreted as spin torques. Each operator, $\hat{O}$, will be expanded in the SIESTA basis, $\{|\varphi_\mu\rangle\}_\mu$, with overlap matrix, $S_{\mu\nu} = \langle\varphi_\mu|\varphi_\nu\rangle$, and the spin degrees of freedom will be expressed within the Pauli notation introduced in Eq. (2.23). For simplicity, we omit here the dependence upon the Brillouin zone wave-vectors, $\boldsymbol{k}$. With such conventions, the matrix elements of the density matrix and of the Hamiltonian operators can be written as

$$\rho_{\mu\nu}^{\sigma\sigma'} = n_{\mu\nu}\delta^{\sigma\sigma'} + \boldsymbol{\mu}_{\mu\nu}\cdot\boldsymbol{\sigma}^{\sigma\sigma'} \qquad \text{and} \qquad H_{\mu\nu}^{\sigma\sigma'} = h_{\mu\nu}\delta^{\sigma\sigma'} + \boldsymbol{\Delta}_{\mu\nu}\cdot\boldsymbol{\sigma}^{\sigma\sigma'}, \tag{3.11}$$

where

$$n_{\mu\nu} = \sum_\sigma \rho_{\mu\nu}^{\sigma\sigma} \qquad \text{and} \qquad \boldsymbol{\mu}_{\mu\nu} = \sum_{\sigma\sigma'} \rho_{\mu\nu}^{\sigma\sigma'}\boldsymbol{\sigma}^{\sigma'\sigma}. \tag{3.12}$$

Although the Hamiltonian operator can take analogous definitions for its spin-independent and -dependent contributions, we choose to define the latter in terms of the functional derivative of the exchange-correlation energy with respect to the different components of the density matrix, as

$$h_{\mu\nu} = \frac{\delta E_{\mathrm{XC}}}{\delta n_{\mu\nu}} \qquad \text{and} \qquad \boldsymbol{\Delta}_{\mu\nu} = \frac{\delta E_{\mathrm{XC}}}{\delta \boldsymbol{\mu}_{\mu\nu}}. \tag{3.13}$$

This helps to elucidate the physical meanings of such potentials. In particular, $\boldsymbol{\Delta}$ embodies the interaction potential generated by the static magnetisation and will be of central importance in the calculation of the spin torques. As already pointed out in §2.1.2, local approximations of the exchange-correlation fields, such as the LDA, yield magnetisations that are always parallel to the local exchange-correlation field. This implies that the exchange field, $\boldsymbol{\Delta}$, will be everywhere proportional to the local magnetisation, namely

$$\boldsymbol{\Delta} = \Delta_0(\rho^0, |\boldsymbol{\mu}|)\frac{\boldsymbol{\mu}}{|\boldsymbol{\mu}|}, \tag{3.14}$$

with Δ_0 an appropriate parametrisation of the exchange correlation potential. By inserting the expansions in Eq. (3.11) into the Liouville equation (3.10) we obtain

$$i\hbar\frac{\partial n}{\partial t} + i\hbar\frac{\partial \boldsymbol{\mu}}{\partial t}\cdot\boldsymbol{\sigma} = \Big[h, n\Big] + \Big[h, \boldsymbol{\mu}\Big]\cdot\boldsymbol{\sigma} + \Big[\boldsymbol{\Delta}, n\Big]\cdot\boldsymbol{\sigma} + 2i(\boldsymbol{\Delta}\times\boldsymbol{\mu})\cdot\boldsymbol{\sigma}, \tag{3.15}$$

where the orbital dependencies are omitted for simplicity. The last term is obtained by using the relation

$$\begin{aligned}\Big[\Delta^\alpha\sigma^\alpha, \mu^\beta\sigma^\beta\Big] &= \Delta^\alpha\mu^\beta\delta_{\alpha\beta} + i\varepsilon_{\alpha\beta\gamma}\Delta^\alpha\mu^\beta\sigma^\gamma - \mu^\beta\Delta^\alpha\delta_{\alpha\beta} - i\varepsilon_{\beta\alpha\gamma}\mu^\beta\Delta^\alpha\sigma^\gamma \\ &= \Big[\Delta^\alpha, \mu^\alpha\Big]\delta_{\alpha\beta} + 2i\big(\boldsymbol{\Delta}\times\boldsymbol{\mu}\big)^\gamma\cdot\sigma^\gamma, \end{aligned} \tag{3.16}$$

where $\alpha,\beta,\gamma = x,y,z$. The first term in the last equation vanishes because of Eq. (3.14). The first terms on the right- and left-hand sides of Eq. (3.15) govern the dynamics of the spin-independent part of the density matrix. The second and third terms on the left-hand side represent the spin-current flux and do not involve any modification of the spin direction, hence do not contribute to the spin torques. Finally, the remaining term expresses the interaction exerted by the static magnetisation, $\boldsymbol{\Delta}$, onto the local spin density, $\boldsymbol{\mu}$. Thus, the general matrix element of the spin torques can be written as

$$\boldsymbol{T}^{\mathrm{tot}}_{\mu\nu} = \frac{2}{\hbar}\left(\boldsymbol{\Delta}\times\boldsymbol{\mu}\right)_{\mu\nu}. \tag{3.17}$$

We note that it is possible to prove that the total spin torques evaluated within density functional theory are identically zero. This result is known as the zero-torque theorem, and it stems from the fact that DFT considers the equilibrium ground-state electron density. This generally holds for the total torque, although it does not exclude the presence of local torques. Nevertheless, in case of local XC potentials the local spin torques also vanish in a system in equilibrium. In fact, the relation expressed in Eq. (3.14) indicates that the cross product between $\boldsymbol{\Delta}$ and $\boldsymbol{\mu}$ is identically zero. We can now limit our attention to systems where the electric current does not significantly alter the electronic structure, hence the order parameter can be assumed to have an adiabatic motion and change slowly in time with respect to the electronic system. In other terms, we assume that the density matrix can be partitioned into an equilibrium, $\hat{\rho}_{\mathrm{eq}}$, and a transport contribution, $\hat{\rho}_{\mathrm{tr}}$, such that the latter component has negligible influence to the order parameter,

$$i\hbar\frac{\partial\hat{\rho}^{\sigma\sigma'}}{\partial t} = \Big[\hat{H}[\hat{\rho}], \hat{\rho}_{\mathrm{eq}} + \hat{\rho}_{\mathrm{tr}}\Big]^{\sigma\sigma'} \simeq \Big[\hat{H}[\hat{\rho}], \hat{\rho}_{\mathrm{eq}}\Big]^{\sigma\sigma'}. \tag{3.18}$$

As a consequence, the current-induced contribution to the electron density, $\hat{\rho}_{\mathrm{CI}}$, is given by

$$i\hbar\frac{\partial\hat{\rho}^{\sigma\sigma'}_{\mathrm{CI}}}{\partial t} = \Big[\hat{H}[\hat{\rho}] - \hat{H}[\hat{\rho}_{\mathrm{eq}}], \hat{\rho}_{\mathrm{eq}}\Big]^{\sigma\sigma'}. \tag{3.19}$$

At this point, the same decomposition done in Eq. (3.15) can be performed for this latter equation of motion. Hence the current-induced torques can be written as

$$\boldsymbol{T}_{\mu\nu} = \frac{2}{\hbar}\big[\boldsymbol{\Delta}_{\mathrm{tr}} \times \boldsymbol{\mu}\big]_{\mu\nu} = \frac{2}{\hbar}\big[(\boldsymbol{\Delta}[\hat{\rho}] - \boldsymbol{\Delta}[\hat{\rho}_{\mathrm{eq}}]) \times \boldsymbol{\mu}\big]_{\mu\nu}. \tag{3.20}$$

These spin torques are the result of the exchange field generated by the transport electron density, $\hat{\rho}_{\mathrm{tr}} = \hat{\rho} - \hat{\rho}_{\mathrm{eq}}$, acting on the equilibrium electrons, represented by $\hat{\rho}_{\mathrm{eq}}$. This must equal the interaction between the equilibrium exchange field and the transport electron density, since the torque in the system is globally conserved. This simple rearrangement allows us to obtain a formula that is simple to implement within SMEAGOL. In fact, the static exchange field can be taken as the spin-dependent Hamiltonian, result of a transport calculation in the limit of vanishing bias voltage, $\boldsymbol{\Delta}_{\mathrm{eq}} \equiv \boldsymbol{\Delta}(0)$. In turn, the quantities related to the transport electrons can be calculated as the difference between the results of a $V = 0$ and a finite bias calculation. Finally, the partial trace over all the orbitals centered on each atom, a, yields an expression for the bias-dependent spin torque acting on a generic atomic position,

$$\boldsymbol{T}_a(V) = \frac{2}{\hbar}\sum_{\mu\in a,\nu,\eta} \boldsymbol{\Delta}_{\mu\nu}(0) \times \big(\boldsymbol{\mu}_{\eta\mu}(V) - \boldsymbol{\mu}_{\eta\mu}(0)\big) S_{\eta\nu}. \tag{3.21}$$

As a consequence, each finite-bias spin torque calculation will require two calculations to be performed for each magnetic configuration: one within the $V = 0$ limit and one at a finite bias, V.

The details of the bias dependence of the spin torque is, in principle, different for different systems (further discussion on this will be presented in the next section). This makes the comparison between the spatial profiles of the STT characteristics of each junction more complicated. Therefore, it is useful to define the torque linear response to a infinitesimally small bias, usually called *torkance*, as

$$\boldsymbol{\tau}^a \equiv \frac{d\boldsymbol{T}_a}{dV} = \frac{2}{\hbar}\sum_{\mu\in a,\nu,\eta} \boldsymbol{\Delta}_{\mu\eta}(0) \times \frac{d\boldsymbol{\mu}_{\eta\mu}}{dV}\Big|_{V=0} S_{\eta\nu}. \tag{3.22}$$

Here the transport spin density is replaced by the derivative of the spin-dependent part of the density matrix with respect to the bias centered at $V = 0$. Importantly, the estimation of the torkance requires a single zero-bias calculation, where the bias derivative is calculated within finite differences using an auxiliary density matrix obtained by applying a tiny bias non-self-consistently. The torkance is equivalent to the finite bias torque (apart from a constant) as far as the electric current depends linearly on the applied bias voltage. However, it can be more sensitive to simulation parameters and the definition here adopted was shown to yield an out-of-plane torkance that is not gauge invariant for asymmetric junctions [94].

3.2 The Fe/MgO/Fe junction

We begin by discussing the features of the spin torques calculated with the approach above presented on the prototypical Fe/MgO/Fe MTJ. The ground state and transport properties in such system were thoroughly analysed with the same implementation in previous works [16, 71, 95, 96, 97]. In particular, all simulation parameters here used were chosen according to the study contained in Ref. [71]. Hence, we will limit the discussion of ground state and general transport properties to the definition of the main features of this system as captured by the SMEAGOL code, focusing on the aspects that are relevant to the spin torques.

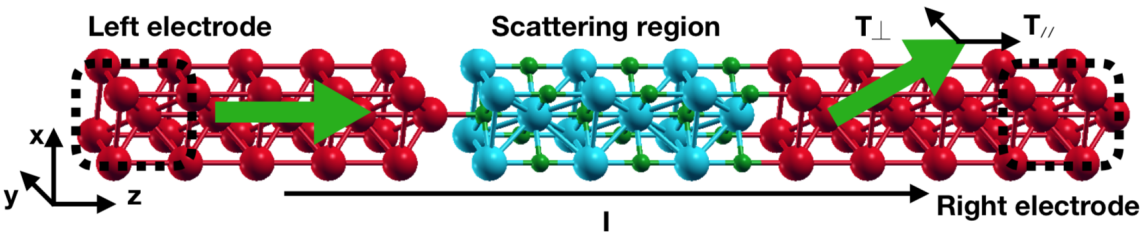

Figure 3.1: Setup for a spin torque calculation of a Fe/MgO/Fe junction. The different color of the spheres correspond to different atomic species: red for Fe, blue for Mg and green for O. The green arrows represent the magnetisation of the two magnetic layers.

The typical junction considered in a transport calculation is represented in Fig. 3.1. The Fe and MgO layers are considered in their equilibrium crystal structures, bcc and salt-like, respectively. A number of different studies have been performed on the formation of Fe/MgO interfaces, see e. g. Ref. [98] and references therein. The magnetic electrodes are generally grown in the (001) direction, and from the literature it is clear that MgO barrier crystallises along the same direction but with the in-plane lattice vectors that are rotated by 45° with respect to the lattice vectors of bcc Fe. In particular, the equilibrium interfacial configuration was shown to have the Fe atoms that are closest to the interface facing O atoms. We remark that the Fe/MgO and MgO/Fe interfaces considered here (and shown in Fig. 3.1) are identical, although they might appear different at a first glance. In fact, one might argue that the positions of the O atoms at the two interfaces differ by a shift of $(a/2, a/2, 0)$, with a here denoting the in-plane lattice constant for the stack. This is because the in-plane positions of O and Mg atoms alternate after each atomic plane, therefore a stack composed of an even number of monolayers naturally has asymmetric interfaces. Nevertheless, one must note that the left- and right-hand side electrodes were also truncated in different ways, so that the atomic configuration at both interfaces has O sites directly facing Fe sites, as predicted in the literature. It was also shown that in real junctions a small difference between the in-plane lattice vectors of the top and bottom electrodes often appears because of the strain due to the lattice mismatch between Fe and MgO ($\sim 3.9\%$). However, including such effect would a require consideration of a large cross section, for which the calculation becomes infeasible. In contrast, the assumption that the in-plane lattice vectors are uniform throughout the system allows us to consider periodic boundary conditions along the directions perpendicular to transport and use a minimal unit cell in the direction perpendicular to the transport. Since the junction is assumed to be sandwiched between two semi-infinite bulk Fe leads, the in-plane constant of the entire stack is set to the equilibrium lattice constant of *bcc* Fe, $a_{\mathrm{Fe}} = 2.866\,\text{Å}$. This sets the in-plane lattice constant of MgO to $a_{\mathrm{MgO}} = \sqrt{2}a_{\mathrm{Fe}} = 4.05\,\text{Å}$, against its equilibrium experimental value of 4.21 Å. The out-of-plane lattice constants for both materials

are chosen so to keep the unit cells cubic, i.e. $c_{\mathrm{Fe}} = a_{\mathrm{Fe}}$ and c_{MgO} =2.027 Å. The typical junction is then constructed with the magnetic layers formed by 5 monolayers (MLs) of bcc Fe and the insulating barrier containing 6 MLs (3 unit cells $\sim$ 1.2 nm) of MgO. We remark here that the 4 atomic layers at the two boundaries of the scattering region have, by construction, the same electronic structure of the bulk material to ensure continuity with the semi-infinite electrodes. This might truncate the tail of long decaying spin torques, hence in some cases thicker magnetic layers are considered.

All calculations are performed by using a cutoff of 600 Ry for the real space mesh and the 2D Brillouin zone (BZ) perpendicular to the transport direction is sampled with a 15 $\times$ 15 Monkhorst pack grid. In general, the use of a GGA exchange-correlation functional is more convenient than an LDA functional for calculations of *bcc* Fe. This is because structure relaxations performed with LDA wrongly estimate Fe to have a *fcc* equilibrium crystal structure, in contrast to the case of GGA. Nevertheless, the band structure calculated within LDA assuming the correct crystal structure has a good agreement with the experimental band structure. In addition, the generalisation of the GGA functional to non-collinear spin calculations is not trivial, and such potentials were not extensively tested in the version of SMEAGOL employed for this thesis. For such reasons, the LDA approximation for the exchange-correlation functional is chosen for all the systems considered in this Chapter. The interested reader can find an extensive study of the electronic and transport properties of Fe/MgO/Fe calculated with both LDA and GGA in Ref. [71]. A double-ζ basis is adopted for s and p orbitals of both Mg and O, with first-ζ orbitals with radial cutoff of 4.0 Å. The calculated band gap at the Γ point is of 4.64 eV, that is significantly smaller than the experimental value of 7.8 eV. Nevertheless, the LDA band gap remains rather large, hence this underestimation will not qualitatively influence the transport properties for small bias voltages. The s orbitals of Fe sites are expressed by a double-ζ polarised (DZP) basis with cutoff radius for the first-ζ of 6.5 Å, while the d orbitals have a double-ζ basis with cutoff radius 5.6 Å. The transmission is evaluated on 500 energy points distributed within $\pm$0.5 eV from the

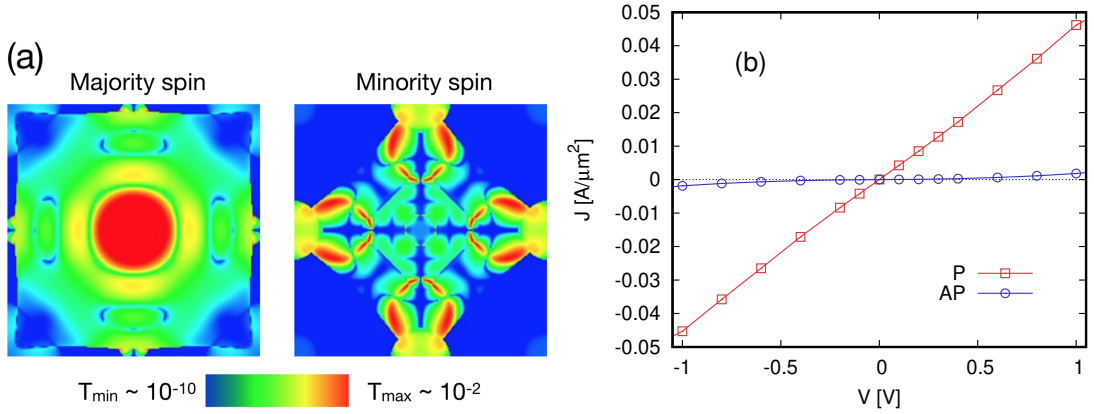

Figure 3.2: Panel (a) : majority (left panel) and minority (right panel) spin transmission coefficients at the Fermi energy plotted over the 2D Brillouin zone in Fe/MgO/Fe for parallel (P) magnetisations. The colored scale indicates the intensity of the coefficient at a given k-vector (in logarithmic scale), with Γ positioned at the centre of each square. Panel (b) : current density for different voltage in Fe/MgO/Fe for parallel (P) and antiparallel (AP) magnetisations.

Fermi energy, using a finer k-points mesh (typically 100×100) than the one employed during the self-consistent cycle.

Fig. 3.2 shows the transmission coefficients resolved over the 2D Brillouin zone calculated at the Fermi energy for a Fe/MgO/Fe junction with parallel (P) magnetisations in the zero-bias limit. The color scale indicates the different intensity of the transmission in a log scale for majority (left-hand side panel) and minority spins (right-hand side panel) depending on the position in the Brillouin zone, with Γ located at the centre of the squares. It is clear that the transmission for majority spins mostly occurs at the center of the Brillouin zone, where, in contrast, the minority spins is strongly suppressed. In other terms, the transport in Fe/MgO/Fe can be regarded as quasi-one dimensional, since electrons propagating in directions that are not parallel to the transport direction are not likely to be transmitted through the insulator. Such feature is a consequence of the spin filtering performed by MgO, that also implies that the current is populated solely by electrons with Δ_1 symmetry. Another important message to be extracted from these results is that the vast

majority of the electronic states that populate the current are characterised by very long wavelengths. This implies that the propagation of the current is not influenced by local alterations of the interface, therefore the ideal interfaces here considered constitute a fair approximation for a realistic interface. These characteristics are maintained when a finite bias is applied, as shown in Ref. [71]. Moreover, the current grows linearly with the intensity of the applied voltage [Fig. 3.2 (b)]. This also holds for the anti-parallel (AP) configuration, although small deviations to the linear dependence appear at lower voltages.

We move now to discuss the spin torques acting on the Fe/MgO/Fe junction. In order for the STT not to be identically zero, the magnetisation of the two magnetic layers need to be misaligned with respect to each other. Since here spin-orbit coupling is neglected, the spin quantisation axis of each layer is independent from the orientation of the crystal structure. Hence, the only relevant quantity is the angle, ϑ, between the magnetisation vector of the left-hand-side magnetic layer, assumed to be pinned along z, and the one of the right-hand-side layer, that by convention lies in the $x-z$ plane. With this notation, the in-plane torque is parallel to the z axis, while the out-of-plane corresponds to the y direction, as shown in Fig. 3.1. All results presented here will assume that the two magnetisations are orthogonal, i.e. $\vartheta = \pi/2$. The calculated spin torques for different angles in fact show to follow the same angular dependence given in Eq. (3.2) for similar systems [99]. Fig. 3.3 displays the calculated out-of-plane and in-plane components of the spin torques acting on a Fe/MgO/Fe junction for $\vartheta = \pi/2$. The out-of-plane component (panel (a)) is non-zero in the proximity of both interfaces between Fe and MgO, which are here indicated by the two vertical lines. This is probably due to the precession of the reflected and transmitted spins induced by the exchange fields of the two magnetic layers. We note that the trend in the torkance (black squares) is in this case different from the one of its finite-bias counterpart (blue circles), that in this case is calculated with a bias voltage of 0.5 V. In particular, the zero-bias torque is almost perfectly symmetric in the two magnetic layers and alternates sign in adjacent monolayers in proximity of the interfaces. In contrast, the finite-bias torque has opposite signs at

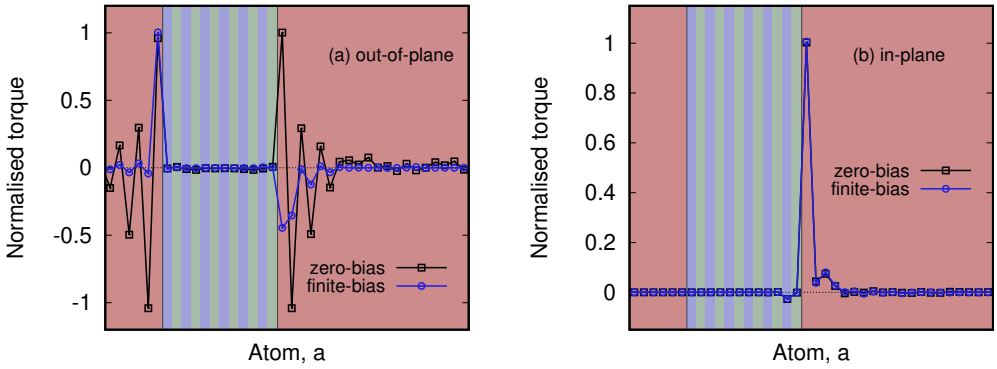

Figure 3.3: In-plane [panel (a)] and out-of-plane [panel (b)] components of the torkance in Fe/MgO/Fe in the zero-bias limit (black squares) and for a bias voltage of 0.5 V (blue circles). These results were obtained for an angle $\vartheta = \pi/2$ between the magnetisations of the reference and free layer.

the two different interfaces and both its intensity and decay range differ in the two magnetic layers. The same considerations, however, do no hold for the in-plane components. In fact, in this case the finite-bias torque and the torkance have the same trend. In particular, the spin-transfer torque can be found only at the MgO/free layer interface, where the spin polarisation of the current is orthogonal to the local magnetisation. While the field-like torkance oscillates in sign and vanishes within few atomic planes, the in-plane component is sharply peaked at the interface and has a faster decay rate. We note that the spatial dependence of the spin torques are somewhat in contrast with the findings of Ref. [100], where the decay is less pronounced and the two components are of similar magnitude. Nevertheless, in such work the 2D Brillouin zone is sampled only at the Γ point, that is a severely reduced mesh with respect to that adopted here. Moreover, the torkances are studied in a Fe/MgO/Fe junction sandwiched between Cu contacts, fact that can significantly alter the spatial trend of the STT, as will be shown later.

The total magnitude of the two components for different biases is shown in Fig. 3.4. We note that the in-plane torque depends linearly on the bias voltage, in contrast to the quadratic dependence of the out-of-plane component. This is in

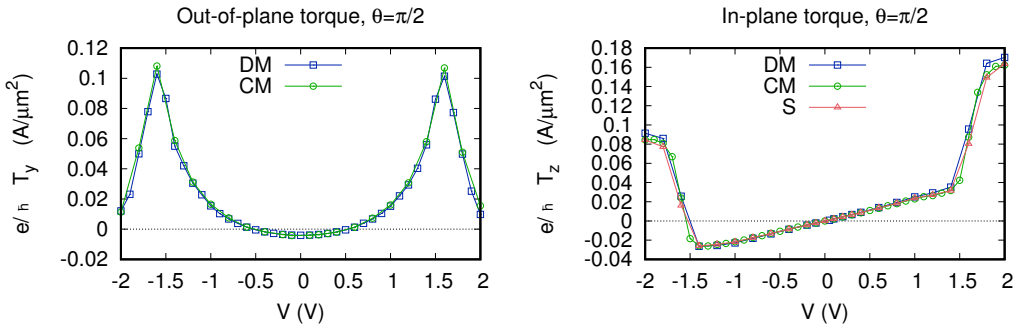

Figure 3.4: Bias dependence of the out-of-plane (a) and in-plane (b) component of the spin torque in Fe/MgO/Fe integrated over the free layer. The spin density method (DM) presented in the previous section is compared to the prediction obtained by the means of conservation of the spin current (CM) and within the Slonczewski model (S).

agreement with results obtained in other works (see e.g. [101]), although it was shown that the quadratic bias dependence is a feature of symmetric interfaces [102, 103]. We also note that for very small biases ($|V|$ <0.1 V) the in-plane and out-of-plane torques have similar magnitude, although the damping-like torque becomes stronger by more than an order of magnitude for higher biases. The sudden change in the $\tau(V)$ behaviour around 1.5 V can be attributed to a significant increase of the current intensity for the minority spin channel for V >1.5 V. In general, the details the bias dependence of transport-related properties in Fe/MgO/Fe have been shown to strongly depend on the line-width of resonant interfacial states [71].

In conclusion, the in-plane spin torques in Fe/MgO/Fe vanish within few atomic layers from the insulator/free layer interface. The out-of-plane component has longer decay and generally lower intensity for low bias voltages. The latter then plays a minimal role in determining the switching properties characteristic of a given materials stack, as will be also shown in more detail in Chapter 4. For such reasons, the analysis in the next sections will only treat the in-plane component of the torque.

3.3 Disorder at the Fe/MgO interface

The analysis of disorder effects in Fe/MgO/Fe offers a formidable challenge from both the theoretical and experimental points of view. In fact, disorder effects are most relevant when they are located in proximity of the metal/insulator interfaces, hence in regions that are embedded in the device and therefore difficult to probe. The most commonly studied effect has probably been the formation of an interfacial FeO layer, that was firstly observed by the means of surface X-ray diffraction [22]. This was demonstrated to strongly suppress the efficiency of the spin filtering and hence of the TMR [23]. In practice, it was shown that the interfacial oxidation is generally not uniform and the oxygen concentration varies depending on the growth technique [104]. The same work also showed that the MgO barrier thickness is not

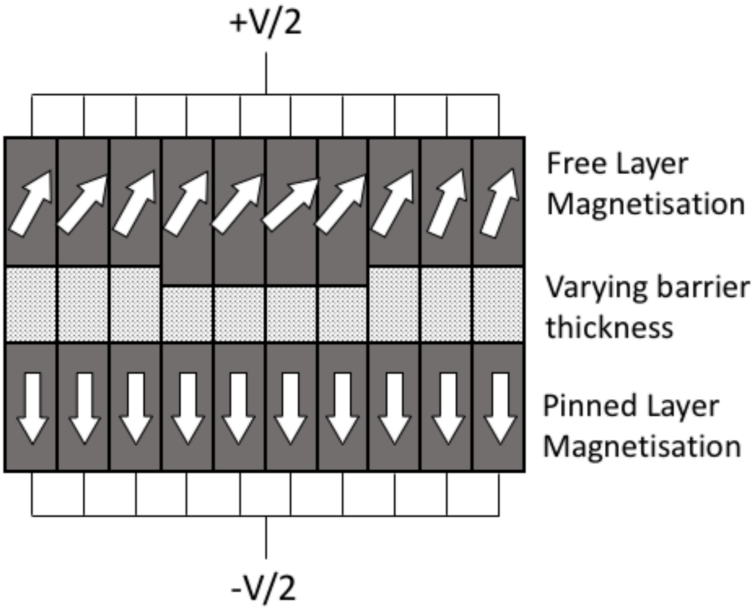

Figure 3.5: Schematic representation of the cell adopted to simulate a disordered barrier. The total cross section is divided into a number of different regions in which the spin currents flow independently (in parallel). This allows us to combine the results of spin torque calculations with different barriers and characterise the spin torques on a larger system.

constant but varies throughout the cross section. The concentration of defects is normally different for the top and bottom interface because of the slight change in the in-plane lattice constant and the diffusion of different elements from the substrate or capping layers. These discrepancies are normally not desirable since asymmetric interfaces are proven to drastically alter the spin currents, yielding in some cases even negative TMRs [105]. Other disorder effects studied in previous works include oxygen vacancies in the MgO barrier [97], misfit dislocations and contamination from impurities (see Refs. [21, 106] for more details). In general, the long wavelengths of the transport electrons imply that the transport properties should not be altered by spatial roughness of the interface. Nevertheless, disorder at the interface may become relevant if, for example, it induces the presence of additional transport channels, therefore significantly modifying the features of the tunnelling current.

Having strong non-uniformity in interfacial defects in Fe/MgO implies that a wide cross section is to be considered in order to realistically reproduce the sparsity of disorder observed in experiments. Such sizes are generally too large to be considered in first principles simulations. Nevertheless, the fact that the transmitted electrons

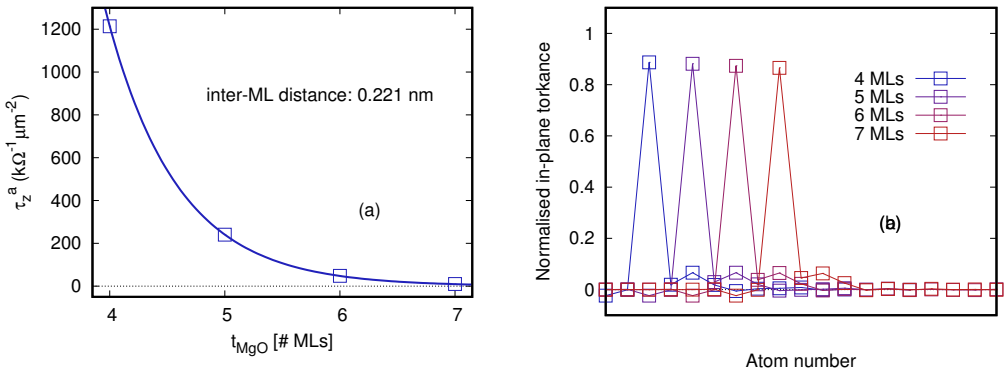

Figure 3.6: Comparison of the in-plane torkance in Fe/MgO/Fe for barriers formed by 4,5,6 and 7 MgO MLs. Panel (a) shows the in-plane torkances summed over the free layer. The line is the result of our best fit to the function $a\exp(-b*x)$, with $a = 787116$ in the units of torkance and $b = 1.61864$. Panel (b) contains the spatial distribution of the normalised in-plane torkance at the insulator/metal interface.

travel parallel to the transport direction allows us to consider the cross section as a number of smaller cells where the current flows relatively independently, namely in parallel [Fig. 3.5]. In this work we consider a Fe/MgO/Fe MTJ where different regions contain different kinds of disorder and analyse the effects on the spin dynamics within the atomistic model described in the next chapter. In particular, we consider regions with different barrier thicknesses and with partially (25%) oxidised MgO/Fe interfaces. We present here the results of spin torques calculations on each different structure, while the details and results of the spin dynamics simulations can be found in §4.3.2.

Fig. 3.6 displays the results of torkance calculations on Fe/MgO/Fe junctions with barriers formed by 4, 5, 6 and 7 monolayers (MLs), i.e. for thicknesses ranging from 0.663 nm to 1.326 nm. Since the current is in the tunnelling regime is maintained, the transmitted current decays exponentially with increasing thickness and the total torkance [panel (a)] follows the same trend. Nevertheless, the spatial decay of the in-plane torkance remains the same for all the barriers considered, as shown in panel (b). Therefore, we can conclude that fluctuations in the barrier thickness overall alter the net amount of torque acting on the free layer but do not alter the spatial dependence of the spin torques. This however does not hold for the case of (partially) oxidised interfaces. In fact, Zhang *et al.* [23] showed that the presence of additional O atoms at the Fe/MgO interface reduces the tunneling current of the Δ_1 majority spin electrons, and hence the TMR. Such alteration of the spin current is then likely to yield spin torques that are qualitatively different to the case of an ideal interface.

Here we estimate the effects of interfacial oxidation on the spin torques by performing a transport calculation on an Fe/MgO/Fe junction with partially oxidised insulator/free layer interface. For such purpose we consider a supercell made of $2 \times 2 \times 1$ unit cells of the Fe/MgO/Fe junction considered earlier in this Chapter. This allows us to study a cross section formed by four different unit cells that are repeated through the use of periodic boundary conditions. We then consider a partially oxidised interface by inserting an extra oxygen atom in one of the four cells

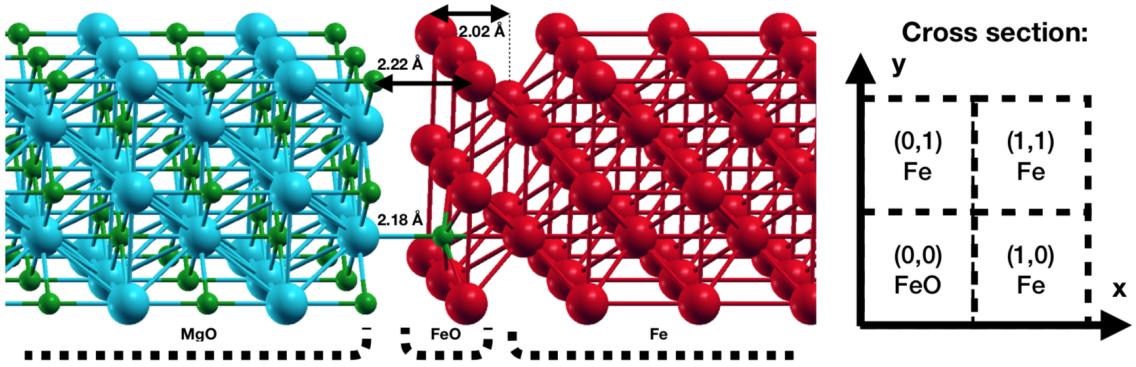

Figure 3.7: Oxidised interface as considered in the supercell calculations. The different color of the spheres corresponds to different atomic species: red for Fe, blue for Mg and green for O. The scheme on the right-hand side shows the notation adopted to identify each unit cell in the cross section. We define the origin of the cartesian axes as the origin for the oxidised cell, hereon also denoted as $(0, 0)$. The remaining unit cells are then identified according to the position of their origin in units of the in-plane lattice constant, namely as $(0, 1)$, $(1, 0)$ and $(1, 1)$.

as shown in Fig. 3.7, thus to obtain an interfacial FeO_x layer with $x = 0.25$. The formation of a uniform FeO layer throughout the entire cross section is in fact rather unlikely. Moreover, the Fe magnetic moments in bulk FeO order antiferromagnetically, hence the correct estimation of the electronic structure of a single ML of FeO would strongly complicate the simulation. The coordinates of the oxidised interface are chosen according to the findings presented in Ref. [23]. In such work different experimental results are considered and combined to estimate the position of the atoms at the interface. The distance between the O atom in the FeO layer and the MgO is set to 2.18 Å, while its distance from the Fe contact is chosen to be 2.06 Å. The Fe atoms belonging to the oxidised layer are then displaced by 0.4 Å towards the Fe contact. The simulation parameters and magnetic configuration for the torque calculation are then kept the same as the ones considered for the ideal interface.

Fig. 3.8 compares the results of transport calculations of Fe/MgO/Fe junctions with ideal (blue squares/lines) and oxidised (red circles/lines) insulator/free layer in-

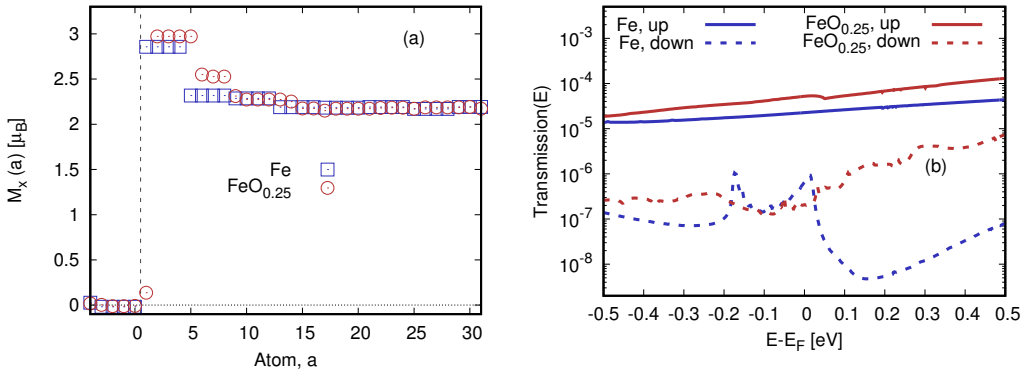

Figure 3.8: Results of transport calculations on Fe/MgO/Fe MTJs with a clean (blue squares/lines) and a 25% oxidised (red circles/lines) insulator/free layer interface. Left: planar average of the atomic magnetic moments in proximity of the interface (centered at 0). Right: energy-dependent transmission coefficients for majority- (full lines) and minority-spin (dashed lines).

terface. Panel (a) shows that the magnetic moments in the FeO layer are slightly enhanced in proximity of the barrier with respect to the clean interface. The difference is particularly marked for Fe atoms in the first non-oxidised layer, and disappears deep in the free layer, as expected from the screening in metals. The majority-spin transmission for parallel magnetisations is very similar in the two cases, while the minority-spin seems to be less energy dependent in the case of the oxidised interface. Despite the similarities just described, the calculated in-plane torkance for the disordered junction has a different spatial trend with respect to the ordered one. In general, the decay is significantly longer-ranged and has different features depending on which portion of the $2 \times 2 \times 1$ supercell is considered. The different panels of Fig. 3.9 show the torkance acting on each section, where the labels refer to the notation introduced in Fig. 3.7. The torkance for the oxidised (0,0) unit cell is displayed in panel (a), panels (b) and (d) are relative to the two sections adjacent to the oxidised one and panel (d) to the opposite one (1,1). The decay range for sections adjacent to the oxidised one is analogous to the one encountered for clean interfaces [see Fig. 3.3 (a)]. The small oscillations of the torkance in the unit cells (0,1) and

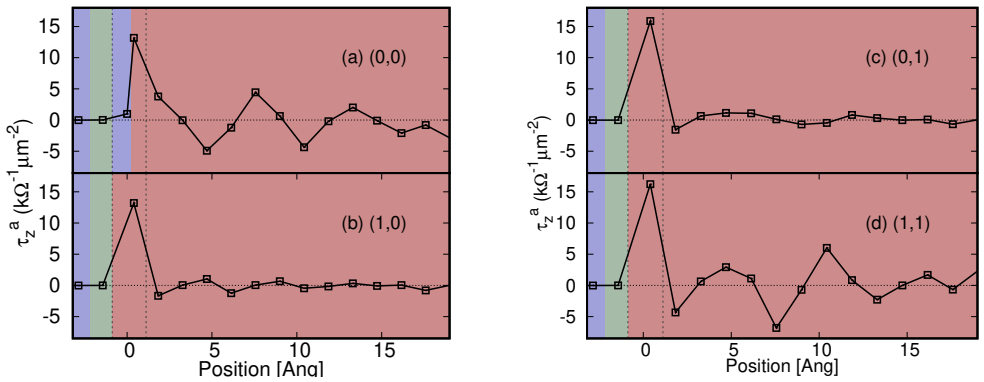

Figure 3.9: Calculated torkance per unit of $\mu_B/2$ and area in a Fe/MgO/$FeO_{0.25}$/Fe junction. Each panel corresponds to a different region of the 2x2 supercell, where and the two vertical dashed lines indicate the position of the MgO/$FeO_{0.25}$ and $FeO_{0.25}$/Fe interfaces. The colored background indicates the atomic species: blue for O, green for Mg and red for Fe.

(1,0) are in fact rather small and are likely due to magnetic moments that are less homogeneous than the case of the ideal interface. The same consideration, however, does not hold for the (0,0) and (1,1) regions, where the oscillations are remarkably more pronounced and propagate further away from the interface. Interestingly, the torkances in such regions have similar features despite the additional O atom is in the (0,0) but not in the (1,1) region. We can then conclude that a local alteration of the ideal barrier may influence the spin torques in a cross section larger than the unitary cell.

The appearance of oscillations in some portions of the cross section indicates that the partial oxidation introduces additional transport channels with respect to a clean interface. In other words, the presence of the additional O atom is sufficient to significantly alter the electronic structure of the atoms in proximity of the interface. As explained before, the electronic states at the Fermi energy for each spin state play an important role in the determination of the decay of the spin torques. This feature is key to the prediction of the spin torques in a given material and will be further analysed in the next section.

3.4 Material dependence of the spin torques

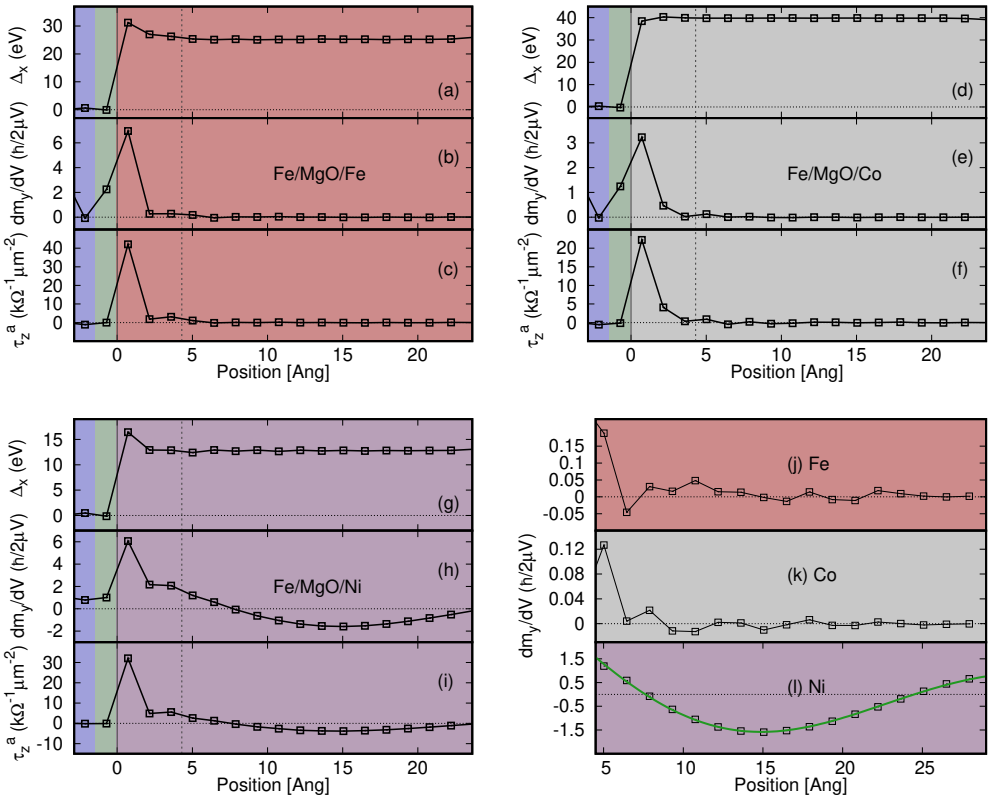

Figure 3.10: Study of the torkance in free layers composed by Fe (top left panel), Co (top right panel), Ni (bottom left panel). In all the panels the colored background indicates the atomic species: blue for O, green for Mg, red for Fe, light grey for Co, violet for Ni. The top left, top right and bottom left figures display the relevant components of [(a), (d), (g)] the exchange and correlation field, $\boldsymbol{\Delta}$, [(b), (e), (h)] the non-equilibrium spin density, $d\boldsymbol{m}/dV$, and [(c), (f), (i)] the torkance per unit of $\mu_B/2$ and area, $\boldsymbol{\tau}$. The bottom right figure shows the details of the decay of the non-equilibrium spin density in (j) Fe, (k) Co and (l) Ni beyond the position indicated by the dashed vertical line in the other figures (note the different scales). The green line in panel (l) represents the best fit of the function in Eq. (3.23) to the underlying data.

We focus here on the study of the spatial decay of the spin torques depending

on the chemical composition of the magnetic free layer. For simplicity, the analysis will be limited to the in-plane torkance acting on free layers positioned at the right-hand side of a Fe/MgO stack where the magnetisation vectors are orthogonal to each other. This allows us to examine the response of each magnetic material to spin currents composed by electrons with the same band symmetry since the latter is defined by the spin filtering of the MgO barrier. We start by comparing the torkance acting on Fe, Co and Ni layers while maintaining the atomic coordinated of the Fe/MgO/Fe system. We consider here free layers composed of 10 atomic layers (2.866 nm) so that the magnetic moments are uniform throughout the stacks. This also allows us to relate the spin torques to the band structure of each material in a framework similar to the one discussed at the beginning of this chapter and proposed in Ref. [89]. We remark that this is not a realistic approximation for Ni and Co, since their equilibrium crystal structures are not *bcc*. The presence of a different crystal structure in contact with MgO might however disrupt the spin filtering, hence produce qualitatively different spin currents. Moreover, maintaining the same crystal structure for all materials facilitates comparison between the different cases. Fig. 3.10 contains our results for the torkance in a Fe (top left), Co (top right) and Ni (bottom left) free layer. Each sub-figure contains the relevant components of (top panels) the exchange and correlation field, $\boldsymbol{\Delta}$, (middle panels) the non-equilibrium spin density, $d\boldsymbol{m}/dV$, and (bottom panels) the torkance, $\boldsymbol{\tau}$. We recall that the XC field is parallel to the local magnetisation, hence it points along the x axis for $\vartheta = \pi/2$ (see Fig. 3.1), while the in-plane component of the torkance is parallel to the z direction. As a consequence, the vector product in the torkance definition of Eq. (3.22) indicates that the component of the non-equilibrium spin density that contributes to the in-plane torkance is along the y axis. We note that the point-by-point vector product between the displayed XC field and non-equilibrium spin density does not give the value of the torkance reported in the figures. In fact, each spatial profile is obtained through the partial trace over the orbitals centered at each atom (e.g. $\boldsymbol{\Delta}_a = \sum_{\mu\in a} \boldsymbol{\Delta}_{\mu\nu}$), hence the point-by-point product does not account for terms that are off-diagonal in the orbital indices.

Our results show that the magnitude of the XC field is almost constant throughout the free layer in all the three cases, with small deviations within a few atomic planes from the interface with MgO. Both the non-equilibrium spin density and the torkance are peaked at the interface and decay as the XC field becomes uniform, a position indicated by the dotted vertical lines in the three figures. In such region the torkance vanishes almost completely for Fe and Co [panels (c) and (f) respectively]. In contrast, a much longer decay range characterises the STT in Ni [panel (i)]. This difference is due to the absence of Δ_1 minority bands at the Fermi energy for $\boldsymbol{k}$-vectors parallel to the transport direction for Fe and Co [Fig. 3.11]. In fact, contributions from different points of the 2D Brillouin zone make the spin current vanish quickly in the free layer. If both majority and minority states are available at E_F, the spin torque will oscillate with a frequency given by $\pi/(k_F^{\downarrow} - k_F^{\uparrow})$ (see §3.1). In order to further analyse the spatial decay of the torque deep in the free layers we display the non-equilibrium spin density far enough from the MgO interface for the three materials (bottom right of Fig. 3.10). Here the spin density was chosen instead of the torque, since the latter is more sensitive to the small variations in magnitude of the magnetic moments. These are in fact not exactly constant and such small modifications are enough to produce the tiny oscillations observed for Fe [panel (j)] and Co [panel (k)]. In contrast, the non-equilibrium spin density in Ni perfectly follows the trend predicted by Ref. [89] [panel (l)]. The green line here represents the result of our best fit to the function

$$\frac{dm_y}{dV}(z) = \frac{A \sin\left(\Delta k(z - z_0)\right)}{\Delta k(z - z_0)}, \tag{3.23}$$

where $\Delta k = k_F^{\downarrow} - k_F^{\uparrow}$. Our best fit estimates Δk to be $0.19\,\text{Å}^{-1}$, which differs from the value of $0.45\,\text{Å}^{-1}$ that can be extracted from the band structure [panels (c) and (g) of Fig. 3.11]. We attribute this inconsistency to a shift in the Fermi energy of the junction with respect of the one of bulk Ni. In other words, the match of the two quantities requires to evaluate the k-vector difference in the band structure of *bcc* Ni at the energy corresponding to E_F as calculated for the Fe/MgO/Ni junction. We estimated the difference in the Fermi energies for the two systems to be around

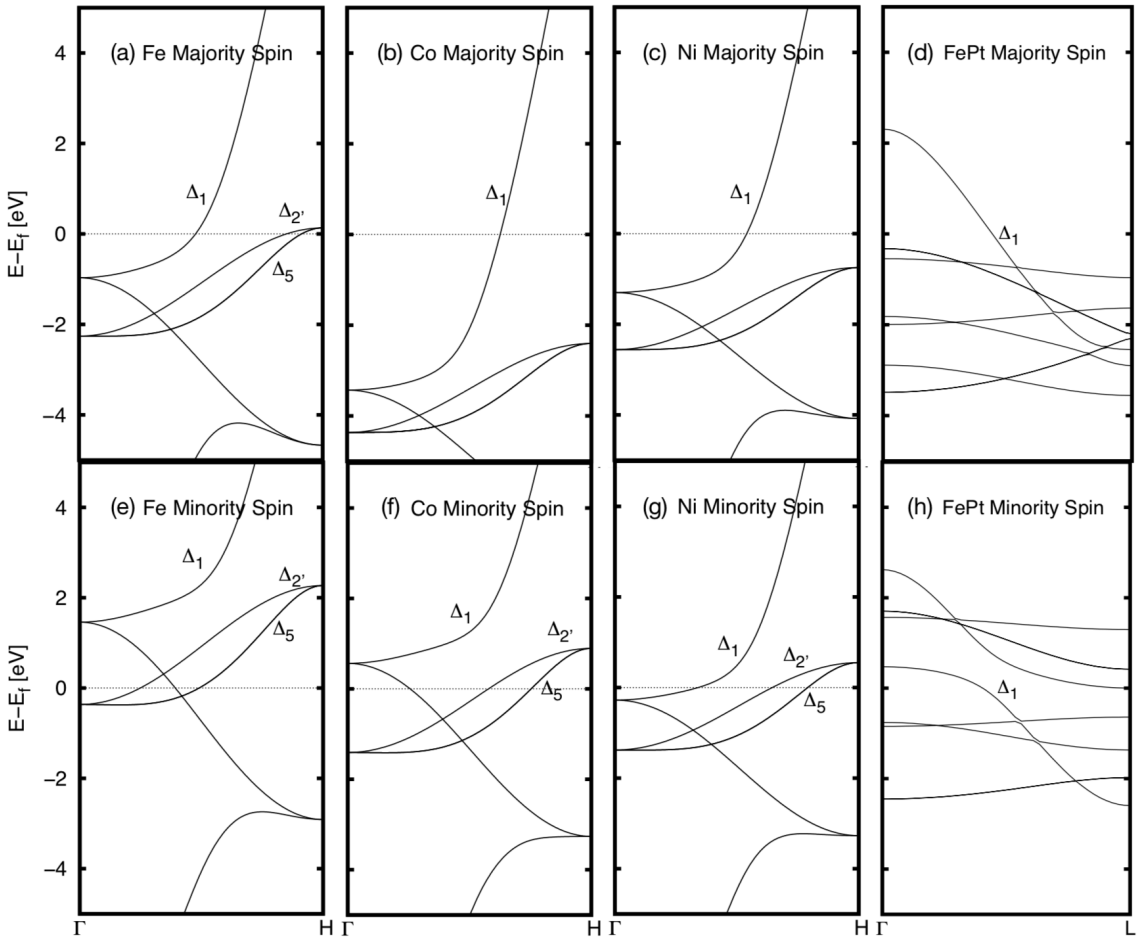

Figure 3.11: Band structure of, from left to right, Fe, Co, Ni and FePt for majority (top panels) and minority (bottom panels) spins for k-vectors parallel to the transport direction. For all materials the in-plane lattice parameter is that of the junction, i.e. of *bcc* Fe, and the structures for Fe, Co and Ni are all *bcc*. The production of the data contained in this Figure and its realisation was performed by Emanuele Bosoni.

0.2 eV, which corresponds to Δk=0.28 Å^{-1}. Such value is closer to the one extracted from the fit, but still inconsistent. Since our best fit seems to perfectly interpolate the data and provides a very accurate estimate of Δk (with error of 0.001%), we conclude that the inconsistency is due to an incorrect extrapolation of the Δk from the band structure. Further investigation will then be necessary to confirm the accuracy of the prediction of the oscillation frequency of STT provided by the best fit.

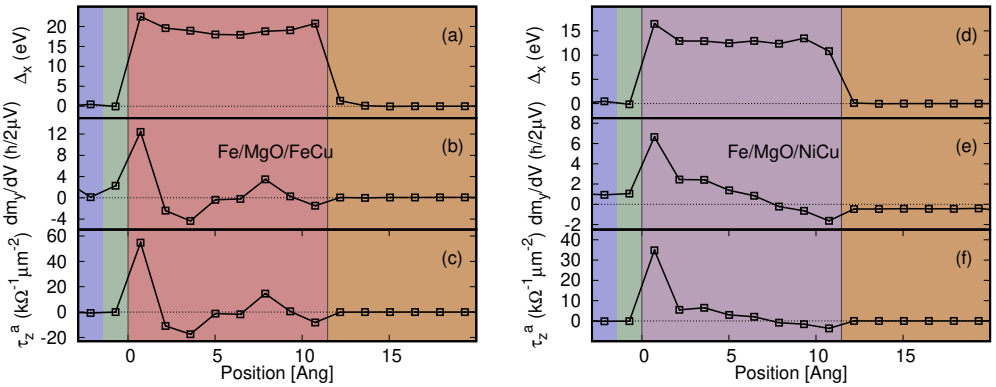

Figure 3.12: Study of the torkance acting on Fe/MgO/Fe/Cu (left) and Fe/MgO/Ni/Cu (right). The colored background indicates the different atomic species: blue for O, green for Mg, red for Fe, purple for Ni and orange for Cu. The top panels display the relevant components of the exchange and correlation field, Δ_x, the middle panels the non-equilibrium spin density, $\mathrm{d}m_y/\mathrm{d}V$, and the bottom panels the torkance per unit of μ_B/e and area, τ_z.

The long range decay of the torkance in Ni has been already reported in previous calculations for Cu/Co/Cu/Ni/Cu multilayers [107, 108]. In such works the authors show that the phase of such oscillations depends on the distance between the two interfaces of Ni with Cu. It has been also shown that the insertion of a metallic seed layer between the insulator and the free magnetic layer also modifies the intensity of the in-plane torque, and the sign of its contribution can be controlled by varying the thickness of such spacers [109].

In order to analyse the influence of non-magnet/ferromagnet interfaces we consider free layers where the ferromagnet is contacted to a Cu electrode. We note that such an interface is often present in experimental realisations of MTJs (see Fig. 1.7). Since the torkance in Fe and Co has rather similar features, we only analyse the Fe/Cu and Ni/Cu free layers. In both cases we consider the ferromagnetic to stacks have a thickness of 8 MLs (1.146 nm). Consistently with our previous system choices, the crystal structure for Cu layers is not adapted to the equilibrium structure of such material but is kept *bcc*. The results displayed in Fig. show that in both cases the

magnetic moments vary slowly between the two interfaces [panels (a) and (d)]. This is more evident for Fe, where the interfacial moment is enhanced at both interfaces. In contrast, the Ni atoms at the Ni/Cu interface have a reduced moment compared to the others. For a Ni/Cu free layer, the torkance (panel (f)) is found to be strikingly similar to the one for a pure Ni layer. In contrast, the presence of the Cu electrode remarkably alters the spatial profile of the torkance in the Fe stack [panel (c)]. In Fe the decay is now significantly longer and oscillating, with the peak at the interface with the insulator being of larger intensity. It is then clear that the argument presented to explain the decay in the free layers made for a single material is not applicable here. This is due to the formation of quantum well states within the magnetic layer that significantly alter electron propagation. The details on how the spin torque varies with the change the contacts will then depend on the details of the magnet/non-magnet interface. This greatly complicates the prediction of the material dependence of STT in presence of multiple interfaces.

3.4.1 The influence of induced magnetic moments in $L1_0$-FePt

Our analysis so far has been focused on materials with a uniform magnetic texture. We have shown that in the absence of additional interfaces the spatial profile of the torque is determined by the position of the Δ_1 majority and minority spin bands with respect to the Fermi energy. We are here interested in exploring the torques in a material whose unit cell includes atomic spins of different magnitudes and verify whether the same arguments apply. With such purpose in mind we consider a series of Fe/MgO/Fe junctions including a stack of $L1_0$ FePt in the free layer. The latter has Δ_1 bands for both spin channels crossing the Fermi level [panels (d) and (h) of Fig. 3.11], hence the torque is expected to have some long range oscillations. The $L1_0$ ordered FePt alloy is of great interest for magnetic recording applications because of its high easy-axis magnetocrystalline anisotropy ($K_u = 7.0 \times 10^6\,\mathrm{Jm}^{-3}$) [110]. Its bulk crystal structure is almost *bcc* where the two nonequivalent sites are occupied

by different species [Fig. 3.13 (a)], with experimental in-plane lattice constant of 2.73 Å and a slight distortion along the (001) direction ($c/a = 0.98$). Interestingly, the presence of Fe induces a magnetic moment on the usually non-magnetic Pt atoms that couples ferromagnetically to the spins on the Fe sites.

Despite the relevant difference in magnitude between the two moments ($\mu_{\mathrm{Pt}} \sim 0.4\ \mu_B$, $\mu_{\mathrm{Pt}} \sim 3.0\ \mu_B$), the interplay between the two moments plays a significant role in the thermodynamical and dynamical properties of the spin system. The similarity of the crystal structure of FePt to *bcc* Fe makes $L1_0$ FePt suitable to be embedded in Fe/MgO-based tunneling junctions, as it was already proposed both in theoretical [111, 112] and experimental works [113]. Here we start by considering a free layer composed entirely by FePt, to then examine the case of an FePt stack inserted between MgO and a Fe electrode. A small seed layer (SL) is then interposed between the FePt stack and the MgO barrier, as often done in experiment to better nucleate the growth of FePt. The inclusion of FePt into Fe/MgO/Fe requires the in-plane lattice constants to match throughout the stack. Hence, the in-plane lattice constant of FePt is adapted to match the one of *bcc* Fe. The atomic coordinates to construct different junctions are then chosen according to the studies contained in Refs. [114, 113]. In particular the out-of-plane lattice constant of FePt is taken to be 3.474 Å, while the inter-plane distances at the MgO/FePt and Fe/FePt interfaces are 2.2 Å and 1.585 Å, respectively. Since the atomic forces in the systems built with such information are comparable to the ones in the Fe/MgO/Fe system, no structural relaxation was performed here.

We start by comparing the energy-dependent transmission coefficients calculated for a FePt (red), Fe (blue) and a FePt/Fe (green) free layer [Fig. 3.13 (b)]. The transmission coefficient for majority spin (full lines) is found to be about 2 orders of magnitude higher for a FePt contact than for an Fe electrode. The spin-up transmission is slightly higher in Fe than in FePt/Fe because of the presence of the additional FePt/Fe interface. The difference between FePt and Fe contacts is less pronounced for minority spin, which are however significantly higher than the FePt/Fe case. These changes in the magnitude of the total transmission will then imply a dif-

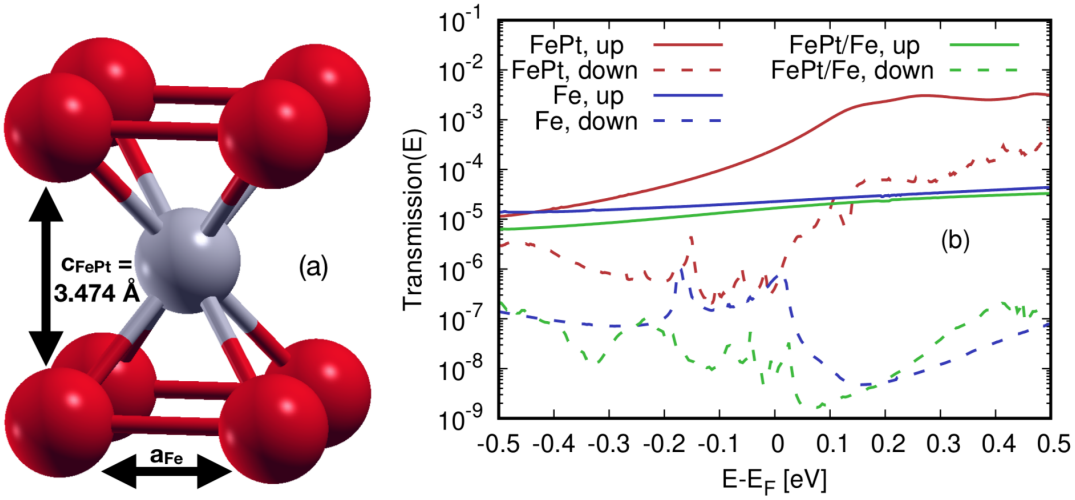

Figure 3.13: Left: unit cell of $L1_0$ FePt with red (gray) spheres representing Fe (Pt) atoms. Right: comparison of the energy dependent transmission coefficients for majority (full lines) and minority (dashed lines) for junctions with FePt (red), Fe (blue) and FePt/Fe (green) free layers.

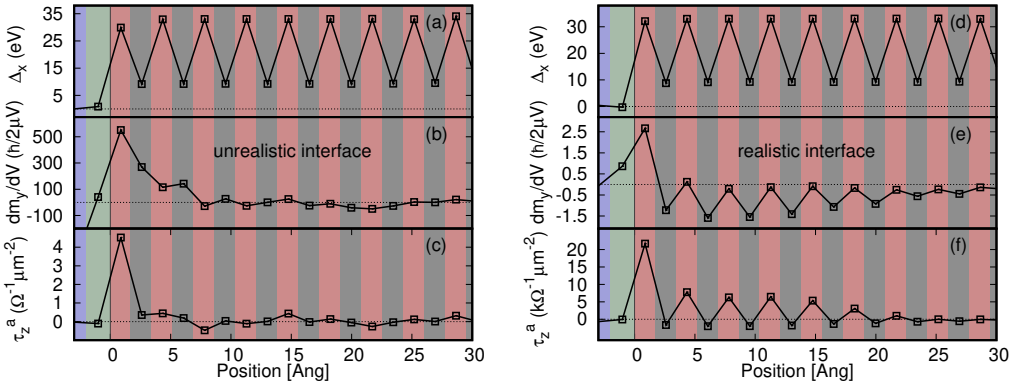

Figure 3.14: Study of the torkance in a FePt free layer in the case of the unrealistically underestimated (left) and the realistic (right) MgO-FePt inter-plane distance. The coloured background indicates the atomic species: blue for O, green for Mg, red for Fe, grey for Pt. The relevant components of (a), (d) the exchange and correlation field, $\boldsymbol{\Delta}$, (b), (e) the non-equilibrium spin density, $\mathrm{d}\boldsymbol{m}/\mathrm{d}V$, and (c), (f) the torkance per unit of μ_B/e and area, $\boldsymbol{\tau}$.

ference in the intensity of the spin torques acting on the different junctions, and, consequently, in the resulting spin dynamics. As a matter of fact, the cause of this drastic difference in the total transmission was found to be an incorrect, strong underestimation of the MgO-FePt inter-layer distance in the Fe/MgO/FePt system, as compared to the (correct) one used for the other junctions. Consequently, the results on the transport properties of the Fe/MgO/FePt junction shown in most of this work are based on a unrealistic crystal structure. Nevertheless, this inconsistency does not qualitatively modify the results here presented. This can be seen by comparing the calculated torkance in the cases of the unrealistic and the realistic interfaces, shown in panels (c) and (f), respectively, of Fig. 3.14. As for the other free layers considered, the STT is peaked at the MgO/free layer interface because of a change in the magnetic moment of the interfacial magnetic atom. The magnetic moments then remain mostly constant within the layer and the torque decays with long range oscillations, as it can be predicted from the presence of Δ_1 bands at the E_F for both spin states [panels (d), (h) of Fig. 3.11]. In the case of the unrealistic interface, such oscillations are strikingly smaller than the peak at the interface, and are rather irregular. In contrast, the spatial profile becomes much more regular when the realistic inter-plane distance is adopted, although the overall torque intensity is about two orders of magnitude smaller than the case of the incorrect interface. We remark that this difference is perfectly consistent with the difference in magnitude in the transmissions of the (unrealistic) Fe/MgO/FePt structure and the other junctions shown in Fig. 3.13 (b).

Given the remarkably strong magnetic anisotropy of $L1_0$ FePt, the inclusion of a thick stack of such material would make difficult to induce magnetisation reversal, as it will be shown in Chapter 4. Therefore, we consider free layers where the FePt stack is truncated by a *bcc* Fe electrode. The results displayed in Fig. 3.15 show that the regular, long-range decay encountered for a pure FePt lead (with a realistic interface) is partially suppressed by the Fe lead. In fact, the spin torque is constant for all atoms in FePt that are not at the MgO interface and then quickly decays in the Fe contact. This effect remains for different thicknesses of the FePt stack

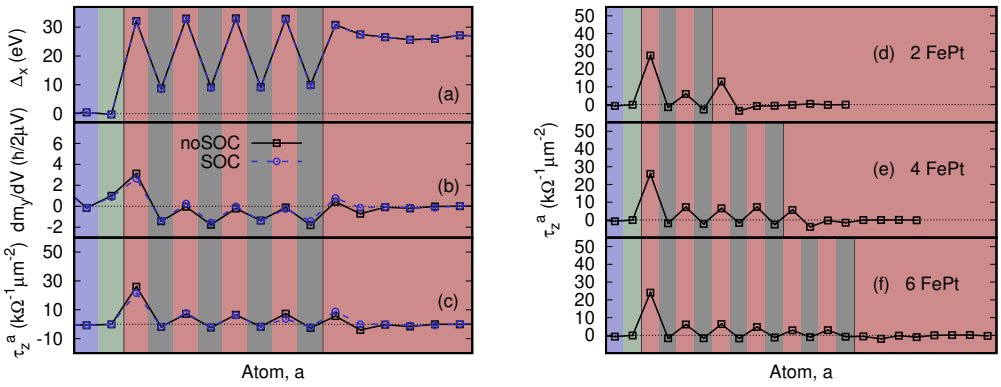

Figure 3.15: Study of the torkance in a FePt/Fe free layer. The coloured background indicates the atomic species: red for Fe, grey for Pt, blue for O, green for Mg. Left panel: the relevant components of (a) the exchange and correlation field, $\boldsymbol{\Delta}$, (b) the non-equilibrium spin density, $\mathrm{d}\boldsymbol{m}/\mathrm{d}V$, and (c) the torkance per unit of μ_B/e and area, $\boldsymbol{\tau}$. Data points represent by black squares are the results of a non-relativistic calculation, while blue circles represent results of a calculation including spin-orbit interactions.

[panels (d), (e) and (f)], although the intensity seems to gradually decay for larger thicknesses. Interestingly, here the sign of the torkance is consistently opposite on Fe and Pt atoms. We attribute this change in the spatial profile of the torkance to the formation of quantum well states within the FePt, in analogy to the case of a Fe/Cu free layer. We note that in panels (a), (b) and (c) the blue circles show the results of a non-relativistic calculation (black squares), which are compared to ones where spin-orbit coupling is included (blue circles). It is then clear that the inclusion of spin-orbit interactions does not bring any significant modification of the torkance. This might be counter intuitive for a system including a heavy element such as Pt. Nevertheless, in the systems of interest for this dissertation spin-orbit interactions are typically of the order of tens of meV, in contrast to the exchange interaction that is three orders of magnitude stronger [see e.g. Fig. 3.15 (a)].

Similar results are obtained when a thin Fe seed layer is interposed between MgO and the FePt stack (Fig. 3.16). The oscillations are here of much smaller magnitude,

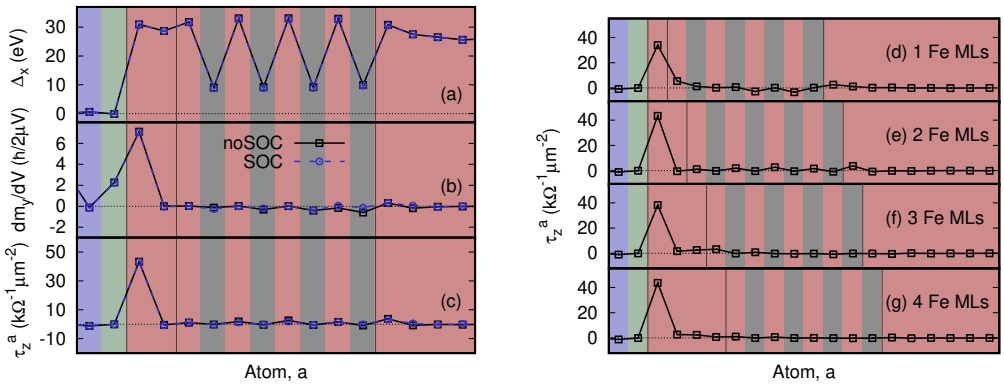

Figure 3.16: Study of the torkance in a Fe/FePt/Fe free layer. In both sub figures the coloured background indicates the atomic species: red for Fe, grey for Pt, blue for O, green for Mg. Left panel: the relevant components of (a) the exchange and correlation field, $\boldsymbol{\Delta}$, (b) the non-equilibrium spin density, $\mathrm{d}\boldsymbol{m}/\mathrm{d}V$, and (c) the torkance per unit of μ_B/e and area, $\boldsymbol{\tau}$. Black squares and blue circles indicate results obtained without and with relativistic corrections, respectively. Right Panel: comparison of the torkance per unit μ_B/e and area of MTJs with (d) 1, (e) 2, (f) 3 and (g) 4 Fe MLs as seed layer.

when compared to those in FePt alone, and they vanish for thick enough seed layer thickness (3 Fe MLs). In fact, the spin current rapidly decays in Fe (as explained above), hence the spin current injected in the FePt gradually decays as the FePt thickness increases. As a result, free layers with thick enough Fe SLs are subject to the same spin torques acting on a pure Fe layer. This however does not hold for seed layers made of materials that allow for long range oscillations, such as the *bcc* Ni, already considered above. Fig. 3.17 displays the results of torkance calculations on Fe/MgO/Ni/FePt/Fe junctions. As in the case of a Fe seed layer, the torque [panel (c)] is strongly peaked at the MgO/Ni interface, but now it does not decay entirely and thus a non-vanishing STT with an oscillatory behaviour persists into the FePt layer. A closer look at the profile of $\boldsymbol{\Delta}$ across the junction [panel (a)] reveals that the exchange and correlation field in Ni is about half of that of Fe [see Figure 3.16(a)]. As a consequence, in Ni the spin accumulation does not relax along the local direction of

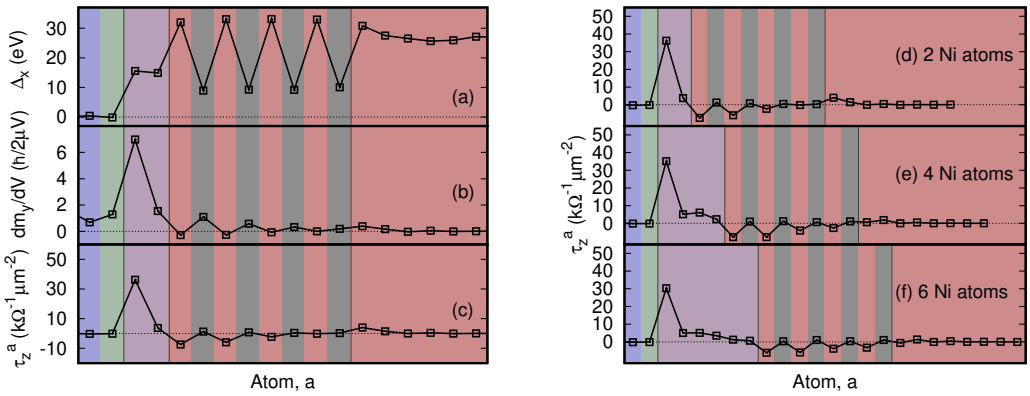

Figure 3.17: Study of the torkance in a Ni/FePt/Fe free layer made of 4 FePt monolayers and a variable number of Fe monolayers inserted between MgO and FePt. Left panel: the relevant components of (a) the exchange and correlation field, $\boldsymbol{\Delta}$, (b) the non-equilibrium spin density, $\mathrm{d}\boldsymbol{m}/\mathrm{d}V$ and (c) the torkance per unit of μ_B/e and area, $\boldsymbol{\tau}$. Black squares and blue circles indicate results obtained without and with relativistic corrections, respectively. Right Panel: comparison of the torkance per unit μ_B/e and area of MTJs with with a seed layer comprising (d) 1, (e) 2, 3 (f) and 4 (g) Fe monolayers. In all panels the coloured background indicates the atomic species: red for Fe, grey for Pt, blue for O, green for Mg.

the magnetization as efficiently as in Fe, a fact that can be appreciated by comparing Fig. 3.17(b) with Fig. 3.16(b). Interestingly, the attenuation of the spin accumulation and thus of the torque is not complete even for relatively thick Ni seed layers, as can be seen in panels (d) through (f). A second interesting observation concerns the phase of the oscillations of the STT in the FePt layer. In fact, for a junction where FePt is in direct contact with the MgO barrier, the torque is positive at the Fe planes and negative (although rather small) at the Pt ones. The same behaviour, although with a much reduced torque is observed for Fe intercalation (in the presence of a Fe seed layer). In contrast when the seed layer is made of Ni the sign of the STT on the FePt layer changes, becoming negative at the Fe planes and positive (although small) at the Pt ones. As a result the total integrated torque over the entire free layer (seed layer plus FePt) for Ni intercalation is two thirds than that obtained with

Fe intercalation.

3.5 Conclusions

In this Chapter we have analysed the spin torques acting on free layers of a variety of Fe/MgO-based magnetic tunnelling junctions by the means of first principles simulations. Previous works predict that the persistence of the torque far from the insulator/magnet interface depends on the presence of open channels for both minority and majority spins at the Fermi level. Since the transport here is dominated by electrons with Δ_1 band symmetry, the STT is short ranged in Fe and Co because of the absence of a Δ_1 minority spin band at the Fermi energy. In contrast, the Δ_1 band crosses the Fermi level for both spin channels in the case of a Ni free layer. The torque then oscillates with a frequency that is given by the difference of the Fermi wavevectors for the two Δ_1 bands. The same argument holds in the case of non-uniform magnetic moments in $L1_0$ FePt, although the induced magnetic moments in Pt make such system more complicated and the decay does not follow the predicted $\sin(z)/z$ decay. Moreover, the presence of an additional interface in the stack (e.g. at the end of the free layer) has been shown to considerably modify the spatial profile of the torque. Finally, we have considered a partially oxidised MgO/Fe interface. We find that a local alteration of the interface can modify the spatial profile of the torkance in a cross section that is larger than the unitary cell.

Chapter 4

Current-driven atomistic spin dynamics

"Chaos, panic and disorder. My work here is done."

- Anonymous

The energy efficiency of a STT-MRAM prototype is essentially measured by the critical current intensity, I_c, required to perform magnetisation switching. Analytical expressions such as those in Eq. (1.7) and Eq. (1.8) provide only a qualitative and coarse estimation, since they are derived from approximated solutions of the LLG equation, by assumption spatially uniform magnetic properties. In contrast, numerical solutions allow one to explicitly account for a number of additional factors such as domain walls motion and material interfaces. For length scales ranging between 10 nm and a few μm the details of the magnetic properties of a system normally do not depend on its atomic structure. In *micromagnetics* simulations the magnetisation is considered as a macroscopic, position-dependent vector, $\boldsymbol{M}(\boldsymbol{r})$, within the continuum approximation. This is, however, not suitable for situations where the reduced length scale or complex magnetic orderings play a significant role in the magnetisation dynamics, or when magnetic phase transitions are of interest. Hence, the electronic structure of the system is to be examined. Nevertheless, in many cases the strong localisation of electrons responsible for the magnetic properties allows us to consider the atomic magnetic moments as strictly localised on the atomic site with dynamical properties that are weakly influenced by their quantum mechanical

nature. As a consequence, they can be represented within a classical Heisenberg-like spin model, where the quantum mechanical effects are represented by some material dependent parameters to be provided as input.

This Chapter starts with a brief historical description of the LLG equation, to then detail a computational approach for its solution in the framework of atomistic classical spin dynamics. An overview of the quantities required for a full parametrisation of the spin dynamics is then presented, together with information on how they can be extracted from first principle calculations and experimental measurements. We then show the capabilities of the approach by studying the properties of the spin models for *bcc* Fe and $L1_0$ FePt. Finally, we combine the results of the spin torques calculations presented in the previous Chapter with the spin dynamics simulations to study current-driven magnetisation switching in the different systems.

All results contained in this Chapter were obtained with a software developed by Dr. Matthew Ellis.

4.1 Modelling the dynamical properties of atomistic spins

The simplest approach to investigate the dynamical magnetic properties of a ferromagnetic object analyses the motion of its total magnetisation vector, $\boldsymbol{M}$, in response to an applied magnetic field, $\boldsymbol{H}_{\text{app}}$. Such dynamics can be decomposed into two separate components: a precession around the direction of the magnetic field and a rotation leading to the alignment between $\boldsymbol{M}$ and $\boldsymbol{H}_{\text{app}}$. The existence of the former can be evinced by considering the equation of motion of the expectation value of the spin operator, $\hat{\boldsymbol{S}}$, interacting with the magnetic field. The spin Hamiltonian in this case is simply given by the Zeeman energy,

$$\hat{\mathcal{H}}_{\text{Zeeman}} = -g_e \mu_B \hat{\boldsymbol{S}} \cdot \boldsymbol{H}_{\text{app}}. \tag{4.1}$$

Hence Ehrenfest's theorem yields

$$\frac{\partial \langle \hat{\boldsymbol{S}} \rangle}{\partial t} = -\frac{i}{\hbar} \langle [\hat{\boldsymbol{S}}, \hat{\mathcal{H}}_{\text{Zeeman}}] \rangle = -\gamma \langle \hat{\boldsymbol{S}} \rangle \times \boldsymbol{H}_{\text{app}}. \tag{4.2}$$

The last term in the equality was obtained by exploiting the commutation relations $[\hat{S}_i, \hat{S}_j] = i\hbar\varepsilon_{ijk}\hat{S}_k$ $(i, j, k = x, y, z)$, and the gyromagnetic ratio of the electron is denoted as $\gamma = \mu_B g_e/\hbar$, where $g_e = 2$ is the Landeéfactor for the electron.

A phenomenological equation of motion for $\boldsymbol{M}$, combining the two contributions to the magnetisation dynamics was first proposed by Landau and Lifshitz (LL) and reads

$$\frac{\partial \boldsymbol{M}}{\partial t} = -\gamma \boldsymbol{M} \times \boldsymbol{H} - \frac{\lambda}{|\boldsymbol{M}|^2} \boldsymbol{M} \times \boldsymbol{M} \times \boldsymbol{H}. \tag{4.3}$$

In their original work [115] the effective magnetic field is defined as $\boldsymbol{H} = -\partial \mathcal{F}/\partial \boldsymbol{M}$, i.e. as the derivative with respect to the magnetisation of the free energy of the system, $\mathcal{F}$. The first term clearly represents the precession, while the second is constructed so that $\boldsymbol{M}$ is driven to point along the direction of the field. This second term effectively adds a *damping* contribution, whose intensity is measured by λ and accounts for relativistic effects that give rise to energy and angular momentum dissipation. Unfortunately, the LL equation was found to be not suitable to describe systems where strong damping is present. This observation was first made by Gilbert [116], who proposed an alternative formulation of the LL equation, later known as the Landau-Lifshitz-Gilbert (LLG) equation, based on a Lagrangian analysis. In this case Eq. (4.3) is modified to become

$$\frac{\partial \boldsymbol{M}}{\partial t} = -\gamma \boldsymbol{M} \times \boldsymbol{H} + \frac{\alpha}{M} \boldsymbol{M} \times \frac{\partial \boldsymbol{M}}{\partial t}. \tag{4.4}$$

In this equation the role of the damping term is made clear by the explicit presence of $\partial \boldsymbol{M}/\partial t$. The two formulations [Eqs. (4.3) and (4.4)] were proven to be mathematically equivalent [117], and the newly defined damping, α, is commonly known as *Gilbert damping*. It is in fact easy to show that the LLG equation can be expressed in a form that is analogous to the LL equation, i.e. with the damping contribution expressed as a triple cross product instead of in terms of the derivative of the magnetisation. This can be done by taking the cross product of both terms of Eq. (4.4)

with $\boldsymbol{M}$,

$$\begin{aligned}\boldsymbol{M}\times\frac{\partial\boldsymbol{M}}{\partial t} &= -\gamma\boldsymbol{M}\times\boldsymbol{M}\times\boldsymbol{H}+\alpha\boldsymbol{M}\times\boldsymbol{M}\times\frac{\partial\boldsymbol{M}}{\partial t}\\ &= -\gamma\boldsymbol{M}\times\boldsymbol{M}\times\boldsymbol{H}+\alpha\left[\boldsymbol{M}\left(\boldsymbol{M}\cdot\frac{\partial\boldsymbol{M}}{\partial t}\right)-\frac{\partial\boldsymbol{M}}{\partial t}M^2\right],\end{aligned} \tag{4.5}$$

where the last term was obtained by employing the definition of the vector triple product $\boldsymbol{a}\times\boldsymbol{b}\times\boldsymbol{c}=\boldsymbol{b}(\boldsymbol{a}\cdot\boldsymbol{c})-\boldsymbol{c}(\boldsymbol{b}\cdot\boldsymbol{b})$. Assuming that the magnitude of the magnetisation is constant over time, the first term in the square bracket vanishes. By inserting Eq. (4.5) back into Eq. (4.4) and by rearranging the terms, it is then straightforward to obtain

$$\frac{\partial\boldsymbol{M}}{\partial t}=-\frac{\gamma}{1+\alpha^2}\boldsymbol{M}\times\left[\boldsymbol{H}+\alpha\frac{\boldsymbol{M}}{M}\times\boldsymbol{H}\right]. \tag{4.6}$$

This second form is generally preferable since it can be propagated in time with standard integration schemes for partial differential equations.

The discussion so far treated the magnetisation within the continuum approximation. However, the results can be easily adapted to a system of atomistic spins by considering an LLG equation for each spin, $\boldsymbol{S}_i$, that will be hereon assumed to be unitary for simplicity. The length of the spin vector can be re-cast into appropriate definition of the spin-Hamiltonian parameters. The equations of motion of the system will then be

$$\frac{\partial\boldsymbol{S}_i}{\partial t}=-\gamma'\boldsymbol{S}_i\times\boldsymbol{H}_i-\alpha\gamma'\boldsymbol{S}_i\times(\boldsymbol{S}_i\times\boldsymbol{H}_i), \tag{4.7}$$

where $\gamma'=\gamma/(1+\alpha^2)$ is a renormalised gyromagnetic factor. The effective magnetic field acting on the i-th spin vector, normalised by the respective saturation magnetic moment, $\mu_{s,i}$, takes of the form

$$\boldsymbol{H}_i=-\frac{1}{\mu_{s,i}}\frac{\partial\mathcal{H}}{\partial\boldsymbol{S}_i}+\boldsymbol{\xi}_i, \tag{4.8}$$

where $\mathcal{H}$ is the spin Hamiltonian and the second term is a stochastic process that transforms the LLG to a Langevin equation. This allows one to include thermal effects that arise from phenomena such as spin-phonon interaction, which are not explicitly accounted for. Since the time correlation of the thermal fluctuations is

normally significantly smaller than the time scale of the spin motion, one can adopt the white noise limit and assume $\boldsymbol{\xi}_i$ to describe Gaussian processes defined by

$$\langle \xi_{i\alpha}(t) \rangle = 0, \tag{4.9}$$

$$\langle \xi_{i\alpha}(t)\xi_{j\beta}(s) \rangle = \frac{2\lambda k_B T}{\gamma \mu_{s,i}} \delta_{ij}\delta_{\alpha\beta}\delta(t-s), \tag{4.10}$$

with i, j denoting the spin indices, while $\alpha, \beta = x, y, z$. In this dissertation the spin Hamiltonian will be assumed to be

$$\mathcal{H} = \mathcal{H}_{\text{Zeeman}} + \mathcal{H}_{\text{exch}} + \mathcal{H}_{\text{ani}}, \tag{4.11}$$

where long-range interactions such as the magnetic dipole-dipole one are omitted due to the relatively small length scales that will be considered. The first term in Eq. (4.11) is the Zeeman energy defined in (Eq. 4.1), $\mathcal{H}_{\text{exch}}$ embodies spin-spin couplings arising from the quantum mechanical exchange interaction introduced in Eq. (2.4), while the last term represents the magnetic anisotropy contribution. The exchange Hamiltonian can be generally written as

$$\mathcal{H}_{\text{exch}} = -\sum_{ij} \boldsymbol{S}_i \boldsymbol{\mathcal{J}}_{ij} \boldsymbol{S}_j \tag{4.12}$$

$$= -\sum_{ij} \left[J_{ij} \boldsymbol{S}_i \cdot \boldsymbol{S}_j + \boldsymbol{S}_i \boldsymbol{\mathcal{J}}_{ij}^{\text{sym}} \boldsymbol{S}_j + \boldsymbol{D}_{ij} \cdot (\boldsymbol{S}_i \times \boldsymbol{S}_j) \right]. \tag{4.13}$$

The isotropic exchange, J_{ij}, is the average of the diagonal terms of the full tensor, $1/3\text{Tr}\boldsymbol{\mathcal{J}}_{ij}$, and expresses the tendency of spins to align with respect to each other but do not specify a preferred spatial orientation. Nevertheless, factors such as the presence of different non-equivalent sites in a unit cell can induce an asymmetry in the diagonal terms of the exchange tensors. The correction to be introduced in these cases is known as symmetric exchange or two-ion anisotropy, and is quantified by $\boldsymbol{\mathcal{J}}_{ij}^{\text{sym}}$. The remaining components of $\boldsymbol{\mathcal{J}}_{ij}$, i.e. those corresponding to off-diagonal, anti-symmetric part of the tensor, are known as Dzyaloshinskii-Moriya (DM) interaction. The DM interaction between two spins originates from spin-orbit coupling and is mediated by a third atom through the super-exchange mechanism [118]. It normally arises in the presence of broken translational symmetry and heavy atoms, such as in

transition metal/Pt bilayers [119]. In all the systems of interest for this thesis the typical strength of the DMI interaction is about 3 orders of magnitude weaker than the other components of the exchange tensor, which makes it relevant for length scales beyond several tens of nm. Given the relatively reduced size of the systems examined, DM interaction will be omitted throughout this thesis. The magnetic anisotropy, $\mathcal{H}_{\text{ani}}$, is generally the result of a number of contributions due to both the underlying electronic structure and the shape of the magnetic layer. It is often modelled through the interplay between a uniaxial and a cubic term, respectively with magnitudes k_u and k_c, as

$$\mathcal{H}_{\text{ani}} = -\sum_i k_u(\boldsymbol{S}_i \cdot \hat{e}_u)^2 - \sum_i \frac{k_c}{2}(S_{ix}^4 + S_{iy}^4 + S_{iz}^4). \tag{4.14}$$

In particular, the sign of the uniaxial anisotropy constant, k_u, determines whether spins prefer to lie along the "easy" axis, $\hat{e}_u$, ($k_u > 0$) or in the plane perpendicular to $\hat{e}_u$ ($k_u < 0$), also known as the easy plane. The cubic anisotropy arises from quadrupole-quadrupole interactions [120] and it is negligible for the systems considered here. The constants introduced above characterise the strength of the anisotropy field at each site of the atomistic model, and in general depend on both the atomic species and the chemical environment. The macroscopic uniaxial anisotropy constant, K_u, plays a key role in magnetisation switching as it determines the energy barrier, $K_u V$, to be overcome in order to pass between two stable states, V being the total volume of the magnet. The macroscopic anisotropy arises from the interplay between the atomistic anisotropy constants and thermal fluctuations, and its temperature dependence usually that can be written as [121]

$$\frac{K_u(T)}{K_u(0)} = \left(\frac{M(T)}{M(0)}\right)^3, \tag{4.15}$$

where $M(T)$ is the total magnetisation at a given temperature, T. This implies that the anisotropy field is reduced at a faster rate than the magnetisation, meaning that the energy barrier at high temperatures is significantly lower.

4.1.1 Parameterising the spin Hamiltonian

The magnetic properties of systems can be explored through the numerical integration of Eq 4.5 which relies on a good parametrisation of the spin Hamiltonian and the Gilbert damping. The results obtained here use an adaptation of the Heun integration scheme, as described in detail in Ref. [122]. However, it is essential to tailor the characteristics of the spin model to each system in order to extract accurate and reliable properties. Given the atomic coordinates and the magnetic moments of a certain system, the model is completely determined by the choice of the Gilbert damping parameter and the form and parameterisation of the spin Hamiltonian, namely by the respective inter-atomic exchange and anisotropy constants. Among the latter quantities the Gilbert damping is the most troublesome one to estimate from a theoretical perspective, as it will be discussed in the next chapter. From an experimental point of view, the damping parameter can be extracted from ferromagnetic resonance (FMR) experiments. In FMR the magnetisation of the sample is perturbed by an external magnetic field and driven into a precession motion, whose frequency can be controlled by the field intensity. The damping constant can then be extracted from the width of the resonant peak. However, such constant coincides with the Gilbert damping only at 0 K because of the presence of spin wave scattering at finite temperatures. Moreover, a number of different mechanisms (e.g. electron transport) are known to modify the strength of damping and the relevance of each contribution is often troublesome to estimate. These complications encourage us to take the atomistic damping constant as a free parameter that is varied among a range of reasonable values. In contrast, a number of methods is available to determine exchange and anisotropy constants from first principles, although their reliability is often limited by the high level of numerical accuracy required.

4.1.1.1 Inter-atomic exchanges

Of all the quantities that characterise the spin model, the exchange constants are probably the most relevant since they play a major role in determining the magnetic

ground state of a system. In general, if the coupling between two spins, $\boldsymbol{S}_i$ and $\boldsymbol{S}_j$, is expressed by a positive exchange constant, $J_{ij} > 0$, the most energetically convenient configuration will correspond to a perfect spin alignment, $\boldsymbol{S}_i \cdot \boldsymbol{S}_j = 1$, i.e. to a ferromagnetic order. In contrast, a negative exchange constant, $J_{ij} < 0$, favours their anti-alignment, which is also referred to as a anti-ferromagnetic coupling. Given that the interaction between classical, atomistic spins is a complex nanoscale quantity, there is not a reliable experimental technique to estimate exchange constants for a generic magnetic configuration. In the simple case of a ferromagnetic ordering in a perfectly ordered crystal, the exchange constant can be estimated from the Curie temperature by using a mean field expression,

$$J_{ij} = \frac{k_B T_C}{\varepsilon z}, \tag{4.16}$$

where z is the number of first nearest neighbours of each atom and ε is a mean field parameter that accounts for how the Curie temperature differs for different crystal structures with the same first-nearest neighbour exchange [123]. This is, however, a rather coarse approximation, since it assumes a uniform exchange at each site. In most cases, the reproduction of the correct magnetic configuration is obtained by specifying a different set of parameters for each non-equivalent pair of sites, each including a number of nearest neighbours. A variety of methods based on DFT calculations can be employed to estimate the desired exchange parameters. Here we describe two of the most commonly used approaches that assume the equivalence between the DFT energy of a given magnetic state and the energy of the classical spin system for the same spin structure. Both these techniques essentially rely on the accurate estimation of the difference between DFT total energies of separate magnetic configurations, therefore they might become not reliable for weak exchange couplings. In such cases, methods that do not rely on energy differences, such as the Green's functions based approach developed by Liechtenstein [124], may be more convenient.

Total energy differences The easiest method to assess the inter-atomic exchange coupling within density functional theory is by the means of differences between the

total energy of different magnetic configurations. Energy differences analogous to the ones discussed here can be used to assess a variety of magnetic properties, and the validity of such techniques is guaranteed by the result known as the magnetic force theorem [125]. In the simple case of two magnetic ions in the unit cell, the energy of the system will depend on the mutual angle between the two atomic spins, θ, and in our model such dependence is assumed to be

$$E(\vartheta) = J_{12}\boldsymbol{S}_1 \cdot \boldsymbol{S}_2 \simeq J_{12}|\boldsymbol{S}_1||\boldsymbol{S}_2|\cos(\vartheta). \tag{4.17}$$

As such, one can perform two DFT calculations for two different angles between the two spins, ϑ_1 and ϑ_2, and estimate the exchange coupling from the difference between the respective total energies as

$$J_{12} = \frac{E(\vartheta_1) - E(\vartheta_2)}{\cos(\vartheta_1) - \cos(\vartheta_2)} \frac{1}{|\boldsymbol{S}_1||\boldsymbol{S}_2|}, \tag{4.18}$$

where for simplicity we have assumed that the intensity of the two spins are constant with the angle. The obvious choice for one of the two angles is, naturally, $\vartheta_1 = 0$, while it is common to set $\vartheta_2 = \pi$. This also makes the approach easily extendable to an arbitrary number of spins, in the unit cell, N. In fact, one can perform a calculation for each of the $N^2/2$ possible configurations that different one another by the flip of one spin. A numerical fit can then yield the values of the exchange parameters that reproduce the set of total energies taken from such calculations.

This choice of angles however heavily relies on the hypothesis that the angle dependence of the energy assumed in Eq. (4.18) corresponds to real one. In practice, this does not always happen and it is not straightforward to verify whether such condition is met or not. In order to overcome this issue it is possible to choose ϑ_2 to be small so that the model covers all angular dependencies that can be approximated as $\cos(\vartheta)$ for small angles, instead of assuming $E(\vartheta)$ to be strictly proportional to a cosine. However, DFT calculations, where atomic moments are slightly misaligned from their equilibrium configuration can be of troublesome realisation, since atomic spins are likely to relax to their preferred direction during the DFT self-consistent cycle. In principle, one can solve this issue by employing constrain density functional

theory (CDFT), where a Lagrange multiplier scheme is employed to limit the phase space to configurations with magnetic moments aligned in the desired direction. In practice, the latter requires significantly increased computational costs and hence it is not suitable to perform a large number of calculations. The other relevant difficulty present in these methods is due to the relatively small energy differences involved, which are often below 1 meV. Since one normally has to consider several magnetic configurations in order to extract a sufficient number of exchange parameters, the total computational costs can become rather elevated. Nevertheless, given a certain set of simulation parameters the computational accuracy can be increased by considering the difference between each set of eigenvalues instead of total energies, namely

$$E(\vartheta_1) - E(\vartheta_2) \equiv \sum_{n\boldsymbol{k}} \left[\eta_{n\boldsymbol{k}}(\vartheta_1)\varepsilon_{n\boldsymbol{k}}(\vartheta_1) - \eta_{n\boldsymbol{k}}(\vartheta_2)\varepsilon_{n\boldsymbol{k}}(\vartheta_2)\right]. \tag{4.19}$$

Spin spiral The most common alternative to avoid the use of total energy differences relies on expressing the spin Hamiltonian as a sum of Fourier components in terms of the wave-vectors, $\boldsymbol{q}$. The Fourier transform of each spin can be written as

$$\boldsymbol{S}_i = \sum_{\boldsymbol{q}} \mathrm{e}^{i\boldsymbol{q}\cdot\boldsymbol{R}_i} \boldsymbol{S}_{\boldsymbol{q}}, \tag{4.20}$$

and the conservation of the spin length, $|\boldsymbol{S}_i|$, dictates that for a fixed wave-vector each spin assumes the form

$$\boldsymbol{S}_i(\boldsymbol{q}) = \begin{pmatrix} \cos(\boldsymbol{q}\cdot\boldsymbol{R}_i)\sin(\vartheta) \\ \sin(\boldsymbol{q}\cdot\boldsymbol{R}_i)\sin(\vartheta) \\ \cos(\vartheta) \end{pmatrix}. \tag{4.21}$$

For simplicity, spins are assumed to be tilted from the z axis by a small angle, ϑ, so that the dependence over the wave-vector in entirely contained is the angle $\varphi^i_{\boldsymbol{q}} = \boldsymbol{q}\cdot\boldsymbol{R}_i$. This implies that, for a given $\boldsymbol{q}$, each atomic spin spatially precedes along the z axis with a fixed angle ϑ, describing a "spin spiral" that gives the name to the method. In the absence of spin-orbit coupling, it is possible to formulate a generalised Bloch theorem in terms of the wave-vectors $\boldsymbol{q}$. As a consequence, each Fourier component can be treated within a unit cell calculation, where the

$\boldsymbol{q}$-dependence is introduced through a phase factor of the form $\exp(i\boldsymbol{q}\cdot\boldsymbol{R}_i)$ [126]. The real-space exchange parameters can then be extracted by mean of a Fourier transform with respect to the spin spiral wave-vectors, $\boldsymbol{q}$.

The spin Hamiltonian written in terms of the Fourier transformed spins defined in Eq. (4.20) takes the form

$$H = -\sum_{ij}\sum_{\boldsymbol{q}\boldsymbol{q}'} J_{ij}\boldsymbol{S}_{\boldsymbol{q}}\cdot\boldsymbol{S}_{\boldsymbol{q}'}\mathrm{e}^{i\boldsymbol{q}\cdot\boldsymbol{R}_i}\mathrm{e}^{i\boldsymbol{q}'\cdot\boldsymbol{R}_j}. \tag{4.22}$$

For now we assume that the unit cell contains only one magnetic species. Since the exchange parameters only depend on the mutual distance between the two spins, it is convenient to rewrite the sum on $j \equiv \boldsymbol{R}_j$ as a sum in terms of the relative position with respect to the i-th spin, $\boldsymbol{d} = \boldsymbol{R}_j - \boldsymbol{R}_i$. The spin Hamiltonian can then be rewritten as

$$H = -\sum_{\boldsymbol{q}} J_{\boldsymbol{q}}|\boldsymbol{S}_{\boldsymbol{q}}||\boldsymbol{S}_{-\boldsymbol{q}}|\cos(\vartheta) \equiv \sum_{\boldsymbol{q}} E(\vartheta,\boldsymbol{q}), \tag{4.23}$$

where

$$J_{\boldsymbol{q}} = \frac{1}{N}\sum_{\boldsymbol{d}} J_d\mathrm{e}^{-i\boldsymbol{q}\cdot\boldsymbol{d}}. \tag{4.24}$$

The energy contribution associated to each vector $\boldsymbol{q}$ and angle ϑ can then be calculated with DFT. For small ϑ, the cosine can be expanded in a Taylor series. Hence, the Fourier component of the exchange parameter can be obtained by using the relation

$$J_{\boldsymbol{q}} = -\frac{1}{2|\boldsymbol{S}_{\boldsymbol{q}}||\boldsymbol{S}_{-\boldsymbol{q}}|}\frac{\partial^2 E(\vartheta,\boldsymbol{q})}{\partial^2\vartheta}. \tag{4.25}$$

This result can then be inserted into Eq. (4.24), which allows us to calculate the exchange coupling between two spins at a generic distance, d. Such method can be easily extended to the case of a generic number of magnetic species, in which the Hamiltonian can be cast in the form

$$H = -\sum_{ij}\sum_{\alpha\beta} J_{ij}^{\alpha\beta}\boldsymbol{S}_i^{\alpha}\cdot\boldsymbol{S}_j^{\beta}, \tag{4.26}$$

where the indices α and β run on the different non-equivalent spins in the unit cell. The formal procedure described above can then be repeated for a fixed pair of

magnetic species, when each new Fourier transform is performed on the sublattice made of all spins of a given species in different cells.

Although this method is more accurate and convenient with respect to energy differences based approaches, it is more computationally expensive for small systems and requires the use of a constrained DFT scheme.

4.1.1.2 Anisotropy

The number of different contributions to magnetic anisotropy makes it a strongly system dependent quantity. This holds also if one considers only the magneto-crystalline contribution. In fact, the chemical environment of an atom is known to strongly influence the anisotropy field acting on its magnetic moment [127]. For example, this is the case of an Fe layer deposited on MgO, where the interface induces a stronger anisotropy on the neighbouring magnetic atoms. In general, the anisotropic field is affected by any additional factor that breaks the symmetry of the atomic environment, such as structural disorder and chemical impurities. As a consequence, experimental values set a useful element of comparison for theoretical predictions, but should be tailored to a given system for accurate results.

The most common way to experimentally determine the magnetic anisotropy of a material is to measure the coercivity field, i.e. the field required to switch the magnetisation between $-M$ and $+M$. For strong enough fields, the switching will be uniform, meaning that the coercive field coincides with the anisotropy field, $H_k = 2K/M_s$. Results of low temperature measurements can then be used to extrapolate the 0 K value of the macroscopic anisotropy constant, which is related to the atomistic constant by the relation

$$k_u = \frac{H_k M_s V_{\text{atom}}}{2}, \tag{4.27}$$

where V_{atom} is the average atomic volume. From a theoretical point of view, k_u can be obtained as the difference in total energy between a calculation with the magnetisation aligned along the easy axis and one parallel to the hard axis. Since the typical energy scales for anisotropy constants are between 1 μeV and 1 meV per atom, as elevated numerical accuracy is essential to correctly capture such effects.

4.2 Spin Hamiltonian for ferromagnetic materials

The purpose of this section is to describe the methodology to practically determine the spin Hamiltonian that reproduces the properties of a given material. We will start by discussing the parameterisation of a simple ferromagnetic material such as bcc Fe. The spin Hamiltonian for this will then be adapted to the case of $L1_0$ FePt. The induced magnetic moment on the Pt atoms makes such material qualitatively different from pure Fe. This complication will be studied within two separate models: one using the approach presented in the previous section, where spin lengths are kept constant, and one where longitudinal spin fluctuations are explicitly taken into account. In conclusion, the formulation of a spin Hamiltonian to study the antiferromagnetic Heusler alloy Mn_3Ga will be presented.

4.2.1 bcc Fe

Bulk *bcc* Fe represents one of the prototypical ferromagnetic materials and its magnetic properties are relatively simple to study and well known. Being an elemental crystal with strongly localised magnetic moments, it can be modelled as a system of spins with uniform length (μ_{Fe} =2.2 μ_{B}) described by the spin Hamiltonian

$$\mathcal{H}_{\text{Fe}} = -\frac{1}{2}\sum_{ij} J_{ij}^{\text{Fe-Fe}} \boldsymbol{S}_i \cdot \boldsymbol{S}_j - \sum_i k_u^{\text{Fe}} S_{iz}^2 - \sum_i \mu_{\text{Fe}}\, \boldsymbol{S}_i \cdot \boldsymbol{H}_{\text{app}}. \tag{4.28}$$

The lattice vectors of the cubic unitary cell are aligned along the cartesian coordinates by assumption, and each of them corresponds to an easy axis. Nevertheless, the interest of this section is simply to study the features of the model around thermodynamical equilibrium, hence a single easy axis along the z direction is considered for simplicity. Moreover, the absence of asymmetry in the crystal structure implies a rather low atomistic anisotropy, $k_u^{\text{Fe}} = 5.65 \times 10^{-25}\,\text{J} = 3.5\,\mu\text{eV}$. For the moment, only first nearest neighbour exchange parameters are considered ($J_{ij}^{\text{Fe-Fe}} = 6.24 \times 10^{-21}\,\text{J} = 44\,\text{meV}$ [128]).

In order to verify the suitability of the chosen parameterisation of the Hamiltonian in Eq. (4.28), it is convenient to perform a set of simulations, where the spins are

allowed to relax to their equilibrium configuration. Since the details of the dynamics are here not of interest, the damping is set to an arbitrary (large) value of 0.1 in order to save computational time. After a small transient the total magnetisation will start to oscillate around its equilibrium value. Hence, it can be extracted by performing a time average. This can be repeated for a range of different temperatures, allowing us to estimate the Curie temperature, T_C, of a given system by fitting to the formula

$$M(T)/M(0) = \begin{cases} (1 - T/T_C)^n & , \quad T \leq T_C \\ 0 & , \quad T > T_C \end{cases}, \tag{4.29}$$

where the exponent, n, depends on the material and is roughly 1/3 for most cubic structures. The comparison of the extracted T_C with its experimental estimation is then a useful measure of the accuracy of the properties predicted by the spin model. Fig. 4.1 (a) displays the temperature dependence of the time averaged total mag-

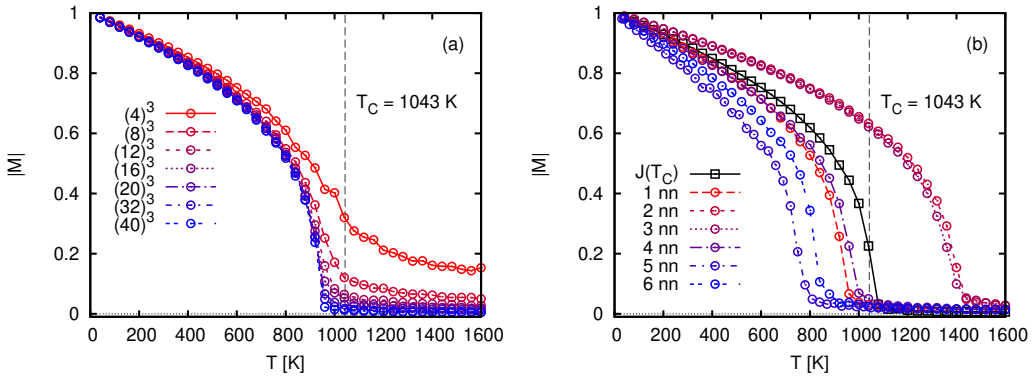

Figure 4.1: Total magnetisation of a bcc Fe cubic cell at different temperatures as predicted by the atomistic model. In both panels the dashed vertical line denotes the position of the experimental Curie temperature. Panel (a) shows results for cells of sizes ranging between 4^3 (red) and 40^3 (blue) with first nearest neighbours exchange parameters. In panel (b) the cell size is fixed to 20^3 and the range of the exchange interaction is varied up to 6 nearest neighbours (red to blue circles) taken. The black squares are obtained by using an effective first nearest neighbour exchange extracted from Eq. (4.16).

netisation for spins in cells of increasing size, that will be heron expressed in terms of the number of unitary cells. Here we consider cubic systems of increasing size, L^3, with L going from 4 to 40, assuming periodic boundary conditions and including only first nearest neighbour exchange parameters (taken from Ref. [128]). For low temperatures, the cell size has little to no influence on the total magnetisation. The differences become more relevant for temperatures close to T_C, although the curves for sizes above 20^3 are almost identical apart from their smoothness at $T = T_C$. It is easy to conclude that the Curie temperature for these simulation is estimated to be around 950 K, against the experimentally measured value of 1043 K. In principle, such underestimation can be corrected by including additional orders of the exchange parameter, although a rather large order might be required. Fig. 4.1 (b) shows the temperature dependence of the total magnetisation for a cell containing $(20)^3$ spins with a growing number of nearest neighbours (coloured circles). It is clear that including extra neighbours does not necessarily improve the estimation of the Curie temperature, and an elevated number of nearest neighbours is not normally convenient because it implies more expensive calculations and requires a growing number of exchange parameters to be calculated. In cases where the interest is limited to thermodynamical properties, it is useful to consider an effective first nearest neighbour exchange parameter extracted from the relation in Eq. (4.16). This choice yields, by construction, a Curie temperature rather close to the one provided as input [black squares in Fig. 4.1 (b)] and allows us to formulate a simple model that correctly reproduces the thermodynamics of the material.

The estimation of T_C is a useful test of the static properties of the model, but its dynamical properties can be probed by performing a ferromagnetic resonance (FMR) simulation. Similarly to the experimental procedure, a magnetic field is applied along the z direction and one can define the magnetisation correlation function as

$$C_{xx}(\omega) = \int dt \mathrm{e}^{-i\omega t} \frac{\langle M_x(0) M_x(t) \rangle}{M^2}. \tag{4.30}$$

The latter can then be related to the dynamical susceptibility through the fluctuation-dissipation theorem [129], which within linear response theory can be written as [130]

$$C_{xx}(\omega) = \frac{2K_B T\alpha}{1+\alpha^2}\left(\frac{\omega_0^2(1+\alpha^2)+\omega^2}{\Omega^4+(2\alpha\omega_0\omega)^2}\right), \tag{4.31}$$

where $\Omega^2 = \omega_0^2(1+\alpha^2) - \omega^2$ and $\omega_0^2 = \gamma H_z(1+\alpha^2)$. This equation can be used to fit the resonance peak and extract the Gilbert damping parameter, α, and the anisotropy field,

$$H_K = \frac{K}{2M} = H_z - H_{\text{app}}. \tag{4.32}$$

The magnitude of the anisotropy field plays an important role in determining the position of the resonant peak in the frequency domain. For low anisotropy systems such as bulk Fe, this implies that the peak is normally found at rather low frequencies, hence its estimation generally requires long simulation times. This problem can be overcome by applying an external magnetic field, so that the resonant frequency is moved away from the very low frequency region. Fig. 4.2 shows the calculated dynamic correlation function for bcc Fe at different temperatures. Such results were obtained with an applied field of 15 T and a simulation time of 1.5 ns. In order to reduce the computational costs a 8^3 cubic cell is used. Hence, the Curie temperature

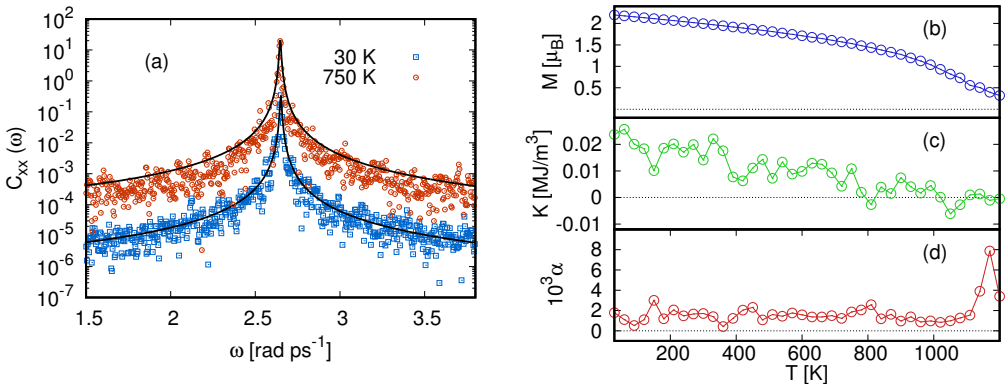

Figure 4.2: Results of a FMR simulation for bcc Fe. Panel (a) shows the FMR spectrum at 30 K (blue symbols) and 750 K (red symbols), where the black lines represent the curves fitted with the function in Eq. (4.31). The figure on the right-hand-side displays the temperature dependence of the total magnetisation (b), the macroscopic anisotropy constant (c) and the Gilbert damping (d) as extracted from the fit results.

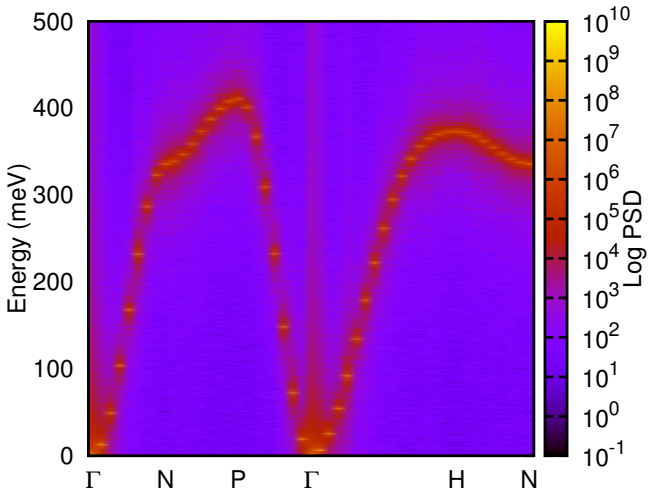

Figure 4.3: Dynamic structure factor for bcc Fe. The colour scale represents the logarithm of the power spectral density (PSD).

is expected to be overestimated with respect to the experimental one (see Fig. 4.1). Panel (a) of Fig. 4.2 shows an example where the position of the peak does not vary significantly with the temperature. We note that the signal is here relatively noisy and the resonant peaks are rather narrow because of the low Gilbert damping of bulk Fe (~ 0.001). This also explains the irregularities in the temperature dependence of the extracted macroscopic anisotropy constant, K, and the Gilbert damping shown in panels (c) and (d). However, it is clear that K vanishes more rapidly than the saturation magnetisation, in agreement with Eq. (4.15), and the damping parameter diverges near the T_C.

Ferromagnetic resonance simulations allow us to probe oscillation modes of the total magnetisation, i.e. where all spins oscillate in a coherent and uniform manner. A more general picture of the spin wave spectrum can be obtained by calculating the dynamic structure factor (DSF),

$$C(\boldsymbol{k},\omega) = \int dt \mathrm{e}^{-i\omega t} \sum_{\boldsymbol{r},\boldsymbol{r}'} \mathrm{e}^{-i\boldsymbol{k}\cdot(\boldsymbol{r}-\boldsymbol{r}')} \big\langle S_x(\boldsymbol{r},0) S_x(\boldsymbol{r}',t) \big\rangle. \tag{4.33}$$

From this formula it is clear that the magnetisation correlation function of Eq. (4.31) correspond to the DSF for $\boldsymbol{k} \equiv \Gamma$. Fig. 4.3 shows the calculated spin-wave spectrum

at 10 K. The colors indicate the logarithm of the power spectral density (PSD), $|C(\boldsymbol{k},\omega|^2$,that can be for different positions in the Brillouin Zone and at different energies. The width of the branches is here rather narrow because of the small Gilbert damping. Since the primitive cell for bcc Fe has a single spin, only an acoustic magnon branch is obtained.

4.2.2 The inclusion of longitudinal spin fluctuations

We present here an extension of the atomistic spin model that allows the spin lengths to vary during the dynamics, as opposed to having a fixed length as in the LLG dynamics. This generalisation is particularly relevant in cases where the length of some of the atomic spins is strongly related to the surrounding atomic moments. In $L1_0$ FePt the Fe atoms cause the appearance of an induced magnetic moment on Pt atoms, which are normally not magnetic. The magnitude of such moments depends on the orientation of the spins at the neighbouring Fe sites. An atomistic spin model accounting for such features was formulated by Mryasov *et al.* and can be found in Ref. [131] together with all the values that will be employed here to parameterise the spin Hamiltonian for FePt. In particular, first principles simulations show that the magnitude and orientation of the Pt moments, $\boldsymbol{S}_i^{\mathrm{Pt}}$, depend linearly on the surrounding Fe atoms and such relation can be expressed as

$$\boldsymbol{S}_i^{\mathrm{Pt}} = \frac{\chi_i^{\mathrm{Pt}}}{\mu_{\mathrm{Pt}}^0} \sum_j J_{ij}^{\text{Fe-Pt}} \boldsymbol{S}_j^{\mathrm{Fe}}, \tag{4.34}$$

where χ_i^{Pt} is the local Pt susceptibility constant and $\mu_{\mathrm{Pt}}^0 = 0.36\mu_B$ is the magnetic moment of the Pt atoms when all the spins of the Fe sites are aligned ($\mu_{\mathrm{Fe}}^0 = 2.86\mu_B$). It is then possible to formulate an extended spin model (ESM) where the Pt degrees of freedom are wrapped within the Fe ones, and FePt can be studied with the following spin Hamiltonian

$$\mathcal{H}_{\mathrm{FePt}}^{ESM} = -\sum_{ij} \widetilde{J}_{ij} \boldsymbol{S}_i^{\mathrm{Fe}} \cdot \boldsymbol{S}_j^{\mathrm{Fe}} - \sum_i k_u^{\mathrm{Fe}} (S_{iz}^{\mathrm{Fe}})^2 - \sum_{ij} d_{ij}^{(2)} \boldsymbol{S}_i^{\mathrm{Fe}} \cdot \boldsymbol{S}_j^{\mathrm{Fe}} + \mathcal{H}_{\mathrm{app}}. \tag{4.35}$$

Importantly, the ESM Hamiltonian includes a symmetric exchange, $d_{ij}^{(2)}$, between Fe spins in order to account for the anisotropy contribution introduced by the strong

spin-orbit coupling interactions in Pt atoms. This factor is essential in order to correctly reproduce the temperature dependence of the first-order (macroscopic) anisotropy that is seen in experiment, to vary as $K(T) \propto M(T)^n$ with an anomalous $n = 2.1$ exponent, opposed to the $n = 3$ exponent predicted for uniaxial anisotropy [132].

Although the ESM reproduces the correct thermodynamical properties of FePt, it is not easily applicable to other materials, since they are likely to require an entirely different parameterisation of the "non-dominant" moments. A valid alternative is to explicitly consider all magnetic moments and relax the constrain on the spin lengths. The LLG equation has then to be reformulated in order to allow for spin length relaxation and now reads

$$\frac{\partial \boldsymbol{S}_i}{\partial t} = -\gamma \boldsymbol{S}_i \times \boldsymbol{H}_i + \gamma\lambda \boldsymbol{H}_i + \boldsymbol{\xi}_i, \tag{4.36}$$

where the same damping parameter, λ, is adopted to determine both the rotational and the longitudinal dissipation. This equation will be hereon referred to as the generalised spin equation of motion (GSE). The spin Hamiltonian now has the form ($\alpha, \beta =$ Fe, Pt)

$$\mathcal{H}^{LSF}_{\text{FePt}} = -\sum_{ij}\sum_{\alpha\beta} J^{\alpha-\beta}_{ij} \boldsymbol{S}^{\alpha}_i \boldsymbol{S}^{\beta}_j - \sum_i \sum_{\alpha} k^{\alpha}_u (\boldsymbol{S}^{\alpha}_{iz})^2 + \mathcal{H}_{\text{app}} + \mathcal{H}_{\text{l}}, \tag{4.37}$$

where the easy axis is assumed to be along z and the anisotropy constant is different for the two species to account for the stronger SO interactions in Pt atoms (k^{Fe}_u =−0.097 meV, k^{Pt}_u =1.427 meV). The longitudinal energy, $\mathcal{H}_l$, is assumed to have the Landau-like Hamiltonian

$$\mathcal{H}_l = \sum_i \sum_{\alpha} \left[A_\alpha |\boldsymbol{S}^{\alpha}_i|^2 + B_\alpha |\boldsymbol{S}^{\alpha}_i|^4 + C_\alpha |\boldsymbol{S}^{\alpha}_i|^6 \right], \tag{4.38}$$

where the parameters A_α, B_α and C_α are to be determined for each species, $\alpha =$ Fe, Pt, since they depend on the local density of states, $D_\alpha(E)$. The set of parameters for a given species can be estimated as the values fitting the function

$$E_{tot}(M) = \int_{-\infty}^{E^{\uparrow}_F} dEED_\alpha(E) + \int_{-\infty}^{E^{\downarrow}_F} dEED_\alpha(E) - \frac{IM^2}{4}, \tag{4.39}$$

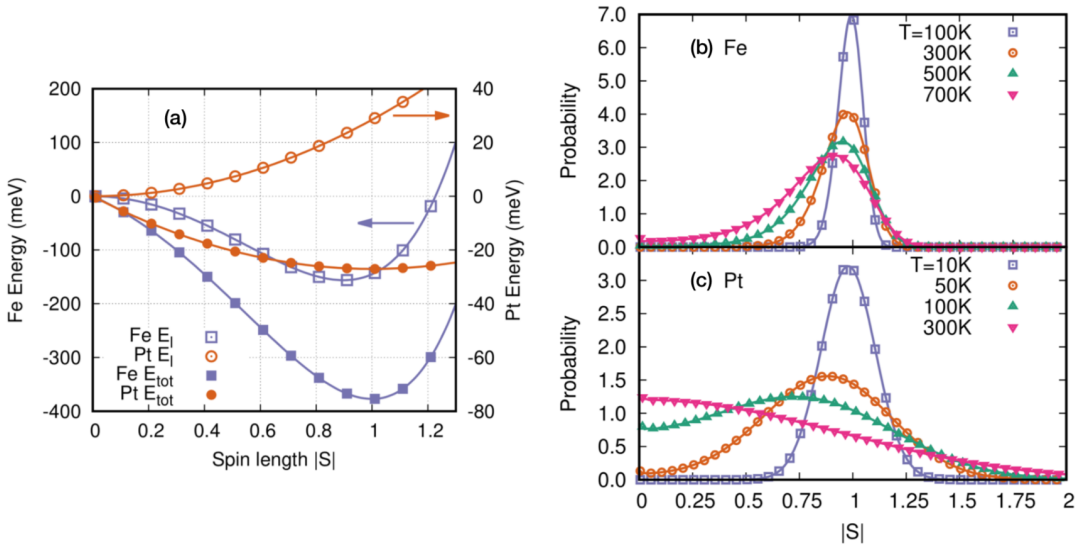

Figure 4.4: The variation of the energy and the probability distributions for the spin length of $L1_0$ FePt during the dynamics described by the GSE. Left: the longitudinal (hollow symbols) and total (full symbols) energies for Fe (blue) and Pt (orange) depending on the respective spin length. The energy scale on the left-hand side refers to Fe spins, the one on the right-hand side to Pt spins, are pointed out by the coloured arrows. Right: probability distribution for the Fe (b) and Pt (c) local spins for different temperatures. Image credit: [134].

where $E_F^{\uparrow}$ and $E_F^{\downarrow}$ are the Fermi energies for majority and minority spins, and the Stoner parameter can be calculated as

$$I = \frac{E_F^{\uparrow} - E_F^{\downarrow}}{M}. \tag{4.40}$$

The energy $E_{tot}(M)$ for a given total magnetisation, M, can be estimated within first principles simulations and for *bcc* Fe this procedure yields A_{Fe} =−441.0 meV, B_{Fe} =150.5 meV and C_{Fe} =50.7 meV [133]. The linear dependence between the Pt and Fe moments expressed in Eq. (4.34) implies that the longitudinal energy for Pt atoms in FePt must be approximately quadratic with the spin length, with energy minimum at $|\boldsymbol{S}_i^{\mathrm{Pt}}| \equiv S^{\mathrm{Pt}} = 0$. This implies that $B_{\mathrm{Pt}} = 0$ and $C_{\mathrm{Pt}} = 0$, while the remaining parameter, A_{Pt}, can be found by writing the equation of motion of

Eq, (4.36) for a system of aligned spins in equilibrium,

$$\frac{\partial S^{\mathrm{Pt}}}{\partial t} = 0 = 2A_{\mathrm{Pt}}S^{\mathrm{Pt}} - \sum_{\alpha} J^{\mathrm{Pt}-\alpha}S^{\alpha} - 2k^{\mathrm{Pt}}S^{\mathrm{Pt}}. \tag{4.41}$$

Since the Fe spin length corresponding to the minimum energy is unitary, we can conclude that the longitudinal energy for Pt is determined by

$$A_{\mathrm{Pt}} = k^{\mathrm{Pt}} + \frac{1}{2}\sum_{\alpha} J^{\mathrm{Pt}-\alpha}. \tag{4.42}$$

Figure 4.4 (a) shows the total and longitudinal energy for each spin species depending on the respective spin length. Hollow symbols show that the longitudinal energies follow the desired trends, with energy minima around $|S| = 1$ for Fe (blue) and $|S| = 0$ for Pt (blue). The remaining panels of the same figure display how the spin length distributions change depending on the temperature. Fe spins [panel (b)] have a rather homogeneous spin length at 100 K, while for higher temperatures the peak of the distribution slightly shifts from $|S| = 1$ towards 0 as the left-hand side tail grows longer. In the case of Pt spins [panel (c)] the distribution is significantly

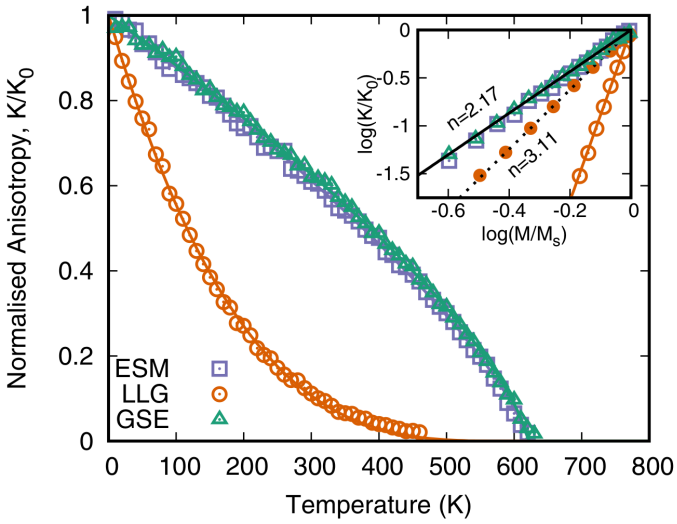

Figure 4.5: Temperature dependence of the anisotropy predicted within the extended spin model (blue squares), by using the Hamiltonian in Eq. (4.37) without the longitudinal energy and the standard LLG equation (orange circles), and by employing the GSE (green triangles). Image credit: [134].

broader and undergoes more rapid variations with increasing temperature, to the point that at 300 K its peak almost coincides with $|S| = 0$. In summary, the parameterisation of the longitudinal fluctuations discussed here allows us to reproduce a temperature dependence for the magnetic anisotropy, which is strikingly similar to the one obtained within the ESM (Fig. 4.5). Both the latter models (blue squares and green triangles) reproduce the same critical exponent, $n = 2.17$, which is rather close to the experimental one of 2.1, in contrast to the value of 3.11 predicted with a spin Hamiltonian with fixed spin lengths (orange circles). Additional comparisons between these three models applied to FePt can be found in Ref. [134].

4.3 Spin-torque driven dynamics in Fe/MgO-based junctions

In Chapter 3 the details of the spatial dependence of the spin torques were shown to be strongly dependent on the material composition of the free layer. However, first principles data alone is not sufficient to determine how the different decay ranges affect the spin dynamics. Here we combine the results of the transport calculations with the atomistic models discussed before to explore the material dependence of the current-driven spin dynamics. The effect of the current on the motion of the classical spin system can be introduced by adding a spin torque term to the LLG equation of Eq. (4.7) to obtain

$$\frac{\partial \boldsymbol{S}_i}{\partial t} = -\gamma' \boldsymbol{S}_i \times \boldsymbol{H}_i - \alpha\gamma' \boldsymbol{S}_i \times (\boldsymbol{S}_i \times \boldsymbol{H}_i) + \frac{1}{\mu_i} \boldsymbol{T}_i(V, |\{\boldsymbol{S}_i\}). \tag{4.43}$$

This is known as the Landau-Lifshitz-Gilbert-Slonczewski (LLGS) equation. There are several ways to map the *ab-initio* spin torques onto the STT term added here. The most general approach is based on calculating the spin torques for an arbitrary number of bias voltages, V, and angles between the magnetisations, ϑ. This allows us to perform a full two-dimensional interpolation of the data set and extrapolate the STT acting on the i-th spin for any given voltage and angle. As an alternative, one can assume the spin torques to a have linear dependence on the bias and have

the same angular dependence predicted by Slonczewski, here contained in Eq. (3.2). Under these hypothesis, the only result needed to characterise the STT is given by a zero-bias calculation for $\vartheta = \pi/2$. Between the two methods, a full-interpolation is clearly preferable, since it has wider range of applicability. Nevertheless, the elevated number of calculations necessary for the interpolation makes it not favorable to study a large number of systems. Moreover, the two schemes were shown to give the same critical voltages for a Co/MgO/Co/Cu junction for low values of the anisotropy and Gilbert damping parameters [99]. For such reasons, here we will parameterise the torques acting on a given free layer as

$$\boldsymbol{T}(V, \boldsymbol{S}_i) = \boldsymbol{T}^{\parallel}(V, \boldsymbol{S}_i) + \boldsymbol{T}^{\perp}(V, \boldsymbol{S}_i) \equiv V\left[\tau_{\parallel}^{i}\boldsymbol{S}_i \times \boldsymbol{S}_i \times \hat{\boldsymbol{P}} + \tau_{\perp}^{i}\boldsymbol{S}_i \times \hat{\boldsymbol{P}}\right], \tag{4.44}$$

where $\tau_{\parallel}^{i}$ and $\tau_{\perp}^{i}$ are the magnitude of the calculated torkance at the i-th site for $\vartheta = \pi/2$ and $\hat{\boldsymbol{P}}$ is the direction of the spin polarisation of the current. We note however that this expression cannot be directly utilised in Eq. (4.43), since the latter equals to the LLG equation in the LL form, i.e. the damping term is not expressed through a time derivative. It is thus necessary to repeat the same derivation described at the beginning of this Chapter by including explicitly the spin torque term, which yields to the reformulation of the torques as

$$\boldsymbol{T}_i = -V\gamma'\left[(\tau_{\parallel}^{i} + \alpha\tau_{\perp}^{i})\boldsymbol{S}_i \times \boldsymbol{S}_i \times \hat{\boldsymbol{P}} + (\tau_{i}^{\perp} + \alpha\tau_{\parallel}^{i})\boldsymbol{S}_i \times \hat{\boldsymbol{P}}\right]. \tag{4.45}$$

Now, both components of the STT appear in both damping-like and field-like motions. Nevertheless, we note that the out-of-plane torque has little or no influence on the switching dynamics, since its intensity, already smaller that the in-plane counterpart, is multiplied by α that is generally between 0.001 and 0.01.

The objective of this section is to analyse the differences between the switching dynamics in junctions with similar properties that are subject to qualitatively different spin torques. This is the case, for example, of Fe and Fe/Cu free layers, where the different electrodes resulted in a significant change in the distribution of the STT of the Fe atoms. The first part of the analysis will focus on the estimation of the critical voltage, V_c, needed for switching, the corresponding switching times and their

temperature dependence. We are then interested into studying the oscillation modes induced by different spatial profiles of the spin torques. These will clearly depend on how the chosen voltage relates to the critical voltage of each junction. Therefore, the analysis will be done by comparing the results of calculations for a voltage of $V = 1.2V_c$. The entire study then critically depends on an accurate estimation of the critical voltage. The latter can be indicatively estimated by performing calculations for different biases, V, and identify the minimum value of V for which magnetisation reversal occurs. Nevertheless, a more accurate estimate for V_c can be obtained by fitting the bias dependence of the switching times with an analytical formula derived assuming uniform switching. Thus, we consider the dynamics of a uniform magnetisation, $\boldsymbol{S}_i \equiv \boldsymbol{M}$, in a magnetic field that is parallel to the z direction, namely

$$\boldsymbol{H} = H\hat{\boldsymbol{z}} = \Big(H_{\text{app}} + H_K m_z\Big)\hat{\boldsymbol{z}}, \tag{4.46}$$

where for simplicity we defined $H_K = 2K_u/M_s$ and $m_z = M_z/M_s$. The z component of the LLGS in this context becomes

$$\frac{\partial m_z}{\partial t} = -\gamma'\alpha\left(H + \frac{\tau_i^{\perp} + \alpha\tau_{\parallel}^i}{\alpha}\right)(m_z^2 - 1), = \omega(m_z + h)(1 - m_z^2) \tag{4.47}$$

where the triple cross product rule $\boldsymbol{a}\times\boldsymbol{b}\times\boldsymbol{c} = \boldsymbol{b}(\boldsymbol{a}\cdot\boldsymbol{c}) - \boldsymbol{c}(\boldsymbol{a}\cdot\boldsymbol{b})$ was used. Moreover, the notation was simplified by defining $\omega = \gamma'\alpha H_K$ and

$$h \equiv h(V, H_{\text{app}}) = \frac{1}{H_K}\left(H_{\text{app}} + \frac{\tau_i^{\parallel} + \alpha\tau_{\perp}^i}{\alpha}\right). \tag{4.48}$$

The equation can now be easily solved by separating the variable and integrating both sides, which yields to the solution

$$\omega(t - t_0) = (1 - h^2)\ln|m_z + h| - (2 + 2h)\ln|1 - m_z| - (2 - 2h)\ln|1 + m_z|. \tag{4.49}$$

The constants resulting from the two integrations were combined in the time t_0 that can be found by imposing the initial condition $m_z(0) = m_0$, and reads

$$t_0 = \frac{1}{2\omega(1 - h^2)}(-2\ln|m_0 + h| + (1 - h)\ln|1 - m_0| + (1 + h)\ln|1 + m_0|). \tag{4.50}$$

Finally, we can define the switching time, t_s, as the time at which the magnetisation vector first crosses the $z = 0$ axis. Inserting this condition in the solution, the switching time can be estimated to be

$$t_s = t_0 + \frac{\ln|h|}{\omega(1-h^2)} T^{\parallel}, \tag{4.51}$$

where here $T^{\parallel}$ quantifies the in-plane component of the torque as written in Eq. (4.45). We remark that this expression depends on both the bias voltage and the applied field. Eq. (4.47) indicates that switching is possible only if $m_z + h \geq 0$, which leads to the condition

$$h(V, H_{\text{app}}) = \frac{1}{H_K}\left(H_{\text{app}} + \frac{\tau_i^{\parallel} + \alpha\tau_{\perp}^{i}}{\alpha}\right) \geq -m_z(0). \tag{4.52}$$

Therefore, the critical voltage for vanishing applied field, V_{c0}, can be found by inverting the equation $h(V, 0) = -m_z(0)$ and reads

$$V_{c0} = -\frac{\alpha m_z(0) H_k}{\tau^{\parallel}}, \tag{4.53}$$

where the out-of-plane torques are omitted for simplicity. As expected, the critical voltage is directly proportional to the anisotropy field and the Gilbert damping, while it is inversely proportional to the strength of the in-plane torques. Moreover, the critical voltage for a finite applied field can be estimated by inserting Eq. (4.53) in the switching condition expressed by Eq. (4.47), namely

$$V_c(H) = V_{c0}\left(1 - \frac{1}{m_z(0)}\frac{H_{\text{app}}}{H_K}\right). \tag{4.54}$$

4.3.1 Fe: different leads

We now move to analyse the current driven-dynamics in Fe and Fe/Cu free layers. We consider a stack of eight atomic planes of *bcc* Fe with a cross section formed by 4×4 unit cells for 0 K simulations, that is increased to 32×32 for finite-temperature ones. The out-of-plane size is here the same as the number of magnetic atoms considered in the torkance calculation for Fe/MgO/Fe/Cu [Fig. 3.4 (a)]. We note that a bigger magnetic stack was considered for the pure Fe free layer [see Fig. 3.3 (b)].

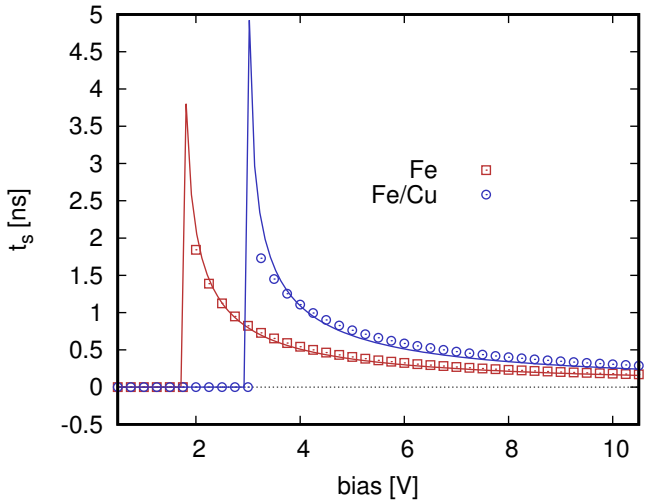

Figure 4.6: Bias dependence of the switching time in Fe (red) and Fe/Cu (blue) free layers at 0 K. The lines represent the result of a fit to the function defined in Eq. (4.51) the spin dynamics data (symbols).

However, the torkance in such case vanishes within a few atomic layers from the interface with the tunnel barrier. Hence, such system can be truncated at an arbitrary position deep enough in the magnetic layer. We remark, however, that in general one should consider the change in the total Gilbert damping due to the reduction of the layer thickness. We use here first nearest neighbour exchange parameters with their intensity chosen so to reproduce the correct Curie temperature of Fe (see section 4.2.1 for more details). Both the magnetic anisotropy constant and the Gilbert damping are known to be significantly different for Fe atoms in bulk or in proximity to an interface with MgO. In order to account for such effects we consider a uniaxial anisotropy constant of 1.602×10^{-23} J and a damping parameter of 0.005. These values are average estimations from the magnetic anisotropy calculations of Ref. [135] and the FMR measurements of Ref. [136].

We start by studying the bias dependence of the dynamics at 0 K in both systems for a range of bias voltages. Figure 4.6 shows the switching times calculated for a simulation cell of $4 \times 4 \times 1$ unit cells, with periodic boundary conditions applied only within the plane. Since at 0 K there are no thermal fluctuations, the dynamics is

deterministic, as opposed to stochastic as at finite temperatures. As a consequence, the switching is rather uniform and a relatively small simulation cell can be adopted. Eq. (4.51) is used here use to fit the data and to estimate the critical voltages. For the Fe and Fe/Cu layers we find 1.75 V and 3.00 V, respectively. We remark that the only difference between the two set of simulations is the value of the spin torques. The simplest way to explain this difference is through an analysis of the total STT acting on each layer. In fact, the total torque for a Fe electrode is found to be about 1.6 times larger than that for the Cu electrode. This factor is significantly close to the inverse of the ratio between the two critical voltages, namely $V_{c0}^{\mathrm{Fe}}/V_{c0}^{\mathrm{Cu}} \sim 1/1.7$. This coarse estimation seems to indicate that the critical voltage scales inversely with the integrated spin torque.

We also note that both critical voltages are above 1.5 V, which defines the limit of validity of the torkance approximation. This implies that the finite bias torques should be actually employed to properly estimate the switching properties of the MTJs. Nevertheless, voltages beyond 1.5 V are likely to drastically modify the tunnelling properties of the junction since at such voltages different orbital symmetries contribute to the current. As a consequence, the STT at high voltages is likely to have a different spatial trend than in the zero-bias limit. Note that the spin-polarisation of the tunnelling current gets reduced for $V \gtrsim 1.5\,\mathrm{V}$. Therefore, we consider switching by applying an additional magnetic external field to reduce the critical voltage to the range of validity of the torkance approximation.

The dependence of the critical voltage with respect to the applied field can be extracted from Eq. (4.54), given the zero-field value, V_{c0}. We apply here a magnetic field of 1 T along the z direction (parallel to the spin-current), so that the critical voltage becomes 0.2955 V for Fe and 0.5066 V for Fe/Cu. We note that the chosen applied field is comparable, but still weaker, than the macroscopic anisotropy field that can be easily calculated ($\sum_i 2k_u m_i$) to be 1.54 T. It is clear that the same voltage applied to both junctions results in a rather different dynamics. Hence, instead of studying the switching at fixed voltages common for both systems, we consider the dynamics for voltages that correspond to a fixed fraction of the critical voltage

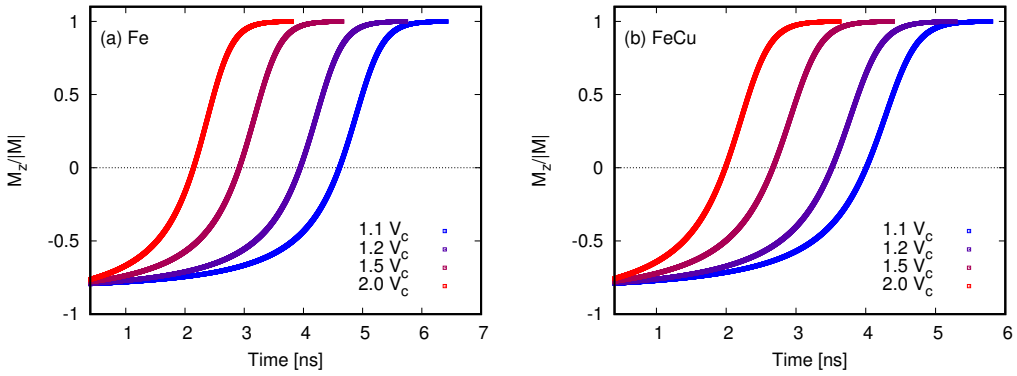

Figure 4.7: Current-induced switching in Fe (a) and Fe/Cu (b) free layers at 0 K for an applied field of 1 T and different voltages.

characteristic of each free layer. This allows one to better compare the influence of the spin torques on the dynamics in the two cases. Figure 4.7 displays the time-dependence of the z component of the total magnetisation in the two systems and for different voltages, that are here quantified in terms of the critical voltage of the specific system [as from Eq. 4.54]. This fact also holds for the switching at finite temperatures, shown in Figure 4.8. In this case the switching is described through a Langevin dynamics in order to include thermal fluctuations. As a consequence, different simulations for the same set of parameters will not produce the same results. Here we simulate the dynamics considering ten different trajectories for each given system, voltage and temperature, that were then averaged to obtain the dashed lines in figure 4.8. We note that the switching times are not remarkably affected by the temperature and are distributed on a rather broad range. In the case of Fe, this is particularly true for voltages close to the critical voltage, although more uniform estimations are found for higher voltages. In addition, the average switching times seem to decrease monotonically with both the temperature and the applied voltage, and are rather uniform for temperatures of 200 K and above. In contrast, the distribution of the switching times for a Fe/Cu free layer remains rather broad for all biases considered. In addition, for low voltages the average switching times are rather uniform for 100 K, 200 K and 300 K.

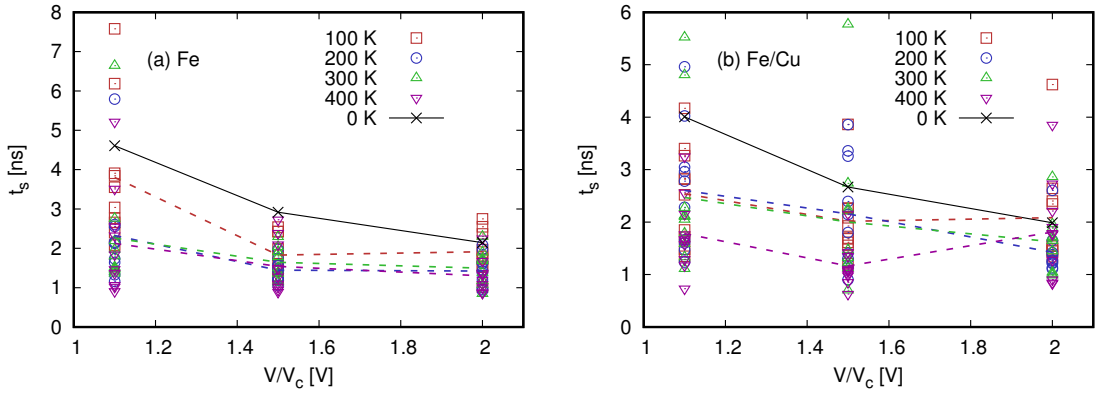

Figure 4.8: Bias dependence of the switching times in (a) Fe and (b) Fe/Cu at 0 K (black), 100 K (red), 200 K (blue), 300 K (green) and 400 K (purple). The dashed lines show the trend of the average switching time for a given finite temperature.

In conclusion, the different trend of the spin torques has significant consequences in the switching dynamics. In fact, we remind that the spin torques are the only factor that is changed when moving from one free layer and the other. In particular, our results show that a sharply decaying torque (as in Fe) implies lower critical voltage and better stability to thermal fluctuations, while the switching times are generally lower for oscillating spin torques. In order to further analyse these differences we consider the time dependence of the correlation between spins at different distances from the insulating barrier. This is quantified by the means of the spin-spin correlation function,

$$C_\alpha^i(t) = \int d\omega \mathrm{e}^{i\omega t} \tilde{S}_0^\alpha(\omega) \tilde{S}_i^\alpha(\omega), \tag{4.55}$$

Here $\alpha = x, y, z$, i runs over the number of spins in the unit cell and the Fourier transform of the orientation of the i-th spin in the unit cell is defined as

$$\tilde{S}_i^\alpha(\omega) = \int \frac{dt}{2\pi} \mathrm{e}^{-i\omega t} S_i^\alpha. \tag{4.56}$$

This quantity allows us to analyse the change in orientation of each spin in the unit cell, $\boldsymbol{S}_i$, with respect to the spin at the interface, that by convention is here denoted as $i = 0$. We note that the time variable that the correlation function depends on does not correspond to the real time, but can be interpreted as a measure of the

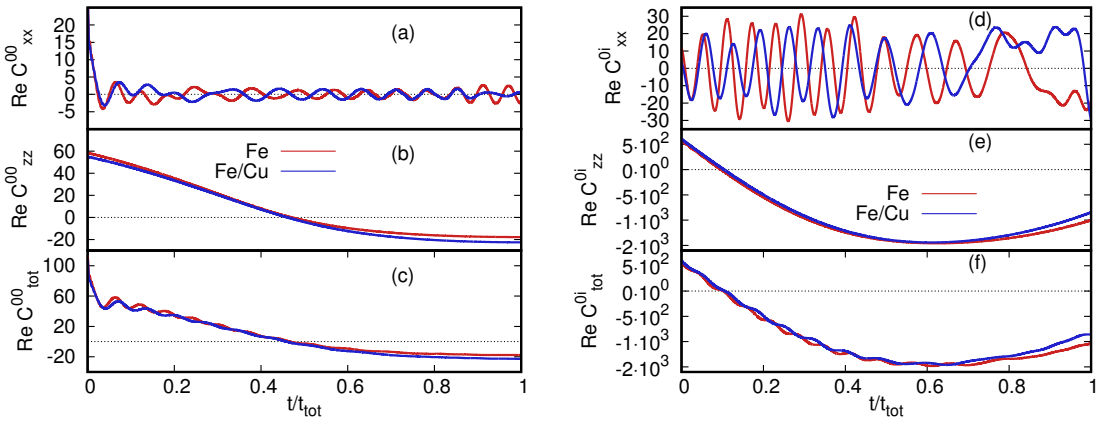

Figure 4.9: Study of time-dependent spin correlations during the magnetisation switching at 0 K for Fe (red) and Fe/Cu (blue) free layers. Left panel: (a) the xx and (b) the zz component and (c) the total auto-correlation function for the spin at the MgO/free layer interface. Right panel: (d) the xx and (e) the zz component and (f) the total correlation function between the interfacial spin and all the others.

time delay. By construction, the spin correlation function is qualitatively different for $i = 0$ and $i \neq 0$. For simplicity, the former case will be hereon called the "auto-correlation" function, and the notation C_α^i will represent the correlation function for $i \neq 0$.

Figure 4.9 shows the different components of the auto-correlation (left-hand side panel) and the spin-spin correlation (right-hand side panel) functions as calculated in the two cases at 0 K and for a voltage of $1.1V_c$. Here the time is normalised over the total simulation time to yield a easier comparison between different trajectories. Since the system has perfect in-plane symmetry the x and y component of the correlation functions are identical. The in-plane auto-correlation function for the the two cases [panel (a)] shows that the different spin torques trends imply different phases of the precession modes for the interfacial spin. The out-of-plane auto-correlation is then very similar in the two cases and basically corresponds to the average switching dynamics of the spins in the first layer. Similar considerations hold for the in-plane and out-of-plane component of the spin-spin correlation [panels (d), (e)]. We note that in this case the correlation functions for the different atoms, $i = 1, \cdots, 7$, are

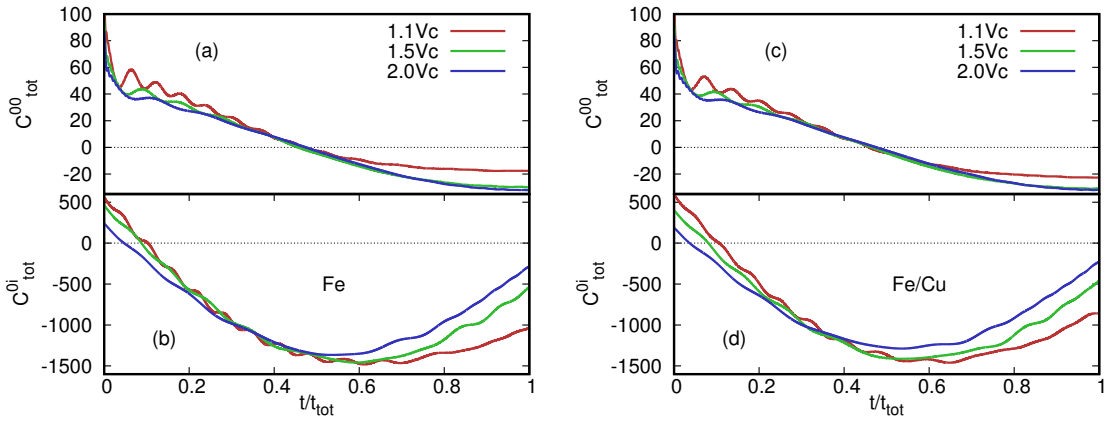

Figure 4.10: Study of the bias dependence of the spin correlations for the switching dynamics in (left panel) Fe and (right panel) Fe/Cu free layers. The top (bottom) panels show the total auto- (spin-spin) correlation functions for each free layer for voltages of (red lines) 1.1, (green lines) 1.5 and (blue lines) 2.0 in units of the critical voltage.

virtually identical to one another. In particular, C_x^i oscillates with different phase in the two cases, thus indicating that different spin torques imply different precession frequencies. Moreover, the trend of C_z^i shows that the first layers move out of synchronisation with respect to the others, although at later times they eventually become correlated. This is explained since the torque always peaks at the first layer. We note that the features just discussed for the in-plane and out-of-plane correlation functions can also be extracted from the total functions [panels (c) and (f)], defined as

$$C_{\rm tot}^{0,i} = C_x^{0,i} + C_y^{0,i} + C_z^{0,i}. \tag{4.57}$$

In fact, it is clear that the out-of-plane component dictates the general profile of $C_{\rm tot}^{0,i}$, while the in-plane modulate such trend by the means of small oscillations.

Figure 4.10 shows the total correlation functions for different bias voltages. The instantaneous correlation, for $t = 0$, decreases for increasing voltage, meaning that stronger V leads to the spins moving one against the other. Both the auto-correlation and the spin-spin correlation has stronger oscillations for lower voltages. From the

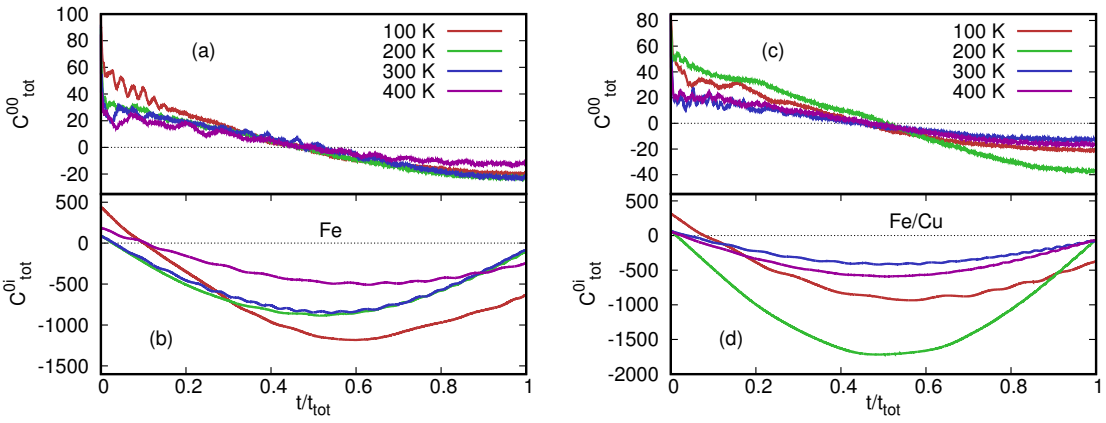

Figure 4.11: Study of the temperature dependence of the spin correlations for the switching dynamics in (left) Fe and (right) Fe/Cu free layers. The top (bottom) panels show the total auto- (spin-spin) correlation functions for each free layer for a voltage of $V = 1.1V_c$ at (red lines) 100 K, (green lines) 200 K, (blue lines) 300 K and (purple lines) 400 K.

top panels we can evince that the spin at the interface has a stronger delay for higher voltages that for $V = 1.1V_c$. In contrast, the spin-spin correlations [bottom panels] approaches the zero-axis strikingly faster for higher voltages. We note that a weaker correlation at the end of the trajectory seems to correspond to lower switching times. We also note that the spin correlations for the two different electrodes are strikingly similar.

We conclude our analysis of Fe and Fe/Cu junctions by discussing the spin correlations at finite temperatures. For simplicity, we present the results for a single trajectory for each temperature and voltage. In each case, we chose the trajectory with switching time closer to the average one for the given simulation parameters, and the respective correlation functions are shown in Fig. 4.11. The results for the different temperatures are here not remarkably different, and no particular trend can be evinced. This can be attributed to the broad distribution range of the switching times, and confirms the elevated temperature instability of the magnetisation switching in Fe and Fe/Cu layers.

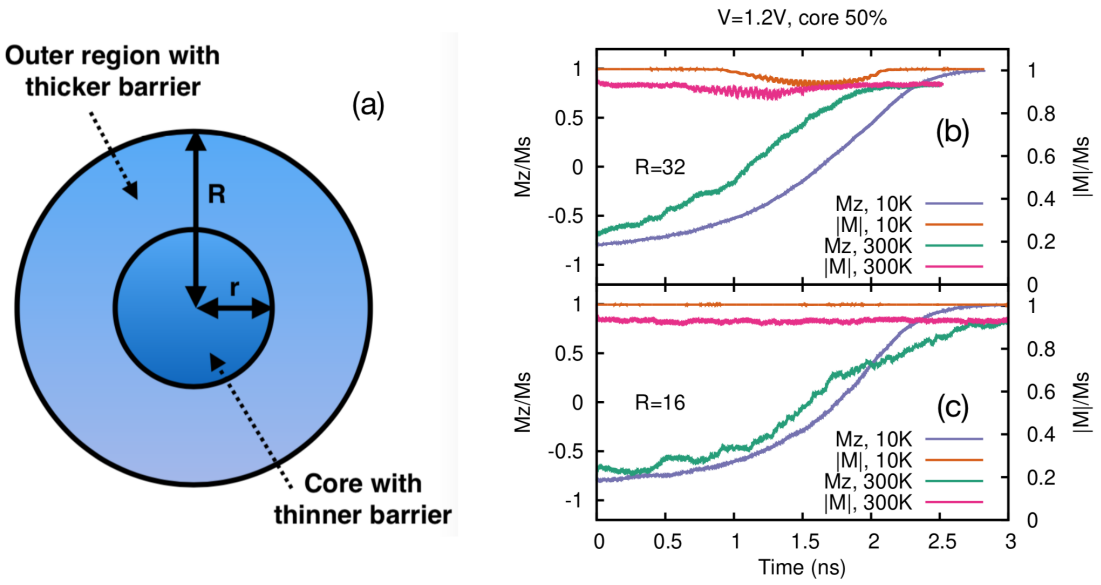

Figure 4.12: Left panel: Graphical representation of the system setup for spin dynamics simulations with disordered barrier. The inner core is here composed by MTJs with a 5 MgO MLs, while 6 MLs are considered for the outer core. Right panel: trajectories of the magnetisation switching at 10 K (purple) and 300 K (green) for disk radii, R, of (b) 32 and (c) 16 unit cells. Courtesy of Dr. Matthew Ellis.

4.3.2 Disordered Fe/MgO/Fe

In the previous Chapter we have explained that the transport properties of Fe/MgO/Fe are strongly influenced by disorder effects. In particular, the results of spin torque calculations for different barrier thicknesses were presented [see Fig. 3.6]. Here such results are combined with atomistic spin dynamics to explore the effects that variations in the barrier thickness have on the switching dynamics. We note that all results here presented on disordered Fe/MgO/Fe structures have been obtained through simulations performed by Dr. Matthew Ellis as part of an on-going collaboration.

We consider a cylindrical simulation cell, where all spins are described by the spin Hamiltonian developed for *bcc* Fe. The disorder is then introduced by assuming that different regions of the cross section are subject to different spin torques, as a consequence of a change in the barrier thickness. In fact, we have previously

shown that the torkance, as the current, decays exponentially with the number of monolayers in the MgO barrier. Here we assume that spins within a radius, r, from the center are deposited above an MgO spacer of 5 MLs, while the rest of the cross section is deposited on a thicker barrier, of 6 MLs [see Fig. 4.12 (a)]. We recall that all the other junctions considered in this thesis contain 6 MgO monolayers. This implies that the outer region will be subjected the same spin torques analysed above (for a Fe electrode), while the STT will be stronger by almost a factor 10 [see Fig. 3.6] in the inner region because of the increase in the tunnelling current. Here we consider an inner region that corresponds to 50% of the total area, for cross sections with a total radius, R, of 16 and 32 unit cells, i.e. R =9.2 nm and R =18.4 nm, respectively.

Figure 4.12 (b) shows the trajectories of the magnetisation for the two different sizes at 10 K and 300 K. Here magnetisation reversal is achieved in the absence of an applied field and for times lower to the ordered junction. Moreover, the switching dynamics seems to be faster for larger systems. This indicates that in this case the switching properties are essentially given by the amount of total torque that acts on the free layer. In other words, the presence of the stronger spin torques in the core region is enough to reduce the switching times and the critical voltage. In addition, a fixed ratio between the inner and outer regions implies that larger systems will be subjected to stronger spin torques. In this case this is true since the intensity of the torkance for 5 MLs is more than twice than the one for 6 MLs. Therefore, for a fixed ratio of 1:1 between the two regions, the total torkance increases with the size of the total system.

A second general message that can be extracted from these simulations is that switching occurs through a domain wall motion. The latter is activated by the stronger torkances in the inner region, although the spin texture does not reflect the difference in the thickness of the underlying barriers. This can be evinced from Fig. 4.13, where we present different snapshots of the dynamics for the two disc sizes. For the smallest cross section [top panels] the domain wall is not distinguishable at 10 K, although some irregularities appear in the spin distribution at 300 K. In contrast, the larger disk clearly displays the presence of a domain wall. The latter is

rather regular and distinct at 10 K while it becomes significantly more irregular at higher temperatures. We remark that in none of the spin distributions presented it is possible to identify the regions with thinner insulating barriers.

4.3.3 $L1_0$ FePt

We conclude the Chapter by comparing the dynamics in a pure FePt lead and in a FePt/Fe free layer. We consider the latter to be composed by 4 FePt and 4 Fe layers, since the torkance rapidly vanishes in Fe. In contrast, the torkance for the FePt layer oscillates deep into the electrode. Nevertheless, the oscillations are

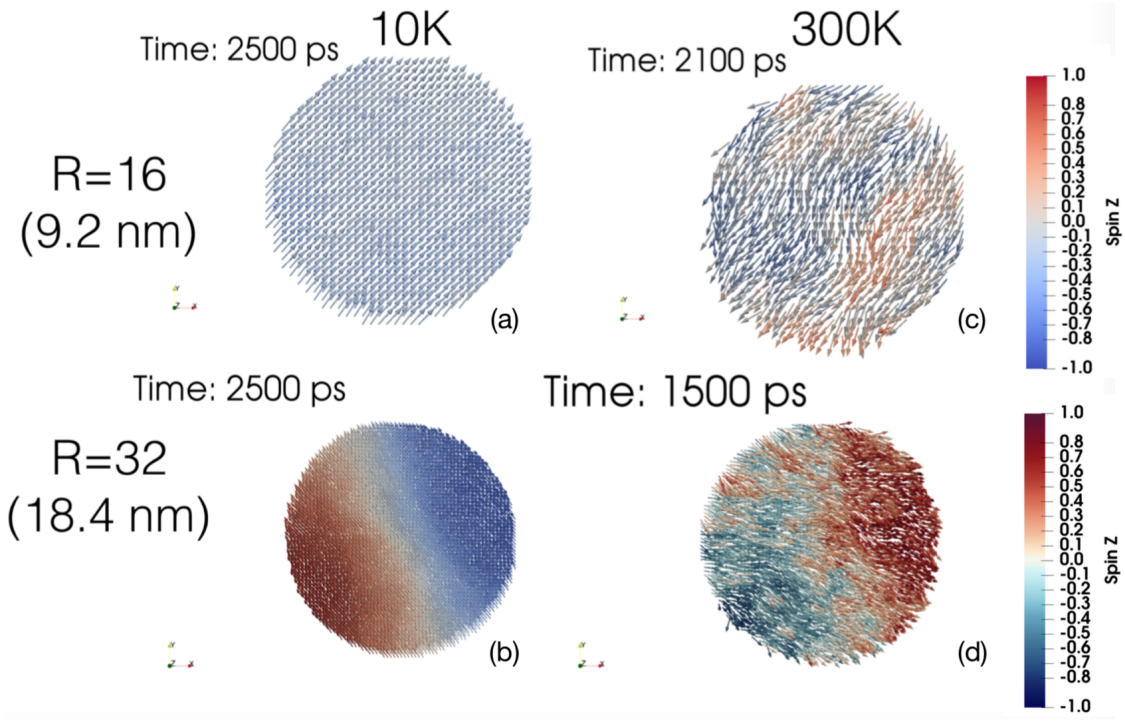

Figure 4.13: Snapshot of the switching dynamics in a disordered Fe/MgO/Fe nanopillar for a constant current of 50 GAm^{-1}. The figures on the left-hand side represent the z component of the atomic spins throughout the disc, where right-hand side panels show the distribution of the current density. Here the linear size of the disorder feature is 2 for the top panels and 4 for the bottom ones. Courtesy of Dr. Matthew Ellis.

rather small, hence a truncation far enough from the interface constitutes a fair approximation. Similarly to the case of Fe and Fe/Cu, one should consider the modifications to the Gilbert damping introduced by the truncation of the layer. In order to allow for a better comparison between the different cases, we consider also here a uniform damping parameter of 0.005. Here we consider a stack of six FePt layers so the two systems will have the same amount of atoms (12). Both spin models are constructed by using the parameterisation for *bcc* Fe and $L1_0$ FePt described above, and longitudinal spin fluctuations will be explicitly included. The details of the simulation methods are analogous to the ones described in the case of Fe and Fe/Cu free layers.

At this point, we remind the reader that in Chapter 3 two sets of results of spin torque calculations were shown for a pure FePt lead: one where the MgO-FePt inter-plane distance is set accordingly to DFT results, and one where the distance is strongly underestimated [see Fig. 3.14 and its discussion]. The most outstanding difference between the two cases is that the torque for the realistic interface is two orders of magnitude smaller than for the unrealistic structure. As a consequence, the critical voltage for the unrealistic structure is expected to be strikingly lower than

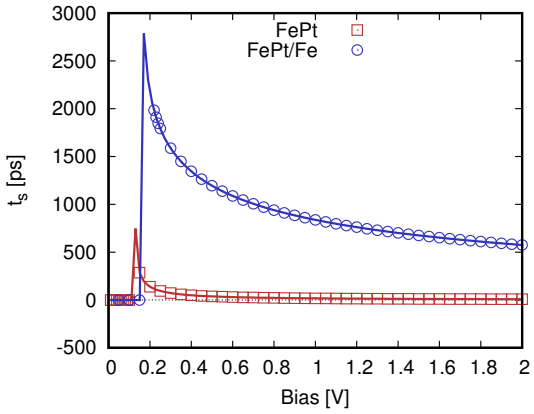

Figure 4.14: Bias dependence of the switching time in FePt (red) and FePt/Fe (blue) free layers at 0 K. A field of 5.5 T was applied in the case of FePt/Fe, while no external field was applied for the FePt layer. The lines represent the result of a fit of the function defined in Eq. (4.51). The corresponding data are the symbols.

for the realistic one, where the spin torques have roughly the same total intensity as a pure *bcc* Fe layer. However, the magnetic anisotropy is strikingly different in the two cases: the macroscopic anisotropy field at 0 K can be estimated to be of 15 T for FePt and a factor 10 lower in Fe. Therefore, the intensity of the applied field required to obtain switching for a realistic Fe/MgO/FePt junction will be even higher than the 1 T field employed to analyse the case of Fe and Fe/Cu free layers. In particular, the simulations have shown that an applied field of 50 T is still not sufficient to reverse the magnetisation in a pure FePt free layer by employing the spin torques calculated for a realistic interface. In contrast, the use of the torques obtained for an underestimated MgO-FePt inter-plane distance yield switching in absence of an applied field with a critical voltage of only 0.129 V. This implies that the current-driven spin dynamics is remarkably more interesting in the case of the unrealistic structure, since the spin torques in realistic junctions are too weak to reverse the magnetisation and become negligible when compared to the applied field required to obtain switching. This differs from the case of a FePt/Fe free layer, as the reduced thickness of the FePt stack yields a strikingly weaker magnetic anisotropy ($H_K = 8.8$ T) and the critical voltage is found to be 10.38 V. We then choose to focus our analysis of magnetisation reversal in FePt-based junctions to the 4FePt/4Fe free layer and to the FePt structure with the unrealistic interface.

The bias dependence of the switching times in the two cases is shown in Fig. 4.14. In order to better compare between the two systems, we adopt an applied field of 5.5 T for the case of FePt/Fe. This choice brings the critical voltage for such structure to 0.158 V, which is comparable to the one obtained for FePt. Despite this, switching occurs at two different time scales in the two systems. Such differences can be better analysed from the data shown in Figure 4.15, where we display the trajectories of the total magnetisation at 0 K for different voltages, expressed in terms of fractions of the critical voltage. In FePt the switching starts close to the zero-time axis and occurs within 1 ns. In contrast, in FePt/Fe layers the magnetisation remains almost constant for more than 0.5 ns and reversal occurs with times as long as 2 ns. Interestingly, the switching times for FePt and FePt/Fe are strikingly more sensitive to temperature

as compared to those of Fe and Fe/Cu [Fig. 4.16]. Nevertheless, the distribution of switching times for a given voltage and temperature is here remarkably narrower. In FePt [panel (a)] each set of temperature and applied voltage have rather distinct switching times. Interestingly, the results at 0 K are not too distant from the average switching times obtained for 100 K. The increase of the voltage implies a significant reduction of the switching times, and such effect is particularly pronounced for lower temperatures. We finally note that the temperature seems to be significantly less relevant for higher voltages. On the contrary, in FePt/Fe [panel (b)] the case of 0 K is strikingly different from the results of finite temperature simulations. In fact, switching times at zero-temperatures are found to be of the order of 2 ns, in contrast with the case of finite temperature, where all switching times are found below the 1 ns threshold. Moreover, the switching times are mostly constant for different applied voltages. This can be attributed to the fact that in this case magnetisation reversal is mostly driven by the applied magnetic field, with the spin torques playing a relatively minor rôle.

We note that switching in FePt occurs at a rather short time scales, with switching times as low as 50 ps. In order to better analyse this result we study the spin correlations for different simulation parameters. Given the presence of a rather strong

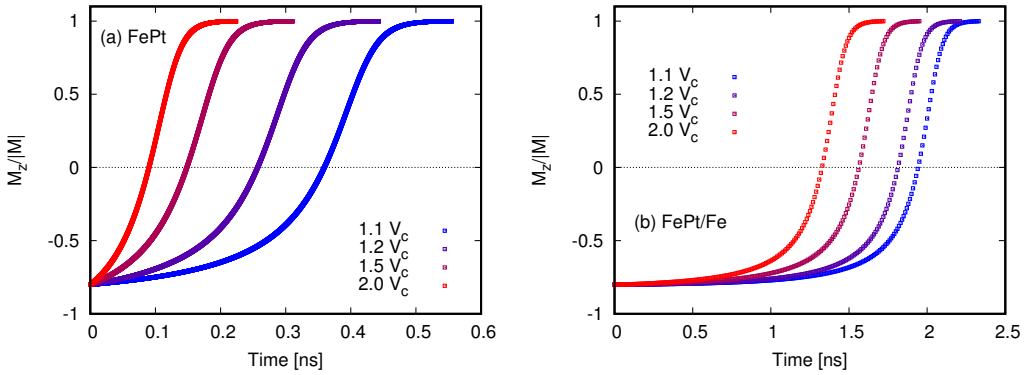

Figure 4.15: Current-induced switching in FePt (a) and FePt/Fe (b) free layers at 0 K A field of 5.5 T is applied in the case of FePt/Fe, while no external field was applied for the FePt layer.

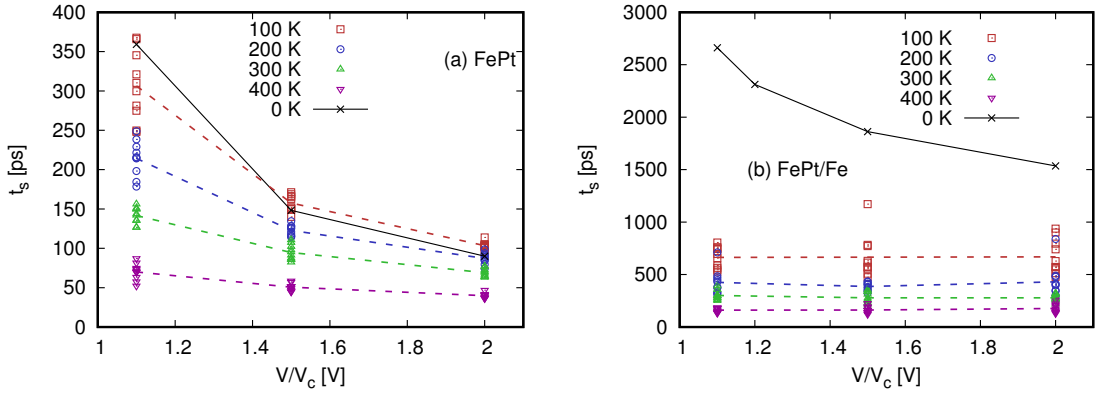

Figure 4.16: Bias dependence of the switching times in (a) FePt and (b) FePt/Fe at 0 K (black symbols), 100 K (red), 200 K (blue), 300 K (green) and 400 K (purple). For data sets obtained at finite temperatures the lines show the trend of the average switching time for a given voltage. A field of 5.5 T is applied in the case of FePt/Fe, while no external field was applied for the FePt layer.

applied field, the case of FePt/Fe is not as interesting as the one of the FePt lead. Hence, the study of spin correlations in FePt/Fe is here omitted. We then used the same methodology adopted for Fe and Fe/Cu, and begin by analysing the auto-correlation and the spin-spin correlation in FePt at 0 K and with a bias voltage equal to $1.1V_c$. Figure 4.17 shows that a rather fast precession frequency characterises the switching dynamics in FePt [panels (a) and (d)]. We also note that the oscillations seem to qualitatively change in time, and this holds for both the auto-correlation and the spin-spin correlation function. In this latter case [panels (d), (e) and (f)] we show that different spins have a slightly different correlation. Here the spin-spin correlations for different spins are represented with different colors, where blue represents the spin that is closest to the interface and red the one at the other opposite of the stack. The phase of the precession is rather similar for all spins, although spins seem to be have a stronger delay with increasing distance from the interface. Note that here no distinction was made between Fe and Pt atoms. In fact, these results show that different spins do not undergo a qualitatively different dynamics. This is because the exchange coupling keeps all spins mostly aligned,

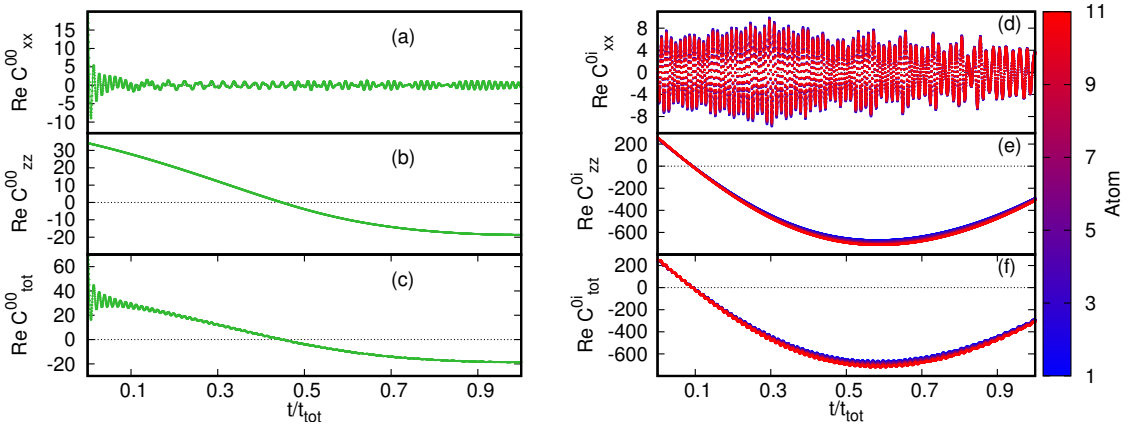

Figure 4.17: Study of time-dependent spin correlations during magnetisation switching at 0 K FePt (red) and FePt/Fe (blue) free layers. Left panel: (a) the xx and (b) the zz component and (c) the total auto-correlation function for the spin at the MgO/free layer interface. Right panel: (d) the xx and (e) the zz component and (f) the total correlation function between the interfacial spin and all the others. The colors indicate the distance of each spin from the interfacial one ($i = 0$), where blue denotes the closest site and red denotes the most far away.

hence their trajectories become indistinguishable one from the other.

We conclude by discussing the bias and temperature dependence of the correlations functions that are presented in Figure 4.18. The data show that the interfacial spin is more strongly correlated for low voltages, where the oscillations induced by the in-plane component are also most visible [panel (a)]. Panel (b) shows that spins further away from the interface are slightly more out of phase with respect to spins in proximity to the interfacial one. This difference, however, becomes less relevant with increasing applied voltage. Moreover, the correlation seems to decrease for higher voltages and almost vanishes at the end of the time window considered (as previously observed). This is particularly interesting, since it implies that stronger spin torques significantly reduce the spin-spin correlations, hence they yield to a meaningful decrease in the switching time. We note that the same consideration is not applicable to the other cases considered because of the presence of the applied magnetic field. Similarly, the decrease of the switching time with the temperature can be explained

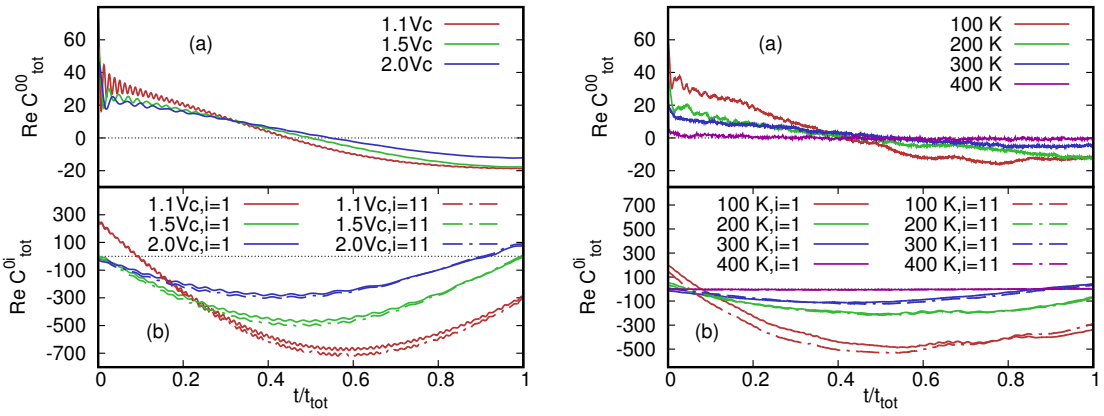

Figure 4.18: Study of the (left) bias and (right) temperature dependence of the spin correlations in a Fe/MgO/FePt junction. The top panels show the auto-correlation functions, while the bottom panels display spin-spin correlations. For the latter case full lines correspond to the closest spin ($i = 1$) to the interfacial one, while dashed lines are relative to the one furthest away from the interface. Left: the different colors represent different applied voltages:

with the decrease of the spin-spin correlations [panels (c) and (d)]. In fact, the correlation functions at 100 K have similar magnitude than in the zero-temperature case. Nevertheless, they are significantly smaller for higher temperatures, and almost vanish at 400 K.

4.4 Conclusions

We have presented a methodology to perform spin dynamics simulations at the atomistic level. We have discussed the spin models to correctly describe the thermodynamical properties of *bcc* Fe and $L1_0$ FePt. We then mapped the spin torques presented in the previous Chapter onto the atomistic models and we compared the current-induced switching in Fe, Fe/Cu, FePt and FePt/Fe free layers. Overall, we find that the critical voltage is determined by the value of the torque integrated over the free layer. The reduced current intensity in Fe, Fe/Cu and FePt/Fe free layers implied the need of an external magnetic field in order to obtain magnetisation reversal with

voltages below 1.5 V. In contrast, switching in a pure FePt layer occurs for a rather low critical voltage (0.129 V) in the absence of an applied magnetic field, and the typical switching times are of an order of magnitude lower than in the other cases considered. Moreover, the higher anisotropy field in FePt-based free layers granted improved thermal stability with respect to Fe and Fe/Cu free layers.

Finally, we have analysed the magnetisation switching in Fe/MgO/Fe junctions in presence of variations in the barrier thickness. Our results show that, also in this case, the integrated torque over the free layer dictates the critical voltage. In addition, we have found that in these systems magnetisation reversal happens through a domain wall motion.

Chapter 5

Antiferromagnetic couplings in Heusler compounds

"Something unknown is doing we don't know what."

- Sir Arthur Eddington

Antiferromagnetic materials have attracted significant attention as potential candidates for novel spintronics applications [137]. In fact, spin dynamics in such materials takes place at typical time scales that are up to three orders of magnitude faster than the one in ferromagnets, i.e. in the THz range as opposed to the GHz [138]. This is because the dynamics in ferromagnets is essentially determined by the anisotropy field, while in antiferromagnets it is given by the exchange coupling between the spins belonging to the different sublattices, that is three orders of magnitude stronger. The possibility of switching antiferromagnets between two stable states has been already proven experimentally [38] and the field of antiferromagnetic spintronics is rapidly growing. As for ferromagnets, the search for novel materials is critical for the development of novel applications. A particularly efficient strategy to explore new materials relies on performing high-throughput calculations on a wide range of structures. Such data can then be used to extract the information needed to optimise the chemical composition of the materials chosen for a given application. Some of such investigations are performed by considering a large number of Heusler compounds. Full-Heusler alloys are intermetallic compounds with chemical

composition of the general form X_2YZ, where X and Y are transition metals and Z is a p-block element. Many of such alloys form in a $L2_1$ crystal structure, that is the result of four interpenetrating fcc lattices and that reduces to *bcc* in the limit case of $X{=}Y{=}Z$. The peculiarity of Heusler compounds is that their properties do not depend on the ones of the elemental crystals for the atomic species they are composed of [139]. This allows one, for example, to obtain a magnetic material by combining elements that in most cases do not exhibit magnetism on their own, such as Mn.

In this Chapter we explore different magnetic properties of the Mn_3Ga and Fe_2MnGa Heusler compounds. In both materials the Mn atoms dominate the magnetic properties and display an antiferromagnetic coupling of some kind. This is particularly interesting in the case of Fe_2MnGa, since at low temperatures the Fe atoms become not magnetic and the material becomes a pure antiferromagnet (with net zero moment). However, at higher temperatures Mn atoms couple ferromagnetically, while a local moment appears at Fe sites and anti-aligns with the moments of the Mn atoms. We begin by developing a spin model to describe the magnetic properties of the ferrimagnetic Mn_3Ga. We then conclude by presenting results of atomistic spin dynamics and spin transport simulations in Fe_2MnGa.

5.1 Ferrimagnetism in Mn_3Ga

The tetragonally distorted Heusler alloy Mn_3Ga has been shown to grow with the $D0_{22}$ structure on a variety of substrates, including MgO [140]. Thin films of this material display high spin polarisation and a strong perpendicular uniaxial anisotropy which make Mn_3Ga rather promising for spintronics applications. The magnetic properties are given by the Mn atoms that occupy the two non-equivalent Wyckoff positions $2b$ and $4a$, shown in Fig. 5.1 (a). Magnetic atoms in equivalent sites couple ferromagnetically, while a strong antiferromagnetic exchange interaction couples atomic spins at non-equivalent positions. Since the $4a$ sites are double the number of the $2b$ sites the system has a net magnetic moment, making this material

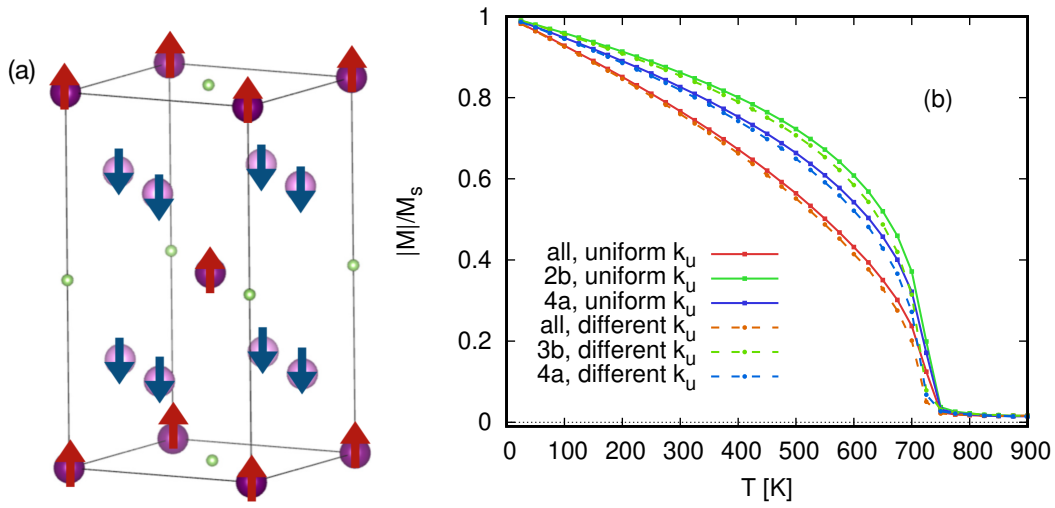

Figure 5.1: Left panel: unit cell for Mn_3Ga. Small spheres represent the Ga atoms, large spheres the Mn atoms. In particular, the red arrows indicate the $2b$ sites, and the blue arrows the $4a$ sites. Right panel: temperature dependence of the average magnetisation for the $2b$ sites (green lines), the $4a$ sites (blue lines) and all sites (orange lines). The full (dashed) lines are obtained assuming uniform (different) anisotropy at non-equivalent sites.

a ferrimagnet rather than an antiferromagnet. The magnetic properties of Mn_3Ga are extensively discussed in Ref. [141]. The magnitude of the magnetic moments is estimated to be 2.99 μ_B at the $2b$ positions and 2.38 μ_B at the $4a$ sites for an ordered ferrimagnetic state. However, the exchange parameters extracted from such state do not reproduce the correct properties for high temperatures. In contrast, the exchange interactions estimated for a paramagnetic disordered local moment state are found to be still antiferromagnetic and to provide a Néel temperature that is close to the experimental value of 770 K [142]. We note that the experimental results have an additional complexity, since the crystal structure undergoes a transition to an hexagonal structure in a similar temperature range.

We parameterise the spin model for Mn_3Ga using the exchange parameters and the anisotropy constant presented in Ref. [140]. Such results were obtained through spin spiral and total energy first principles calculations. In particular, the authors

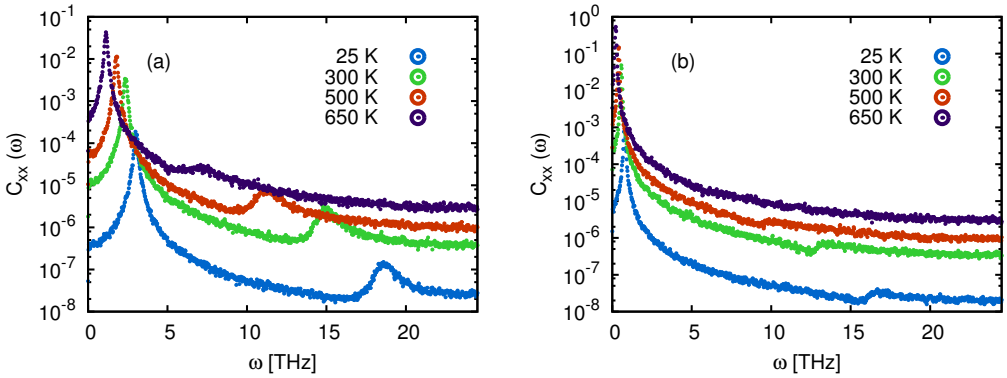

Figure 5.2: FMR spectrum for Mn_3Ga at different temperatures with (a) uniform and (b) different anisotropy for non-equivalent sites. We find two different resonant modes, one at lower frequency (∼20 THz) and a second, weaker, one at a higher frequency.

report a total uniaxial anisotropy constant of 0.900 meV, while they find the values of 0.765 meV and −0.031 meV for 4*a* and 2*b* sites, respectively. These results indicate that the moments at 2*b* sites prefer to align within the plane, hence the spin-collinearity of the magnetic ground state must come from the strong exchange coupling between 4*a* and 2*b* sites (∼400 meV). We then perform two separate sets of calculations: one where the uniaxial anisotropy is kept uniform for all sites, and one where a different anisotropy constant is assigned to non-equivalent sites. Fig. 5.1 (b) displays the calculated temperature dependence of the average total magnetisation at 2*b* sites (green lines), 4*a* sites (blue lines) and all sites (orange lines) in the two cases for systems composed of 20 × 20 × 20 unit cells. It is clear that magnetic ordering is lost beyond T ∼750 K, temperature that is compatible with the Néel temperature estimated from experimental data. Interestingly, the total average moment at 4*a* sites vanishes more rapidly than the one at 2*b* sites. Moreover, we note that the two different choices of atomistic anisotropy do not make a substantial difference in the temperature dependence of the magnetic ordering.

Nevertheless, the site-dependence of the uniaxial anisotropy seems to play a significant role for the spin-spin correlations. Fig. 5.2 shows the results of FMR simulations

at different temperatures for the two anisotropy choices. In both cases two distinct resonant peaks can be identified, in contrast to the case of *bcc* Fe discussed above. The arising of multiple resonant peaks is common in the presence of nonequivalent moments in the unit cell. In particular, systems with antiferromagnetic ordering are known to display two separate oscillation modes. A first mode is analogous to the one found in ferromagnets and corresponds to a uniform precession of the magnetisation, and is normally found at frequencies of the order of 1-10 GHz, namely at a time scale similar to that of ferromagnets. In the case of an antiferromagnetic-like ordering, this translates in a in-phase precession of the spins of the two sublattices. The second mode, often called antiferromagnetic mode, is found at significantly higher frequencies ($\sim$ 1 THz) and is the result of the nonequivalent spins oscillating out of phase and competing one against the other. The latter can be found in both spectra, with frequencies between 1 THz and 4 THz for uniform anisotropy [panel (a)] and slightly below the THz range for a site-dependent anisotropy constant [panel (b)]. Interestingly, an additional high-frequency oscillation mode is captured by our FMR simulations. In fact, a second resonant peak appears in the 15-20 THz frequency range at low temperatures. The latter is particularly pronounced in the case of uniform anisotropy, while it is barely visible for site-dependent k_u. The position of the peak then rapidly changes with the increase of temperature, and gradually merges with the dominant peak as T approaches the Curie temperature. The strikingly high frequency of the secondary peak, together with its sensitivity to the site-dependence of the anisotropy, indicates that the corresponding resonant mode is the result of the competition between the two sublattices, and maybe characteristic of the present system.

In order to better analyse the differences between the two sets of simulations we now focus our attention to the sole ferromagnetic (lower frequency) mode. Its larger intensity allows in fact to fit the peak at all temperatures and for both anisotropy choices. Fig. 5.3 (a) shows the resonant peak at some representative temperatures, where the black lines represent the best fit. The remaining panels of the figure display the information that can be extracted from the fit of the resonant peak to the

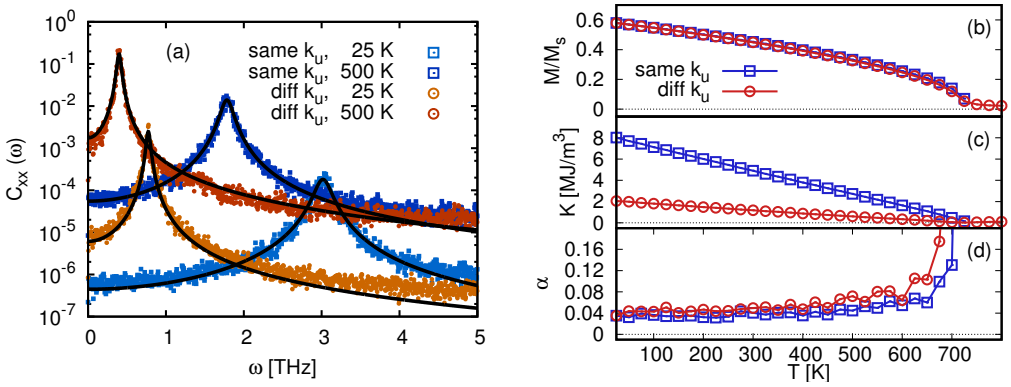

Figure 5.3: Left panel: low frequency FMR spectrum for Mn_3Ga at different temperatures with uniform anisotropy constant at all sites. The black lines show the result of the best fit according to Eq. (4.31) of the resonant peak. Right panel: (b) the total magnetisation, (c) the macroscopic anisotropy constant and (d) the Gilbert damping extracted from the fitting of the low frequency resonant peak for different temperatures.

formula contained in Eq. (4.31). We note that the expression used to fit the linewidth is not fully appropriate. In fact, the strength of the exchange coupling should be explicitly included to correctly estimate the resonant peak in antiferromagnetic materials. Nevertheless, to the best of our knowledge the respective analytical form is not currently available in literature. In particular, the total magnetisation, the macroscopic anisotropy constant and the macroscopic damping are displayed in panels (b), (c) and (d), respectively. It seems there is little or no difference between the two cases in the temperature dependence of the magnetisation. We note that the predicted total magnetisation at 0 K corresponds to the difference between the atomic moments at the two sites. Small changes appear in the trend of the macroscopic damping, that in both cases is enhanced by an order of magnitude with respect to the input value of 0.005. In fact, a site-dependent k_u seems to imply a slightly stronger damping (red circles), difference that increases with the temperature. We note that the irregularities that we observed at high temperatures are likely due to a decrease in the accuracy, especially for the case of non-uniform anisotropy since the

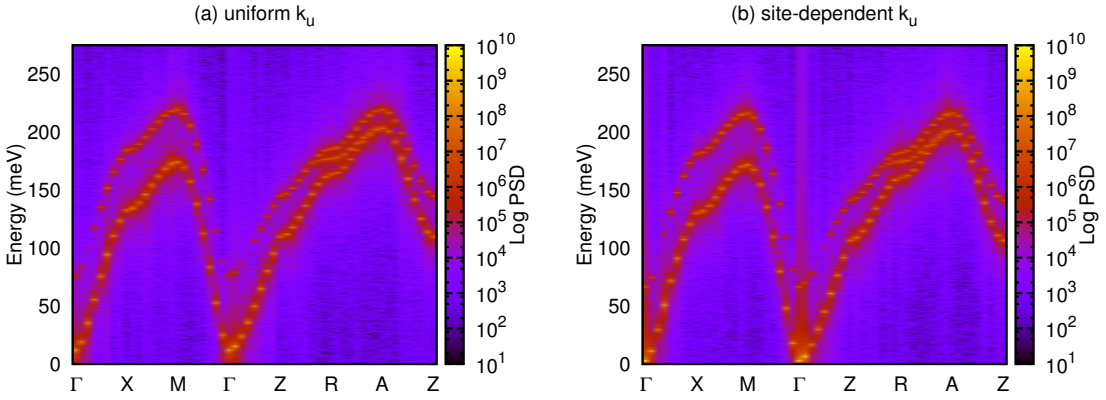

Figure 5.4: Dynamic structure factor for Mn_3Ga at 10 K with (a) uniform and (b) different anisotropy for nonequivalent sites.

peaks become more narrow and close to the zero frequency axis. In opposition to the magnetisation and damping, the macroscopic anisotropy constant has a relevantly different temperature dependence in the two cases.

We conclude our analysis of Mn_3Ga by calculating the dynamics structure factor [Fig. 5.4]. The differences between the positions of the FMR peaks discussed above here translate in an different energy shift of the branches at the Γ point for the different anisotropy choices. Apart from this, the two spectra are rather similar. In both cases two acoustic modes can be identified, of similar shapes but at different energies. Moreover, peaks belonging to lower energy branch seem to be of stronger intensity than the other, especially in the low energy spectrum. Interestingly, the two branches are connected by a third branch for wave vectors of the form $(0t1)$ and $(t11)$ with $0 \leq t \leq 1$, corresponding to the Z-R and R-A segments.

5.2 Multi-scale modelling of Fe_2MnGa

We now move to discuss the magnetic properties of the Fe_2MnGa Heusler compound. The peculiarity of this material lies in its high structural instability, as it may crystallise in a variety of crystalline phases that correspond to generalisations of the *fcc* or *bcc* structures (see e.g. Ref. [143] and references therein). In addition, the magnetic

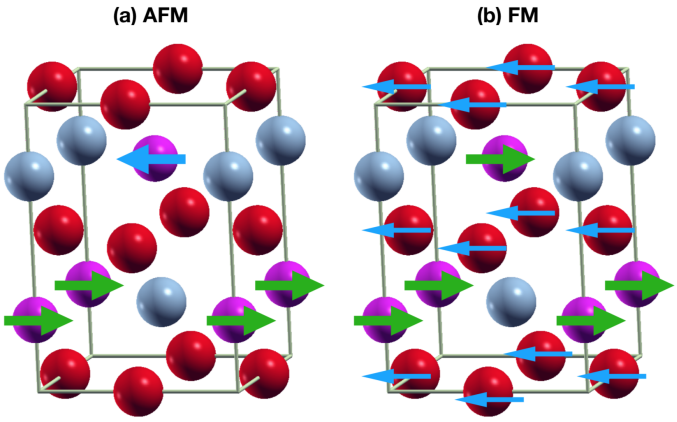

Figure 5.5: Magnetic unit cell of Fe_2MnGa. The arrows show the atomic magnetic moments in the (a) ferromagnetic (FM) and (b) anti-ferromagnetic configuration. The different colors of the spheres defines the atomic species: red for Fe, violet for Mn and gray for Ga.

ground state is also unstable. It is generally believed to be antiferromagnetic at temperatures below 200 K, with the Mn atoms carrying all the moment and the Fe ones being diamagnetic. At higher temperatures the Mn moments align ferromagnetically, while the Fe ones are also magnetic with moments that couple antiferromagnetically to Mn. We will hereon distinguish between the two phases by referring to the sign of the Mn-Mn coupling. In other words, the low-temperature phase will be called antiferromagnetic (AFM) and the high-temperature one ferromagnetic (FM), although the latter corresponds to a ferrimagnetic phase. Overall, the magnetic ordering seems to be strongly system dependent and the transition between the two states was observed at a number of different temperatures [144, 145, 146]. Nevertheless, the Curie temperature is commonly identified to be above 700 K [147], making this material suitable for possible applications.

We consider here Fe_2MnGa in the cubic $L2_1$ structure with an in-plane lattice constant of 5.732 Å. Such value is slightly different from the predicted lattice constants for the two phases, estimated to be 5.701 Å and 5.694 Å for the FM and AFM phase, respectively [148]. This choice, however, matches the lattice constant of *bcc*

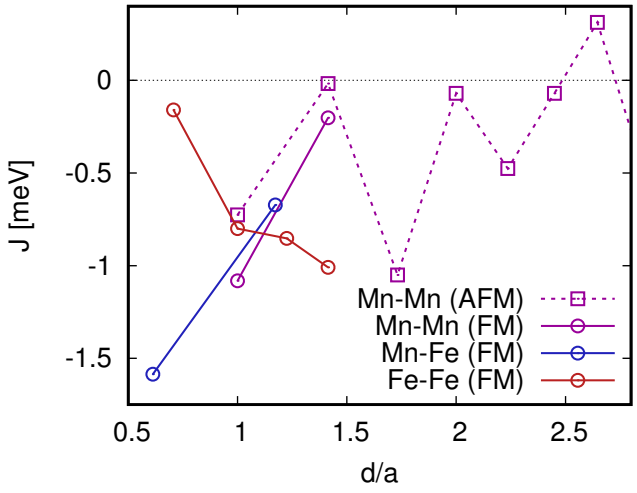

Figure 5.6: Calculated inter-atomic exchange parameters for Mn-Mn (purple), Mn-Fe (blue) and Fe-Fe (red) sites depending on the inter-site distance expressed in units of the in-plane lattice constant, a. Data points represented by circles are obtained with aligned Mn moments, while the ones denoted with squares are obtained with antiferromagnetically coupled Mn moments. Calculations performed by Dr. Matthew Ellis.

Fe and allows Fe_2MnGa to be employed as the free layer of a Fe/MgO-based MTJ. Fig. 5.5 displays the unit cell that will be employed for all calculations, where the arrows identify the orientation of the atomic spins for each magnetic phase. In the AFM configuration, the moments of the Mn atoms alternate sign in adjacent planes along the z direction, configuration often known as AF1. We note that this cell is obtained as the in-plane rotation by $\pi/4$ of the standard unit cell. This allows us to half the size of the cross section, hence to reduce significantly the computational costs, especially for the transport calculations.

A series of DFT calculations was performed by collaborators of the author of this thesis in order to investigate the magnetic ground states of Fe_2MnGa. In particular, Emanuele Bosoni employed the SIESTA code to study MgO/Fe_2MnGa interfaces and estimate the magnetocrystalline anisotropy, while Dr. Matthew Ellis performed spin spiral calculations with the ELK code [65] in order to assess the exchange param-

eters. The generic result to be drawn from these calculations is that the magnetic moments at the Fe sites is incredibly sensitive to the orientation of spins at the neighbouring sites. This can be expected since the antiferromagnetic ordering on a fcc lattice is subject to geometric frustration [149]. Nevertheless, moments at the Fe sites behave as induced moments and seem not to be strongly coupled to the adjacent Mn atoms. In fact, the exchange interactions extracted are found to be rather weak and very long ranged [Fig. 5.6]. We note that all exchange couplings are one or two orders of magnitude small with respect to the values that are typical of the other materials examined in this thesis. Nevertheless, it seems that the stronger exchange interaction is the one that couples Fe and Mn sites. The calculation of the magneto-crystalline anisotropy constant was also attempted by the means of total energy differences for both bulk systems and for MgO/Fe_2MnGa interfaces. However, the resulting estimates are rather close to the calculation accuracy and we can only deduce that $|k_u|$ <10 µeV. These results make it not possible to propose a reliable first principles parameterisation of the spin models. The case of the AF configuration is made simpler by the presence of a single magnetic species in the unit cell. Therefore, we limit our analysis at the atomistic scale to model the AF phase. This is done by employing an effective first nearest neighbour exchange parameter chosen to reproduce the AF-to-FM transition temperature of 250 K predicted in Ref. [148]. The resulting model is then used to study the ferromagnetic resonance and spin-wave dispersion in the AF configuration of Fe_2MnGa and compare them to the case of Mn_3Ga. We conclude the Chapter by presenting results of spin transport calculations for a Fe/MgO/Fe_2MnGa MTJ for both the magnetic phases of the Heusler compound.

5.2.1 Atomistic model

Heisenberg fcc antiferromagnets were shown to have a first-order transition point at $T_N = 0.446|J_1|$, where J_1 is the first nearest-neighbour exchange coupling [149]. Furthermore, the AF1 magnetic order corresponds to the absolute energy minimum in presence of a weak ferromagnetic second-nearest neighbour exchange. Thus, we

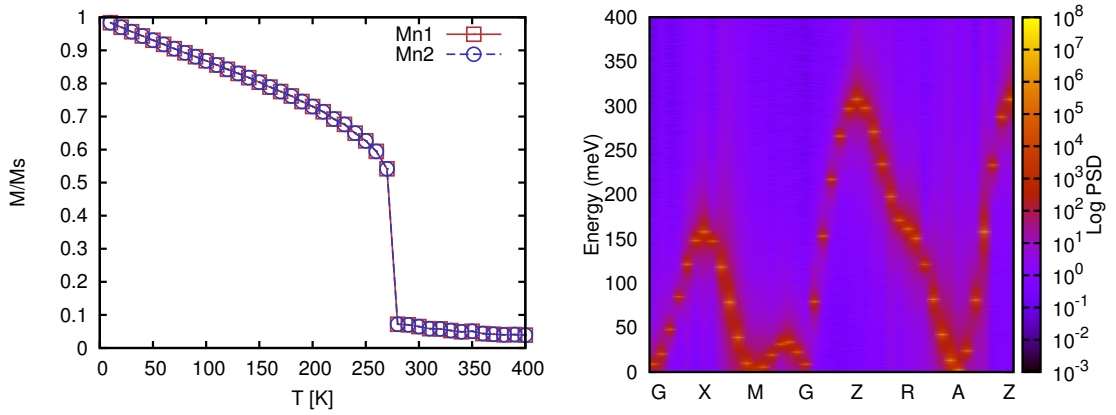

Figure 5.7: Left panel: temperature dependence of the average spin for each sublattice in AF Fe_2MnGa. Right panel: magnon spectrum for AF Fe_2MnGa.

model AF Fe_2MnGa by considering an effective first-nearest neighbour exchange constant of $J_1 = -250k_B/0.466 = -47.50\,\text{meV}$ and a small second-nearest neighbour coupling of 1.0 meV. We then increase the anisotropy constant until the system displays a stable magnetic configuration.

Figure 5.7 (a) shows the temperature dependence of the average total spin for each sublattice obtained for $k_u = 10\,\mu\text{eV}$. It is evident that a phase transition occurs at 280 K, although the total spin does not vanish completely for higher temperatures. This simple result seems to indicate that the AF-FM transition can be explained with the breakdown of the AF ordering because of temperature effects. Since the spin alignment is lost above the transition temperature, induced moments appear on the neighbouring Fe atoms. The ferromagnetic coupling between the Mn atoms is thus effectively induced by a strong antiferromagnetic coupling between the Mn and the Fe sites. We note that this hypothesis is consistent with the inter-atomic exchange couplings presented in Fig. 5.6. Potentially, this information can be used to construct a spin model for the FM state. Nevertheless, the dependence of the moment at the Fe sites on the orientation of the neighbouring Mn atoms is still unclear and requires further investigation. Therefore, in this Thesis we limit the study of the spin models to the case of an AF coupled Mn atoms and non-magnetic Fe sites.

We continue by presenting the calculated dynamic structure factor for Fe_2MnGa [Fig. 5.7]. It is evident that the results are remarkably different from the ones obtained for Mn_3Ga. In fact, a single magnon branch appears in the magnon spectrum for Fe_2MnGa, in contrast with what was found for Mn_3Ga. Consistent differences are also encountered in the FMR spectrum [Fig. 5.8]. Here a single resonant peak appears for the temperature range considered. We note that the resonant frequency is well detached from the low frequency range for temperatures above the phase transition temperature ($\sim$280 K). We note that our best fit seems to estimate correctly the peaks around the resonant frequency, although it fails to reproduce the trend of the correlation function for the other frequencies. This inconsistency is probably due to the use of the analytical expression for the FMR linewidth in ferromagnets, that do not includes exchange interactions, as already pointed out in the previous section. This is in contrast to the previously examined spin models, for which the expression of Eq. (4.31) was a good approximation for a wider range of frequencies. The total average spin extracted from our best fit is shown in panel (b), and grows linearly with the temperature. The macroscopic anisotropy constant [panel (c)] steadily grows with the temperature, to then maintain almost the same value from about 100 K until the phase transition temperature, T_N. At such temperature, both the macroscopic anisotropy and the Gilbert damping [panel (d)] diverge. We remark however that the resonant frequency for such temperatures is probably beyond the frequency resolution of the simulation parameters. Thus, the extracted information for temperatures close to or higher than T_N might not be reliable. Finally, we remark that for Fe_2MnGa the difference between the damping parameter extracted from the fit and the value used as input (also here 0.005) is even more pronounced than in the case of Mn_3Ga.

We can conclude that the AF phase of Fe_2MnGa can be modelled within effective second-nearest neighbour exchange parameters that can be adapted to reproduce the correct phase transition temperature. After the phase transition, magnetic ordering is not completely lost and spins at Mn sites become misaligned. This implies that non-zero magnetic moments arise at Fe sites, hence the Fe-Mn antiferromagnetic

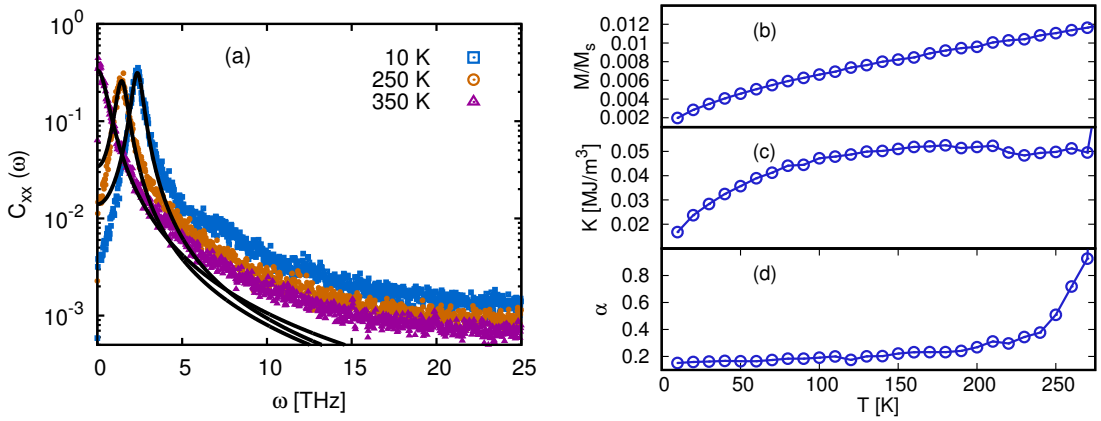

Figure 5.8: Results of ferromagnetic resonance simulations in antiferromagnetic Fe2MnGa. Left: FMR spectrum for the AF configuration of Fe_2MnGa at different temperatures. The black lines show the result of our best fit of the resonant peak. Right: temperature dependence of [panel (b)] the total magnetisation, [panel (c)] the macroscopic anisotropy constant and [panel (c)] the Gilbert damping extracted from the fitting of the resonant peak.

exchange coupling induces a magnetic configuration with aligned Mn sites. The strength of such exchange interaction can be effectively quantified by the means of the Curie temperature (700 K). It is then possible to use this information to construct an effective parameterisation for the FM configuration. In fact, the calculated exchange parameters of Fig. 5.6 show that the Mn-Mn exchanges are not strikingly different for the two magnetic configurations. The main challenge left to complete the parameterisation of a spin model for Fe_2MnGa is then the determination of the dependence between the magnetic moments at Fe sites and the electronic environment.

5.2.2 Spin transport

We now present the results of quantum transport calculations for Fe/MgO/Fe_2MnGa junctions. These systems are once again based on the prototypical Fe/MgO/Fe MTJ. In principle, a minimal in-plane 2×2 supercell is needed, given that the in-plane

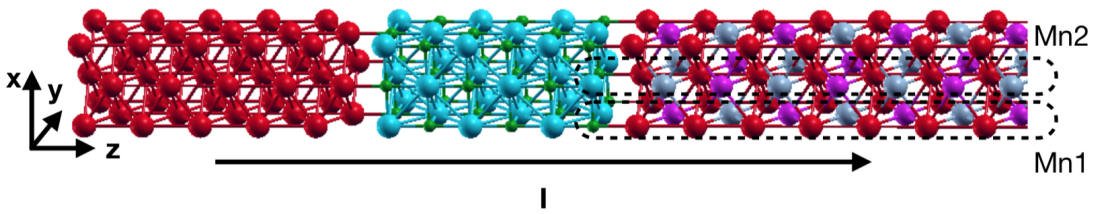

Figure 5.9: Representation of a Fe/MgO/Fe_2MnGa junction. The different color of the spheres corresponds to different atomic species: red for Fe, blue for Mg, green for O, violet for Mn and gray for Ga. The dashed lines identify the two nonequivalent planes in Fe_2MnGa along the transport direction. The plane denoted as Mn1 contains the closest Mn to the MgO interface, while in the plane Mn2 the first site after the interfacial Fe atoms is occupied by Ga.

lattice constant of Fe_2MnGa is double with respect to that of *bcc* Fe. However, the magnetic ground states of Fe_2MnGa can be equally reproduced with a cell that is rotated by $\pi/4$. This allows us to consider a cross section that is only twice, instead of four times, wider then the cell employed for standard Fe/MgO/Fe structures. Since Fe_2MnGa is formed by alternating Fe-Fe and Mn-Ga planes, the stack has two possible terminations. Of the two, the Fe termination yields an interface that is completely analogous to the *bcc* Fe/MgO interface. In fact, we remark that the substitution of Mn and Ga atoms with Fe atoms in the Fe_2MnGa structure yields a lattice that is equivalent to *bcc* Fe. In contrast, the properties of the other interface are much less known. For such reason, we consider only the Fe-terminated interface and perform transport calculations on the structure displayed in Fig. 5.9. A series of SIESTA calculations for different insulator/free layer distances showed that the most energetically convenient configuration is found for 2.16 Å, that is equivalent to an inter-plane distance at the Fe/MgO interface. In order to maintain the features of the current discussed in Chapter 3, all simulation parameters are chosen consistently with the choices made for the Fe/MgO/Fe case. We note, however, that the use of an LSDA XC potential does not reproduce the same magnitude of the magnetic moments obtained with GGA potentials, that in contrast reproduce the experimen-

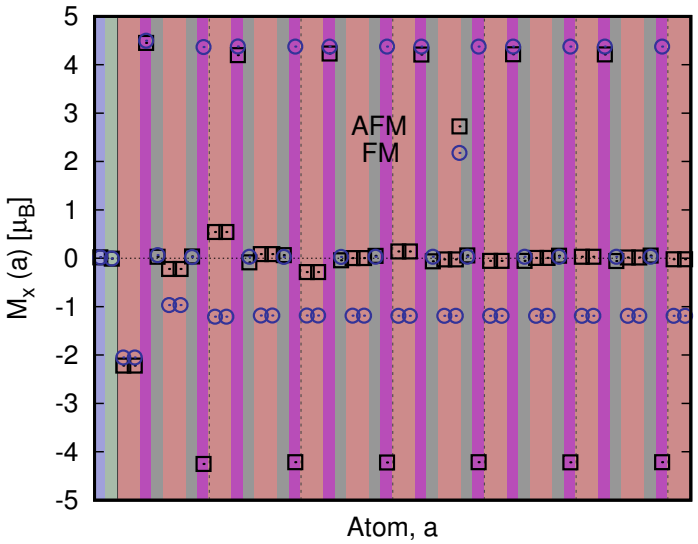

Figure 5.10: Atomic magnetic moments in the free layer of a Fe/MgO/Fe_2MnGa junction with aligned (blue circles) and anti-aligned (black squares) Mn atoms. The colored background defines the atomic species: red for Fe, violet for Mn, gray for Ga, blue for O and green for Mg.

tal values [see Table 5.1]. Nevertheless, LSDA maintains the same ordering of the magnetic configurations as GGA. Therefore, we choose to adopt the LSDA potential despite these discrepancies in order to yield a better comparison with the other free layers considered above.

The calculated magnetic moments in the free layer of the Fe/MgO/Fe_2MnGa junction are shown in Figure 5.10. These calculations were performed with the mo-

	AIMS (GGA)	SIESTA (GGA)	SIESTA (LDA)
$\lvert m_{\mathrm{Mn}}\rvert$ (FM/AF)	2.66/2.54 μ_B	2.65/2.48 μ_B	4.27/4.07 μ_B
$\lvert m_{\mathrm{Fe}}\rvert$ (FM/AF)	0.26/0.05 μ_B	0.29/0.0 μ_B	1.15/0.00 μ_B

Table 5.1: Magnetic moments in Fe_2MnGa for the ferromagnetic (FM) and antiferromagnetic (AFM) configurations as predicted by SIESTA and by the all-electron code AIMS [66]. Courtesy of Emanuele Bosoni.

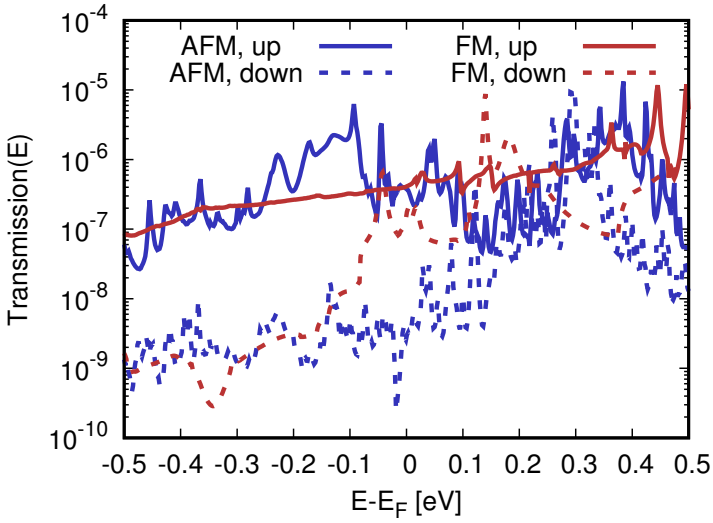

Figure 5.11: Energy dependent transmission coefficients for majority- (full lines) and minority-spin (dashed lines) for the FM (red lines) and AFM (blue lines) configuration of a Fe/MgO/Fe_2MnGa junction.

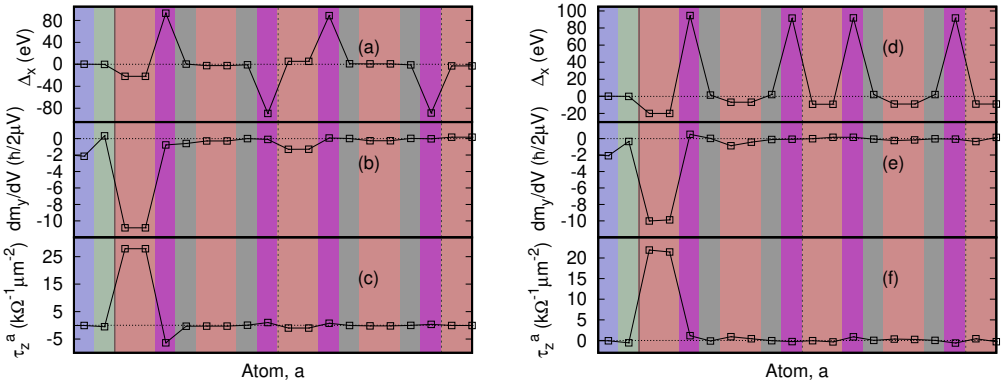

Figure 5.12: Study of the torkance in Fe_2MnGa free layers with AFM (left) and FM (right) magnetic ordering. In all panels the colored background indicates the atomic species: blue for O, green for Mg, red for Fe, gray for Ga, pink for Mn. The top panels display the relevant components of the exchange and correlation field, $\mathbf{\Delta}$, the middle panels the non-equilibrium spin density, $\mathrm{d}\boldsymbol{m}/\mathrm{d}V$, and the bottom panels the torkance per unit of μ_B/e and area, $\boldsymbol{\tau}$.

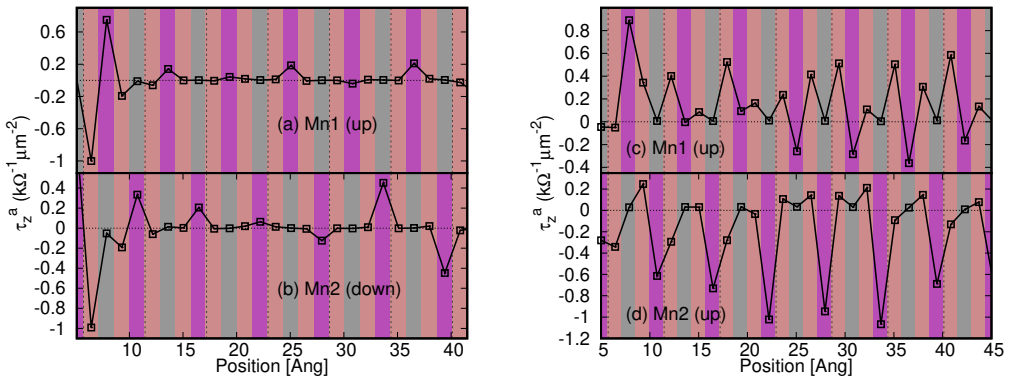

Figure 5.13: Calculated torkance per unit of μ_B/e and ares in Fe_2MnGa free layers with AFM (left) and FM (right) magnetic ordering. In all panels the colored background indicates the atomic species: blue for O, green for Mg, red for Fe, gray for Ga, pink for Mn. Top panels and bottom panels show the torkance acting on the plane Mn1 (top panels) and the plane Mn2 (bottom panels) as function of the distance from the interface.

ment of the Mn closest to the MgO interface aligned with the reference layer. While the moments in the FM configuration (blue circles) are not significantly different from their bulk values, in the AFM state a sizable magnetic moment is induced at Fe sites in proximity of MgO (black squares). In particular, the moments of the Fe atoms in contact with MgO have almost the same magnitude as in the FM state, and non-vanishing Fe moments can be found as far as 4 unit cells ($\sim 2.29\,\text{nm}$). This is in contrast with the results obtained for bulk systems for LSDA or GGA, and confirms how sensitive the Fe atomic moments are to the local atomic environment. The enhanced irregularity in the electronic structure for the AFM state can also be evinced by looking at the energy dependent transmission coefficients for the two junctions [Fig. 5.11]. It is clear that in both cases the spin polarisation is rather sensitive to small changes of the Fermi energy. As a result, in the systems considered the FM phase (red lines) have significantly smaller spin polarisation than the AFM phase (blue lines). Nevertheless, the transmission coefficients for the AFM configuration have an energy dependence that is strikingly more irregular than their FM

counterpart.

The results of torkance calculations (for $\vartheta = \pi/2$) for both magnetic phases is displayed in Fig. 5.12. The presence of the interfacial Fe atoms together with the small spin polarisation causes the spin current to be lost almost entirely within the first atomic layer. We remark that this interface is analogous to the MgO/*bcc* Fe one, hence the spin torques can be expected to have a similar decay. We also note that little or no torque is present at Mn sites. This might be counter-intuitive, especially for the case of the AF configuration, since Mn moments dominate the magnetic ground state of the system. On one hand, the fact that the torques act only on Fe atoms is rather interesting, since it means that the current-induced dynamics will be driven through the induced Fe moments. On the other hand, the simulation of the STT-driven dynamics of this system clearly requires a spin model that explicitly includes spins at Fe sites. As discussed in the previous subsection, such a model cannot be formulated with the data currently at our disposal. Therefore, multi-scale calculations of current-driven dynamics in Fe_2MnGa are here not presented.

We conclude this Chapter by examining in more detail the decay of the STT as function of the position for Fe_2MnGa. The analysis is performed by separating the contributions from the two nonequivalent planes that are identified by the dashed rectangles in Fig. 5.9. We denote as Mn1 the plane containing the closest atom to the MgO interface, while we will refer to the other plane as Mn2. Figure 5.13 shows the decay of the STT as function of the position from the interface for the Mn1 plane (top panels) and for the Mn2 plane (bottom panels). It is evident that the torque is slightly different for the two planes for both magnetic configurations. Interestingly, this is especially true for the case of ferromagnetically coupled Mn atoms [panels (c) and (d)]. Similarly to the results on Fe/MgO/FePt, the presence of a inhomogeneous magnetic texture does not allow for a regular decay of the STT. Moreover, we note that the oscillations here observed are of rather small magnitude and probably suffer from numerical noise.

5.3 Conclusions

We have presented a study of antiferromagnetic couplings in the Mn_3Ga and Fe_2MnGa Heusler compounds. The spin model for Mn_3Ga was characterised by employing results of first principles calculations found in literature, and we find a Curie temperature comparable the experimental one. The calculated ferromagnetic resonance spectrum displays a peak at a strikingly high frequency, of the order of 120 THz, which is shown to be quickly diminish for higher temperatures and vanishes close to the T_C. To the best of our knowledge, this peak was not predicted elsewhere and might be characteristic of the Mn_3Ga system.

The strong dependence of Fe moments to the magnetic and chemical environment makes the full parameterisation of the spin model for Fe_2MnGa not tractable with the data currently available. An effective spin model was formulated for the antiferromagnetic configuration, characteristic of low temperatures. The latter, together with the calculated inter-atomic exchanges, indicate that the AF to FM transition is due to the breakdown of the AF interaction between Mn atoms and to the establishment of a strong antiferromagnetic coupling between Mn and the induced moments at Fe sites. The importance of the induced magnetic moments for the study of Fe_2MnGa was also analysed by the means of quantum transport simulations. In fact, our results show that the dominant contribution to the spin torques is found at Fe sites for both the FM and the AF configurations.

Chapter 6

Parameter-free modelling of magnetic damping

"That's easy. An afternoon of coding, tops."

- Dr. Alessandro Lunghi, PhD

All the studies of the spin dynamics presented above were performed by assuming damping parameters that are consistent with experimentally extracted values. The ferromagnetic resonance linewidth can in fact be related to the magnetic damping, as shown in Chapter 4. However, a number of different mechanisms can contribute to the broadening of the resonant peaks, including spin-pumping [150] and magnon dissipation through Stoner excitations [151] or magnon-magnon interactions [152]. Each of the latter is influenced by the presence of impurities and other lattice imperfections [153] or layer thickness [154] and each mechanism is strongly temperature dependent [155]. The interplay of the different contributions critically complicates the estimation of the bulk value of the Gilbert damping for a given material. For such reason theoretical efforts often neglect the aforementioned mechanisms, collectively known as extrinsic contributions, to focus on the damping originating from electronic, or intrinsic, origin. The latter was firstly identified by Landau and Lifshitz [115] and arises because spin-orbit interaction breaks the spin rotational invariance and enable dissipation through phonons or electron scattering. This implies that the intrinsic contribution can be calculated given the sole knowledge of the electronic structure of a material. A large number of different methods to numerically evaluate

the damping was developed, an extensive review of these can be found in Ref. [156]. A first set of approaches is based on calculating the magnetic susceptibility, often within linear response theory, thus simulating a ferromagnetic resonance experiment [157]. These can often be computationally expensive since they require an appropriate energy resolution of the FMR peak. An alternative way is to relate the Gilbert damping to the dissipation induced by the spin-orbit torque response. This strategy was first proposed by Kamberský and is commonly known as torque correlation model (TCM) [158]. It can be formulated by estimating the interaction between a uniform spin excitation and a bath of conduction electrons. The latter can be quantified by the operators $\hat{\phi}^{\pm}$, that in absence of dipole interactions can be written as [159]

$$\hat{\phi}^{\pm} = \frac{\hbar}{N_s}[\hat{S}^{\pm}, \hat{H}_{\mathrm{SO}}]. \tag{6.1}$$

Here $\hat{S}^{\pm}$ are the ladder operators for electronic spins, $\hat{H}_{\mathrm{SO}}$ describes the spin-orbit interaction and N_s is a normalising factor accounting for the total magnetisation of the system. Dissipation effects can then be estimated by calculating the net magnon decay rate, τ_b, within the Fermi golden rule,

$$\frac{1}{2\pi\tau_b(\omega)} = \sum_{\mu\nu} |\phi^{-}_{\mu\nu}|^2 \big(f(E_\mu) - f(E_\nu)\big)\delta(E_\mu - E_\nu - \omega), \tag{6.2}$$

where μ, ν run over the electronic degrees of freedom, E_μ is the eigenvalue for the state $|\mu\rangle$, $\langle\mu|\hat{\phi}^{-}|\nu\rangle = \phi^{-}_{\mu\nu}$ and $f(E)$ is the Fermi-Dirac distribution centered around the Fermi energy. The relation between the Gilbert damping and τ_b can then be extracted from the Fourier transformed LLG equation and the damping parameter can be written as

$$\alpha = \lim_{\omega\to 0} \frac{1}{2\omega\tau_b} = \lim_{\omega\to 0} \sum_{\mu\nu} |\hat{\phi}^{+}_{\mu\nu}|^2 \big[f(E_\mu) - f(E_\nu)\big]\delta(E_\mu - E_\nu - \omega). \tag{6.3}$$

Other approaches that follow a similar strategy can be found in Refs. [160, 88].

A number of different calculations of damping parameters can be found in literature, e.g. see Refs. [161, 162]. The vast majority of them however were performed within either tight-binding models or the multi-scattering Korringa-Kohn-Rostoker (KKR) method [163]. The need of a system-specific parameterisation or the elevated

computational costs then make the systematic application of such methods to a vast range of materials not practically feasible. Moreover, the resulting Gilbert damping strongly depends on the choice of the finite life-time of electronic states. In real systems this is determined by the presence of several dissipation mechanisms such as inelastic electron-electron scattering or electron-phonon interactions. In practical simulations, these effects are normally accounted for by introducing a uniform energy broadening, η. Critically, the calculated damping can differ by orders of magnitude for different values of η (see e.g. Ref. [164]). In particular, the behaviour of the Gilbert damping for the limit of clean low-temperature systems, i.e. for $\eta \to 0$, is still debated [156]. A theoretical estimation of the broadening is not easily achievable because of the variety of mechanisms to be considered and their different relevance in different materials and physical conditions. As a consequence, the prediction and comparison of the damping parameter of a large number of materials is not achievable with the current methodologies.

We present here a novel method to estimate the Gilbert damping parameter that is suitable to be implemented in standard DFT codes and that does not require the input of an electronic life-time. It is based on the assumption that the relaxation of an electronic system to its equilibrium magnetic configuration is activated by the sole spin-orbit interaction and does not strictly depend on the energy dissipation mechanism. From a classical spin dynamics perspective, this process can be seen as the motion of the magnetisation in the effective field given by sole magneto-crystalline anisotropy. If all atomic spins uniformly relax to equilibrium, the characteristic spin relaxation time, τ, can be directly related to the Gilbert damping. We begin by showing how such relation can be found by the means of an approximated analytical solution of the LLG equation. Then, a novel approach to estimate the spin relaxation time from electronic structure calculations is presented. Although the latter is valid for a general Hamiltonian, particular attention will be dedicated to the case of a KS-like Hamiltonian.

6.1 Spin relaxation time and Gilbert damping

As explained above, the spin relaxation time is intimately related to the Gilbert damping parameter. We will show here how a quantitative relation between the two quantities can be established assuming that the magnetic moments uniformly rotate to equilibrium. For simplicity, we consider a uniform, constant applied field applied along the z direction, $\boldsymbol{H} = H\hat{\boldsymbol{z}}$. In these conditions, the LLG equation expressed in the LL form [see Eq. (4.6)] can be cast in the form

$$\begin{cases} \frac{\partial m_x}{\partial t} = -\omega_p m_y - \alpha\omega_p m_x m_z \\ \frac{\partial m_x}{\partial t} = +\omega_p m_x - \alpha\omega_p m_y m_z \\ \frac{\partial m_z}{\partial t} = \alpha\omega_p(1 - m_z^2), \end{cases} \tag{6.4}$$

where $\boldsymbol{m}$ indicates the normalised magnetisation vector, $\boldsymbol{M}/M$, and $\omega_p = \gamma H/(1 + \alpha^2)$. We remind that γ is the gyromagnetic ratio for the electron and α is the Gilbert damping. Since the equation for the z component is independent from the others, it can be integrated to find

$$m_z(t) = \tanh\big(\alpha\omega_p(t - t_0)\big), \tag{6.5}$$

where t_0 can be determined by specifying the value of $m_z(t)$ at $t = 0$. In order to solve the remaining equations we define the auxiliary variables

$$n_x = \frac{m_x}{\sqrt{1 - m_z^2}}, \qquad n_y = \frac{m_y}{\sqrt{1 - m_z^2}}, \tag{6.6}$$

so that the time derivative of, e.g. m_x, can be rewritten as

$$\frac{\partial m_x}{\partial t} = \sqrt{1 - m_z^2}\left(\frac{\partial n_x}{\partial t} - \alpha\omega_p n_x m_z\right). \tag{6.7}$$

The original equations in the new variables now become

$$\begin{cases} \frac{\partial n_x}{\partial t} = -\omega_p n_y \\ \frac{\partial n_y}{\partial t} = +\omega_p n_x, \end{cases} \tag{6.8}$$

Performing an additional time derivative then allows us to express them as the differential equations of two uncoupled harmonic oscillators,

$$\begin{cases} \frac{\partial^2 n_x}{\partial t^2} = -\omega_p^2 n_x \\ \frac{\partial^2 n_y}{\partial t^2} = -\omega_p^2 n_y, \end{cases} \tag{6.9}$$

which admit solutions of the form

$$\begin{cases} n_x(t) = A\cos(\omega_p t + \varphi) + B\sin(\omega_p t + \varphi) \\ n_y(t) = C\cos(\omega_p t + \varphi) + D\sin(\omega_p t + \varphi), \end{cases} \tag{6.10}$$

with A, B, C, D and φ being constants to determine through the initial conditions. Assuming the initial conditions $n_x(0) = 1$ and $n_y(0) = 0$, the constants can be determined to be $A = D = 1$ and $B = C = \varphi = 0$. Moreover, using the relation $1 - m_z^2 = 1 - \tanh^2(\alpha\omega_p t) = \operatorname{sech}^2(\alpha\omega_p t)$ the solutions can be expressed in terms of the original variables as

$$\begin{cases} m_x(t) = \cos(\omega_p t)\operatorname{sech}(\alpha\omega_p t) \\ m_y(t) = \sin(\omega_p t)\operatorname{sech}(\alpha\omega_p t) \\ m_z(t) = \tanh\big(\alpha\omega_p(t - t_0)\big). \end{cases} \tag{6.11}$$

These simple expressions allow us to infer which quantities determine the precession frequency and the relaxation time. The former is simply given by the quantity $\omega_p = \gamma H/(1 + \alpha^2)$, hence it is mostly controlled by the strength of the magnetic field. We remark that the damping constant plays a rather minor role here. Common values for α are found between 0.001 and 0.1, therefore its effect on the precession motion is at most to reduce slightly the effect of the field. Focusing now on the motion of the z component of the magnetisation, it is clear that the spin relaxation time can be defined as

$$\tau = \frac{1}{\alpha\omega_p} = \frac{1 + \alpha^2}{\alpha\gamma H}. \tag{6.12}$$

This relation indicates that τ is determined given the Gilbert damping, α, and the intensity of the effective magnetic field, H. In turn, the Gilbert damping parameter can be estimated given the knowledge of the spin relaxation time and the effective

field. In materials where the inter-atomic exchange is strong enough, all spins will uniformly relax to the equilibrium orientation and the effective field can be represented only by the magnetocrystalline anisotropy field. The strength of the latter can be quantified by the means of electronic structure calculations, as shown in §4.1.1.2. Therefore, the determination of the damping parameter for a given material corresponds to the calculation of the atomic spin relaxation time. A novel approach for the estimation of the latter starting from electronic structure calculations will be presented in the next section.

6.2 Density functional theory method for spin relaxation time calculations

Suppose that at an initial time, $t = t_0$, the direction of the magnetization, $\mathbf{M}(t)$, of a magnetic layer is rotated by a small angle, φ, from the equilibrium orientation, $\boldsymbol{M}_0$. For small deviation angles and strong inter-atomic exchange couplings, all atomic spins will rotate uniformly under the influence of the magneto-crystalline anisotropy field. After a certain time, τ, the angle, $\vartheta(t)$, that $\boldsymbol{M}(t)$ forms with $\boldsymbol{M}_0$ will vanish to recover the ground state magnetic configuration. In atomistic spin models this process is controlled by the Gilbert damping parameter. From the electronic point of view, the relaxation takes place thanks to the transfer of energy from the spin degrees of freedom to the electronic ones and to the environment (phonons, etc.), and is essentially mediated by the spin-orbit interaction. The strength of this dissipation mechanism is thus encoded in the coupling between the electronic and the spin degrees of freedom, while the remaining components act as a thermal bath through which energy can be dispersed. Therefore, the spin relaxation time, τ, can be evaluated in first approximation by considering an isolated system in which spin relaxation occurs as a rearrangement of the electronic level population that aligns the magnetisation with the equilibrium direction. As such, it can be extracted from the dynamics of the electronic system alone. The approach here proposed reformu-

lates the quantum Liouville equation so that it can be analytically solved for small angles. This will allow us to define the spin relaxation time in terms of the time-independent derivatives of the electron density and of the Hamiltonian with respect to the deviation angle, ϑ.

We begin by assuming that the spin motion is adiabatic with respect to the electron dynamics. This is reasonable since in most cases the dynamics of the two systems happens at two distinct time-scales, fs and ps or ns for electrons and spins, respectively. In such context the magnetisation can be assumed to evolve from one equilibrium electronic state to another. In other terms, the magnetisation vector at a given time t can be related to the spin-dependent electron density operator, $\hat{\rho}$, of the corresponding magnetic configuration of the electronic system,

$$\boldsymbol{M}(t) = \mathrm{Tr}\big\{\hat{\rho}(t)\boldsymbol{\sigma}\big\}. \tag{6.13}$$

Here, Tr denotes the trace over both spatial and spin degrees of freedom. Assuming that the magnetisation magnitude, $M = |\boldsymbol{M}|$, does not change during the dynamics, the magnetic configuration at the time t can be described by the angle defined as

$$\cos\vartheta(t) = \frac{1}{M^2}\boldsymbol{M}_0 \cdot \boldsymbol{M}(t) = \frac{1}{M^2}\boldsymbol{M}_0 \cdot \mathrm{Tr}\big\{\hat{\rho}(t)\boldsymbol{\sigma}\big\}. \tag{6.14}$$

We note that under our assumptions the equilibrium vector $\boldsymbol{M}_0$ has the same direction of the magneto-crystalline contribution to the anisotropy field and it is time-independent. Since the only time-dependent quantity for each term in the equality Eq. (6.14) is, respectively, $\vartheta(t)$, $\boldsymbol{M}(t)$ and $\hat{\rho}(t)$, the motion of one of the three can be expressed through either of the two. As a consequence, we can study the relaxation of the magnetisation to equilibrium by considering the sole angle, $\vartheta(t)$. Moreover, at all times $\vartheta(t)$ uniquely corresponds to an electronic configuration encoded in $\hat{\rho}(t)$, hence the time-dependence of the latter can be replaced by an angle dependence, i.e. $\hat{\rho}(t) \equiv \hat{\rho}\big(\vartheta(t)\big)$. An equation of motion for the deviation angle can then be obtained by performing the time derivative of the first and third term of Eq. (6.14), and reads

$$\frac{\partial\vartheta(t)}{\partial t}\sin\vartheta(t) = -\frac{1}{M^2}\boldsymbol{M}_0 \cdot \frac{\partial}{\partial t}\Big(\mathrm{Tr}\big\{\hat{\rho}(t)\boldsymbol{\sigma}\big\}\Big). \tag{6.15}$$

The second term can then be evaluated through the quantum Liouville equation associated to the generic Hamiltonian, $\hat{H}$, so that the angle dynamics is given by

$$\frac{\partial \vartheta}{\partial t} \sin \vartheta = \mathcal{C}\big(\vartheta\big), \tag{6.16}$$

where

$$\mathcal{C}(\vartheta) = \frac{i}{\hbar} \frac{\boldsymbol{M}_0}{M^2} \cdot \mathrm{Tr}\Big\{ \Big[\hat{H}(\vartheta), \hat{\rho}(\vartheta)\Big] \boldsymbol{\sigma} \Big\}. \tag{6.17}$$

This definition is valid assuming that the Hamiltonian of the system is functionally dependent on the density matrix. In such case the same one-to-one correspondence existing between $\hat{\rho}(t)$ and $\vartheta(t)$ can be naturally extended to $\hat{H}(t)$. Within linear response theory, the "commutator", $\mathcal{C}(\vartheta)$, can be expanded in a Taylor series around the equilibrium angle, $\vartheta = 0$,

$$\mathcal{C}(\vartheta) = \mathcal{C}^{(0)} + \mathcal{C}^{(1)}\vartheta + \frac{1}{2}\mathcal{C}^{(2)}\vartheta^2 + \mathcal{O}(\vartheta^3), \tag{6.18}$$

where we have defined for simplicity

$$\mathcal{C}^{(n)} = \frac{\partial^n \mathcal{C}}{\partial \vartheta^n}\Big|_{\vartheta=0}, \quad \text{for} \quad n \leq 1. \tag{6.19}$$

The zero-th order coefficient, $\mathcal{C}^{(0)}$, is proportional to the commutator between the Hamiltonian and the density matrix at equilibrium, hence is zero by definition. The small ϑ expansion of $\sin\vartheta$ then allows us to write Eq. (6.16) as

$$\frac{\partial \vartheta}{\partial t}\big(\vartheta + \mathcal{O}(\vartheta^3)\big) = \mathcal{C}^{(1)}\vartheta + \frac{1}{2}\mathcal{C}^{(2)}\vartheta^2 + \mathcal{O}(\vartheta^3), \tag{6.20}$$

where the expansion is truncated at the 2$^{\text{nd}}$ order in ϑ. At this point we note that in order for the equation to admit the trivial solution $\vartheta(t) = 0$ the first order coefficient, $\mathcal{C}^{(1)}$, should also identically vanish. As a consequence, we obtain to the simple result

$$\frac{\partial \vartheta}{\partial t} = \frac{1}{2}\mathcal{C}^{(2)}\vartheta. \tag{6.21}$$

We remark that the coefficient $\mathcal{C}^{(2)}$ does not depend on the angle, ϑ, nor on the time. Therefore, the equation can be easily integrated to obtain the elegant solution

$$\vartheta(t) = \varphi \ \mathrm{e}^{i\eta t} \ \mathrm{e}^{-t/\tau}, \tag{6.22}$$

where

$$\eta = \frac{1}{2}\mathrm{Im}\mathcal{C}^{(2)} = \frac{1}{2\hbar}\frac{\boldsymbol{M}_0}{M^2}\cdot \mathrm{Re}\frac{\partial^2}{\partial\vartheta^2}\mathrm{Tr}\Big\{\Big[\hat{H},\hat{\rho}\Big]\boldsymbol{\sigma}\Big\}, \tag{6.23}$$

$$\tau^{-1} = -\frac{1}{2}\mathrm{Re}\mathcal{C}^{(2)} = \frac{1}{2\hbar}\frac{\boldsymbol{M}_0}{M^2}\cdot \mathrm{Im}\frac{\partial^2}{\partial\vartheta^2}\mathrm{Tr}\Big\{\Big[\hat{H},\hat{\rho}\Big]\boldsymbol{\sigma}\Big\}. \tag{6.24}$$

Eq. (6.22) indicates that the deviation angle exponentially vanishes with a decay rate given by the relaxation time, τ. The latter is defined in terms of the derivatives of the electron density and the Hamiltonian with respect to the deviation angle, that can be expressed within finite differences. Therefore, these quantities can be estimated by performing electronic structure calculations for different magnetic configurations.

We note that this approach can be included in the family of spin-torque response methods. In fact, a more explicit expression for the commutator in Eq. (6.24) was already derived above [see Eq. 3.15)]. Maintaining the same notation adopted in §3.1.1, i.e. $\hat{\rho} = \hat{n} + \hat{\boldsymbol{\mu}}\cdot\boldsymbol{\sigma}$ and $\hat{\rho} = \hat{h} + \hat{\boldsymbol{\Delta}}\cdot\boldsymbol{\sigma}$, its second derivative can be written as

$$\begin{aligned}\frac{\partial^2}{\partial\vartheta^2}\sum_{\sigma\sigma'}\Big[\hat{H},\hat{\rho}\Big]\Big|_{\vartheta=0} &= \Big[\hat{h}(0),\hat{\boldsymbol{\mu}}''\Big] + \Big[\hat{h}'',\hat{\boldsymbol{\mu}}(0)\Big] + 2\Big[\hat{h}',\hat{\boldsymbol{\mu}}'\Big] \\ &+ \Big[\hat{\boldsymbol{\Delta}}(0),\hat{n}''\Big] + \Big[\hat{\boldsymbol{\Delta}}'',\hat{n}(0)\Big] + 2\Big[\hat{\boldsymbol{\Delta}}',\hat{n}'\Big] \\ &+ 2i\Big(\hat{\boldsymbol{\Delta}}(0)\times\hat{\boldsymbol{\mu}}'' + \hat{\boldsymbol{\Delta}}''\times\hat{\boldsymbol{\mu}}(0) + 2\hat{\boldsymbol{\Delta}}'\times\hat{\boldsymbol{\mu}}'\Big),\end{aligned} \tag{6.25}$$

where primed and double-primed quantities are first and second derivatives, while $\hat{\rho}(0)$ and $\hat{H}(0)$ denote the equilibrium density matrix and Hamiltonian, respectively. The commutators on the right-hand side correspond to the alteration of the spin flux during the spin dynamics and are likely to not substantially contribute to the relaxation time. On the contrary, the different cross products correspond to the variation of the spin torques during the spin relaxation. However, the definition of τ in Eq. (6.24) indicates that the relaxation time is related to the imaginary part of such commutator. Therefore, the spin relaxation time, hence the damping, is here related to the imaginary part of the spin torques induced by the change in the orientation of the magnetisation. In addition, we note that this approach accounts for both the change of conduction electrons and static moments (represented by $\hat{\boldsymbol{\Delta}}$), which is in opposition to standard spin-torque methods. This can be important to analyse

systems, where the magnetic moments critically depend on the atomic environment. Moreover, the current model can be easily generalised to estimate atom-dependent spin relaxation times. This operation is made simpler by assuming a localised basis set, such as atomic orbitals on which to construct the electronic structure theory. The use of electronic structure methods based non-localised basis functions, such as plane waves, is possible but requires a transformation to a localised basis (e.g. through Wannier functions). The atomic magnetic moments for a given electronic configuration can then be calculated by performing the partial (rather than total) trace, Tr_a of the density matrix operator over basis functions localised on a given site, a,

$$\boldsymbol{M}(t) = \sum_a \boldsymbol{m}_a(t) = \sum_a \mathrm{Tr}_a\big\{\hat{\rho}(t)\boldsymbol{\sigma}\big\}. \tag{6.26}$$

The deviation angle can then be defined for each atom by the relation

$$\cos\vartheta_a(t) = \frac{1}{Mm_a}\boldsymbol{M}_0 \cdot \boldsymbol{m}_a(t) = \frac{1}{Mm_a}\boldsymbol{M}_0 \cdot \mathrm{Tr}_a\big\{\hat{\rho}(t)\boldsymbol{\sigma}\big\}, \tag{6.27}$$

where $m_a = |\boldsymbol{m}_a|$. We remark that $\boldsymbol{M}_0$ plays the role of reference equilibrium direction, hence can be taken to be different for different atoms, if required. The derivation is now completely analogous to the one shown for a total angle, and yields the atom-specific spin relaxation time

$$\tau_a^{-1} = \frac{1}{2\hbar}\frac{\boldsymbol{M}_0}{Mm_a} \cdot \mathrm{Im}\frac{\partial^2}{\partial\vartheta^2}\mathrm{Tr}_a\bigg\{\Big[\hat{H},\hat{\rho}\Big]\boldsymbol{\sigma}\bigg\}. \tag{6.28}$$

This generalisation allows the methodology to be applied to a generic magnetic texture, including antiferromagnets and ferrimagnets.

We remark that the electronic broadening does not explicitly appear in such method. In this context, our scheme may be included at the DFT level for the electronic structure calculations needed to evaluate the derivatives within finite differences. The accurate estimation of the latter for different magnetic configurations is the main obstacle to be overcome to achieve a working implementation of this approach. In fact, a practical calculation of the spin relaxation time relies on an accurate estimation of the differences in the electronic structure for different configurations around equilibrium. This may not be possible with DFT accuracy. Therefore,

we attempted the implementation of our approach by using a mean-field tight-binding Hamiltonian of the form,

$$\sum_{\nu k\sigma'} \left\{ \delta_{lk}\delta_{\sigma\sigma'} t_{\mu\nu} + \delta_{\mu\nu}\delta_{lk} \left[\delta_{\sigma\sigma'} (\varepsilon_l + E_0 V^{\mathrm{C}}_{\mu l\sigma}) + \delta_{lk} \boldsymbol{\sigma}_{\sigma\sigma'} \cdot \boldsymbol{V}^{\mathrm{X}}_{\mu i} \right] + \delta_{\mu\nu} V^{\mathrm{SO}}_{l\sigma,k\sigma'} \right\} \psi^n_{\mu l\sigma} = E^n \psi^n_{\nu k\sigma'}, \tag{6.29}$$

where

$$V^{\mathrm{C}}_{\mu l\sigma} = (U + 2J) n_{\mu l\bar{\sigma}} + (U - \frac{J}{2}) \sum_{l \neq k} n_{\mu k}, \qquad \boldsymbol{V}^{\mathrm{X}}_{\mu k} = -J \sum_{l \neq k} \boldsymbol{S}_{\mu l}, \tag{6.30}$$

$$E_0 = -\frac{1}{N} \sum_{\mu l} \left[(U + 2J) n_{\mu l\uparrow} n_{\mu l\downarrow} + (U - \frac{J}{2}) \sum_{l<k} \sum_{\sigma\sigma'} n_{\mu l\sigma} n_{\mu k\sigma'} - J \sum_{l<k} \boldsymbol{S}_{\mu l} \boldsymbol{S}_{\mu k} \right]. \tag{6.31}$$

Here μ, ν run over atomic sites, $l, k = 1, \cdots, 5$ label the different d orbitals and σ, σ' denote the spin states, with $\bar{\sigma}$ indicating the opposite state of σ. The electronic configuration is defined by the occupations of the electronic state at the site μ with orbital l and spin state σ, $n_{\mu l\sigma}$, and the respective orientation of the electronic spin, $\boldsymbol{S}_{\mu k}$. The model is parameterised by the Coulomb integral, U, the exchange integral, J, the inter-atomic hopping parameters, $t_{\mu\nu}$, and the on-site energies, ε_l, that are tuned to simulate the presence of the crystal field. We note that such formulation is fully spin-rotational invariant. The ground-state configuration for a fixed orientation of the total magnetisation can then be found self-consistently, where the desired direction of the magnetisation is obtained by the means of a Lagrange multiplier.

Unfortunately, we were not able to obtain a working implementation of the model just described with the time at our disposal. Hence, here we have limited our discussion to the derivation of the approach and we postpone the analysis of numerical results to future works.

6.3 Summary

We have presented an overview of the difficulties in the theoretical estimation of the magnetic damping parameter. A novel method based on expressing the relaxation

dynamics in terms of the electronic degrees of freedom was presented. The equation of motion for the angle, ϑ, expressing the magnetisation misalignment from equilibrium was cast in the form of an exponential decay controlled by a relaxation time, τ. An atom-specific expression for the latter was derived in terms of the derivatives of the electron density and Hamiltonian with respect to ϑ. Such derivatives can in principle be calculated within finite difference methods given the electronic structure of the system for different magnetisation configurations.

Chapter 7

Conclusions and future work

"Life is not so much about beginnings or endings, it's about going on and on and on. "

- Anna Quindlen

We presented a multi-scale study of current-driven spin dynamics in magnetic tunnelling junctions. An overview of the features of such prototype devices was presented in Chapter 1, together with the material requirements to produce efficient spintronics applications.

In Chapter 2 we described the main concepts behind density functional theory and how it can be combined with non-equilibrium Green's functions to yield the transport properties of nano-scale systems. In Chapter 3 such methodology was employed to analyse the spin torques acting on different ferromagnetic free layers of Fe/MgO-based MTJs. We found that the spatial profile of the STT can be essentially predicted by examining the band symmetry of states populating the Fermi energies for the two spin channels. If the band structure of the ferromagnet allows for transport channels of both spin states, the spin torques slowly decay with a frequency that is given by the difference of the Fermi wave-vectors for the two spin channels. If one of the two spin channels cannot propagate in the ferromagnet, the STT decays exponentially in the free layer. This prediction, however, is not as accurate in presence of non-ideal interfaces and non-uniform magnetic textures. In fact, we find that a 25% oxidation

of the MgO/Fe interface produces a longer decay range than an ideal interface. Moreover, the of quantum well states present in the Fe stack in a Fe/Cu free layer yield an oscillating spatial profile, that is in contrast to the sharp decay in a pure Fe free layer. Similar effects induce a difference between the spin torques acting on FePt and FePt/Fe free layers. The case of $L1_0$ FePt layers is particularly interesting, since a non-vanishing torque acts on the induced moment at the Pt sites. Moreover, the STT has a long range decay within the FePt stacks, and such behaviour is not easily predicted as the case of free layers with uniform magnetic texture. Finally, we found that such oscillations are still observed in the presence of a small Fe seed layer, and the torque changes sign in the case of Ni seed layers.

In Chapter 4 we discussed an approach to simulate the spin dynamics at the atomistic level. Spin models capable to reproduce the thermodynamical properties of *bcc* Fe and $L1_0$ FePt were extensively described. The *ab-initio* spin torques discussed in Chapter 3 were then used as input for the spin dynamics simulations, in order to investigate the influence of the spatial profile of the spin torques in the magnetisation switching. We compared the switching properties and the spin-spin correlations in Fe, Fe/Cu and FePt free layers. We found that the critical voltage is essentially determined by the value of the torque integrated over the free layer. In addition, magnetisation reversal was found to be several times faster in free layers containing $L1_0$ FePt stacks than in the other cases. Moreover, the typical switching times of a FePt free layer were found to be mostly uniform for a given temperature and applied voltage, and to significantly decrease with increasing temperature. In contrast, in Fe and Fe/Cu layers the switching times distribute over a rather large spectrum of values, implying a rather poor stability to temperature fluctuations. Finally, we have considered the spin dynamics in a MTJ with a tunnelling barrier of different thickness and we found that the magnetisation switching occurs through a magnetic domain wall motion. Nevertheless, we remark that the spin torque is not qualitatively different throughout the cross section, since the different barrier thickness only modifies its intensity. This, however, may be different if one were to include also a partial oxidation of the insulator/free layer interface, that was shown

to effectively alter the spatial profile of the STT. Therefore, the combination of additional types of disorder may allow one to further investigate the nature of the magnetisation switching in disordered systems.

Chapter 5 was dedicated to the study of antiferromagnetic orderings in the Mn_3Ga and Fe_2MnGa Heusler compounds. Our results of FMR simulations in Mn_3Ga show the presence of an oscillation mode at frequencies that are an order of magnitude higher than the antiferromagnetic mode. To the best of our knowledge, such oscillation mode was never reported in other investigations, and its origins remain unclear and will require further analysis. We then showed that the induced moments at Fe sites in Fe_2MnGa are of fundamental importance for the determination of the magnetic properties of such compound. We showed that an effective model can be formulated for the AF phase and that the ferromagnetic alignment between the Mn moments at high temperatures can be attributed to the antiferromagnetic exchange coupling between Mn and Fe. Finally, we showed that for the Fe-terminated interface of Fe_2MnGa contacted to Fe/MgO, the transport properties are highly sensitive to the position of the Fermi energy. This implies that finite voltage calculations, as opposed to the zero-bias limit here considered, are likely to provide valuable additional information on the transport properties of the system. Moreover, the fact that the spin torque is mostly focused on the Fe moments indicates that the spin dynamics is also controlled by the magnitude of the induced moments. This made the analysis of current-driven dynamics on such systems not tractable within this Thesis. Nevertheless, the formulation of a spin model to reproduce the magnetic properties of Fe_2MnGa may be possible given an appropriate parameterisation of the moments at the Fe sites, which can then be included in the dynamics within the longitudinal spin fluctuations approach presented here. Such parameterisation may be achieved by considering several different orientations of the spins at the Mn sites by the means of constrained DFT calculations.

Finally, in Chapter 6 we presented a novel approach to calculate the Gilbert damping parameter from first principle simulations, although the numerical verification of the method was not achieved to date. Nevertheless, a successful imple-

mentation of such method would allow us to assess the Gilbert damping starting from few DFT calculations. In addition, the model could be easily extended to explicitly include factors such as electron-phonon interactions, and hence would allow the examination of specific dissipation mechanisms. This would improve our global understanding of the material dependence of spin dynamics at the atomistic level.

Appendix A

List of publications

- Mario Galante, Matthew O. A. Ellis, Stefano Sanvito, *Non-trivial spatial dependence of the spin torques in $L1_0$ FePt-based magnetic tunneling junctions*, Phys. Rev. B **99** 014401 (2019)

- Matthew O. A. Ellis, Mario Galante, Stefano Sanvito, *The role of longitudinal fluctuations in $L1_0$ FePt*, Phys. Rev. B **100** 214434 (2019)

Bibliography

[1] *The International Roadmap for Devices and Systems: 2017.* `https://irds.ieee.org/images/files/pdf/2017/2017IRDS_MM.pdf`. 1

[2] A. D. Buck. *Ferroelectrics for Digital Information Storage and Switching* (1952). 1

[3] C. H. Sie, A. V. Pohm, P. Uttech, A. Kao, R. Agrawal. *Chalcogenide Glass Bistable Resistivity Memory.* IEEE MAG-6:592 (1970). 1

[4] N. F. Mott. *The Electrical Conductivity of Transition Metals.* Proc. Roy. Soc. A 153:669 (1936). 1.1.1

[5] A. Fert, I. A. Campbell. *Two-Current COnduction in Nickel.* PRL 21:1190 (1968). 1.1.1

[6] P. Grünberg, R. Schreiber, Y. Pang, M. B. Brodsky, H. Sowers. *Layered Magnetic Structures: Evidence for Antiferromagnetic Coupling of Fe Layers across Cr Interlayers.* Phys. Rev. Lett. 57:2442 (1986). 1.1.1

[7] M. N. Baibich, J. M. Broto, A. Fert, F. N. Van Dau, F. Petroff, P. Etienne, G. Creuzet, A. Friederich, J. Chazelas. *Giant Magnetoresistance of (001)Fe/(001)Cr Magnetic Superlattices.* Phys. Rev. Lett. 61:2472 (1988). 1.1.1

[8] G. Binasch, P. Grünberg, F. Saurenbach, W. Zinn. *Enhanced magnetoresistance in layered magnetic structures with antiferromagnetic interlayer exchange.* Phys. Rev. B 39:4828 (1989). 1.1.1

[9] J. Bass, W. P. J. Pratt. *Current-perpendicular (CPP) magnetoresistance in magnetic metallic multilayers.* JMMM 200:274 (1999). 1.1.1, 1.1.1

[10] A. Fert, L. Piraux. *Magnetic nanowires.* JMMM 200:338 (1999). 1.1.1

[11] A. Vedyayev, M. Chshiev, N. Ryzhanova, B. Dieny, C. Cowache, F. Brouers. *A unified theory of CIP and CPP giant magnetoresistance in magnetic sandwiches.* JMMM 172:53 (1997). 1.1.1

[12] M. Julliére. *Tunnelling between ferromagnetic films.* Physics letters A 54:225 (1975). 1.1.2

[13] A. V. Khvalkovskiy, D. Apalkov, S. Watts, R. Chepulskii, R. S. Beach, A. Ong, X. Tang, A. Driskill-Smith, W. H. Butler, R. B. Visscher, D. Lottis, E. Chen, V. Nikitin, M. Krounbi. *Basic pinciples of STT-MRAM cell operation in memory arrays.* J. Phys. D: Appl. Phys. 46:074001 (2013). 1.2

[14] J. S. Moodera, L. R. Kinder, T. M. Wong, R. Meservey. *Large Magnetoresistance at Room Temperature in Ferromagnetic Thin Film Tunnel Junctions.* PRL 74:3273 (1995). 1.1.2

[15] T. Miyazaki, N. Tezuka. *Giant magnetic tunnelling effect in $Fe/Al_2O_3/Fe$ junction.* JMMM 139:L231 (1995). 1.1.2

[16] I. Rungger. *Computational methods for electron transport and their application in nanodevices By.* Ph.D. thesis, Trinity College Dublin (2008). 1.3, 2.2.2, 2.2.2.1, 2.2.2.2, 2.2.2.3, 2.2.2.4, 3.2

[17] W. H. Butler, X.-G. Zhang, T. C. Schulthess, J. M. MacLaren. *Spin-dependent tunneling conductance of Fe/MgO/Fe sandwiches.* Physical Review B 63(5):054416 (2001). 1.1.2

[18] J. Mathon, A. Umerski. *Theory of tunneling magnetoresistance of an epitaxial Fe/MgO/Fe(001) junction.* Phys. Rev. B 63:220403 (2001). 1.1.2

[19] S. Yuasa, T. Nagahama, A. Fukushima, Y. Suzuki, K. Ando. *Giant room-temperature magnetoresistance in single-crystal Fe/MgO/Fe magnetic tunnel junctions.* Nature Materials 3(12):868 (2004). 1.1.2

[20] S. S. P. Parkin, C. Kaiser, A. Panchula, P. M. Rice, B. Hughes, M. Samant, S.-H. Yang. *Giant tunnelling magnetoresistance at room temperature with MgO (100) tunnel barriers.* Nature materials 3(12):862 (2004). 1.1.2

[21] S. G. Wang, R. C. C. Ward, T. Hesjedal, X.-G. Zhang, C. Wang, A. Kohn, Q. L. Ma, J. Zhang, H. F. Liu, X. F. Han. *Interface Characterization of Epitaxial Fe/MgO/Fe Magnetic tunnel junctions.* J. Nanosci. Nanotechnol. 12:1006 (2012). 1.1.2, 3.3

[22] H. L. Meyerheim, R. Popescu, J. Kirschner, N. Jedrecy, M. Sauvage-Simkin, B. Heinrich, R. Pinchaux. *Geometrical and compositional structure at metal-oxide interfaces: MgO on Fe(001).* Physical review letters 87(7):076102 (2001). 1.1.2, 3.3

[23] X.-G. Zhang, W. H. Butler, A. Bandyopadhyay. *Effects of the iron-oxide layer in Fe-FeO-MgO-Fe tunneling junctions.* Phys. Rev. B 68:092402 (2003). 1.1.2, 3.3, 3.3, 3.3

[24] J. Slonczewski. *Current-driven excitation of magnetic multilayers.* Journal of Magnetism and Magnetic Materials 159(1-2):L1 (1996). 1.1.3, 3.1

[25] L. Berger. *Emission of spin waves by a magnetic multilayer traversed by a current.* Phys. Rev. B 54:9353 (1996). 1.1.3

[26] A. Brataas, A. D. Kent, H. Ohno. *Current-induced torques in magnetic materials.* Nature materials 11(5):372 (2012). 1.5, 1.1.3

[27] D. M. Edwards, F. Federici, J. Mathon, A. Umerski. *Self-consistent theory of current-induced switching of magnetization.* Physical Review B - Condensed Matter and Materials Physics 71(5):1 (2005). 1.1.3

[28] T. J. Silva, W. H. Rippard. *Developments in nano-oscillators based upon spin-transfer point-contact devices.* JMMM pages 1260–1271 (2010). 1.1.3

[29] X.-G. Zhang, W. H. Butler. *Large magnetoresistance in bcc* Co/MgO/Co *and* FeCo/MgO/FeCo *tunnel junctions.* PRB 70:172407 (2004). 1.2

[30] S. Yuasa, D. D. Djayaprawira. *Giant tunnel magnetoresistance in magnetic tunnel junctions witht a crystalline MgO(001) barrier.* J. of Phys. D: App. Phys. page R337 (2007). 1.2, 1.2

[31] D. D. Djayaprawira, K. Tsunekawa, M. Nagai, H. Maehara, S. Yamagata, N. Watanabe, S. Yuasa, Y. Suzuki, K. Ando. *230% room-temperature magnetoresistance in CoFeBMgOCoFeB magnetic tunnel junctions.* Applied Physics Letters 86(9):1 (2005). 1.2

[32] D. C. Ralph, M. D. Stiles. *Spin transfer torques.* Journal of Magnetism and Magnetic Materials 320(7):1190 (2008). 1.2

[33] S. Ikeda, K. Miura, H. Yamamoto, K. Mizunuma, H. D. Gan, M. Endo, S. Kanai, J. Hayakawa, F. Matsukura, H. Ohno. *A perpendicular-anisotropy CoFeB-MgO magnetic tunnel junction.* Nature materials 9(9):721 (2010). 1.2

[34] H. X. Yang, M. Chshiev, B. Dieny, J. H. Lee, A. Manchon, K. H. Shin. *First-principles investigation of the very large perpendicular magnetic anisotropy at Fe|MgO and Co|MgO interfaces.* Phys. Rev. B 84:054401 (2011). 1.2

[35] M. Gajek, J. J. Nowak, J. Z. Sun, P. L. Trouilloud, E. J. O'Sullivan, D. W. Abraham, M. C. Gaidis, G. Hu, S. Brown, Y. Zhu, R. P. Robertazzi, W. J. Gallagher, D. C. Worledge. *Spin torque switching of 20 nm magnetic tunnel junctions with perpendicular anisotropy.* Applied Physics Letters 100(13):1 (2012). 1.2.1

[36] B. Dieny, R. Sousa, S. Bandiera, M. Castro Souza, S. Auffret, B. Rodmacq, J. P. Nozieres, J. Herauilt, E. Gapihan, I. L. Prejbeanu, C. Ducuet, C. Portemont,

K. Mackay, B. Cambou. *Extended scalability and functionalitis of MRAM based on thermally assisted writing.* 2011 IEDM . 1.2.1

[37] H. Sukegawa, S. Mitani, T. Ohkubo, K. Inomata, K. Hono. *Low-resistive monocrystalline Mg-Al-O barrier magnetic tunnel junctions for spin-transfer magnetization switching.* Applied Physics Letters 103(14) (2013). 1.2.1

[38] P. Wadley, B. Howells, J. Železný, C. Andrews, V. Hills, R. P. Champion, V. Novák, K. Olejník, F. Maccherozzi, S. S. Dhesi, S. Y. Martin, T. Wagner, J. Wunderlich, F. Freimuth, Y. Mokrousov, J. Kuneš, J. S. Chauhan, M. J. Grzybowski, A. W. Rushforth, K. W. Edmonds, B. L. Gallagher, Jungwirth. *Electrical switching of an antiferromagnet.* Science 351:587 (2016). 1.2.1, 5

[39] J. Železný, P. Wadley, K. Olejnik, A. Hoffman, H. Ohno. Nat. Phys. 14:220 (2018). 1.2.1

[40] R. F. L. Evans, W. J. Fan, P. Chureemart, T. A. Ostler, M. O. A. Ellis, R. W. Chantrell. J. Phys.: Condens. Matter page 103202 (2014). 1.3

[41] J. F. Janak. *Uniform susceptibilities of metallic elements.* PRB 16:255 (1977). 2

[42] J. M. Soler, E. Artacho, J. D. Gale, A. Garcìa, J. Junquera, P. Ordejòn, D. Sànchez-Portal. *SIESTA Method For Ab Initio Order-N Materials Simulation, The.* J. Phys.: Condens. Matter 14(11):2745 (2002). 2, 2.1.3

[43] A. R. Rocha, V. M. García-suárez, S. W. Bailey, C. J. Lambert, J. Ferrer, S. Sanvito. *Towards molecular spintronics.* Nature Materials 4(4):335 (2005). 2

[44] A. R. Rocha, V. M. García-Suárez, S. Bailey, C. Lambert, J. Ferrer, S. Sanvito. *Spin and molecular electronics in atomically generated orbital landscapes.* Physical Review B - Condensed Matter and Materials Physics 73(8) (2006). 2, 2.2.2

[45] R. M. Martin. *Electronic Structure: Basic Theory and Practical Methods.* Cambridge University Press (2008). 2.1.1, 2.1.2

[46] J. Kondo. *Resistance Minimum in Dilute Magnetic Alloys.* Progress of Theoretical Physics 32(1):37 (1964). 2.1.1

[47] W. Nolting, W. M˘ ller, C. Santos. *Ferromagnetic Kondo-lattice model.* J. Phys. A: Math Gen. 36:9275 (2003). 2.1.1

[48] A. Altland, B. Simons. *Condensed Matter Field Theory.* Cambridge University Press (2006). 2.1.1

[49] M. Crisan, H. Jones. *Coexistence of Superconductivity and Ferromagnetism in the s-d Model.* J. of Low Temp. Phys. 18:297 (1975). 2.1.1

[50] P. Hohemberg, W. Kohn. *Inhomogeneous electron gas.* Physical Review B 136(3B):B864 (1964). 2.1.2

[51] K. Schönhammer, O. Gunnarson, R. M. Noak. *Density-functional theory on a lattice: Comparison with exact numerical results for a model with strongly correlated electrons.* PRB 52:2504 (1995). 2.1.2

[52] C. Fiolhais, F. Nagueira, M. Marques. *A primer in density functional theory.* Springer (2003). 2.1.2

[53] V. I. Anisimov, J. Zaanen, O. K. Andersen. Phys. Rev. B 44:943 (1991). 2.1.2

[54] J. P. Perdew, J. A. Chevay, S. H. Vosko, K. A. Jackson, M. R. Pederson, D. J. Singh, C. Fiolhai. *Atoms, molecules, solids, and surfaces: Applications of the generalised gradient approximation for exchange and correlation.* PRB 46:6671 (1992). 2.1.2

[55] *Abinit.* `https://www.abinit.org/`. 2.1.2.1, 2.1.3

[56] S. Sharma, J. K. Dewhurst, C. Ambrosch-Draxl, S. Kurth, N. Helbig, S. Pittalis, S. Shallcross, L. Nordström, E. K. U. Gross. *First-Principles Approach to*

Noncollinear Magnetism: Towards Spin Dynamics. Phys. Rev. Lett. 98:196405 (2007). 2.1.2.1

[57] G. Scalmani, M. J. Frisch. *A New Approach to Noncollinear Spin Density Functional Theory beyond the Local Density Approximation*. J. Chem. Theory Comput. 8:2193 (2012). 2.1.2.1

[58] I. W. Bulik, G. Scalmani, M. J. Frisch, G. E. Scuseria. *Noncollinear density functional theory having proper invariance and local torque properties*. Physical Review B - Condensed Matter and Materials Physics 87(3):1 (2013). 2.1.2.1

[59] H. A. Bethe, E. E. Salpeter. *Quantum Mechanics of One- and Two-Electron Systems* (1957). 2.1.2.1

[60] B. Kaduk, T. Kowalczyk, T. Van Voorhis. *Constrained Density Functional Theory*. Chem. Rev. 112:321 (2011). 2.1.2.2

[61] J. Kubler. *Theory of Itinerant Electron Magnetism*. Oxford University Press (2000). 2.1.2.2

[62] D. Hobbs, G. Kresse, J. Hafner. Phys. Rev. B 62:11556 (2000). 2.1.2.2

[63] P. Liu, S. Khmelevskyi, B. Kim, M. Marsman, D. Li, X. Chen, D. D. Sarma, G. Kresse, C. Franchini. Phys. Rev. B 92:054428 (2015). 2.1.2.2

[64] A. Bencini, F. Totti. J. Chem. Theory Comput. 5:144 (2009). 2.1.2.2

[65] *Elk*. `http://elk.sourceforge.net/`. 2.1.3, 5.2

[66] *FHI-aims*. `https://aimsclub.fhi-berlin.mpg.de/`. 2.1.3, 5.1

[67] *Vienna Ab-initio Simulation Package*. `https://www.vasp.at/`. 2.1.3

[68] *Quantum Espresso*. `https://www.quantum-espresso.org/`. 2.1.3

[69] *CP2K*. `https://www.cp2k.org/`. 2.1.3

[70] N. Troullier, J. L. Martins. *Efficient pseudopotentials for plane-wave calculations.* Phys. Rev. B 43:1993 (1991). 2.1.3.1

[71] I. Rungger, O. Mryasov, S. Sanvito. *Resonant electronic states and I-V curves of Fe/MgO/Fe(100) tunnel junctions.* Physical Review B - Condensed Matter and Materials Physics 79(9):2 (2009). 2.1, 2.2.2.4, 3.2, 3.2, 3.2, 3.2

[72] L. Kleinman. *Relativistic norm-conserving pseudopotential.* Phys. Rev. B 21:2630 (1980). 2.1.3.1

[73] L. Fernàndez-Seivane, M. A. Oliveira, S. Sanvito, J. Ferrer. *On-site approximation for spin-orbit coupling in linear combination of atomic orbitals density functional methods.* J. of Phys.: Condens. Matter 18:7999. 2.1.3.1

[74] E. Artacho, D. Sànchez-Portal, P. Ordejòn, A. Garcìa, J. M. Soler. *Linear-Scaling ab-initio Calculations for Large and Complex Systems.* Physica Status Solidi 215:809 (1999). 2.1.3.2

[75] S. Huzinaga, J. Andzelm, E. Radzio-Andzelm, Y. Sakai, H. Tatewaki, M. Koblukowski. *Gaussian Basis Sets for Molecular Calculations.* Elsevier: Berlin (1984). 2.1.3.2

[76] A. J. Cohen, P. Mori-Sánchez, W. Yang. *Insights into Current Limitations of Density Functional Theory.* Science 321:792 (2008). 2.1.4

[77] G. Rickayzen. *Green's Functions and Condensed Matter* (1980). 2.2

[78] A. Kamenev. *Field theory of non-equilibrium systems* (2011). 2.2

[79] S. Datta. Superlattices and Microstructures 28:253 (2000). 2.2

[80] S. Datta. *Electronic transport in mesoscopic systems* (1995). 2.2

[81] G. Stefanucci, R. van Leeuwen. *Nonequilibrium Many-Body Theory of Quantum Systems* (2013). 2.2, 2.2.1, 2.2.1.2

[82] A. L. Fetter, J. D. Walecka. *Quantum Theory of Many-Particle Systems* (2003). 2.2.1

[83] L. V. Keldysh. Sov. Phys. JETP 20:1018 (1965). 2.2.1

[84] S. Sanvito, C. J. Lambert, J. H. Jefferson, a. M. Bratkovsky. *General Green's-function formalism for transport calculations with spd Hamiltonians and giant magnetoresistance in Co- and Ni-based magnetic multilayers.* Phys. Rev. B 59(18):936 (1999). 2.2.2.1, 2.2.2.1

[85] I. Rungger, S. Sanvito. *Algorithm for the construction of self-energies for electronic transport calculations based on singularity elimination and singular value decomposition.* Physical Review B - Condensed Matter and Materials Physics 78(3):1 (2008). 2.2.2.1

[86] A. R. Rocha. *SMEAGOL (version 1.0)* (2005). `http://www.physics.udel.edu/~bnikolic/QTTG/shared/docs/Smeagol-1.0.pdf`. 2.2.2.4

[87] A. S. Núñez, A. H. MacDonald. *Theory of spin transfer phenomena in magnetic metals and semiconductors.* Solid State Communications 139(1):31 (2006). 3, 3.1.1

[88] A. Brataas, Y. Tserkovnyak, G. E. W. Bauer. *Scattering theory of Gilbert damping.* Physical Review Letters 101(3):1 (2008). 3.1, 6

[89] M. D. Stiles, A. Zangwill. *Anatomy of spin-transfer torque.* Physical Review B - Condensed Matter and Materials Physics 66(1):144071 (2002). 3.1, 3.1, 3.4, 3.4

[90] T. Min, J. Z. Sun, R. Beach, D. Tang, P. Wang. *Back-hopping after spin torque transfer induced magnetization switching in magnetic tunneling junction cells.* J. Appl. Phys. 105:07D126 (2009). 3.1

[91] S.-C. Oh, S.-Y. Park, A. Manchon, M. Chshiev, J.-H. Han, H.-W. Lee, J.-E. Lee, K.-T. Nam, Y. Jo, Y.-C. Kong, B. Dieny, K.-J. Lee. *Bias-voltage depen-*

dence of perpendicular spin-transfer torque in asymmetric MgO-based magnetic tunnel junctions. Nat. Phys. 5:898 (2009). 3.1

[92] P. M. Haney, D. Waldron, R. A. Duine, A. S. Núñez, H. Guo, A. H. MacDonald. *Current-induced order parameter dynamics: Microscopic theory applied to Co/Cu/Co spin valves.* Physical Review B 77(5):059901 (2007). 3.1.1

[93] P. M. Haney, R. A. Duine, A. S. Núñez, A. H. MacDonald. *Current-induced torques in magnetic metals: Beyond spin-transfer.* Journal of Magnetism and Magnetic Materials 320(7):1300 (2008). 3.1.1

[94] F. Mahfouzi, B. Nikolic. *How to construct the proper gauge invariant densty matrix in strady state nonequilibrium; applications to spin-transfer and spin-orbit torques.* Spin 3:130002 (2013). 3.1.1

[95] I. Rungger, A. R. Rocha, O. Mryasov, O. Heinonen, S. Sanvito. *Bias Dependent TMR in Fe/MgO/Fe(100) Tunnel Junctions.* MRS Proceedings 941:0941–Q01 (2006). 3.2

[96] J. Peralta-Ramos, A. M. Llois, I. Rungger, S. Sanvito. *I-V curves of Fe/MgO (001) single- and double-barrier tunnel junctions.* Phys. Rev. B 78:024430 (2008). 3.2

[97] Y. Xie, I. Rungger, K. Munira, M. Stamenova, S. Sanvito, A. W. Ghosh. *STT: A Multiscale Picture.* In J. Atulasimha, S. Bandyopadhyay, editors, *Nanomagnetic and Spintronic Devices for Energy-Efficient Memory and Computing.* John Wiley & Sons, Chichester, UK (2016). 3.2, 3.3

[98] X. Feng, O. Bengone, M. Alouani, S. Lebégue, I. Rungger, S. Sanvito. *Effects of structural relaxation on calculations of the interface and transport properties of Fe/MgO(001) tunnel junctions.* Phys. Rev. B 79:174414 (2009). 3.2

[99] M. O. A. Ellis, M. Stamenova, S. Sanvito. *Multiscale modeling of current-induced switching in magnetic tunnel junctions using* ab-initio *spin-transfer torques.* Phys. Rev. B 96:224410 (2017). 3.2, 4.3

[100] C. Heiliger, M. D. Stiles. *Ab Initio Studies of the Spin-Transfer Torque in Magnetic Tunnel Junctions*. Phys. Rev. Lett. 100:186805 (2008). 3.2

[101] X. Jia, K. Xia, Y. Ke, H. Guo. *Nonlinear bias dependence of spin-transfer torque from atomic first principles*. Phys. Rev. B 84:014401 (2011). 3.2

[102] I. Theodonis, N. Kioussis, A. Kalitsov, M. Chshiev, W. H. Butler. *Anomalous bias dependence of spin torque in magnetic tunnel junctions*. Physical Review Letters 97(23):2 (2006). 3.2

[103] Y. H. Tang, N. Kioussis, A. Kalitsov, W. H. Butler, R. Car. *Influence of asymmetry on bias behavior of spin torque*. Physical Review B - Condensed Matter and Materials Physics 81(5):1 (2010). 3.2

[104] C. Tusche, H. L. Meyerheim, N. Jedrecy, G. Renaud, A. Ernst, J. Henk, P. Bruno, J. Kirshner. *Oxygen-Induced Symmetrization and Structureal Coherency in Fe/MgO/Fe(001) Magnetic Tunnel Junctions*. Phys. Rev. Lett. 95:176101 (2005). 3.3

[105] C. Heiliger, P. Zahn, B. Y. Yarovsky, I. Mertig. *Influence of the interface structure on the bias dependence of tunneling magnetoresistance*. Phys. Rev. B 72:180406(R) (2005). 3.3

[106] U. Halisdemir. *Probing the impact of structural defects on spin dependent tunneling using photons* (2016). 3.3

[107] S. Wang, Y. Xu, K. Xia. *First-principles study of spin-transfer torques in layered systems with noncollinear magnetization*. Physical Review B - Condensed Matter and Materials Physics 77(18):1 (2008). 3.4

[108] K. Carva, I. Turek. *Landauer theory of ballistic torkances in noncollinear spin valves*. Physical Review B - Condensed Matter and Materials Physics 80(10):1 (2009). 3.4

[109] J. Xiao, G. E. W. Bauer, A. Brataas. *Spin-transfer torque in magnetic tunnel junctions: Scattering theory.* Physical Review B - Condensed Matter and Materials Physics 77(22):1 (2008). 3.4

[110] L. Zhang, Y. K. Takahashi, A. Perumal, K. Hono. *L10-ordered high coercivity (FePt)AgC granular thin film for perpendicular recording.* J. Magn. Magn. Mat. 322:18 (2010). 3.4.1

[111] Y. Taniguchi, Y. Miura, K. Abe, M. Shirai. *Theoretical studies on spin-dependent conductance in FePt/MgO/FePt(001) magnetic tunnel junctions.* IEEE Transactions on Magnetics 44(11 PART 2):2585 (2008). 3.4.1

[112] W. Zhu, D. Xiao, Y. Liu, S. J. Gong, C.-G. Duan. *Picosecond electric field pulse induced coherent magnetic switching in MgO/FePt/Pt(001)-based tunnel junctions: a multiscale study.* Scientific Reports 4:4117 (2014). 3.4.1

[113] A. Kohn, N. Tal, A. Elkayam, A. Kovacs, D. Li, S. Wang, S. Ghannadzadeh, R. C. C. Ward. *Structure of epitaxial L10-FePt/MgO perpendicular magnetic tunnel junctions.* Applied Physics Letters 102(6):062403 (2013). 3.4.1

[114] R. Cuadrado, R. W. Chantrell. *Interface magnetic moments enhancement of FePt-L10/MgO(001): An ab initio study.* Physical Review B 89(February):094407 (2014). 3.4.1

[115] L. Landau, E. Lifshitz. *On the theory of the dispersion of magnetic permeability in ferromagnetic bodies.* Phys. Zeitsch. der Sow. 8:153 (1935). 4.1, 6

[116] T. Gilbert. *Classics in Magnetics A Phenomenological Theory of Damping in Ferromagnetic Materials.* IEEE Transactions on Magnetics 40(6):3443 (2004). 4.1

[117] S. Iida. *The difference between Gilbert's and Landau-Lifshitz's equations.* J. Phys. Chem. Solids 24:625 (1962). 4.1

[118] T. Moriya. *Anisotropic superexchange interaction and weak ferromagnetism.* Phys. Rev. 120:91 (1960). 4.1

[119] K. Sanghoon, *et al.* *Correlation of the Dzyaloshinskii-Moriya interaction with Heisenberg exchange and orbital asphericity.* Nat. Comm. 9:1648 (2018). 4.1

[120] J. H. van Vleck. *On the Anisotropy of Cubic Ferromagnetic Crystals.* Phys. Rev. 52:1178 (1937). 4.1

[121] E. R. Callen, H. B. Callen. *Static Magnetoelastic Coupling in Cubin Crystals.* Phys. Rev. 129:578 (1963). 4.1

[122] M. Ellis. *Simulations of Magnetic Reversal Properties in Granular Recording Media* (2015). 4.1.1

[123] D. A. Garanin. Phys. Rev. B 53:11593 (1996). 4.1.1.1

[124] A. Liechtenstein, M. Katsnelson, V. Antropov, V. Gubanov. *Local spin density functional approach to the theory of exchange interactions in ferromagnetic metals and alloys.* Journal of Magnetism and Magnetic Materials 67(1):65 (1987). 4.1.1.1

[125] P. Bruno. *Exchange Interaction Parameters and Adiabatic Spin-Wave Spectra of Ferromagnets: A "Renormalized Magnetic Force Theorem".* Phys. Rev. Lett. 90:087205 (2003). 4.1.1.1

[126] G. Bihlmayer. *Non-Collinear Magnetism: Exchange Parameter and T_C.* Comput. Nanosc.: Do It Yourself! 31:447 (2006). 4.1.1.1

[127] J. M. D. Coey. *Magnetism and Magnetic Materials* (2012). 4.1.1.2

[128] M. Pajda, J. Kudrnovský, I. Turek, V. Drchal, P. Bruno. Ab initio *calculations of exchange interactions, spin-wave stiffness constants, and Curie temperatures of Fe, Co, and Ni.* Phys. Rev. B 64:174402 (2001). 4.2.1, 4.2.1

[129] R. Kubo. *The fluctuation-dissipation theorem.* Rep. Prog. Phys. 29:255 (1966). 4.2.1

[130] B. A. *Ferromagnetic resonance in arrays of highly anisotropic nanoparticles.* Eur. Phys. J. B 52:297 (2006). 4.2.1

[131] O. N. Mryasov, U. Nowak, K. Y. Guslienko, R. W. Chantrell. *Temperature-dependent magnetic properties of FePt: Effective spin Hamiltonian model.* Europhys. Lett. 69:805 (2005). 4.2.2

[132] C. Zener. *Classical Theory of the Temperature Dependence of Magnetic Anisotropy Energy.* Phys. Rev. 96:1335 (1954). 4.2.2

[133] P.-W. Ma, S. L. Dudarev. *Longitudinal magnetic fluctuations in Langevin spin dynamics.* Phys. Rev. B 86:054416 (2012). 4.2.2

[134] M. O. A. Ellis, M. Galante, S. Sanvito. Phys. Rev. B 100:214434 (2019). 4.4, 4.5, 4.2.2

[135] A. Hallal, H. X. Yang, B. Dieny, M. Chshiev. *Anatomy of perpendicular anisotropy of Fe/MgO magnetic tunnel junctions: First-principles insight.* Phys. Rev. B 88:184423 (2013). 4.3.1

[136] S. Iihama, S. Mizukami, H. Naganuma, M. Oogane, Y. Ando, T. Miyazaki. *Gilbert damping constants of Ta/CoFeB/MgO(Ta) thin films measured by optical detection of precessional magnetization dynamics.* Phys. Rev. B 89:174416 (2014). 4.3.1

[137] *Focus: Antiferromagnetic Spintronics.* Nature Physics 14 (2018). 5

[138] T. Jungwirth, J. Sinova, A. Manchon, X. Marti, J. Wunderlich, C. Felser. *The multiple directions of antiferromagnetic spintronics.* Nat. Phys. 14:200 (2018). 5

[139] T. Graf, S. S. P. Parkin, C. Fesler. *Heusler Compounds: A Material Class With Exceptional Properties.* IEEE Trans. Magn. 47:367 (2011). 5

[140] K. Rode, N. Baadji, D. Betto, Y.-C. Lau, H. Kurt, M. Venkatesan, P. Stamenov, S. Sanvito, J. M. D. Coey, E. Fonda, E. Otero, F. Choueikani,

P. Ohresser, F. Porcher, G. André. *Site-specific order and magneticm in tetragonal Mn3Ga thin films.* Phys. Rev. B 87:184429 (2013). 5.1

[141] S. Khmelevskyi, A. V. Ruban, P. Mohn. *Magnetic ordering and exchange interactions in structural modifications of Mn3Ga alloys: Interplay of frustration, atomic order, and off-stoichiometry.* Phys. Rev. B 93:184404 (2016). 5.1

[142] H. Kurt, K. Rode, M. Venkatesan, P. Stamenov, J. M. D. Coey. *High spin polarization in epitaxial films of ferrimagnetic Mn_3Ga.* Phys. Rev. B 83:020405(R) (2011). 5.1

[143] Y. N. Kudryavtsev, N. V. Uvarov, J. Dubowik. *Optical properties of Fe-Mn-Ga alloys.* J. Phys.: Condens. Matter 31:235501 (2019). 5.2

[144] T. Gasi, A. K. Nayak, M. Nicklas, C. Felser. *Structural and magnetic properties of the Heusler compound Fe2MnGa.* J. App. Phys. 113:17E301 (2013). 5.2

[145] E. C. Passamani, C. Larica, G. Viali, J. R. Andrez, A. Y. Takeuchi, V. P. Nascimento, V. A. P. Rodriguez, C. Rojas-Ayala, E. Baggio-Saitovitch. *In γ-Fe_2MnGa Heusler alloy do Fe and Mn sublattices magnetically couple parallel or antiparallel at low temperatures?* Journal of Alloys and Compounds 628:164 (2015). 5.2

[146] Y. V. Kudryavtsev, A. E. Perekos, N. V. Uvarov, M. R. Kolchiba, K. Synoradzki, J. Dubowik. *Mixed structural face-centered cubic and body-centered cubic orders in near stoichiometric Fe2MnGa alloys.* J. Appl. Phys. 119:205103 (2016). 5.2

[147] Y. V. Kudryavtsev, N. V. Uvarov, V. N. Iermolenko, J. Glavatskyy, Dubowik. *Electronic structure, magnetic and optical properties of Fe2MnGa Heusler alloy.* Acta Materialia 60:4780 (2012). 5.2

[148] J. Balluff. *Antiferromagnetics Heusler Compounds for Spintronics* (2017). 5.2, 5.2

[149] M. V. Gvozdikova, M. E. Zhitomirsky. *A Monte Carlo Study of the First-Order Transition in a Heisenberg FCC Antiferromagnet.* JETP Letters 81:236 (2005). 5.2, 5.2.1

[150] Y. Tserkovnyak, A. Brataas, G. E. W. Bauer. *Enhanced gilbert damping in thin ferromagnetic films.* Physical review letters 88(11):117601 (2002). 6

[151] V. Korenman, R. E. Prange. *Anomalous Damping of Spin Waves in Magnetic Metals.* Phys. Rev. B 6:2769 (1972). 6

[152] J. Lindner, K. Lenz, E. Kosubek, K. Baberschke, D. Spoddig, R. Meckenstock, J. Pelzl, Z. Frait, D. L. Mills. *Non-Gilbert-type damping of the magnetic relaxation in ultrathin ferromagnets: Importance of magnon-magnon scattering.* Phys. Rev. B 68:060102(R) (2003). 6

[153] R. D. McMicheal, D. J. Twisselmann, A. Kunz. *Localised Ferromagnetic in Inhomogeneous Thin Films.* Phys. Rev. Lett. 90:227601 (2003). 6

[154] E. Šimánek, B. Heinrich. *Gilbert damping in magnetic multilayers.* Physical Review B 67(14):144418 (2003). 6

[155] D. M. Edwards. *The absence of intraband scattering in a consistent theory of Gilbert damping in pure metallic ferromagnets.* J. Phys.: Condens. Matter 28:086004 (2016). 6

[156] F. S. M. Guimarães, J. R. Suckert, J. Chico, J. Bouaziz, M. dos Santos Dias, S. Lounis. *Comparative study of methodologies to compute the intrinsic Gilbert damping: interrelations, validity and physical consequences.* J. of Phys.: Cond. Matt. 31:255802 (2019). 6, 6

[157] A. T. Costa, R. B. Muniz. *Breakdown of the adiabatic approach for magnetisation damping in metallic ferromagnets.* Phys. Rev. B 92:014419 (2015). 6

[158] V. Kamberský. *On ferromagnetic resonance damping in metals.* Czechoslovak Journal of Physics 26(12):1366 (1976). 6

[159] V. Kamberský. *Spin-orbital Gilbert damping in common magnetic metals.* Phys. Rev. B 76:134416 (2007). 6

[160] H. Ebert, S. Mankovsky, P. J. Kelly. *Ab-initio calculation of the Gilbert damping parameter via linear response formalism.* PRL 066603(3):0 (2011). 6

[161] S. Mankovsky, D. Ködderitzsch, G. Woltersdorf, H. Ebert. *First principles calculations of the Gilbert damping parameter via the linear response formalism with application to magnetic transition metals and alloys.* Phys. Rev. B 87:014430 (2013). 6

[162] J. Chico, S. Keshavarz, Y. Kvashnin, M. Pereiro, I. Di Marco, C. Etz, O. Eriksson, A. Bergman, L. Bergqvist. *First-principles studies of the Gilbert damping and exchange interactions for half-metallic Heuslers alloys.* Physical Review B 93:214439 (2016). 6

[163] P. Mavropoulos, N. Papanikolaou. *The Korringa-Kohn-Rostoker (KKR) Green Function Method I. Electronic Structure of Periodic Systems.* Comput. Nanosci.: Do It Yourself! 31:131 (2006). 6

[164] E. Barati, M. Cinal, D. M. Edwards, A. Umerski. *Gilbert damping in magnetic layered systems.* Physical Review B - Condensed Matter and Materials Physics 90(1):1 (2014). 6